Order Number: 42248

Université Lille 1 - Sciences et Technologies

Doctoral School **ED Régionale SPI 72**

University Department **Laboratoire de Mécanique de Lille (LML)**

Thesis defended by **Ramon Silva Martins**

Defended on **25th November, 2016**

In order to become Doctor from Université Lille 1 - Sciences et Technologies

Academic Field **Mechanics, Energetics, Materials**

Speciality **Fluid Mechanics**

Thesis Title

Numerical simulation of turbulent viscoelastic fluid flows

Flow classification and preservation of positive-definiteness of the conformation tensor

Committee members

Referees	Manuel Alves		Associate Professor at FEUP - Univ. do Porto
	Charles-Henri Bruneau		Professor at IMB - Univ. de Bordeaux
Guests	Alexandre Delache		Lecturer at LMFA - Univ. de Saint-Étienne
	Silvia Hirata		Lecturer at Université de Lille 1
Supervisors	Laurent Thais	Supervisor	HDR Lecturer at Univ. de Lille 1
	Gilmar Mompean	Co-Supervisor	Professor at Univ. de Lille 1

Université Lille Nord de France
Pôle de Recherche et d'Enseignement Supérieur

Université de Lille 1 Sciences et Technologies

Université Lille 1 - Sciences et Technologies

Doctoral School **ED Régionale SPI 72**

University Department **Laboratoire de Mécanique de Lille (LML)**

Thesis defended by **Ramon Silva Martins**

Defended on **25th November, 2016**

In order to become Doctor from Université Lille 1 - Sciences et Technologies

Academic Field **Mechanics, Energetics, Materials**

Speciality **Fluid Mechanics**

Thesis Title

Numerical simulation of turbulent viscoelastic fluid flows

Flow classification and preservation of positive-definiteness of the conformation tensor

Committee members

Referees	Manuel Alves		Associate Professor at FEUP - Univ. do Porto
	Charles-Henri Bruneau		Professor at IMB - Univ. de Bordeaux
Guests	Alexandre Delache		Lecturer at LMFA - Univ. de Saint-Étienne
	Silvia Hirata		Lecturer at Université de Lille 1
Supervisors	Laurent Thais	Supervisor	HDR Lecturer at Univ. de Lille 1
	Gilmar Mompean	Co-Supervisor	Professor at Univ. de Lille 1

Université Lille 1 - Sciences et Technologies

École doctorale **ED Régionale SPI 72**

Unité de recherche **Laboratoire de Mécanique de Lille (LML)**

Thèse présentée par **Ramon Silva Martins**

Soutenue le **25 novembre 2016**

En vue de l'obtention du grade de docteur de l'Université Lille 1 - Sciences et Technologies

Discipline **Mécanique, Énergétique, Matériaux**

Spécialité **Mécanique des Fluides**

Titre de la thèse

Simulation numérique d'écoulements turbulents de fluides visco-élastiques

Classification d'écoulements et préservation de la positivité du tenseur de conformation

Composition du jury

Rapporteurs	Manuel Alves		professeur agrégé au FEUP - Univ. do Porto
	Charles-Henri Bruneau		professeur à l'IMB - Univ. de Bordeaux
Invités	Alexandre Delache		MCF au LMFA - Univ. de Saint-Étienne
	Silvia Hirata		MCF à l'Université de Lille 1
Directeurs de thèse	Laurent Thais	directeur	MCF HDR à l'Univ. de Lille 1
	Gilmar Mompean	co-directeur	professeur à l'Univ. de Lille 1

Keywords: viscoelastic flows, flow classification, vortex identification, objectivity, turbulent channel flow, drag reduction, turbulence, direct numerical simulation, artificial diffusion, FENE-P, conformation tensor

Mots clés : écoulements viscoélastiques, classification d'écoulements, identification de vortex, objectivité, écoulement turbulent en canal plan, réduction de la traînée, turbulence, simulation numérique directe, diffusion artificielle, FENE-P, tenseur de conformation

This thesis has been prepared at

Laboratoire de Mécanique de Lille (LML)
Boulevard Paul Langevin
Cité Scientifique
59655 Villeneuve d'Ascq Cedex
France

☎ (33)(0)3 20 33 71 52
(33)(0)3 20 33 71 53
lml@univ-lille1.fr
Web Site http://lml.univ-lille1.fr/lml/

Laboratoire Mécanique Lille

*To my maternal grandparents, Hilda (*in memoriam*) and Nilo,*
and my paternal grandparents, Hilda and Doiles.

Acknowledgements

To live abroad (in France) during the last four years in order to obtain my Ph.D. was a live-changing experience.

I have to start thanking my wife, Maíra Casagrande Martins, for her love, friendship and complicity. I've learned so much from her that we both cannot even imagine! By giving up of many things, she joined me in this journey and made each day of mine richer and more interesting. This is part of what I can translate into words. Thank you for everything you did and do for me, and for being such a tremendous woman beside me.

I am extremely thankful to all my family as well, who supported me even being thousands of kilometres away. I am specially grateful for my parents, for everything they have taught me and for their unconditional support.

I feel very grateful for my supervisors, Laurent Thais and Gilmar Mompean, for receiving me with attention, kindness and scientific spirit.

I came to France for a doctorate, but the most valuable gain I had was to know some spectacular people who became my "french family" (even if most of them are not French!). These people contributed to this time in France to be much more pleasant than expected. Thanks a lot Virginie, Youssef, Tibisay, Kalyan, Laís, Andrea, Laura, Sandro, Emmanuelle and family, Annick, Gilmar and family, Fred, Lionel and David. I feel obligated to highlight some of them for being more than friends: Aboulaye, Natália, João Rodrigo and Dário, you have been angels in my life. Thanks for being amazing and part of my life!

I am very thankful for Edson Soares for presenting me to Gilmar Mompean and being essential for this experience.

I also thank Roney Thompson for his friendship and partnership during these last four years. He has always been an inspiration to me.

I thank the Brazilian Government by means of CNPq for the financial support.

Huge thanks for the professors, secretaries and all staff from Polyech'Lille, Laboratoire de Mécanique de Lille and Université de Lille for their help.

Finally, I thank all the people who contributed, even unintentionally, to my life to be more pleasant during these last four years.

Numerical simulation of turbulent viscoelastic fluid flows

Flow classification and preservation of positive-definiteness of the conformation tensor

Abstract

The purpose of this work is to provide an enhancement of the knowledge about the polymer-induced drag reduction phenomenon by considering some aspects of its numerical simulation and the changes that occur in the flow kinematics. In the first part, the square root and kernel root-k formulations for the conformation tensor in the FENE-P model were implemented and showed to preserve the positiveness of the conformation tensor. However they led to numerical divergence due to the loss of boundedness of the conformation tensor. This constraint was violated even with the inclusion of artificial diffusion. The damping effect of artificial diffusion helped to ensure numerical stability, but led to relative drag reduction from 22% to 42% lower than expected from traditional methods. In the second part, the composition of two classic flow classification criteria was evaluated by means of the dynamic terms in the evolution equation of the strain-rate tensor. The λ_2-criterion was criticised due to the lack of clarity concerning some assumptions. The analyses of the Q-criterion suggest that the well-known weakening of vortical regions in drag-reducing flows is a consequence of non-linear interactions between the polymer stress and flow dynamics. Moreover, the use of objective flow classification criteria provided richer information concerning the flow kinematics. Finally, the thickening of the buffer layer in drag-reducing flows was visualised.

Keywords: viscoelastic flows, flow classification, vortex identification, objectivity, turbulent channel flow, drag reduction, turbulence, direct numerical simulation, artificial diffusion, FENE-P, conformation tensor

---

Simulation numérique d'écoulements turbulents de fluides visco-élastiques

Classification d'écoulements et préservation de la positivité du tenseur de conformation

Résumé

Le but de ce travail est de fournir une amélioration de la connaissance sur le phénomène de la réduction de la traînée induite par polymère en considérant certains aspects de sa simulation numérique et les changements qui se produisent dans la cinématique de l'écoulement. Dans un premier temps, les transformations du type racine carrée et *kernel* racine-k pour le tenseur de conformation du modèle FENE-P ont été implémentées afin d'assurer la positivité du tenseur de conformation. Cependant, ces approches divergent en raison du caractère non-borné du tenseur de conformation. Cette contrainte n'a pas été respectée, même avec l'inclusion de diffusion artificielle. L'effet d'amortissement de la diffusion artificielle a permis d'assurer la stabilité numérique, mais il aboutit à une réduction de la traînée relative de 22% à 42% plus faible que prévue par les approches standards. Dans un second temps, on a évalué la composition de deux critères classiques de classification d'écoulements à l'aide des termes dynamiques dans l'équation d'évolution du tenseur de déformation. Le critère λ_2 a été critiqué en raison du manque de clarté concernant certaines hypothèses. Les analyses du critère Q suggèrent que l'affaiblissement bien connu des régions tourbillonnaires dans les écoulements avec réduction de traînée est une conséquence des interactions non linéaires entre la tension polymérique et la dynamique de l'écoulement. En outre, l'utilisation de critères de classification d'écoulements objectifs a fourni des informations plus riches concernant la cinématique de l'écoulement. Enfin, l'épaississement de la zone tampon dans les écoulements avec réduction de traînée a été visualisé.

Mots clés : écoulements viscoélastiques, classification d'écoulements, identification de vortex, objectivité, écoulement turbulent en canal plan, réduction de la traînée, turbulence, simulation numérique directe, diffusion artificielle, FENE-P, tenseur de conformation

---

Laboratoire de Mécanique de Lille (LML)
Boulevard Paul Langevin – Cité Scientifique – 59655 Villeneuve d'Ascq Cedex – France

Acronyms

A | C | D | E | F | G | H | L | M | O | S

A

AVSS Adaptive Viscoelastic Stress Splitting. 12, 13

C

CUBISTA Convergent and Universally Bounded Interpolation Scheme for the Treatment of Advection. 12, 13

D

DNS Direct Numerical Simulation. 2, 4, 14, 23, 62, 84, 115

E

EEME Explicitly Elliptic Momentum Equation. 12
EVSS Elastic-Viscous Stress Splitting. 12, 13

F

FENE Finitely Extensible Nonlinear Elastic. 10, 15, 21, 22

G

GAD Global Artificial Diffusion. 16, 17

H

HWNP High Weissenberg Number Problem. 11

L

LAD Local Artificial Diffusion. 17

M

MDR Maximum Drag Reduction. 15
MPI Message Passing Interface. 39, 85

O

ODE Ordinary Differential Equations. xxi, 43–46, 133–136, 163
OpenMP Open Multi-Processing. 39

S

SPD Symmetric Positive Definite. 2, 24, 49

Contents

List of Tables

List of Figures

General Introduction

Motivation

The motion of fluids has always been a field of interest throughout history. Wind, vortices, buoyancy, convection, flight, navigation, pipe flow and many other aspects of fluid flow have been investigated until our days.

With the formalisation of Fluid Mechanics, mainly after the contributions of Sir Isaac Newton, Poisson, Navier and Stokes (among many other remarkable scientists), the motion of many fluids could be predicted by the Navier-Stokes equation. This notorious equation describes the motion of low-molecular-weight fluids, notwithstanding several complex questions remain open and under investigation. Even more complex issues appear in the study of fluids whose motions can not be described by the Navier-Stokes equations. These fluids are known as *non-Newtonian* fluids. There are several examples of non-Newtonian fluids which are part of our daily lives by different ways, such as blood, toothpaste, printer ink, yogurt, butter, nail polish, etc.

Among the non-Newtonian fluids, a variety of behaviours are possible, such as plasticity, viscoplasticity, thixotropy, elastoplasticity, elasticity, and viscoelasticity. We are particularly interested here in the flow of high-molecular-weight polymeric fluids, which present *viscoelastic* behaviour. "Visco" because they can somewhat resist shear as a viscous fluid. "Elastic" because they may respond to some degree as an elastic solid, deforming elastically and storing energy to, then, release it and recover partially their original shape.

Viscoelastic fluids involve several "*fascinating*" (as qualified by Bird and Curtiss [1]) and sometimes also challenging phenomena. Bird, Armstrong, and Hassager [2, Chapter 3] showed and explained various effects of viscoelastic fluid flow, including rod-climbing, extrudate swell, the tubeless siphon, drag reduction in turbulent flow and vortex inhibition. The latter two will be somehow explored, in this thesis.

Polymer-induced drag reduction and its numerical simulation

Over the last 20 years, the Direct Numerical Simulation (DNS) of viscoelastic fluid flows has been providing relevant information on the polymer-induced drag reduction phenomenon [3, 4]. After the pioneering DNS of Sureshkumar, Beris, and Handler [5], several numerical works have helped to enhance the knowledge about this phenomenon: Dimitropoulos and co-workers [6–9], De Angelis et al. [10], Min and co-workers [11, 12], Dubief et al. [13], Housiadas and co-workers [14–17], Dallas, Vassilicos, and Hewitt [18], Thais and co-workers [19–22] among others provided enriching data and discussions about the polymer-induced drag reduction. The polymer contribution to the Newtonian solvent is usually taken into account by means of a dumbbell model. Most of such models make use of a conformation tensor to describe polymer orientation [23].

By definition, the conformation tensor is Symmetric Positive Definite (SPD)[1]. Nevertheless, numerical simulations of turbulent flows of viscoelastic fluids using high-order schemes usually face non-physical high-wavenumber instabilities (the so called Hadamard instabilities [24]) that cause the loss of the positive-definiteness of the conformation tensor. Consequently, the uncontrolled growth of the non-SPD points leads to non-physical results and the simulation usually break down after a few iterations.

Several proposals to overcome this issue are available in the literature. One that has been largely used is the addition of an artificial stress diffusion [25] that brings an elliptical character to the hyperbolic evolution equation for the conformation tensor. Since diffusion has no physical meaning at the simulated scales (even for a DNS), the results obtained with this method will always be confronted to the question of how intrusive this additional term is with respect to the original model [26]. A less invasive alternative is to apply the artificial diffusion only to the domain points where the SPD condition is not fulfilled (e.g. [27]). Also, alternatives without any artificial term do exist. They are usually based on flux-limiter schemes to overcome the typical exponential growth on the field of the conformation tensor due to the steep gradients inherent to high-precision simulations of viscoelastic flows [18, 28–30].

More recent solutions propose transformations to be applied to the conformation tensor in order to enforce mathematically its positive-definiteness [31–34]. Some of these transformations however have not yet been tested in the context of turbulent viscoelastic shear flows exhibiting drag reduction, which brings us to part of the scope of this thesis.

The polymer-induced drag reduction is known to change flow dynamics. One of the most evident changes in wall turbulence of viscoelastic fluid is the weakening and elongation of vortices [35]. Motivated by this changes, the evaluation of different

[1] A symmetric matrix $\boldsymbol{M}$ is SPD if $\boldsymbol{z} \cdot \boldsymbol{M} \cdot \boldsymbol{z}^T > 0$ for arbitrary (non-zero) $\boldsymbol{z}$.

motions in the context of turbulent drag-reducing flows and the proper identification and interpretation is also being considered here.

Vortex identification and flow classification in the context of turbulent viscoelastic fluid flows

The concept of a *vortex* is still cause for dissension within the scientific community. There is not a true consensus for the definition of a vortex. There are indeed several mathematical quantities available in the literature to identify a vortex. Some of them are very popular, such as the Q-criterion by Hunt, Wray, and Moin [36], Δ-criterion by Chong, Perry, and Cantwell [37], λ_2-criterion by Jeong and Hussain [38], λ_{ci}-criterion by Zhou et al. [39]. Despite this hazy definition, what is consensual is that there are coherent rotating structures whose dynamics plays an important role in different transport phenomena, such as heat transfer, mixing, combustion, noise generation, aero- and hydrodynamic drag and other typically turbulent flows.

Vortex identification and flow classification are closely linked, since, the ideas regarding vortex involve fluid rotation and one of the interests of flow classification is to separate, for instance, rotational and extensional regions of a flow.

Besides the issue of defining a vortex, other discussions gravitating over properties that flow classification criteria must have also persist. One of them is whether a flow classification criterion should be invariant to arbitrary translating-rotating reference frame or to constant speed translations only. In other words, respectively, should a criterion enjoy Euclidean invariance or Galilean invariance only would be enough? Historically, the majority of flow classification criteria are Galilean invariant, but some authors claim that a solid criterion should be objective (or Euclidean frame indifferent), *i.e.* invariant to any possible transformation.

In the context of viscoelastic flows, other questions arise: When applied to a viscoelastic fluid flow, should a flow classification criterion take into account rheological parameters or not? If one uses a criterion that was conceived for a Newtonian fluid in a viscoelastic fluid flow, how to interpret such results? Moreover, it is known that the polymer coil-stretch process affects vortex dynamics, but is it possible to go more into details? These are questions we will explore in this work.

Objectives

The flow of viscoelastic fluids is a field in which numerous questions remain open due to the complexity of the phenomena. Among the open questions, we shall address the following in the present work:

1. *Transformations for the conformation tensor in the numerical simulation of turbulent polymer-induced drag-reducing flows.*
   The objective here is to evaluate the performance of more recent formulations for the conformations tensor that preserve the definite-positiveness of the conformation tensor. More precisely, the square-root [33] and the root^k kernel [34] transformations will be applied to turbulent channel flows. The need for maintaining (or not) an artificial stress diffusion in order to preserve numerical stability will also be assessed.

2. *Vortex identification and flow classification in the context of turbulent viscoelastic flows and the role of objectivity.*
   The goal here is to analyse the behaviour of objective versions of classic criteria available in the literature. The exercise will be conducted for several benchmark flows, such as the ABC flow, the abrupt contraction and the turbulent channel flow.

   Furthermore, recent flow classification criteria [40] which are naturally objective will be applied to the same flows. Finally, the contribution of polymers to the identification of vortices and its dynamics is investigated in the context of turbulent channel flow of viscoelastic fluids.

In both of these fronts, we will use the `nnewt_solve` algorithm developed by Thais et al. [19]. This code is a massively parallel scheme conceived to perform DNS of turbulent drag-reducing flows. It uses hybrid Fourier spectral and sixth-order compact finite differences schemes for spatial discretisation, and time marching can be up to fourth-order accurate. The parallelism is facilitated by a two-dimensional MPI Cartesian grid, together with OpenMP multi-threading.

Regarding the first objective, the algorithm will be adapted to model the evolution equation for the transformation of the conformation tensor. The second objective involves mostly post-processing methodologies and theoretical discussions on the identification of vortices.

Organisation of the document

This document is divided in two parts along the two objectives mentioned above.

Part I consists on the application of transformations to the conformation tensor with the aim to avoid the loss of evolution in the simulation of turbulent wall-bounded viscoelastic fluid flows due to the lack of positive-definiteness of the conformation tensor. The need for maintaining or not an artificial stress diffusion is also assessed.

Part II comprises theoretical discussions on the role of objectivity in flow classification and vortex identification. In a first moment, we discuss how the flow classification criteria are impacted by the presence of polymers and how to take that into account when trying to make conclusions on the flow dynamics of viscoelastic fluids. Then, preliminary results for laminar and analytical flows are discussed. Finally, several criteria are applied to turbulent channel flows of both Newtonian and viscoelastic fluids.

A portion of the results contained in this part is a compilation of the following works that have been published (journal paper and book chapter):

- Ramon S. Martins, Anselmo S. Pereira, Gilmar Mompean, Laurent Thais and Roney L. Thompson. *An objective perspective for classic flow classification criteria.* Comptes Rendus Mécanique, 344, pp. 52–59, 2016.

- Ramon S. Martins, Anselmo S. Pereira, Gilmar Mompean, Laurent Thais and Roney L. Thompson. *On Objective and Non-objective Kinematic Flow Classification Criteria.* In: Progress in Wall Turbulence 2: Understanding and Modelling. Eds. Michel Stanislas, Javier Jimenez, and Ivan Marusic. Cham: Springer International Publishing, 2016. pp. 419–428.

Part I

Evaluation of root-type transformations for the conformation tensor applied to turbulent channel flows of viscoelastic fluids

Chapter 1

Numerical simulation of viscoelastic fluid flow: State of the art

The flow of viscoelastic fluids is fascinating because of the strange effects associated with them. The Newtonian fluid mechanics has been quite explored and reasonably explained. However, viscoelastic fluids behave differently. They exhibit non-linear and time dependent responses to deformation. Moreover, the stress is also anisotropic, *i.e.* it can present different behaviour according to the direction. These characteristics lead to instabilities that may appear in several geometries and at different flow regimes.

From a numerical point of view, these effects are generally reproduced with the aid of viscoelastic fluid models. These models try to capture the essence of viscoelasticity and to simulate the effect of polymer solutions. Many options are now available in the literature, leading to several type of models: differential, integral, linear, nonlinear. Among these groups, there is an important class of models that approximates polymer molecules diluted in a Newtonian solvent as a set of beads and springs (see Fig. 1.1).

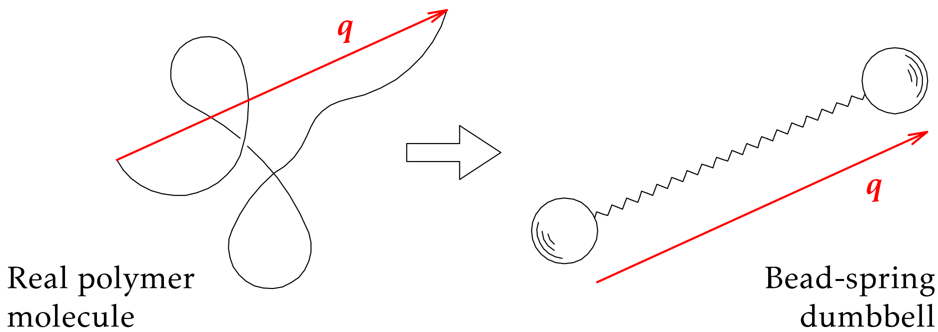

Figure 1.1 – Schematic representation of a real polymer molecule and its physical representation as a bead-spring dumbbell. The vector $\boldsymbol{q}$ is the *end-to-end* vector.

The beads represent very small polymer monomers while the springs connecting them act like a restoring force that virtually represent the tendency of polymer chains to coil. These models are also referred to as dumbbell models. Hookean (linear) springs present infinite extensibility and, even so, can reasonably reproduce lots of viscoelastic phenomena. One of the most used Hookean dumbbell models is the Oldroyd-B model [23].

On the other hand, limiting the polymer stretch leads to an important class of models known as Finitely Extensible Nonlinear Elastic (FENE) models [23]. Besides the more realist physical foundation behind these models (when compared to linear elastic models), they are able to better approach combinations of a given polymer-solvent by varying its parameters.

One drawback of the FENE model is that it does not have a closure that allows its implementation for numerical calculations on general transport phenomena. In an effort to obtain results with such a promising methodology, several closures have been proposed, as, for instance, FENE-P [41], FENE-CR [42], FENE-L and FENE-LS [43, 44], FENE-CD [45], FENE-DT [46], FENE-QE [47].

Usually, the interesting viscoelastic effects are time-dependent and, some of them, get more intense with increasing elasticity. When performing simulations of unsteady viscoelastic fluid flows, however, it is quite common to find limitations due to numerical instabilities.

1.1 The conformation tensor and its properties

Dumbbell models are usually based on a tensor that carries information about the configuration of each individual polymer molecule. This tensor is usually named *conformation tensor* and is formed by the components of the *end-to-end vector* that connects the polymer chain ends [23]. Because of its physical meaning and mathematical representation, the conformation tensor is symmetric and positive definite (SPD) and must remain so. In particular, in the FENE-P model, the conformation tensor receives another constraint due to the approximation proposed by Peterlin [41]. This approximative closure consists on a pre-averaging in space for the end-to-end vector. Consequently, the trace of the conformation is then bounded by the square of the maximum chain extensibility imposed by the pre-averaging.

Vaithianathan and Collins [26] point out three issues associated to the conformation tensor in numerical simulations.

- *Positiveness (or positive-definiteness) of the conformation tensor.*
  Negative eigenvalues are equivalent to locally negative viscosity. Thus, the loss of positive-definiteness gives rise to instabilities that may lead to non-physical results or even numerical divergence.

- *Boundedness of the conformation tensor.*

For models that consider a finite extensibility to the polymer chain (such as the FENE-P model), special attention should be given to the trace of the conformation tensor, which indicates how stretched the polymer molecules are. For instance, in the FENE-P model, the trace is bounded by the theoretical upper value of the chain extensibility squared. All the same, highly extensional flows may give rise to numerical errors due to overextension of the conformation tensor. When this happens, the restoring force changes sign, leading to divergence. The authors comment that solving the equations implicitly may partially alleviate this, but the price is a much slower convergence rate.

- *Lack of a dissipation mechanism.*
  If, for any reason, steep gradients are generated in the conformation tensor, the polymer stress divergence might increase without bound. The authors state that, physically, a molecular mechanism is expected to truncate this growth, but no diffusion term is included in most used models.

These three points are challenges for the scientific community involved in the simulation of viscoelastic flows. Notably, the third issue concerns turbulent flows, in which sharp gradients are more common.

In an effort to better understand how the properties of the conformation tensor affect the simulation of viscoelastic flows, the literature review presented below is split in three sections. Each section contains the main effects observed under specific conditions, the limitations of their numerical simulations and the main solutions available. The first section is dedicated to laminar flows, the second section presents the special case of elastic turbulence, and the third section discusses (inertial) turbulent phenomena, such as drag reduction, on which our attention is focused here.

1.2 High Weissenberg Number Problem and loss of positiveness in viscoelastic flows

Simulating viscoelastic flows in complex geometries has been a challenge to the scientific community. According to Keunings [48], "ever since the early attempts of the mid 1970's, researchers have repeatedly met with an outstanding problem, namely the failure of their numerical schemes to provide solutions beyond some critical value of the Weissenberg number [...]". This has been often referred to as the High Weissenberg Number Problem (HWNP). The critical Weissenberg number depends on the geometry and on the model (constitutive equation) used for the polymer solution.

In order to understand the HWNP, the problem has been addressed from different fronts. Basically, mathematical and numerical explanations were sought.

Rutkevich [49–52] firstly explored the evolutionary conditions of viscoelastic flows using Maxwellian fluids. In the work of Joseph, Renardy, and Saut [53], the change of (mathematical) type of the system of equations was investigated and the concept of Hadamard instability [24] in this context was introduced. The authors claim that small instabilities caused by ill-posed initial(-boundary) value problems may lead to oscillations that grow exponentially. Physically, it may warn about instabilities, but, in the context of numerical simulation, this leads to divergence [54]. Following that, several fluid models and flows were explored [24, 55–59].

In the late 1980's some first workarounds were proposed. The concomitant advances in parallel computation and numerical methods lead to the further evolution of more successful simulations that were able to explore slightly higher elasticity values and more complex flows with more accuracy and stability. We present in the following the main methods that contributed to such evolution.

1.2.1 Some remedies available

The first strategies consisted of manipulating the constitutive equation so that their elliptic character could be somehow split from the hyperbolic one. This leads to numerical stability, mainly because of the smoothing character coming with ellipticity. This was the case, for instance, for the following schemes: Explicitly Elliptic Momentum Equation (EEME) [60], Elastic-Viscous Stress Splitting (EVSS) [61], and Adaptive Viscoelastic Stress Splitting (AVSS) [62]. Even though these solutions were the first proposed to stabilise the simulation of viscoelastic fluid flows, they are still quite used nowadays, sometimes combined with more recent methods.

Alves, Oliveira, and Pinho [63] came up with a high resolution scheme that limits the flux of advection terms with good iterative convergence. The so called Convergent and Universally Bounded Interpolation Scheme for the Treatment of Advection (CUBISTA) was tested in a code based on finite-volume, for Newtonian flows over a backward-facing step, and viscoelastic flows past a cylinder and in a sudden contraction. For the viscoelastic flows, the CUBISTA scheme was also used for the advection term in the constitutive equation, leading to better stability and accuracy.

By using a unique decomposition to the velocity gradient, Fattal and Kupferman [31] reported a new logarithmic transformation for the conformation tensor. The authors were inspired by the idea of smoothing the steep gradients that arise in the field of the conformation tensor. They applied their methodology to the lid-driven cavity flow of a FENE-CR [42] fluid without the need of an artificial stress diffusion. Using a finite difference framework, they stated that their scheme remains stable at moderately high Weissenberg numbers. Later, the authors presented more detailed results with an Oldroyd-B fluid [32] and affirm that for sufficiently high Weissenberg numbers, strong oscillations lead to divergence.

More recently, Balci et al. [33] showed that there is also a unique square-root transformation for the conformation tensor that can guarantee its positive-definiteness. The authors presented the formulation for both Oldoryd-B and FENE-P fluids. However, they performed simulations of Stokesian flows using Oldroyd-B fluids without any artificial stress diffusion. Higher Weissenberg numbers could be achieved with improved stability and accuracy, although limitations were still found with increasing elasticity. The authors highlighted the easy implementation and the low CPU requirements of their formulation compared to logarithmic transformation. Their statement is based on the fact that their method does not require the calculation of eigenvalues and eigenvectors of the conformation tensor at every time step.

Afonso, Pinho, and Alves [34] gathered the decomposition of the velocity gradient by Fattal and Kupferman [31] and the idea of applying transformations to the conformation tensor to present a generic framework for a large group of matrix transformations. The so-called *kernel* transformation has shown to recover the log- and square-root-conformation formulations. The method was tested for a confined cylinder flow of an Oldroyd-B fluid for various logarithm-based and root-based models (among others). They concluded that the kernel transformation can be used to gain numerical stability, but the best choice of kernel function depends on its capacity of smoothing gradients in the conformation field and still preserve its positiveness. It is important to remark that the square-root formulation deriving from the kernel transformation differs from the originally proposed by Balci et al. [33]. The main difference is that, in the kernel transformation framework, the calculation of eigenvalues and eigenvectors of the conformation tensor is required in the whole domain at every time step.

The alternatives cited above have been tested in different contexts in laminar viscoelastic flows. Among many others, one may cite the use of EVSS and AVSS to simulate extrudate swell [64], EVSS to simulate 180° bent planar channel and in a 4:1 planar contraction [65], lid-driven cavity, flow past a cylinder, 4:1 contraction using the square-root and the logarithm conformations with the CUBISTA scheme [66], the log-conformation to simulate a lid-driven cavity [67] and the flow past a cylinder [68], the square-root transformation combined with the CUBISTA scheme to solve the lid-driven cavity flow, the flow around a confined cylinder, the cross-slot flow and the impacting drop free surface problem [69], a combination of the kernel conformation with CUBISTA scheme to simulate the Poiseuille flow in a channel, the lid-driven cavity flow and the extrudate-swell free surface flow with Oldroyd-B fluid [70], and, more recently, the Weissenberg effect [71] using the kernel-conformation.

1.3 Elastic turbulence: nor simply laminar, neither merely turbulent

The flow of polymer solutions at vanishing Reynolds number and high level of elasticity indicates chaotic fluctuations in time and space, similar to those observed in (inertial) turbulent flows. It is known now that this phenomenon is purely elastic and it is usually referred to as *elastic turbulence* [72].

Experiments suggest that the onset of elastic turbulence is associated to curvilinear streamlines. Therefore, most of successful numerical simulations of this phenomenon so far have been carried out using curvilinear geometries or imposing forces to the flow field that produces circular motion.

In the curvilinear geometry context, Thomas, Sureshkumar, and Khomami [73] performed DNS of 3D time-dependent Taylor-Couette flows of a FENE-P fluid. The authors found instabilities of elastic origin demonstrating spatial and time variation patterns. For these simulations, the authors adapted a fully spectral algorithm previously used for turbulent channel flows [5] that uses artificial diffusion to avoid the loss of positiveness and ensure stability (see the next section for more information on the use of artificial diffusion). More recently, Feng-Chen et al. [74] simulated curvilinear channel flow driven by pressure gradient. The authors used a Giesekus [75] model also with the addition of artificial diffusion (as proposed by [25]) to avoid steep oscillations and undershoot/overshoot. They present a brief and preliminary explanation of intermittent energy pumping in the flow.

Concerning wall-free flows with an imposed curvilinear force term, Berti and coauthors [76, 77] conducted DNS of Kolmogorov flows using the Oldroyd-B model with the Cholesky decomposition proposed by Vaithianathan and Collins [26] to guarantee the maintenance of positiveness for the conformation tensor. Stationary states transits to a chaotic state when properly excited over a critical Weissenberg number. The power spectrum of velocity fluctuations in chaotic state is found to be close to experimental results. Thomases and Shelley [78] performed simulations of 2D periodic Stokesian flows using the Oldroyd-B model in a pseudospectral code. They found two transitions: one being steady and asymmetric and the other being oscillatory.

Results using a classic straight channel flow are also available. On one hand, Hong-Na et al. [79] added a sinusoidal force term to both the momentum equation and the Giesekus constitutive equation of their DNS to excite the flow, usually stable. The authors conclude that large shear rates are important to elastic turbulence, because, at the regions where they occur, strong stretching and more intense vortical activity are observed. On the other hand, Samanta et al. [80] introduced the concept of *elasto-inertial turbulence*. They performed pipe flow experiments and DNS of channel flows using the FENE-P model with local artificial diffusion (see the next section for further information about local artificial diffusion). The authors stress that their results contain a non-negligible amount of inertia, but, still, it seems to be related to elastic turbulence. They found that the transition point to turbulence is delayed when polymer solutions are compared to their relative Newtonian cases. Moreover, they noticed that elastic instabilities that appear at the regions of large shear rate lead to friction factors comparable to the Maximum Drag Reduction (MDR) regime (further information on MDR is available in the next section).

In a very recent paper, Ray and Vincenzi [81] used a shell model that imitates the Fourier modes of the velocity field and of the polymer configuration field for a viscoelastic fluid flow without the information on the spatial structure of these fields. The resulting formulation is like a reduced low-dimensional version of the FENE model [23]. The authors verify the transitional and the chaotic states of elastic turbulence for different Weissenberg numbers and polymer concentrations, concluding that these two parameters show similar influence on the transition to elastic turbulence. Moreover, they claim that the physical mechanisms that lead to elastic turbulence do not depend on the boundary conditions, nor on the mean flow.

In short, even though elastic turbulence is a recent discovery and the methodology for its numerical simulation is still being discussed, some important results are already available. Regarding the issues related to the conformation tensor, since elastic turbulence has a lot in common with inertial turbulence, its simulation undergoes the same limitations. To avoid that, artificial diffusion is mostly used. This and other solutions to overcome the numerical instabilities associated to turbulent viscoelastic flows are presented in the next section.

1.4 Turbulent viscoelastic flows: the drag reduction phenomenon

The dilution of very small amounts of high-molecular-weight polymers in a Newtonian fluid may lead to a diminution of pressure drop in turbulent flows. This phenomenon, known as polymer-induced drag reduction, has been explored since its first observations in the 1930's, by Forrest and Grierson [82] and in the 1940's by Toms [83] and Mysels [84]. Almost 80 years later, even though many advances have been made, a complete and consensual theory on the mechanism of drag reduction is still being sought.

Virk, Mickley, and Smith [85] provided a systematic experimental analysis of the polymer-induced drag reduction phenomenon in turbulent pipe flows. The author investigated the onset of the phenomenon and found an asymptotic upper limit usually referred to as Maximum Drag Reduction MDR. The sensitivity of the phenomenon and its features were tested for varying polymer's concentration, molecular weight, and

Reynolds number.

Two major theories try to explain the polymer-induced drag reduction phenomenon. Lumley [86] and Seyer and Metzner [87] proposed independently that the polymers chains are stretched due to the turbulent flow outside the viscous sublayer, leading to an increase of the effective viscosity in the turbulent region. The thickness of the viscous sublayer and of the buffer layer is therefore increased, reducing the velocity gradient near the wall, and, consequently, the drag. Because its explanation is based on the increase of effective viscosity, this theory is mostly known as *viscous theory*.

Tabor and de Gennes [88] came up with the idea that, due to its elastic properties, polymers store part of the turbulent energy in the buffer layer. When the elastic (stored) energy becomes comparable to the turbulent energy, the energy cascade is affected. Since the length of elastic scales associated to this action is larger than the Kolmogorov scale, the buffer layer is thickened and drag is reduced. This proposed mechanism is known as *elastic theory*.

The direct numerical simulation (DNS) of this phenomenon has been helping to clarify some physical issues related to it. DNS provides precious information about the interaction between polymer chains and the flow field which lead to new viewpoints of the phenomenon that sometimes could not be obtained experimentally.

By performing the direct numerical simulation of turbulent pipe flows and using a constitutive equation that relates the elongational viscosity to the second and third invariants of the rate-of-strain tensor, Den Toonder, Nieuwstadt, and Kuiken [89] were able to conclude that not only the effect of polymer stretch is relevant to the drag reduction mechanism, but the polymer compression (or coiling) motion is important as well.

Orlandi [90] simulated a channel flow using a constitutive equation for which the elongational viscosity is a function of the rate of the strain rate to the rotation rate. The author reproduced qualitative results of the polymer drag reduction phenomenon for a minimal channel. The results were obtained using a pseudospectral algorithm (Chebishev polynomials + Fourier expansions). Concerning time integration, the referred algorithm treated viscous terms with implicit schemes, while nonlinear terms were treated explicitly.

Beris and Sureshkumar [91] presented a fully spectral simulations of a three-dimensional turbulent channel flow using various viscoelastic fluids: the upper convected Maxwell [92], the Oldroyd-B [23] and the Chilcott-Rallison (FENE-CR) [42] models. They used a mixed explicit/implicit time-integration algorithm. The authors also investigated the effect of an artificial stress diffusion term on the stability of turbulent channel flows using the Oldroyd-B model [25]. This technique is known as Global Artificial Diffusion (GAD). They concluded that with an appropriate stress diffusion, the numerical stability is considerably enhanced without significant changes in the flow characteristics. Later, Sureshkumar, Beris, and Handler [5] conducted direct numerical simulations of turbulent channel flows with the FENE-P model [23]. Very good qualitative agreement was observed when comparing their results to the tendencies of statistics and dynamics of experimental drag reduction results. However, even if this solution is largely used by Beris and co-workers [5, 14–17, 93] and other groups [6, 10, 19, 20, 94], it brings a non-physical term into the equation, which must be adjusted to be as small as possible.

In a first effort to find less intrusive approaches, Min and co-workers [11, 12, 27] introduced the idea of Local Artificial Diffusion (LAD). Instead of considering the artificial stress diffusion globally, *i.e.* to the whole domain (actually, with the exception of boundary points), they applied the artificial diffusion locally, only at locations where the constraints for the conformation tensor were being violated. This methodology has been proved to also provide stability and physical results in accordance with the literature trends. More precisely, their results using LAD in a third-order compact upwind difference scheme led to more drag reduction than those with GAD. The authors claim that the dissipative error caused by local artificial diffusion term is negligible since the calculation points in which such term is needed change with time marching and do not pass 0.5% of the total grid points of the tested cases. The same method has been successfully used by Dubief and co-authors in [13, 95].

Two decompositions that preserve both positiveness and boundedness (if the model predicts so) of the conformation tensor have been proposed by Vaithianathan and Collins [26]. One of them consists of applying an eigendecomposition to the conformation tensor and evolving its eigenvalues and eigenvectors separately. The other one is based on a Cholesky decomposition to a mapped conformation tensor along with a logarithm transformation applied to the decomposed tensor. These two methods were applied to the FENE-P model and tested for isotropic turbulent flows. Comparisons with the standard conformation formulation with and without artificial diffusion were also conducted. By performing uncoupled simulations (in which the polymer field does not affect the velocity field), the authors showed that both proposed decompositions eliminate the occurrence of negative eigenvalues of the conformation tensor. With the standard formulation with artificial diffusion, the frequency of their occurrence is only attenuated, meaning that negative eigenvalues are still occurring.

In a later publication by Vaithianathan et al. [28], it was discussed that the numerical scheme used in [26] did preserve the positiveness of the conformation tensor, but not its conservation. They argued that, in fact, regarding spectral and high-order compact schemes, artificial diffusion seems to be the solution to discontinuities in the field of the conformation tensor that causes undershoots or overshoots in the conformation tensor, which may lead to negative eigenvalues. They claim however that capturing the polymer strength around discontinuities is essential to calculate turbulent flows of polymer solutions. They assert that spectral and high-order compact schemes are not naturally appropriate to solve hyperbolic equations. Moreover, possible alternatives are somehow difficult to deal with. Thus, they opted for a second-order finite-difference bound-preserving scheme which was originally conceived to guarantee the positiveness of scalar field based on flux limiters, but that they extended to tensor fields. The authors reported unconditionally stable results of the new algorithm for homogeneous turbulence. The effect of artificial stress diffusion was tested and resulted in a diminution of the drag reduction percentage of 10-15% and underestimation of polymer stretching.

Yu and Kawaguchi [29] introduced a high-resolution flux-limiter algorithm with which they were able to simulate drag-reducing channel flows using the Giesekus model without any artificial diffusion. The effect of artificial diffusion was assessed with another algorithm of their own. They reported higher drag reduction regimes (percentages) with their new algorithm. Beris and Housiadas [96] argue that the stress diffusivity used by Yu and Kawaguchi [29] is higher than usual for spectral methods. Moreover, if one is interested on the mechanisms of polymer stretching and flow dynamics in various time and spatial scales, spectral methods are very suitable.

By adapting the periodic algorithm of Vaithianathan et al. [28] to wall-bounded flows, Dallas, Vassilicos, and Hewitt [18] performed drag-reducing channel flows without any artificial assumption for FENE-P fluids. At the same time, Housiadas, Wang, and Beris [17] combined the log-conformation together with a mapping scheme that preserves the boundedness of the conformation tensor. Their algorithm is almost fully spectral, the only exception being a second-order finite-difference multigrid scheme to solve the stress diffusion term added to the constitutive equation.

It is worth noting that the simulation of homogeneous isotropic turbulence of viscoelastic fluids also requires special attention on the loss of evolution, but they will not be concerned here. Just to cite a few examples of applications in this context, De Angelis et al. [97] used the artificial diffusion [5, 25], Perlekar, Mitra, and Pandit [98] made use of the Cholesky decompostion proposed by [26], and Cai, Li, and Zhang [99] applied the eigendecomposition in [28].

Chapter 2

Mathematical modelling and numerical method

The introduction in the previous chapter substantiates that the simulation of turbulent viscoelastic flows is not trivial, since it involves numerical instabilities coming from the hyperbolic nature of the constitutive equations that potentially grow due to the lack of a dissipation mechanism in the model. Basically, two options should be weighted to overcome this: either one privileges the spatial accuracy of spectral and high-order compact schemes and use an artificial stress diffusion that smooths the shocks in the conformation tensor, or the somewhat intrusive artificial diffusion is avoided, by using flux limiter schemes paying the price of lower order accuracy (typically second order).

In this chapter, the mathematical models and numerical methods are presented. The DNS code used here considered originally the standard conformation tensor formulation for FENE-P fluids with the inclusion of a global artificial stress diffusion to avoid the breakdown due to the loss of positive-definiteness. The minimum diffusivity coefficient was properly adjusted to provide numerical stability. In general, with this approach, the amount of grid points in which the conformation tensor presents non-positive eigenvalues corresponds to at most 1% of the total number of grid points.

The formulations for the square-root and the kernel transformations are presented and the need to maintain or not the artificial stress diffusivity for these formulations is also evaluated.

2.1 Basic equations

For the three-dimensional channel flow considered here, the position vector $\boldsymbol{x}^*$ reads $\boldsymbol{x}^* = (x_1^*, x_2^*, x_3^*) = (x^*, y^*, z^*)$, where x^* is the stream-wise direction, y^* is the wall-normal direction, and z^* is the span-wise direction[1]. The channel has dimensions (L_x^*, L_y^*, L_z^*),

[1] A superscript asterisk is used to denote dimensional variables.

corresponding to the same respective directions above. Figure 2.1 provides a schematic representation of the geometry.

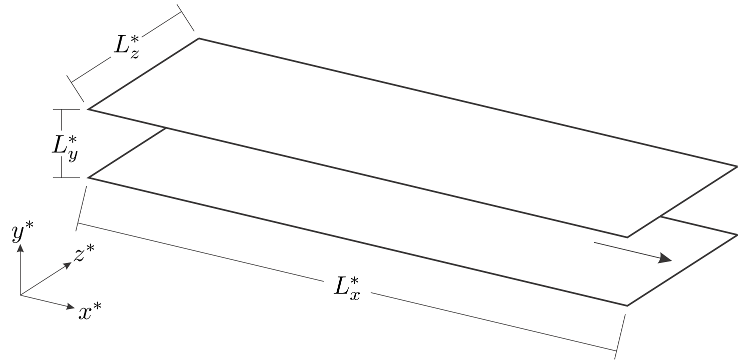

Figure 2.1 – Schematic representation of the channel geometry.

The flow satisfies the mass conservation equation (or continuity equation). Assuming the fluid to be incompressible, this reads

$$\boldsymbol{\nabla}^* \cdot \boldsymbol{u}^* = 0 \quad . \tag{2.1}$$

The generalised form of the Navier-Stokes equations (the balance of momentum) is

$$\frac{D\boldsymbol{u}^*}{Dt^*} = \frac{\partial \boldsymbol{u}^*}{\partial t^*} + \boldsymbol{u}^* \cdot \boldsymbol{\nabla}^* \boldsymbol{u}^* = -\frac{1}{\rho}\boldsymbol{\nabla}^* p^* + \frac{1}{\rho}\boldsymbol{\nabla}^* \cdot \boldsymbol{T}^* \quad , \tag{2.2}$$

where $\boldsymbol{u}^*$ is the velocity vector with entries $(u_1^*, u_2^*, u_3^*) = (u^*, v^*, w^*)$, corresponding respectively to the directions (x^*, y^*, z^*). The dimensional time is represented by t^*. The velocity gradient $\boldsymbol{\nabla}^*\boldsymbol{u}^*$ has entries $\nabla^* u_{ij}^* \boldsymbol{e}_i \otimes \boldsymbol{e}_j = \partial u_j^* / \partial x_i^* \boldsymbol{e}_i \otimes \boldsymbol{e}_j$. It is important to introduce also the transpose of the velocity gradient[2], $\boldsymbol{L}^* = \boldsymbol{\nabla}^* \boldsymbol{u}^{*T}$. The pressure is represented here by p^* and ρ^* stands for the fluid density. The symbol $\boldsymbol{\nabla}^*()$ corresponds to the gradient operator, while $\boldsymbol{\nabla}^* \cdot ()$ stands for the divergence operator. The material derivative is indicated by $D()/Dt$.

The boundary conditions for the velocity field are: periodicity in the homogeneous directions (stream-wise, x^*, and span-wise, z^*) and no-slip wall condition at the walls.

In this generalised representation of the Navier-Stokes equations, the stress tensor $\boldsymbol{T}^*$ may be split into two parts,

$$\boldsymbol{T}^* = \boldsymbol{T_N}^* + \boldsymbol{T_P}^* \quad , \tag{2.3}$$

in which

$$\boldsymbol{T_N}^* = 2\mu_0^* \beta \boldsymbol{D}^* \quad , \tag{2.4}$$

[2]The expression *velocity gradient* is used interchangeably for $\boldsymbol{\nabla}^*\boldsymbol{u}^*$ or $\boldsymbol{L}^*$ and for the non-dimensional $\boldsymbol{\nabla u}$ or $\boldsymbol{L}$.

takes into account the Newtonian contribution, while $\boldsymbol{T_P}^*$ represents the polymeric contribution. In Eq. (2.4), β is the ratio of the solvent dynamic viscosity, μ_S^*, to the total zero-shear-rate solution dynamic viscosity, $\mu_0^* = \mu_S^* + \mu_{p0}^*$ (where μ_{p0}^* is the polymeric zero-shear-rate dynamic viscosity), and $\boldsymbol{D}^*$ is the rate-of-strain tensor, defined as the symmetric part of the velocity gradient, $\boldsymbol{D}^* = (\boldsymbol{L}^* + \boldsymbol{L}^{*T})/2$. The value of β works as an indicator for the polymer concentration, so that the limit of $\beta = 1$ yields the Newtonian case. The contribution, $\boldsymbol{T_P}^*$, due to the presence of polymers is defined by the constitutive equation chosen to model it and is proportional to $1-\beta$ (see Subsection 2.1.1 below).

The equations are made non-dimensional using the bulk velocity U_b^* as a velocity scale and the channel half width $h^*(= L_y^*/2)$ as a length scale. The time scale thus becomes h^*/U_b^*. The non-dimensional variables and operators are

$$\boldsymbol{u} = \frac{\boldsymbol{u}^*}{U_b^*} \quad , \quad t = \frac{t^* U_b^*}{h^*} \quad , \quad \boldsymbol{x} = \frac{\boldsymbol{x}^*}{h^*} \quad , \quad p = \frac{p^*}{\rho^* U_b^{*2}} \quad , \quad \boldsymbol{\nabla} = h^* \boldsymbol{\nabla}^* \quad , \tag{2.5}$$

The non-dimensional form of Eqs. (2.1) and (2.2) is

$$\boldsymbol{\nabla} \cdot \boldsymbol{u} = 0 \quad , \tag{2.6}$$

$$\frac{\partial \boldsymbol{u}}{\partial t} + \boldsymbol{u} \cdot \boldsymbol{\nabla} \boldsymbol{u} = -\boldsymbol{\nabla} p + \frac{\beta}{Re_h} \Delta \boldsymbol{u} + \frac{1}{Re_h} \boldsymbol{\nabla} \cdot \boldsymbol{\Xi} \quad . \tag{2.7}$$

In Eq. (2.7) above, the bulk Reynolds number, Re_h, is based on the channel half gap, h, and calculated as $Re_h = h^* U_b^* / \nu_0^*$ (ν_0^* being the total zero-shear-rate kinematic viscosity defined as μ_0^*/ρ^*). The term $\boldsymbol{\Xi}$ is the extra-stress tensor which contains non-dimensional the polymer contribution ($\boldsymbol{T_P}^*$) and reads

$$\boldsymbol{\Xi} = \frac{h^*}{\mu_0^* U_b^*} \boldsymbol{T_P}^* \quad . \tag{2.8}$$

In order to close the problem formed by the set of Eqs. (2.6) and (2.7) we need a model for $\boldsymbol{\Xi}$ which is given by the constitutive equation.

2.1.1 Constitutive equations: modelling polymer solutions

In the present work, the FENE model with the closure proposed by Peterlin [41] (known as the FENE-P model [23]) was chosen to account for the polymeric stress, $\boldsymbol{\Xi}$. This model has been largely used in the context of turbulent drag-reducing flows due to its relatively simple second-order closure.

The FENE-P model requires the solution of the phase-averaged configuration tensor, $\boldsymbol{c}$, usually named *conformation tensor*. The non-dimensional conformation tensor is defined as $\boldsymbol{c} = \langle \boldsymbol{q}^*\boldsymbol{q}^* \rangle / \langle \boldsymbol{q}^*\boldsymbol{q}^* \rangle_{eq}$, where $\boldsymbol{q}^*$ is the *end-to-end* vector which represents the configuration of polymer molecules in the model, the angles, $\langle \cdot \rangle$, indicate a phase average, and $\langle \boldsymbol{q}^*\boldsymbol{q}^* \rangle_{eq}$ represents the configuration in the equilibrium state. The equilibrium state is given by the relation $\langle \boldsymbol{q}^*\boldsymbol{q}^* \rangle_{eq} = (k_B^* T^*/H^*)\boldsymbol{I}$, where k_B^*, T^* and H^* stand for the Boltzmann constant, the absolute temperature and the dumbbell spring constant. The (dimensional) polymer stress contributing to the momentum equation is

$$\boldsymbol{T_P}^* = \mu_0^*(1-\beta)\left[\frac{f\,(\mathrm{tr}(\boldsymbol{c}))\,\boldsymbol{c} - \boldsymbol{I}}{\lambda^*}\right] \quad , \tag{2.9}$$

in which $\boldsymbol{I}$ stands for the identity tensor and λ^* is the fluid's relaxation time. The function $f\,(\mathrm{tr}(\boldsymbol{c}))$ is the Peterlin function that provides the closure for the FENE-P model and is defined as

$$f\,(\mathrm{tr}(\boldsymbol{c})) = \frac{L^2 - 3}{L^2 - \mathrm{tr}(\boldsymbol{c})} \quad . \tag{2.10}$$

The closure proposed by Peterlin [41] is precisely what limits the trace of the conformation tensor, $\mathrm{tr}(\boldsymbol{c})$, with the square of the maximum chain extensibility, L.

Using Eqs. (2.5) and (2.9), the extra-stress, $\boldsymbol{\Xi}$, assumes the non-dimensional form

$$\boldsymbol{\Xi} = \frac{1-\beta}{Wi_h}\left[f\,(\mathrm{tr}(\boldsymbol{c}))\,\boldsymbol{c} - \boldsymbol{I}\right] \quad . \tag{2.11}$$

where Wi_h is the bulk Weissenberg number given by $\lambda^* U_b^*/h^*$. Note that if $\boldsymbol{c} = \boldsymbol{I}$, the polymer stress is null. This state is called *equilibrium state* of the polymer molecule.

The maximum extensibility of the polymer chain, L, and the relaxation time scale, λ^*, are the rheological parameters for the FENE-P model allowing to relate simulations with real combinations of polymer-solvent. It is worth noticing that a FENE-P fluid, just like other typical viscoelastic fluids, is "shear-thinning" [2], *i.e.* its (apparent) shear viscosity decreases with increasing shear rate. The relaxation time scale is most commonly expressed by means of the Weissenberg number, Wi_h.

Finally, the evolution equation for the conformation tensor, $\boldsymbol{c}$, reads

$$\frac{\mathrm{D}\boldsymbol{c}}{\mathrm{D}t} - \boldsymbol{c}\cdot\boldsymbol{\nabla u} - \boldsymbol{\nabla u}^T\cdot\boldsymbol{c} + \frac{f\,(\mathrm{tr}(\boldsymbol{c}))\,\boldsymbol{c} - \boldsymbol{I}}{Wi_h} = 0 \quad . \tag{2.12}$$

Equation (2.12), together with Eqs. (2.6) and (2.7), forms the basic set of equations to be solved in the flow of viscoelastic fluids.

2.1.2 The inclusion of an artificial stress diffusion to the constitutive equations for the FENE-P model

As discussed in Chapter 1, the original algorithm by Thais et al. [19] considers an artificial stress diffusion as proposed by Sureshkumar and Beris [25] in order to avoid the uncontrolled growth of Hadamard instabilities during time evolution. With a dimensionless artificial stress diffusivity, D_c, a dissipation term proportional to $D_c\Delta\boldsymbol{c}$ is thus added to Eq. (2.12), yielding

$$\frac{\mathrm{D}\boldsymbol{c}}{\mathrm{D}t} - \boldsymbol{c}\cdot\nabla\boldsymbol{u} - \nabla\boldsymbol{u}^T\cdot\boldsymbol{c} + \frac{f\left(\mathrm{tr}(\boldsymbol{c})\right)\boldsymbol{c} - \boldsymbol{I}}{Wi_h} = \frac{D_c}{Re_h}\Delta\boldsymbol{c} \quad , \tag{2.13}$$

where D_c is given by κ^*/ν_0^*, which is the equivalent of the inverse of the Schmidt number, Sc, with κ^* being the dimensional artificial diffusivity.

The original algorithm by Thais et al. [19] solves the system formed by Eqs. (2.7) and (2.13) (with continuity) to perform DNS of viscoelastic channel flows. Regarding the value of D_c, it has been formerly adjusted to be as small as possible still providing numerical stability. The presence of the artificial diffusion term does not avoid the appearance of non-SPD for the conformation tensor during the calculations. Instead, it controls the number of points that lose the SPD property and ensures that Hadamard instabilities do not propagate indefinitely.

The addition of an elliptic (diffusion) term to the hyperbolic equation of the conformation tensor implies the need for boundary conditions. Hence, the equations are first evolved in time without artificial diffusion and the intermediate values obtained are used as boundary conditions for $\boldsymbol{c}$ (see more details in Section 2.4).

As exposed in Chapter 1, one of the goals of the present work is to investigate how recent propositions to avoid the loss of the SPD property performs under turbulent channel flows. In the following sections, we will present the formulation of two promising methods: the square-root [33] and the kernel root^k [34] transformations.

2.2 The square-root transformation

The combination of loss of positiveness in viscoelastic fluid flows and open questions around viscoelastic phenomena has been inspiring the scientific community to find solutions over the last 30 years, approximately. However, some recent ideas have not been explored in the frame of turbulent viscoelastic flows.

The square-root transformation, by Balci et al. [33], is a promising proposition based on the unique square-root of a SPD tensor. The eigenvalues of the square-root tensor,

$\boldsymbol{b} = \boldsymbol{c}^{1/2}$, can be obtained from

$$\boldsymbol{\Lambda}^{\boldsymbol{b}} = \boldsymbol{Q}_{\boldsymbol{c}}^T \cdot \boldsymbol{c}^{\frac{1}{2}} \cdot \boldsymbol{Q}_{\boldsymbol{c}} \quad , \tag{2.14}$$

where $\boldsymbol{Q}_{\boldsymbol{c}}$ is the orthogonal tensor containing the components of the eigenvectors of $\boldsymbol{c}$ in columns. The operation in Eq. (2.14) diagonalises $\boldsymbol{c}$ and takes the square-root of its eigenvalues, resulting in the diagonal tensor $\boldsymbol{\Lambda}^{\boldsymbol{b}}$, which represents the square-root of $\boldsymbol{c}$ on the basis of the eigenvectors of $\boldsymbol{c}$. To obtain the square-root tensor on the basis of the problem, the inverse rotation (compared to Eq. (2.14)) must be applied, yielding

$$\boldsymbol{b} = \boldsymbol{Q}_{\boldsymbol{c}} \cdot \boldsymbol{\Lambda}^{\boldsymbol{b}} \cdot \boldsymbol{Q}_{\boldsymbol{c}}^T \quad . \tag{2.15}$$

The tensor $\boldsymbol{b}$ has been proven to be unique and SPD [33], and to remain so when evolving over time, given an SPD initial condition. From tensor $\boldsymbol{b}$, the conformation tensor may be recovered by the following operation

$$\boldsymbol{c} = \boldsymbol{b}^T \cdot \boldsymbol{b} \quad , \tag{2.16}$$

and, the square-root tensor $\boldsymbol{b}$ being symmetric, Eq. (2.16) also reads $\boldsymbol{c} = \boldsymbol{b} \cdot \boldsymbol{b}$. The key idea of the square-root method is that Eq. (2.16) is a mathematical constraint for $\boldsymbol{c}$ to be SPD.

It is now required to derive the evolution equation for the square-root tensor using the original equation for $\boldsymbol{c}$. This follows Balci et al. [33] and the derivation proposed by Chen et al. [66].

Firstly, replacing Eq. (2.16) into Eq. (2.12) yields

$$\frac{D(\boldsymbol{b}^T \cdot \boldsymbol{b})}{Dt} - \boldsymbol{b}^T \cdot \boldsymbol{b} \cdot \nabla \boldsymbol{u} - \nabla \boldsymbol{u}^T \cdot \boldsymbol{b}^T \cdot \boldsymbol{b} + \frac{f(\mathrm{tr}(\boldsymbol{c}))\, \boldsymbol{b}^T \cdot \boldsymbol{b} - \boldsymbol{I}}{Wi_h} = 0 \quad , \tag{2.17}$$

which can be rearranged and multiplied on the left by $\boldsymbol{b}^{-T} (= (\boldsymbol{b}^{-1})^T)$ and on the right by $\boldsymbol{b}^{-1}$ to yield

$$\boldsymbol{b}^{-T} \cdot \frac{D\boldsymbol{b}^T}{Dt} + \frac{D\boldsymbol{b}}{Dt} \cdot \boldsymbol{b}^{-1} - \boldsymbol{b} \cdot \nabla \boldsymbol{u} \cdot \boldsymbol{b}^{-1} - \boldsymbol{b}^{-T} \cdot \nabla \boldsymbol{u}^T \cdot \boldsymbol{b}^T + \frac{f(\mathrm{tr}(\boldsymbol{c}))\, \boldsymbol{I} - \boldsymbol{b}^{-T} \cdot \boldsymbol{b}^{-1}}{Wi_h} = 0 \quad . \tag{2.18}$$

It is easy to manipulate Eq. (2.18) so that, on one side, all the terms are post-multiplied by $\boldsymbol{b}^{-1}$, and all the terms on the other side are pre-multiplied by $\boldsymbol{b}^{-T}$, giving

$$\left[\frac{D\boldsymbol{b}}{Dt} - \boldsymbol{b} \cdot \nabla \boldsymbol{u} + \frac{f(\mathrm{tr}(\boldsymbol{c}))\, \boldsymbol{b} - \boldsymbol{b}^{-T}}{2Wi_h} \right] \cdot \boldsymbol{b}^{-1} = -\boldsymbol{b}^{-T} \cdot \left[\frac{D\boldsymbol{b}^T}{Dt} - \nabla \boldsymbol{u}^T \cdot \boldsymbol{b}^T + \frac{f(\mathrm{tr}(\boldsymbol{c}))\, \boldsymbol{b}^T - \boldsymbol{b}^{-1}}{2Wi_h} \right] \quad , \tag{2.19}$$

Regarding Eq. (2.19), it is easily verified that one side is minus the transpose of the other. Therefore, each side of this equation is anti-symmetric. Let us define an anti-symmetric tensor, $\boldsymbol{a}$, and split Eq. (2.19) into two equal equations, yielding

$$\left[\frac{D\boldsymbol{b}}{Dt} - \boldsymbol{b}\cdot\nabla\boldsymbol{u} + \frac{f(\mathrm{tr}(\boldsymbol{c}))\,\boldsymbol{b} - \boldsymbol{b}^{-T}}{2Wi_h}\right]\cdot\boldsymbol{b}^{-1} = \boldsymbol{a} \quad , \tag{2.20}$$

and

$$-\boldsymbol{b}^{-T}\cdot\left[\frac{D\boldsymbol{b}^T}{Dt} - \nabla\boldsymbol{u}^T\cdot\boldsymbol{b}^T + \frac{f(\mathrm{tr}(\boldsymbol{c}))\,\boldsymbol{b}^T - \boldsymbol{b}^{-1}}{2Wi_h}\right] = \boldsymbol{a} \quad . \tag{2.21}$$

Since the goal here is to find an evolution equation for the square-root of the conformation tensor, one can either multiply Eq. (2.20) on the left by $\boldsymbol{b}$ or Eq. (2.21) on the right by $\boldsymbol{b}^T$, which respectively gives

$$\frac{D\boldsymbol{b}}{Dt} - \boldsymbol{b}\cdot\nabla\boldsymbol{u} - \boldsymbol{a}\cdot\boldsymbol{b} + \frac{f(\mathrm{tr}(\boldsymbol{c}))\,\boldsymbol{b} - \boldsymbol{b}^{-T}}{2Wi_h} = 0 \quad , \tag{2.22}$$

and

$$\frac{D\boldsymbol{b}^T}{Dt} - \nabla\boldsymbol{u}^T\cdot\boldsymbol{b}^T + \boldsymbol{b}^T\cdot\boldsymbol{a} + \frac{f(\mathrm{tr}(\boldsymbol{c}))\,\boldsymbol{b}^T - \boldsymbol{b}^{-1}}{2Wi_h} = 0 \quad . \tag{2.23}$$

Since $\boldsymbol{b} = \boldsymbol{b}^T$, these equations can be rewritten as

$$\frac{D\boldsymbol{b}}{Dt} - \boldsymbol{b}\cdot\nabla\boldsymbol{u} - \boldsymbol{a}\cdot\boldsymbol{b} + \frac{f(\mathrm{tr}(\boldsymbol{c}))\,\boldsymbol{b} - \boldsymbol{b}^{-1}}{2Wi_h} = 0 \quad , \tag{2.24}$$

and

$$\frac{D\boldsymbol{b}}{Dt} - \nabla\boldsymbol{u}^T\cdot\boldsymbol{b} + \boldsymbol{b}\cdot\boldsymbol{a} + \frac{f(\mathrm{tr}(\boldsymbol{c}))\,\boldsymbol{b} - \boldsymbol{b}^{-1}}{2Wi_h} = 0 \quad . \tag{2.25}$$

Let us now define the tensor

$$\boldsymbol{r} = \boldsymbol{b}\cdot\nabla\boldsymbol{u} + \boldsymbol{a}\cdot\boldsymbol{b} \quad . \tag{2.26}$$

First, note that its transpose is $\boldsymbol{r}^T = \nabla\boldsymbol{u}^T\cdot\boldsymbol{b} - \boldsymbol{b}\cdot\boldsymbol{a}$, and that Eqs. (2.24) and (2.25) contain respectively $\boldsymbol{r}$ and $\boldsymbol{r}^T$. Furthermore, these equations are equal. Thus, replacing $(-\boldsymbol{b}\cdot\nabla\boldsymbol{u} - \boldsymbol{a}\cdot\boldsymbol{b})$ and $(-\nabla\boldsymbol{u}^T\cdot\boldsymbol{b} + \boldsymbol{b}\cdot\boldsymbol{a})$ by $-\boldsymbol{r}$ and $-\boldsymbol{r}^T$ in the referred equations, we conclude that $\boldsymbol{r} = \boldsymbol{r}^T$, and, therefore, $\boldsymbol{r}$ is symmetric. So, the relation $r_{ij} = r_{ji}$ yields the following linear system

$$\begin{pmatrix} b_{11}+b_{22} & b_{23} & -b_{13} \\ b_{23} & b_{11}+b_{33} & b_{12} \\ -b_{13} & b_{12} & b_{22}+b_{33} \end{pmatrix} \begin{pmatrix} a_{12} \\ a_{13} \\ a_{23} \end{pmatrix} = \begin{pmatrix} t_1 \\ t_2 \\ t_3 \end{pmatrix} \quad , \tag{2.27}$$

where the terms $t_{1,2,3}$ are given by

$$\begin{aligned} t_1 &= (b_{12}\nabla u_{11} - b_{11}\nabla u_{12}) + (b_{22}\nabla u_{21} - b_{12}\nabla u_{22}) + (b_{23}\nabla u_{31} - b_{13}\nabla u_{32}) \\ t_2 &= (b_{13}\nabla u_{11} - b_{11}\nabla u_{13}) + (b_{33}\nabla u_{31} - b_{13}\nabla u_{33}) + (b_{23}\nabla u_{21} - b_{12}\nabla u_{23}) \\ t_3 &= (b_{13}\nabla u_{12} - b_{12}\nabla u_{13}) + (b_{23}\nabla u_{22} - b_{22}\nabla u_{23}) + (b_{33}\nabla u_{32} - b_{23}\nabla u_{33}) \end{aligned} \quad , \tag{2.28}$$

and the entries of $\boldsymbol{a}$ can be calculated as a function of $\boldsymbol{b}$ and $\nabla\boldsymbol{u}$ solving for Eq. (2.27).

2.2.1 The inclusion of an artificial stress diffusion into the square-root formulation

For numerical stability purposes, it is common to include an artificial stress diffusion term to the evolution equation of the conformation tensor when simulating turbulent viscoelastic fluid flows. Regarding the square-root transformation, a first approach, analogous to the proposition by Sureshkumar and Beris [25], is to add a term proportional to $D_b\Delta\boldsymbol{b}$ to the evolution equation of the square-root conformation (Eq. (2.24)). This equation containing the artificial stress diffusion reads

$$\frac{D\boldsymbol{b}}{Dt} - \boldsymbol{b}\cdot\nabla\boldsymbol{u} - \boldsymbol{a}\cdot\boldsymbol{b} + \frac{f\left(\mathrm{tr}(\boldsymbol{c})\right)\boldsymbol{b} - \boldsymbol{b}^{-1}}{2Wi_h} = \frac{D_b}{Re_h}\Delta\boldsymbol{b} \quad . \tag{2.29}$$

An alternative approach is to use Eq. (2.13), which includes stress diffusion into the evolution equation, as a starting point, and henceforth apply the square-root transformation. This solution is more consistent from a mathematical viewpoint (see Appendix B in [33]). Applying the square-root transformation to Eq. (2.13) yields

$$\frac{D(\boldsymbol{b}^T\cdot\boldsymbol{b})}{Dt} - \boldsymbol{b}^T\cdot\boldsymbol{b}\cdot\nabla\boldsymbol{u} - \nabla\boldsymbol{u}^T\cdot\boldsymbol{b}^T\cdot\boldsymbol{b} + \frac{f\left(\mathrm{tr}(\boldsymbol{c})\right)\boldsymbol{b}^T\cdot\boldsymbol{b} - \boldsymbol{I}}{Wi_h} = \frac{D_c}{Re_h}\Delta(\boldsymbol{b}^T\cdot\boldsymbol{b}) \quad . \tag{2.30}$$

Note, however, that

$$\Delta(\boldsymbol{b}^T\cdot\boldsymbol{b}) = \Delta\boldsymbol{b}^T\cdot\boldsymbol{b} + \boldsymbol{b}^T\cdot\Delta\boldsymbol{b} + 2\left[\left(\frac{\partial\boldsymbol{b}}{\partial x}\right)^2 + \left(\frac{\partial\boldsymbol{b}}{\partial y}\right)^2 + \left(\frac{\partial\boldsymbol{b}}{\partial z}\right)^2\right] \quad . \tag{2.31}$$

Analogously to the previous procedure, multiplying Eq. (2.30) on the left by $\boldsymbol{b}^{-T}$ and on the right by $\boldsymbol{b}^{-1}$ leads to

$$\begin{aligned} &\boldsymbol{b}^{-T}\cdot\frac{D\boldsymbol{b}^T}{Dt} + \frac{D\boldsymbol{b}}{Dt}\cdot\boldsymbol{b}^{-1} - \boldsymbol{b}\cdot\nabla\boldsymbol{u}\cdot\boldsymbol{b}^{-1} - \boldsymbol{b}^{-T}\cdot\nabla\boldsymbol{u}^T\cdot\boldsymbol{b}^T + \frac{f\left(\mathrm{tr}(\boldsymbol{c})\right)\boldsymbol{I} - \boldsymbol{b}^{-T}\cdot\boldsymbol{b}^{-1}}{Wi_h} = \\ &\quad \frac{D_c}{Re_h}\boldsymbol{b}^{-T}\cdot\left\{\Delta\boldsymbol{b}^T\cdot\boldsymbol{b} + \boldsymbol{b}^T\cdot\Delta\boldsymbol{b} + 2\left[\left(\frac{\partial\boldsymbol{b}}{\partial x}\right)^2 + \left(\frac{\partial\boldsymbol{b}}{\partial y}\right)^2 + \left(\frac{\partial\boldsymbol{b}}{\partial z}\right)^2\right]\right\}\cdot\boldsymbol{b}^{-1} \quad , \end{aligned} \tag{2.32}$$

Rearranging terms:

$$
\begin{aligned}
&\left\{\frac{D\boldsymbol{b}}{Dt} - \boldsymbol{b}\cdot\nabla\boldsymbol{u} + \frac{f\left(\mathrm{tr}(\boldsymbol{c})\right)\boldsymbol{b} - \boldsymbol{b}^{-T}}{2Wi_h} - \right.\\
&\qquad \left. - \frac{D_c}{Re_h}\boldsymbol{b}^{-T}\cdot\left[\frac{1}{2}\boldsymbol{b}^T\cdot\Delta\boldsymbol{b} + \frac{1}{2}\Delta\boldsymbol{b}^T\cdot\boldsymbol{b} + \left(\frac{\partial\boldsymbol{b}}{\partial x}\right)^2 + \left(\frac{\partial\boldsymbol{b}}{\partial y}\right)^2 + \left(\frac{\partial\boldsymbol{b}}{\partial z}\right)^2\right]\right\}\cdot\boldsymbol{b}^{-1} = \\
&\qquad - \boldsymbol{b}^{-T}\cdot\left\{\frac{D\boldsymbol{b}^T}{Dt} - \nabla\boldsymbol{u}^T\cdot\boldsymbol{b}^T + \frac{f\left(\mathrm{tr}(\boldsymbol{c})\right)\boldsymbol{b}^T - \boldsymbol{b}^{-1}}{2Wi_h} - \right.\\
&\qquad \left. - \frac{D_c}{Re_h}\left[\frac{1}{2}\Delta\boldsymbol{b}^T\cdot\boldsymbol{b} + \frac{1}{2}\boldsymbol{b}^T\cdot\Delta\boldsymbol{b} + \left(\frac{\partial\boldsymbol{b}}{\partial x}\right)^2 + \left(\frac{\partial\boldsymbol{b}}{\partial y}\right)^2 + \left(\frac{\partial\boldsymbol{b}}{\partial z}\right)^2\right]\cdot\boldsymbol{b}^{-1}\right\} \quad .
\end{aligned}
\tag{2.33}
$$

Similarly to Eq. (2.19), one side of Eq. (2.33) is the negative transpose of the other, meaning that both sides are anti-symmetric.

Now, let us define

$$
\begin{aligned}
\boldsymbol{h} =& \boldsymbol{b}^{-T}\cdot\left[\frac{1}{2}\Delta\boldsymbol{b}^T\cdot\boldsymbol{b} + \left(\frac{\partial\boldsymbol{b}}{\partial x}\right)^2 + \left(\frac{\partial\boldsymbol{b}}{\partial y}\right)^2 + \left(\frac{\partial\boldsymbol{b}}{\partial z}\right)^2\right] = \\
& \boldsymbol{b}^{-1}\cdot\left[\frac{1}{2}\Delta\boldsymbol{b}\cdot\boldsymbol{b} + \left(\frac{\partial\boldsymbol{b}}{\partial x}\right)^2 + \left(\frac{\partial\boldsymbol{b}}{\partial y}\right)^2 + \left(\frac{\partial\boldsymbol{b}}{\partial z}\right)^2\right] \quad ,
\end{aligned}
\tag{2.34}
$$

and make Eq. (2.33) equal to the anti-symmetric tensor $\boldsymbol{a}^*$. Multiplying the left-hand side of Eq. (2.33) on the right by $\boldsymbol{b}$ yields

$$
\frac{D\boldsymbol{b}}{Dt} - \boldsymbol{b}\cdot\nabla\boldsymbol{u} - \boldsymbol{a}^*\cdot\boldsymbol{b} - \frac{D_c}{Re_h}\boldsymbol{h} + \frac{f\left(\mathrm{tr}(\boldsymbol{c})\right)\boldsymbol{b} - \boldsymbol{b}^{-1}}{2Wi_h} = \frac{D_c}{Re_h}\frac{1}{2}\Delta\boldsymbol{b} \quad , \tag{2.35}
$$

and multiplying the right-hand side on the left by $\boldsymbol{b}^T$ yields

$$
\frac{D\boldsymbol{b}}{Dt} - \nabla\boldsymbol{u}^T\cdot\boldsymbol{b} + \boldsymbol{b}\cdot\boldsymbol{a}^* - \frac{D_c}{Re_h}\boldsymbol{h}^T + \frac{f\left(\mathrm{tr}(\boldsymbol{c})\right)\boldsymbol{b} - \boldsymbol{b}^{-1}}{2Wi_h} = \frac{D_c}{Re_h}\frac{1}{2}\Delta\boldsymbol{b} \quad . \tag{2.36}
$$

Comparing Eqs. (2.35) and (2.36), the following equation appears

$$
-\boldsymbol{b}\cdot\nabla\boldsymbol{u} - \boldsymbol{a}^*\cdot\boldsymbol{b} - \frac{D_c}{Re_h}\boldsymbol{h} = -\nabla u^T\cdot\boldsymbol{b} + \boldsymbol{b}\cdot\boldsymbol{a}^* - \frac{D_c}{Re_h}\boldsymbol{h}^T \quad . \tag{2.37}
$$

Similarly to the case without any artificial stress diffusion, it is possible to define

$$
\boldsymbol{r}^* = \boldsymbol{b}\cdot\nabla\boldsymbol{u} + \boldsymbol{a}^*\cdot\boldsymbol{b} + \frac{D_c}{Re_h}\boldsymbol{h} \quad , \tag{2.38}
$$

and to conclude that $\boldsymbol{r}^* = \boldsymbol{r}^{*T}$, and, therefore, that $\boldsymbol{r}^*$ is symmetric. Using $r^*_{ij} = r^*_{ji}$, the following linear system shows up

$$\begin{pmatrix} b_{11}+b_{22} & b_{23} & -b_{13} \\ b_{23} & b_{11}+b_{33} & b_{12} \\ -b_{13} & b_{12} & b_{22}+b_{33} \end{pmatrix}\begin{pmatrix} a^*_{12} \\ a^*_{13} \\ a^*_{23} \end{pmatrix} = \begin{pmatrix} t^*_1 \\ t^*_2 \\ t^*_3 \end{pmatrix} \quad , \tag{2.39}$$

where the terms $t^*_{1,2,3}$ are given by

$$\begin{aligned} t^*_1 &= t_1 + \tfrac{D_c}{Re_h}(h_{21}-h_{12}) \\ t^*_2 &= t_2 + \tfrac{D_c}{Re_h}(h_{31}-h_{13}) \\ t^*_3 &= t_3 + \tfrac{D_c}{Re_h}(h_{32}-h_{23}) \end{aligned} \quad , \tag{2.40}$$

in which the terms $t_{1,2,3}$ are those in Eq. (2.28).

A simpler way to include artificial diffusion in the square-root formulation

Analysing the manipulation made by Balci et al. [33], a simpler way to consider the artificial stress diffusion is suggested here. The resulting equations are equivalent, but with the advantage of easier implementation and faster calculation.

Going back to Eq. (2.32), we can manipulate differently, to obtain

$$\begin{aligned} &\left\{\frac{D\boldsymbol{b}}{Dt} - \boldsymbol{b}\cdot\nabla\boldsymbol{u} + \frac{f\left(\mathrm{tr}(\boldsymbol{c})\right)\boldsymbol{b}-\boldsymbol{b}^{-T}}{2Wi_h} - \right.\\ &\qquad \left. -\frac{D_c}{Re_h}\boldsymbol{b}^{-T}\cdot\left[\boldsymbol{b}^T\cdot\Delta\boldsymbol{b} + \left(\frac{\partial\boldsymbol{b}}{\partial x}\right)^2 + \left(\frac{\partial\boldsymbol{b}}{\partial y}\right)^2 + \left(\frac{\partial\boldsymbol{b}}{\partial z}\right)^2\right]\right\}\cdot\boldsymbol{b}^{-1} = \\ &\qquad -\boldsymbol{b}^{-T}\cdot\left\{\frac{D\boldsymbol{b}^T}{Dt} - \nabla\boldsymbol{u}^T\cdot\boldsymbol{b}^T + \frac{f\left(\mathrm{tr}(\boldsymbol{c})\right)\boldsymbol{b}^T-\boldsymbol{b}^{-1}}{2Wi_h} - \right.\\ &\qquad \left. -\frac{D_c}{Re_h}\left[\Delta\boldsymbol{b}^T\cdot\boldsymbol{b} + \left(\frac{\partial\boldsymbol{b}}{\partial x}\right)^2 + \left(\frac{\partial\boldsymbol{b}}{\partial y}\right)^2 + \left(\frac{\partial\boldsymbol{b}}{\partial z}\right)^2\right]\cdot\boldsymbol{b}^{-1}\right\} \quad . \end{aligned} \tag{2.41}$$

Note that both sides in Eq. (2.41) are anti-symmetric as well.

Now, an analogous but simpler term $\boldsymbol{h}^*$ can be defined as

$$\boldsymbol{h}^* = \boldsymbol{b}^{-T}\cdot\left[\left(\frac{\partial\boldsymbol{b}}{\partial x}\right)^2 + \left(\frac{\partial\boldsymbol{b}}{\partial y}\right)^2 + \left(\frac{\partial\boldsymbol{b}}{\partial z}\right)^2\right] = \boldsymbol{b}^{-1}\cdot\left[\left(\frac{\partial\boldsymbol{b}}{\partial x}\right)^2 + \left(\frac{\partial\boldsymbol{b}}{\partial y}\right)^2 + \left(\frac{\partial\boldsymbol{b}}{\partial z}\right)^2\right] \quad , \tag{2.42}$$

Note that $\boldsymbol{h}^*$ is not a function of the Laplacian of $\boldsymbol{b}$, which is a considerable improvement in terms of computation. Using another anti-symmetric tensor, $\boldsymbol{a}^{**}$, the evolution equation for $\boldsymbol{b}$ reads

$$\frac{D\boldsymbol{b}}{Dt} - \boldsymbol{b}\cdot\nabla\boldsymbol{u} - \boldsymbol{a}^{**}\cdot\boldsymbol{b} - \frac{D_c}{Re_h}\boldsymbol{h}^* + \frac{f\left(\mathrm{tr}(\boldsymbol{c})\right)\boldsymbol{b}-\boldsymbol{b}^{-1}}{2Wi_h} = \frac{D_c}{Re_h}\Delta\boldsymbol{b} \quad , \tag{2.43}$$

where $\boldsymbol{a}^{**}$ is obtained by solving the following linear system

$$\begin{pmatrix} b_{11}+b_{22} & b_{23} & -b_{13} \\ b_{23} & b_{11}+b_{33} & b_{12} \\ -b_{13} & b_{12} & b_{22}+b_{33} \end{pmatrix} \begin{pmatrix} a_{12}^{**} \\ a_{13}^{**} \\ a_{23}^{**} \end{pmatrix} = \begin{pmatrix} t_1^{**} \\ t_2^{**} \\ t_3^{**} \end{pmatrix} \quad , \tag{2.44}$$

where the terms $t_{1,2,3}^{**}$ are given by

$$\begin{aligned} t_1^{**} &= t_1 + \tfrac{D_c}{Re_h}(h_{21}^* - h_{12}^*) \\ t_2^{**} &= t_2 + \tfrac{D_c}{Re_h}(h_{31}^* - h_{13}^*) \\ t_3^{**} &= t_3 + \tfrac{D_c}{Re_h}(h_{32}^* - h_{23}^*) \end{aligned} \quad . \tag{2.45}$$

2.2.2 Implementation of the square-root formulation

Starting from a code that considers the standard conformation tensor with artificial diffusion, the changes needed to the square-root formulation are relatively small. Basically, the following steps have been performed:

- Transformation of the initial field of $\boldsymbol{c}$ into a field of its square-root, $\boldsymbol{b}$, using Eqs. (2.14) and (2.15);
- Calculation of the anti-symmetric tensor $\boldsymbol{a}$ (or $\boldsymbol{a}^*$ or $\boldsymbol{a}^{**}$ depending on the specific formulation considered) and replacement of $\boldsymbol{a}$ (or equivalent) in place of $\nabla \boldsymbol{u}^T$;
- Calculation of the inverse of $\boldsymbol{b}$[3] and replacement of $\boldsymbol{b}^{-1}$ in place of $\boldsymbol{I}$;
- Assembly of the term $\boldsymbol{h}$ (or equivalent) if needed;
- Inverse transformation (Eq. (2.16)) when $\boldsymbol{c}$ is required[4].

2.3 The kernel transformation

Inspired by previous methods proposed to ensure the positive-definiteness of the conformation tensor, Afonso, Pinho, and Alves [34] arrived at a general and versatile family of transformations. Since it is based on a particular decomposition for the velocity gradient, this decomposition is presented below.

[3] Since $\boldsymbol{b}$ is SPD, its inverse can be easily obtained using adjunct and determinant.

[4] In the particular case of the trace of $\boldsymbol{c}$ in the Peterlin function, as shown by Balci et al. [33], $\mathrm{tr}(\boldsymbol{c}) = ||\boldsymbol{b}||^2 = \mathrm{tr}(\boldsymbol{b}^T \cdot \boldsymbol{b})$ and can thus be easily calculated in terms of $\boldsymbol{b}$.

2.3.1 A special decomposition for the velocity gradient

Fattal and Kupferman [31] proposed a unique decomposition for the velocity gradient tensor. The decomposition consists in writing the velocity gradient on the basis of the eigenvectors of the conformation tensor to find the following tensors,

$$\widetilde{\boldsymbol{L}} = \widetilde{\nabla \boldsymbol{u}}^T = \boldsymbol{Q}_{\boldsymbol{c}}^T \cdot \nabla \boldsymbol{u}^T \cdot \boldsymbol{Q}_{\boldsymbol{c}} = \widetilde{\boldsymbol{B}} + \widetilde{\boldsymbol{\Omega}} + \widetilde{\boldsymbol{N}}(\boldsymbol{\Lambda}^{\boldsymbol{c}})^{-1} \quad , \tag{2.46}$$

where $\boldsymbol{Q}_{\boldsymbol{c}}$ represents the orthogonal tensor composed by the eigenvectors of the conformation tensor in columns, $\boldsymbol{\Lambda}^{\boldsymbol{c}}$ is the diagonal tensor containing the eigenvalues of $\boldsymbol{c}$, $\widetilde{\boldsymbol{B}}$ is a diagonal tensor, and $\widetilde{\boldsymbol{\Omega}}$ and $\widetilde{\boldsymbol{N}}$ are anti-symmetric tensors.

Defining $\boldsymbol{B} = \boldsymbol{Q}_{\boldsymbol{c}} \cdot \widetilde{\boldsymbol{B}} \cdot \boldsymbol{Q}_{\boldsymbol{c}}^T$, $\boldsymbol{\Omega} = \boldsymbol{Q}_{\boldsymbol{c}} \cdot \widetilde{\boldsymbol{\Omega}} \cdot \boldsymbol{Q}_{\boldsymbol{c}}^T$, and $\boldsymbol{N} = \boldsymbol{Q}_{\boldsymbol{c}} \cdot \widetilde{\boldsymbol{N}} \cdot \boldsymbol{Q}_{\boldsymbol{c}}^T$, and using $\boldsymbol{c} = \boldsymbol{Q}_{\boldsymbol{c}} \cdot \boldsymbol{\Lambda}^{\boldsymbol{c}} \cdot \boldsymbol{Q}_{\boldsymbol{c}}^T$, the decomposition (2.46) also reads

$$\boldsymbol{L} = \nabla \boldsymbol{u}^T = \boldsymbol{B} + \boldsymbol{\Omega} + \boldsymbol{N} \boldsymbol{c}^{-1} \quad . \tag{2.47}$$

It is worth noting that $\boldsymbol{B}$ is symmetric and commutes with $\boldsymbol{c}$, and $\boldsymbol{\Omega}$ and $\boldsymbol{N}$ are anti-symmetric.

Substitution of the decomposition (2.47) in Eq. (2.12) gives

$$\frac{D\boldsymbol{c}}{Dt} - (\boldsymbol{\Omega} \cdot \boldsymbol{c} - \boldsymbol{c} \cdot \boldsymbol{\Omega}) - 2\boldsymbol{B}\boldsymbol{c} + \frac{f\,(\mathrm{tr}(\boldsymbol{c}))\,\boldsymbol{c} - \boldsymbol{I}}{Wi_h} = 0 \quad , \tag{2.48}$$

where

$$\widetilde{B}_{ij} = \widetilde{\nabla u}_{ij} \quad , \tag{2.49}$$

and

$$\widetilde{\Omega}_{ij} = \frac{\Lambda^{\boldsymbol{c}}_{ii} \widetilde{\nabla u}_{ij} + \Lambda^{\boldsymbol{c}}_{jj} \widetilde{\nabla u}_{ji}}{\Lambda^{\boldsymbol{c}}_{jj} - \Lambda^{\boldsymbol{c}}_{ii}} \quad . \tag{2.50}$$

Equation (2.48) can also be expressed in its eigendecomposed version (originally shown by Vaithianathan and Collins [26]), by applying the chain derivative rule on $\boldsymbol{\Lambda}^{\boldsymbol{c}} = \boldsymbol{Q}_{\boldsymbol{c}}^T \cdot \boldsymbol{c} \cdot \boldsymbol{Q}_{\boldsymbol{c}}$, yielding

$$\frac{D\boldsymbol{\Lambda}^{\boldsymbol{c}}}{Dt} = \frac{D(\boldsymbol{Q}_{\boldsymbol{c}}^T \cdot c \cdot \boldsymbol{Q}_{\boldsymbol{c}})}{Dt} = \frac{D\boldsymbol{Q}_{\boldsymbol{c}}^T}{Dt} \cdot c \cdot \boldsymbol{Q}_{\boldsymbol{c}} + \boldsymbol{Q}_{\boldsymbol{c}}^T \cdot \frac{Dc}{Dt} \cdot \boldsymbol{Q}_{\boldsymbol{c}} + \boldsymbol{Q}_{\boldsymbol{c}}^T \cdot c \cdot \frac{D\boldsymbol{Q}_{\boldsymbol{c}}}{Dt} \quad . \tag{2.51}$$

Substitution of Eq. (2.48) in Eq. (2.51) yields

$$\frac{D\boldsymbol{\Lambda}^{\boldsymbol{c}}}{Dt} = \boldsymbol{\Lambda}^{\boldsymbol{c}} \cdot \boldsymbol{\mathcal{Q}} - \boldsymbol{\mathcal{Q}} \cdot \boldsymbol{\Lambda}^{\boldsymbol{c}} + \widetilde{\boldsymbol{\Omega}} \cdot \boldsymbol{\Lambda}^{\boldsymbol{c}} - \boldsymbol{\Lambda}^{\boldsymbol{c}} \cdot \widetilde{\boldsymbol{\Omega}} + 2\widetilde{\boldsymbol{B}} \cdot \boldsymbol{\Lambda}^{\boldsymbol{c}} - \frac{f\,(\mathrm{tr}(\boldsymbol{c}))\,\boldsymbol{\Lambda}^{\boldsymbol{c}} - \boldsymbol{I}}{Wi_h} \quad , \tag{2.52}$$

where $\boldsymbol{\mathcal{Q}} = \boldsymbol{Q}_{\boldsymbol{c}}^T \cdot \frac{D\boldsymbol{Q}_{\boldsymbol{c}}}{Dt} = -\frac{D\boldsymbol{Q}_{\boldsymbol{c}}^T}{Dt} \cdot \boldsymbol{Q}_{\boldsymbol{c}} = -\boldsymbol{\mathcal{Q}}^T$. Thus, the tensor $\boldsymbol{\mathcal{Q}}$ is anti-symmetric, as $\widetilde{\boldsymbol{\Omega}}$. Therefore, these two tensors cannot contribute to the evolution of (the diagonal tensor)

$\mathbf{\Lambda}^c$. Equation (2.52) can be split into two parts, one for the diagonal terms and another one for the off-diagonal terms, which respectively yields

$$\frac{D\mathbf{\Lambda}^c}{Dt} = 2\widetilde{\boldsymbol{B}} \cdot \mathbf{\Lambda}^c - \frac{f\,(\mathrm{tr}(\boldsymbol{c}))\,\mathbf{\Lambda}^c - \boldsymbol{I}}{Wi_h} \quad , \tag{2.53}$$

and

$$\boldsymbol{\mathcal{Q}} \cdot \mathbf{\Lambda}^c - \mathbf{\Lambda}^c \cdot \boldsymbol{\mathcal{Q}} = \widetilde{\mathbf{\Omega}} \cdot \mathbf{\Lambda}^c - \mathbf{\Lambda}^c \cdot \widetilde{\mathbf{\Omega}} \quad . \tag{2.54}$$

Note that, from Eq. (2.54), we have that $\boldsymbol{\mathcal{Q}} = \widetilde{\mathbf{\Omega}}$.

2.3.2 A general transformation

The kernel operation applies for any transformation function $\Bbbk()$ applied to the conformation tensor being continuous, invertible and differentiable, yielding the following relation

$$\Bbbk(\boldsymbol{c}) = \boldsymbol{Q_c} \cdot \Bbbk(\mathbf{\Lambda}^c) \cdot \boldsymbol{Q}_{\boldsymbol{c}}^T \quad . \tag{2.55}$$

The kernel transformation is based not only on the decomposition presented above, but also on the fact that, generally, every analytic function of a diagonal matrix, $\boldsymbol{d}$, can be computed entry-wise as follows

$$\Bbbk(\mathrm{diag}(d_{11}; d_{22}; \ldots; d_{nn})) = \mathrm{diag}(\Bbbk(d_{11}); \Bbbk(d_{22}); \ldots; \Bbbk(d_{nn})) \quad . \tag{2.56}$$

The kernel transformation operates on the magnitude of the extension of the polymeric conformation without changing its eigendirections. For the evolution equation of the kernel function, the chain derivative rule is used, yielding

$$\frac{\partial \Bbbk({\Lambda^c}_{ii})}{\partial t} = \frac{\partial {\Lambda^c}_{ii}}{\partial t} \cdot \frac{\partial \Bbbk({\Lambda^c}_{ii})}{\partial {\Lambda^c}_{ii}} = \frac{\partial {\Lambda^c}_{ii}}{\partial t} \cdot J_{ii} \quad , \tag{2.57}$$

where $\boldsymbol{J}$ is the (diagonal) gradient matrix defined as

$$\boldsymbol{J} = \mathrm{diag}\left(\frac{\partial \Bbbk({\lambda^c}_1)}{\partial {\lambda^c}_1}; \frac{\partial \Bbbk({\lambda^c}_2)}{\partial {\lambda^c}_2}; \frac{\partial \Bbbk({\lambda^c}_3)}{\partial {\lambda^c}_3} \right) \quad . \tag{2.58}$$

Equation (2.53) can be used into Eq. (2.57) to give

$$\frac{D\Bbbk(\mathbf{\Lambda}^c)}{Dt} = 2\widetilde{\boldsymbol{B}} \cdot \mathbf{\Lambda}^c \cdot \boldsymbol{J} - \frac{f\,(\mathrm{tr}(\boldsymbol{c}))\,\mathbf{\Lambda}^c - \boldsymbol{I}}{Wi_h} \cdot \boldsymbol{J} \quad , \tag{2.59}$$

The evolution equation for the kernel function, $\Bbbk(\boldsymbol{c})$, can be obtained using the chain derivative rule for the relation $\Bbbk(\boldsymbol{c}) = \boldsymbol{Q_c}\Bbbk(\boldsymbol{\Lambda^c})\boldsymbol{Q_c^T}$,

$$\frac{D\Bbbk(\boldsymbol{c})}{Dt} = \frac{D(\boldsymbol{Q_c}\cdot\Bbbk(\boldsymbol{\Lambda^c})\cdot\boldsymbol{Q_c^T})}{Dt} = \frac{D\boldsymbol{Q_c}}{Dt}\cdot\Bbbk(\boldsymbol{\Lambda^c})\cdot\boldsymbol{Q_c^T} + \boldsymbol{Q_c}\cdot\frac{D\Bbbk(\boldsymbol{\Lambda^c})}{Dt}\cdot\boldsymbol{Q_c^T} + \boldsymbol{Q_c}\cdot\Bbbk(\boldsymbol{\Lambda^c})\cdot\frac{D\boldsymbol{Q_c^T}}{Dt} \quad . \tag{2.60}$$

Using Eq. (2.59) and some relations shown before, the evolution equation for the kernel function takes the form:

$$\frac{D\Bbbk(\boldsymbol{c})}{Dt} - (\boldsymbol{\Omega}\cdot\Bbbk(\boldsymbol{c}) - \Bbbk(\boldsymbol{c})\cdot\boldsymbol{\Omega}) - 2\mathbb{B} + \frac{1}{Wi_h}\mathbb{H} = 0 \quad , \tag{2.61}$$

where

$$\mathbb{B} = \boldsymbol{Q_c}\cdot\widetilde{\boldsymbol{B}}\cdot\boldsymbol{\Lambda^c}\cdot\boldsymbol{J}\cdot\boldsymbol{Q_c^T} \quad , \tag{2.62}$$

and

$$\mathbb{H} = \boldsymbol{Q_c}\cdot\mathcal{H}(\boldsymbol{\Lambda^c})\cdot\boldsymbol{J}\cdot\boldsymbol{Q_c^T} \quad , \tag{2.63}$$

with $\mathcal{H}(\boldsymbol{\Lambda^c}) = f\,(\mathrm{tr}(\boldsymbol{c}))\,\boldsymbol{\Lambda^c} - \boldsymbol{I}$ for a FENE-P fluid.

2.3.3 The root^k kernel transformation

One of the advantages of the kernel transformation is that, rather than being restricted to the square-root transformation, it allows a general root-type transformation for a given root k. The root^k kernel transformation is then defined as

$$\Bbbk(\boldsymbol{c}) = \boldsymbol{c}^{\frac{1}{k}} = \boldsymbol{Q_c}\cdot(\boldsymbol{\Lambda^c})^{\frac{1}{k}}\cdot\boldsymbol{Q_c^T} \quad . \tag{2.64}$$

The conformation tensor can be recovered with the following inverse operation

$$\boldsymbol{c} = \Bbbk(\boldsymbol{c})^k \quad . \tag{2.65}$$

For the root^k kernel transformation, the diagonal gradient matrix $\boldsymbol{J}$ takes the form

$$\boldsymbol{J} = \mathrm{diag}\left(\frac{\partial{\lambda^c}_1^{\frac{1}{k}}}{\partial{\lambda^c}_1};\frac{\partial{\lambda^c}_2^{\frac{1}{k}}}{\partial{\lambda^c}_2};\frac{\partial{\lambda^c}_3^{\frac{1}{k}}}{\partial{\lambda^c}_3}\right) = \frac{(\boldsymbol{\Lambda^c})^{\frac{1-k}{k}}}{k} \quad . \tag{2.66}$$

Moreover, following Eqs. (2.62) and (2.63), tensors $\mathbb{B}$ and $\mathbb{H}$ are respectively calculated as follows

$$\mathbb{B} = \boldsymbol{Q_c}\cdot\widetilde{\boldsymbol{B}}\cdot\boldsymbol{\Lambda^c}\cdot\boldsymbol{J}\cdot\boldsymbol{Q_c^T} = \boldsymbol{Q_c}\cdot\widetilde{\boldsymbol{B}}\cdot\boldsymbol{\Lambda^c}\cdot\frac{(\boldsymbol{\Lambda^c})^{\frac{1-k}{k}}}{k}\cdot\boldsymbol{Q_c^T} = \frac{1}{k}\boldsymbol{Q_c}\cdot\widetilde{\boldsymbol{B}}\cdot(\boldsymbol{\Lambda^c})^{\frac{1}{k}}\cdot\boldsymbol{Q_c^T} = \frac{1}{k}\boldsymbol{B}\Bbbk(\boldsymbol{c}) \quad , \tag{2.67}$$

and

$$\begin{aligned}\mathbb{H} = \boldsymbol{Q_c} \cdot \mathcal{H}(\boldsymbol{\Lambda^c}) \cdot \boldsymbol{J} \cdot \boldsymbol{Q_c^T} = \boldsymbol{Q_c} \cdot [f(\mathrm{tr}(\boldsymbol{c}))\boldsymbol{\Lambda^c} - \boldsymbol{I}] \cdot \frac{(\boldsymbol{\Lambda^c})^{\frac{1-k}{k}}}{k} \cdot \boldsymbol{Q_c^T} = \\ \frac{1}{k}\boldsymbol{Q_c} \cdot \left[f(\mathrm{tr}(\boldsymbol{c}))(\boldsymbol{\Lambda^c})^{\frac{1}{k}} - (\boldsymbol{\Lambda^c})^{\frac{1-k}{k}}\right] \cdot \boldsymbol{Q_c^T} = \frac{1}{k}\left(f(\mathrm{tr}(\boldsymbol{c}))\mathbb{k}(\boldsymbol{c}) - \mathbb{k}(\boldsymbol{c})^{1-k}\right) \quad .\end{aligned} \tag{2.68}$$

The evolution equation for the root^k kernel transformation is then expressed as

$$\frac{D\mathbb{k}(\boldsymbol{c})}{Dt} - (\boldsymbol{\Omega} \cdot \mathbb{k}(\boldsymbol{c}) - \mathbb{k}(\boldsymbol{c}) \cdot \boldsymbol{\Omega}) - \frac{2}{k}\boldsymbol{B}\mathbb{k}(\boldsymbol{c}) + \frac{1}{kWi_h}\left(f(\mathrm{tr}(\boldsymbol{c}))\mathbb{k}(\boldsymbol{c}) - \mathbb{k}(\boldsymbol{c})^{1-k}\right) = 0 \quad . \tag{2.69}$$

It is easy to check that replacing k by 2 recovers the square-root kernel transformation, which reads

$$\frac{D\mathbb{k}(\boldsymbol{c})}{Dt} - (\boldsymbol{\Omega} \cdot \mathbb{k}(\boldsymbol{c}) - \mathbb{k}(\boldsymbol{c}) \cdot \boldsymbol{\Omega}) - \boldsymbol{B}\mathbb{k}(\boldsymbol{c}) + \frac{1}{2Wi_h}\left(f(\mathrm{tr}(\boldsymbol{c}))\mathbb{k}(\boldsymbol{c}) - \mathbb{k}(\boldsymbol{c})^{-1}\right) = 0 \quad . \tag{2.70}$$

Equation (2.70) is equivalent to Eq. (2.24). Indeed, in this particular case, $\mathbb{k}(\boldsymbol{c}) = \boldsymbol{b}$, and thus

$$\boldsymbol{\Omega} \cdot \boldsymbol{b} - \boldsymbol{b} \cdot \boldsymbol{\Omega} + \boldsymbol{B} \cdot \boldsymbol{b} = \boldsymbol{b} \cdot \nabla\boldsymbol{u} + \boldsymbol{a} \cdot \boldsymbol{b} \quad . \tag{2.71}$$

2.3.4 The inclusion of an artificial stress diffusion for the kernel root^k transformation

Regarding the inclusion of an artificial diffusion into the equations for the kernel root^k formulation at least two approaches are again possible: adding a diffusive term directly to the evolution equation for $\mathbb{k}(\boldsymbol{c})$ (Eq. (2.69)) or consider a diffusion term in the standard conformation tensor (as in Eq. (2.13)) and apply the kernel transformation.

The first proposition simply adds a term proportional to the Laplacian of $\mathbb{k}(\boldsymbol{c})$ into Eq. (2.69), which gives

$$\frac{D\mathbb{k}(\boldsymbol{c})}{Dt} - (\boldsymbol{\Omega} \cdot \mathbb{k}(\boldsymbol{c}) - \mathbb{k}(\boldsymbol{c}) \cdot \boldsymbol{\Omega}) - \frac{2}{k}\boldsymbol{B}\mathbb{k}(\boldsymbol{c}) + \frac{1}{kWi_h}\left(f(\mathrm{tr}(\boldsymbol{c}))\mathbb{k}(\boldsymbol{c}) - \mathbb{k}(\boldsymbol{c})^{1-k}\right) = \frac{D_k}{Re_h}\Delta\mathbb{k}(\boldsymbol{c}) \quad . \tag{2.72}$$

In a second approach, the kernel transformation is applied to Eq. (2.13) instead of Eq. (2.12) so that the artificial diffusion term would also be transformed.

Let us focus first on the diffusion term. What changes is that an extra term would be added to Eq. (2.59) to give

$$\frac{D\mathbb{k}(\boldsymbol{\Lambda^c})}{Dt} = 2\widetilde{\boldsymbol{B}} \cdot \boldsymbol{\Lambda^c} \cdot \boldsymbol{J} - \frac{f(\mathrm{tr}(\boldsymbol{c}))\boldsymbol{\Lambda^c} - \boldsymbol{I}}{Wi_h} \cdot \boldsymbol{J} + \frac{D_c}{Re_h}\Delta\mathbb{k}(\boldsymbol{\Lambda^c}) \cdot \boldsymbol{J} \quad , \tag{2.73}$$

Following the procedure in Eq. (2.60) would lead now to

$$\frac{D\mathbb{k}(\boldsymbol{c})}{Dt} - (\boldsymbol{\Omega}\cdot\mathbb{k}(\boldsymbol{c}) - \mathbb{k}(\boldsymbol{c})\cdot\boldsymbol{\Omega}) - 2\mathbb{B} + \frac{1}{Wi_h}\mathbb{H} = \frac{D_c}{Re_h}\mathbb{D} \quad , \tag{2.74}$$

with $\mathbb{D} = \boldsymbol{Q_c}\cdot\Delta\boldsymbol{\Lambda^c}\cdot\boldsymbol{J}\cdot\boldsymbol{Q_c^T}$. Now, for the root^k formulation, $\boldsymbol{J}$ was already shown to be $(1/k)(\boldsymbol{\Lambda^c})^{\frac{1-k}{k}}$, which makes the new tensor $\mathbb{D}$ related to the diffusion like

$$\mathbb{D} = \boldsymbol{Q_c}\cdot\Delta\boldsymbol{\Lambda^c}\cdot\boldsymbol{J}\cdot\boldsymbol{Q_c^T} = \frac{1}{k}\boldsymbol{Q_c}\cdot\Delta\boldsymbol{\Lambda^c}\cdot(\boldsymbol{\Lambda^c})^{\frac{1-k}{k}}\cdot\boldsymbol{Q_c^T} = \frac{1}{k}\Delta\mathbb{k}(\boldsymbol{c})^k\cdot\mathbb{k}(\boldsymbol{c})^{1-k} \quad . \tag{2.75}$$

The evolution equation of the root^k with artificial diffusion would then assume the form

$$\begin{aligned}\frac{D\mathbb{k}(\boldsymbol{c})}{Dt} - (\boldsymbol{\Omega}\cdot\mathbb{k}(\boldsymbol{c}) - \mathbb{k}(\boldsymbol{c})\cdot\boldsymbol{\Omega}) - \frac{2}{k}\boldsymbol{B}\mathbb{k}(\boldsymbol{c}) + \\ + \frac{1}{kWi_h}\left(f(\mathrm{tr}(\boldsymbol{c}))\mathbb{k}(\boldsymbol{c}) - \mathbb{k}(\boldsymbol{c})^{1-k}\right) = \frac{D_c}{Re_h}\frac{1}{k}\Delta\mathbb{k}(\boldsymbol{c})^k\cdot\mathbb{k}(\boldsymbol{c})^{1-k} \quad .\end{aligned} \tag{2.76}$$

Note the complexity of this new term on the right-hand side of Eq. (2.76). It involves not only the (already calculated) term $\mathbb{k}(\boldsymbol{c})^{1-k}$ but also $\Delta\mathbb{k}(\boldsymbol{c})^k$, which, as a matter of fact, equals $\Delta\boldsymbol{c}$. Extra operations regarding eigenvalues, eigenvectors and rotations are needed, all of them computationally expensive.

2.3.5 The implementation of the kernel root^k formulation

The kernel root^k formulation requires more code changes compared to the square-root method. The main steps for the kernel root^k formulation are:

- Transformation of the initial field of $\boldsymbol{c}$ into a field of its kernel root^k function, $\mathbb{k}(\boldsymbol{c})$, using Eq. (2.64);
- Calculation of the tensors $\widetilde{\boldsymbol{B}}$ and $\widetilde{\boldsymbol{\Omega}}$ (Eqs. (2.49) and (2.50)), as well as their respective rotated tensors $\boldsymbol{B}$ and $\boldsymbol{\Omega}$;
- Calculation of the term $\mathbb{k}(\boldsymbol{c})^{1-k}$;
- Computation of the inverse transformation (Eq. (2.65)) when $\boldsymbol{c}$ is required.

It is worth noting that almost all operations described above involve knowing the eigenvalues and eigenvectors of $\boldsymbol{c}$ at every time step, leading to considerable increase of CPU time.

2.4 Numerical method

In this section, a brief description of the numerical method to solve the evolution equations is provided.

The original algorithm, named `nnewt_solve` [19] has been used to provide a better understanding of the drag reduction phenomenon over the last 5 years [19–22]. Since the code is well documented in [19], the reader is referred to this reference for further information.

2.4.1 Time discretisation

Momentum equation

Firstly, let us recall the non-dimensional equation for momentum balance, in index notation, which yields

$$\frac{\partial \boldsymbol{u}}{\partial t} + \boldsymbol{u} \cdot \boldsymbol{\nabla} \boldsymbol{u} = -\boldsymbol{\nabla} p + \frac{\beta}{Re_h} \Delta \boldsymbol{u} + \frac{1}{Re_h} \boldsymbol{\nabla} \cdot \boldsymbol{\Xi} \quad . \tag{2.7}$$

In Eq. (2.7) above, pressure, advection and polymer stress are treated explicitly, whereas the diffusion term is treated implicitly. Assembling the advection and polymer stress terms in a vector $\boldsymbol{H}$ gives

$$\boldsymbol{H} = \boldsymbol{u} \cdot \boldsymbol{\nabla} \boldsymbol{u} - \frac{1}{Re_h} \boldsymbol{\nabla} \cdot \boldsymbol{\Xi} \quad . \tag{2.77}$$

In the present algorithm, this vector is treated with the Adams-Bashforth scheme from second to fourth order (user defined). In all simulations performed here the second-order scheme was used. Thus, Eq. (2.77) at the current time step, n, is discretised as

$$\boldsymbol{\mathcal{H}}^{n}(\boldsymbol{u}, \boldsymbol{c}) = \frac{3}{2} \boldsymbol{H}(\boldsymbol{u}^{n}, \boldsymbol{c}^{n}) - \frac{1}{2} \boldsymbol{H}(\boldsymbol{u}^{n-1}, \boldsymbol{c}^{n-1}) \quad . \tag{2.78}$$

For the diffusion term, an (user defined) implicit Adams-Moulton scheme is used. Second and third orders are available, but, here again, only second-order runs were done. Therefore, only the second-order formulation (Crank-Nicolson scheme) will be presented. The Laplacian term is discretised as follows

$$\boldsymbol{\mathcal{L}}^{n+1}(\boldsymbol{u}) = \frac{1}{2} \left(\Delta \boldsymbol{u}_{*}^{n+1} + \Delta \boldsymbol{u}^{n} \right) \quad , \tag{2.79}$$

where $\boldsymbol{u}_{*}^{n+1}$ is the intermediate velocity at the time-step $n+1$ and its associated discretised equation is

$$\frac{\mathbf{u}_{*}^{n+1} - \mathbf{u}^{n}}{\delta t} + \boldsymbol{\mathcal{H}}^{n}(\boldsymbol{u}, \boldsymbol{c}) = -\boldsymbol{\nabla} p^{n} + \frac{\beta}{Re_h} \boldsymbol{\mathcal{L}}^{n+1}(\boldsymbol{u}) \quad . \tag{2.80}$$

The discretised momentum equation considering second-order Adams-Bashforth scheme for advection and polymer stress, and Crank-Nicolson scheme for diffusion takes the form

$$\left(\frac{\boldsymbol{I}}{\delta t} - \frac{\beta}{2Re_h}\Delta\right)\delta\boldsymbol{u}_*^{n+1} = -\frac{3}{2}\boldsymbol{H}(\boldsymbol{u}^n, \boldsymbol{c}^n) + \frac{1}{2}\boldsymbol{H}(\boldsymbol{u}^{n-1}, \boldsymbol{c}^{n-1}) + \frac{\beta}{2Re_h}\Delta\boldsymbol{u}^n - \boldsymbol{\nabla}p^n \quad , \tag{2.81}$$

subject to the Dirichlet boundary conditions $\delta u_*^{n+1} = \delta w_*^{n+1} = 0$ at the walls. At this point, the increment for the intermediate velocity remains $\delta v_*^{n+1} = v_*^{n+1} - v^n = v_*^{n+1}$. The intermediate velocity, v_*^{n+1} , is used further on for the pressure boundary condition.

Equation (2.81) is solved in terms of the velocity increment $\delta\boldsymbol{u}_*^{n+1} = \boldsymbol{u}_*^{n+1} - \boldsymbol{u}^n$. However, the intermediate velocity field, $\boldsymbol{u}_*^{n+1} = \boldsymbol{u}^n + \delta\boldsymbol{u}_*^{n+1}$, is not solenoidal. Thus, a pressure correction of the form $\delta p^{n+1} = p^{n+1} - p^n$ is applied, leading to

$$\boldsymbol{u}^{n+1} = \boldsymbol{u}_*^{n+1} - \delta t\boldsymbol{\nabla}\left(\delta p^{n+1}\right) \quad . \tag{2.82}$$

To enforce a divergence-free velocity field, $\boldsymbol{u}^{n+1}$, the pressure correction must satisfy the Poisson equation

$$\Delta(\delta p^{n+1}) = \frac{1}{\delta t}\boldsymbol{\nabla}\cdot\boldsymbol{u}_*^{n+1} \quad . \tag{2.83}$$

The pressure increment equation is solved on a staggered grid subject to the Neumann boundary conditions $\partial(\delta p^{n+1})/\partial y = v_*^{n+1}/\delta t$.

Hence, marching in time the (pressure-velocity) fields follows this procedure:

- solve the Helmholtz equation (2.81) for the velocity increment, $\delta\boldsymbol{u}_*^{n+1}$;
- obtain the intermediate velocity field, $\boldsymbol{u}_*^{n+1} = \boldsymbol{u}^n + \delta\boldsymbol{u}_*^{n+1}$;
- solve the Poisson equation (2.83); and
- finally update the velocity field with and the pressure field as $p^{n+1} = p^n + \delta p^{n+1}$.

Conformation tensor equation

Let us retake the evolution equation for the conformation tensor with artificial diffusion included,

$$\frac{\mathrm{D}\boldsymbol{c}}{\mathrm{D}t} - \boldsymbol{c}\cdot\boldsymbol{\nabla}\boldsymbol{u} - \boldsymbol{\nabla}\boldsymbol{u}^T\cdot\boldsymbol{c} + \frac{f\,(\mathrm{tr}(\boldsymbol{c}))\,\boldsymbol{c} - \boldsymbol{I}}{Wi_h} = \frac{D_c}{Re_h}\Delta\boldsymbol{c} \quad . \tag{2.13}$$

Analogously to the momentum equation, the diffusion term is treated with a Crank-Nicolson scheme while all the other terms are treated with a second-order Adams-Bashforth scheme. Again, let us gather the explicit terms in a tensor $\boldsymbol{H_c}$, as follows

$$\boldsymbol{H_c} = \boldsymbol{u}\cdot\boldsymbol{\nabla}\boldsymbol{c} - \boldsymbol{c}\cdot\boldsymbol{\nabla}\boldsymbol{u} - \boldsymbol{\nabla}\boldsymbol{u}^T\cdot\boldsymbol{c} + \frac{f\,(\mathrm{tr}(\boldsymbol{c}))\,\boldsymbol{c} - \boldsymbol{I}}{Wi_h} \quad . \tag{2.84}$$

As a first step, the conformation tensor field is updated at the walls without any artificial diffusion, which yields the intermediate field

$$\boldsymbol{c}_*^{n+1} = \boldsymbol{c}^n - \delta t\left[\frac{3}{2}\boldsymbol{H}_{\boldsymbol{c}}(\boldsymbol{u}^n,\boldsymbol{c}^n) - \frac{1}{2}\boldsymbol{H}_{\boldsymbol{c}}(\boldsymbol{u}^{n-1},\boldsymbol{c}^{n-1})\right] \quad . \tag{2.85}$$

The increment to the conformation tensor, $\delta\boldsymbol{c}^{n+1} = \boldsymbol{c}^{n+1} - \boldsymbol{c}^n$, is obtained through solution of the Helmholtz equation

$$\left(\frac{\boldsymbol{I}}{\delta t} - \frac{D_0}{2Re_h}\Delta\right)\delta\boldsymbol{c}^{n+1} = -\frac{3}{2}\boldsymbol{H}_{\boldsymbol{c}}(\boldsymbol{u}^n,\boldsymbol{c}^n) + \frac{1}{2}\boldsymbol{H}_{\boldsymbol{c}}(\boldsymbol{u}^{n-1},\boldsymbol{c}^{n-1}) + \frac{D_0}{2Re_h}\Delta\boldsymbol{c}^n \quad . \tag{2.86}$$

subject to the boundary conditions $\delta\boldsymbol{c}^{n+1} = \boldsymbol{c}_*^{n+1} - \boldsymbol{c}^n$ at the walls.

Once Eq. (2.86) is solved, the conformation tensor is updated with

$$\boldsymbol{c}^{n+1} = \boldsymbol{c}^n + \delta\boldsymbol{c}^{n+1} \quad . \tag{2.87}$$

It is important to highlight that, concerning time discretisation, no changes were necessary for the implementation of the square-root and the kernel formulations. Basically, the variable $\boldsymbol{c}$ is replaced by its transformed one, and some terms in the tensor $\boldsymbol{H}_{\boldsymbol{c}}$ change accordingly with the model.

2.4.2 Spatial discretisation

The numerical code uses Fourier (spectral) discretisation in the stream- and span-wise (homogeneous) directions, x and z respectively. In the wall-normal direction, y, the discretisation with high-order compact finite difference schemes.

Equations in the Fourier space

The flow equations are 2D-Fourier transformed in the two homogeneous directions. The (complex) fields in Fourier space will be identified with an over-hat, ˆ. For the momentum equation for the calculation of the velocity increment, the 2D-Fourier transformation yields

$$\begin{aligned}\left\{\frac{\boldsymbol{I}}{\delta t} + \frac{\beta}{2Re_h}\left(|\boldsymbol{k}|^2\boldsymbol{I} - \frac{\mathrm{d}^2}{\mathrm{d}y^2}\right)\right\}\widehat{\delta\boldsymbol{u}}_*^{n+1} = \\ -\frac{3}{2}\widehat{\boldsymbol{H}}(\boldsymbol{u}^n,\boldsymbol{c}^n) + \frac{1}{2}\widehat{\boldsymbol{H}}(\boldsymbol{u}^{n-1},\boldsymbol{c}^{n-1}) + \frac{\beta}{2Re_h}\left(-|\boldsymbol{k}|^2\boldsymbol{I} + \frac{\mathrm{d}^2}{\mathrm{d}y^2}\right)\hat{\boldsymbol{u}}^n - \boldsymbol{\nabla}_s\hat{p}^n \quad ,\end{aligned} \tag{2.88}$$

in which $\boldsymbol{k} = k_x\boldsymbol{e}_x + k_z\boldsymbol{e}_z$, with k_x and k_z are the wave-numbers in the stream-wise and span-wise directions, respectively. The operator $\mathrm{d}/\mathrm{d}y$ indicates the finite difference approximation for the wall-normal derivative $\partial/\partial y$ (see basic information about finite difference tools below) and $\nabla_s = (jk_x, \mathrm{d}/\mathrm{d}y, jk_z)^t$ is the hybrid gradient operator, with $j = \sqrt{-1}$.

For the pressure increment equation, one gets

$$\left(|\boldsymbol{k}|^2 \boldsymbol{I} - \frac{\mathrm{d}^2}{\mathrm{d}y^2}\right)\widehat{\delta p}^{n+1} = \frac{1}{\delta t}\nabla_s \cdot \hat{\boldsymbol{u}}_*^{n+1} \quad . \tag{2.89}$$

Finally, for the conformation tensor increment, the 2D-Fourier transformed equation reads

$$\begin{aligned} &\left\{\frac{\boldsymbol{I}}{\delta t} + \frac{D_0}{2Re_h}\left(|\boldsymbol{k}|^2 \boldsymbol{I} - \frac{\mathrm{d}^2}{\mathrm{d}y^2}\right)\right\}\widehat{\delta \boldsymbol{c}}^{n+1} = \\ &\quad -\frac{3}{2}\widehat{\boldsymbol{H}_{\boldsymbol{c}}}(\boldsymbol{u}^n, \boldsymbol{c}^n) + \frac{1}{2}\widehat{\boldsymbol{H}_{\boldsymbol{c}}}(\boldsymbol{u}^{n-1}, \boldsymbol{c}^{n-1}) + \frac{D_c}{2Re_h}\left(-|\boldsymbol{k}|^2 \boldsymbol{I} + \frac{\mathrm{d}^2}{\mathrm{d}y^2}\right)\hat{\boldsymbol{c}}^n \quad . \end{aligned} \tag{2.90}$$

Finite difference scheme

First and second derivatives in the wall-normal direction, y, are obtained by means of high-order compact finite difference schemes. The Hermitian technique used to obtain the first and second derivatives of a function $f(\xi)$ on equidistant grid-points ξ_i (with $i = 1, N+1$) follows from solution of the tri-banded linear systems

$$\boldsymbol{C}\boldsymbol{f}' = \boldsymbol{D}\boldsymbol{f} \quad \text{and} \quad \boldsymbol{A}\boldsymbol{f}'' = \boldsymbol{B}\boldsymbol{f} \quad , \tag{2.91}$$

where $\boldsymbol{f} = (f_1, f_2, \cdots, f_N, f_{N+1})^t$, f_i is $f(\xi)$ evaluated at $\xi_i \in [a,b]$, $\boldsymbol{f}' = \mathrm{d}\boldsymbol{f}/\mathrm{d}\xi$, and $\boldsymbol{f}'' = \mathrm{d}^2\boldsymbol{f}/\mathrm{d}\xi^2$. The generation of the banded matrices $\boldsymbol{A}$, $\boldsymbol{B}$, $\boldsymbol{C}$, and $\boldsymbol{D}$ is facilitated by the finite difference stencils by Lele [100] and Carpenter, Gottlieb, and Abarbanel [101], which are detailed in the paper by Thais et al. [19].

The scheme used is of sixth order for core points and fifth order for boundary points and first points off the boundaries. We insist in particular that the second-order derivative is *directly* evaluated with a sixth-order scheme, not by taking two successive first-order derivatives. This ensures spectral-like precision in the wall-normal direction.

In this direction, the equidistant grid points $\{\xi_1 = a, \xi_2, \xi_3, \cdots, \xi_N, \xi_{N+1} = b\}$ in an interval $[a,b]$ separated by a distance $h = b - a$ are stretched by a hyperbolic mapping function in order to increase the resolution near the walls where strong gradients occur.

The stretching function used transforms an equidistant discretisation, ξ_i, of $N+1$ grid points within the interval $[a,b] = [-1,1]$ in a clustered set of non-uniform $N+1$ points, y_i, in $[-1,1]$. The stretching function is

$$y = (1/s)\tanh[\xi \tanh^{-1}(s)] \quad , \tag{2.92}$$

where s is a positive parameter proportional to the degree of clustering near the walls, with $s \to 0$ reverting to a regular equidistant mesh.

First and second derivatives on the non-uniform grid are calculated as a function of the derivatives on the uniform grid following the chain rule for derivation as follows

$$\frac{\partial f}{dy} = \gamma_1 \frac{\partial f}{\partial \xi}, \quad \frac{\partial^2 f}{\partial y^2} = \gamma_1^2 \frac{\partial^2 f}{\partial \xi^2} + \gamma_2 \frac{\partial f}{\partial \xi} \quad , \tag{2.93}$$

in which $\gamma_j = \left(\partial^j \xi / \partial y^j\right)$ are the Jacobian of order j of the stretching function. Finally, considering Eqs. (2.91) and (2.93), the approximation of the first and second derivatives of a function f on a non-uniform grid spacing are computed as

$$\frac{\mathrm{d}\boldsymbol{f}}{\mathrm{d}y} = \left\{\boldsymbol{\sigma_1} \boldsymbol{C}^{-1} \boldsymbol{D}\right\} \boldsymbol{f} \quad , \tag{2.94}$$

and

$$\frac{\mathrm{d}^2 \boldsymbol{f}}{\mathrm{d}y^2} = \left\{\left[\boldsymbol{\sigma_1}^2 \boldsymbol{A}^{-1} \boldsymbol{B}\right] + \left[\boldsymbol{\sigma}_2 \boldsymbol{C}^{-1} \boldsymbol{D}\right]\right\} \boldsymbol{f} \quad , \tag{2.95}$$

where the tensors $\boldsymbol{\sigma}$ are defined as $\boldsymbol{\sigma}_k = \gamma_k \boldsymbol{I}$. Note that linear system of Eqs. (2.94) and (2.95) preserve their tri-banded property on the irregular grid, which guaranties numerical efficiency.

2.4.3 Further comments on the algorithm

The code uses de-aliasing in the homogeneous directions and filtering in the wall-normal direction to get rid of the typical accumulation of energy at high wave-numbers in spectral turbulent simulations.

Furthermore, it is important to remark that the algorithm was conceived for massively parallel environments using Message Passing Interface (MPI) and Open Multi-Processing (OpenMP) implementation.

Detailed information concerning the parallel aspects of the code are available in reference [19].

Chapter 3

Results and Discussions

In this Chapter, the results for turbulent channel flows using the square-root and the kernel root^k formulations are compared with those obtained with the standard conformation tensor formulation.

Attempts to run turbulent channel simulations without any artificial diffusion have not converged. Therefore, different approaches to include artificial diffusion have been assessed.

At a first step, the effect of artificial diffusion is evaluated on laminar flows where analytical or pseudo-analytical solutions can be used for validation. The convergence of each formulation is then discussed for turbulent channel flows, including the difference in terms of CPU time, stability and sensitivity to the artificial stress diffusion. Finally, some concluding remarks are presented, followed by a few suggestions for further investigation.

3.1 Summary of the approaches to include artificial diffusion

None of the attempts to simulate turbulent channel flows using either the square-root or the kernel root^k transformation without artificial diffusion succeed. Even if the positiveness of the conformation tensor is preserved, the turbulent flows present steep gradients in both velocity and conformation tensor fields to rise numerical errors that lead to unbounded values for the conformation tensor, rapidly causing divergence.

In view of this scenario, we consider here the inclusion of artificial diffusion to the constitutive equations. Regarding the addition of artificial diffusivity, for the conformation tensor, the idea of Sureshkumar, Beris, and Handler [5] is followed, giving

$$\frac{\mathrm{D}\boldsymbol{c}}{\mathrm{D}t} - \boldsymbol{c}\cdot\nabla\boldsymbol{u} - \nabla\boldsymbol{u}^T\cdot\boldsymbol{c} + \frac{f\,(\mathrm{tr}(\boldsymbol{c}))\,\boldsymbol{c} - \boldsymbol{I}}{Wi_h} = \frac{D_c}{Re_h}\Delta\boldsymbol{c} \quad , \tag{2.13}$$

However, for the transformed conformation equations, two general approaches were presented in Chapter 2. In the approach 1, the tensor transformations are applied to Eq. (2.13), *i.e.* the standard formulation for the conformation tensor with the inclusion of stress diffusion. This procedure is more consistent from the mathematical point of view and, hereafter, it will be referred to as "*a priori* approach". On the other hand, approach 2 considers the transformation of the original equation of the FENE-P model without any artificial diffusion (Eq. (2.12)) and adds a term proportional to the Laplacian of the transformed conformation tensor directly into the resulting equation. The term "*a posteriori* approach" will be used to refer to this more simplistic approach.

For the root-type kernel transformation, the "*a priori* approach" yields

$$\begin{aligned} \frac{D\mathbb{k}(\boldsymbol{c})}{Dt} - (\boldsymbol{\Omega}\cdot\mathbb{k}(\boldsymbol{c}) - \mathbb{k}(\boldsymbol{c})\cdot\boldsymbol{\Omega}) - \frac{2}{k}\boldsymbol{B}\mathbb{k}(\boldsymbol{c}) + \\ + \frac{1}{kWi_h}\left(f\left(\mathrm{tr}(\boldsymbol{c})\right)\mathbb{k}(\boldsymbol{c}) - \mathbb{k}(\boldsymbol{c})^{1-k}\right) = \frac{D_c}{Re_h}\frac{1}{k}\Delta\mathbb{k}(\boldsymbol{c})^k\cdot\mathbb{k}(\boldsymbol{c})^{1-k} \quad , \end{aligned} \tag{2.76}$$

which is quite inconvenient because of the terms that appear as powers of the transformed conformation tensor. Therefore, this approach has not been considered here. On the other hand, the "*a posteriori* approach" gives

$$\frac{D\mathbb{k}(\boldsymbol{c})}{Dt} - (\boldsymbol{\Omega}\cdot\mathbb{k}(\boldsymbol{c}) - \mathbb{k}(\boldsymbol{c})\cdot\boldsymbol{\Omega}) - \frac{2}{k}\boldsymbol{B}\mathbb{k}(\boldsymbol{c}) + \frac{1}{kWi_h}\left(f\left(\mathrm{tr}(\boldsymbol{c})\right)\mathbb{k}(\boldsymbol{c}) - \mathbb{k}(\boldsymbol{c})^{1-k}\right) = \frac{D_k}{Re_h}\Delta\mathbb{k}(\boldsymbol{c}) \quad , \tag{2.72}$$

and can be easily adapted from the standard conformation tensor formulation with artificial diffusion since the diffusion term is alike.

Similarly, the "*a posteriori* approach" to the square-root conformation leads to

$$\frac{D\boldsymbol{b}}{Dt} - \boldsymbol{b}\cdot\nabla\boldsymbol{u} - \boldsymbol{a}\cdot\boldsymbol{b} + \frac{f\left(\mathrm{tr}(\boldsymbol{c})\right)\boldsymbol{b} - \boldsymbol{b}^{-1}}{2Wi_h} = \frac{D_b}{Re_h}\Delta\boldsymbol{b} \quad , \tag{2.29}$$

and will be assessed as well.

Moreover, the "*a priori* approach" was shown to have two possible formulations for the square-root formulation: one with the term $\boldsymbol{h}$ proposed by Balci et al. [33], leading to

$$\frac{D\boldsymbol{b}}{Dt} - \boldsymbol{b}\cdot\nabla\boldsymbol{u} - \boldsymbol{a}^{*}\cdot\boldsymbol{b} - \frac{D_c}{Re_h}\boldsymbol{h} + \frac{f\left(\mathrm{tr}(\boldsymbol{c})\right)\boldsymbol{b} - \boldsymbol{b}^{-1}}{2Wi_h} = \frac{1}{2}\frac{D_c}{Re_h}\Delta\boldsymbol{b} \quad , \tag{2.35}$$

and the other, proposed here, considering the term $\boldsymbol{h}^{*}$ instead, according to

$$\frac{D\boldsymbol{b}}{Dt} - \boldsymbol{b}\cdot\nabla\boldsymbol{u} - \boldsymbol{a}^{**}\cdot\boldsymbol{b} - \frac{D_c}{Re_h}\boldsymbol{h}^{*} + \frac{f\left(\mathrm{tr}(\boldsymbol{c})\right)\boldsymbol{b} - \boldsymbol{b}^{-1}}{2Wi_h} = \frac{D_c}{Re_h}\Delta\boldsymbol{b} \quad . \tag{2.43}$$

In short, we added artificial diffusion to the constitutive equations considered here using different approaches. A summary of these choices is shown in Tab. 3.1.

Method	Inclusion of artificial diffusion	Notes	Corresponding Equation	Nomenclature
standard	direct		(2.13)	std
square-root	*a priori*	term $\boldsymbol{h}$	(2.35)	sqrt (h)
	a priori	term $\boldsymbol{h}^*$	(2.43)	sqrt (h*)
	a posteriori		(2.29)	sqrt
kernel	*a priori*	not used	(2.76)	-
	a posteriori		(2.72)	kernel

Table 3.1 – Summary of approaches to include artificial diffusion.

3.2 Results for laminar channel flow

The modified algorithm using the square-root and the kernel transformations has been preliminary tested for the laminar Poiseuille flow. For these cases, the bulk Reynolds number, Re_h, is fixed at 1, the Weissenberg number is $Wi_h = 10$, and the polymer maximum extensibility, L, equals 100. The domain lengths (L_x, L_y, L_z), normalised with the channel half-gap, h, are respectively $(2\pi, 2, \pi)$. The mesh considered for laminar simulations is $N_x \times N_y \times N_z = 16 \times 49 \times 8$.

In a first approach, no artificial diffusion was included to any formulation. The profiles of the four non-null components of the conformation tensor for the case without artificial diffusion are depicted in Fig. 3.1.

The conformation tensor is normalised by the square of the maximum chain extensibility, L^2. The square-root and kernel root^k formulations - the latter with $k = 2$ and 4 - are compared to analytical solutions obtained with the BVPSUITE [102] (see Appendix A for more information). The analytical solutions presented in Fig. 3.1 are those obtained for the set of ODE representing the square-root formulation without artificial diffusion. The conformation tensor is recovered by computing $\boldsymbol{c} = \boldsymbol{b} \cdot \boldsymbol{b}$.

Observation of Fig. 3.1 suggests that all transformations recover the analytical solution with satisfactory precision. In order to validate both the solution of the ODE and the numerical results for the transformed conformation formulations, the l^2-norm [1] of the difference between each solution method and the numerical solution for the

[1]The l^2-norm of each component (ij) of the conformation tensor is calculated as

$$l^2 = \sqrt{(c_{ij}^{sol} - c_{ij}^{ss})^2} / (\sqrt{c_{ij}^{ss}})^2 \tag{3.1}$$

where c_{ij}^{sol} are the non-null components of the conformations tensor coming from one of the solution methods considered here (solution of ODE, square-root formulation or kernel root^k formulation) and c_{ij}^{ss}

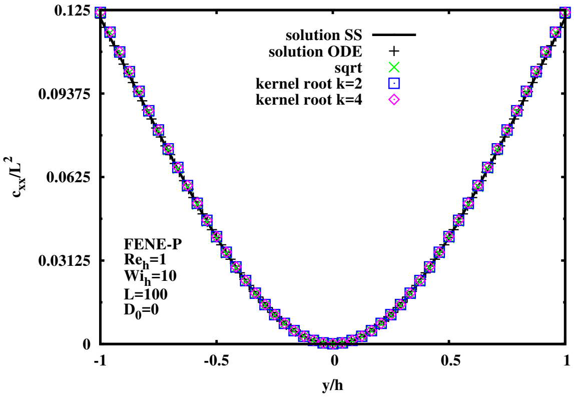

(a) Stream-wise component, c_{xx}

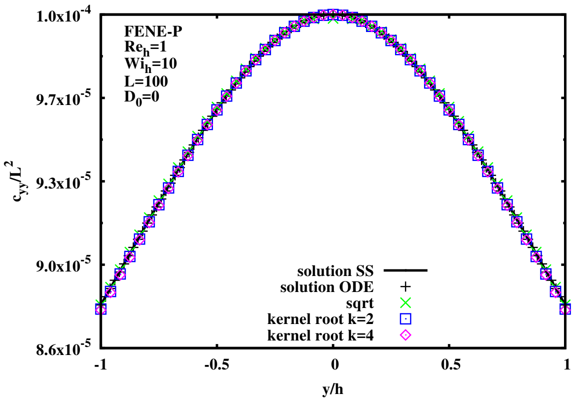

(b) Wall-normal component, c_{yy}

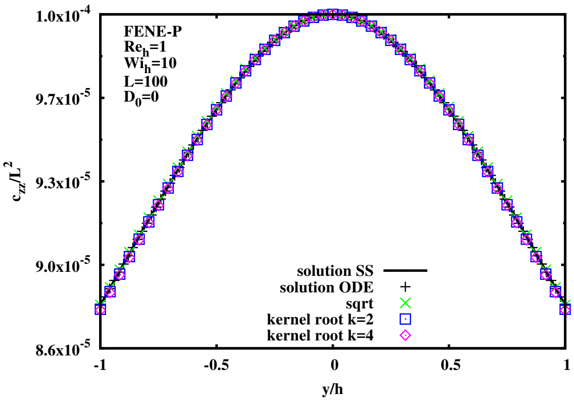

(c) Span-wise component, c_{zz}

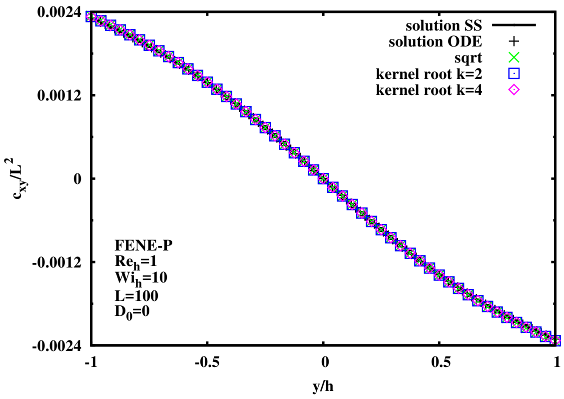

(d) Shear-wise component, c_{xy}

Figure 3.1 – Profiles of normalized components of the conformation tensor without artificial diffusion. ($D_\alpha = 0$)

steady state provided by Sureshkumar, Beris, and Handler [5] is calculated for each non-null component of the conformation tensor and is shown in Tab. 3.2.

Method	c_{xx}	c_{yy}	c_{zz}	c_{xy}
solution ODE	1.857×10^{-9}	2.947×10^{-10}	2.947×10^{-10}	1.503×10^{-9}
square-root	8.389×10^{-3}	5.930×10^{-4}	5.307×10^{-4}	6.146×10^{-3}
kernel root $k = 2$	1.003×10^{-2}	5.113×10^{-4}	5.113×10^{-4}	4.464×10^{-3}
kernel root $k = 4$	1.036×10^{-2}	6.660×10^{-4}	6.660×10^{-4}	4.121×10^{-3}

Table 3.2 – l^2-norm measuring the difference between each solution method and the analytical solution for the steady state flow without artificial diffusion for each non-null component of the conformation tensor.

Table 3.2 shows that the solution of the system of ODE using the BVPSUITE [102] provides good results with l^2-norms from $\sim 10^{-10} - 10^{-9}$. The largest values of l^2

are the components of the steady-state solution for conformation tensor available in Sureshkumar, Beris, and Handler [5] (see Appendix A).

are always associated to the stream-wise component of the conformation tensor, c_{xx}, which is indeed the most stretched one. The l^2-norm of the results obtained with the transformed conformation tensor formulations are approximately 6 order of magnitudes of those coming from the solution of the ODE. However, it is important to remark that the mesh used by the BVPSUITE [102] to solve the system of ODE contains 101 points, while the laminar simulations were performed with 49 points in the wall-normal direction.

The main component c_{xx} (Fig. 3.1a) has a parabolic profile with positive concavity, meaning that the greatest polymer stream-wise stretching is near to the wall. As predicted by the set of equations, components c_{yy} and c_{zz} (Figs. 3.1b and 3.1c, respectively) present local maximum at the channel centreline. Stretching in those directions is globally negligible relative to the stream-wise direction.

Finally, the shear component, c_{xy} (Fig. 3.1d), presents maximum values near the wall and has an inflexion point at the channel centreline with slightly negative concavity in the lower half-channel.

Even though no artificial diffusion is needed to simulate laminar viscoelastic channel flows, the effect of the diffusion term on the results is now evaluated.

To do so, a small (dimensionless) stress diffusivity of $D_\alpha = 10^{-6}$ is added to the respective models. [2] This is the above-defined "*a posteriori* approach". The results are displayed in Fig. 3.2. Again, the analytical results are from the square-root formulation with *a posteriori* inclusion of artificial diffusion.

At this level of dissipation, artificial diffusion plays a negligible role in almost all components of the conformation tensor. The only exception is the wall-normal component, c_{yy}, for which a small trough appears around the channel centreline. This occurs for all formulations and for the analytical solution as well, indicating that this is not a numerical issue, but a result of mathematical changes in the equations. This behaviour is detailed in the zoom box in Fig. 3.2b. Note that the curves do not have a maximum at $y = 0$ like for the component c_{zz} (Fig. 3.2c). Instead, they all bend downwards. Moreover, a closer look indicates that, the values for the kernel formulation oscillates around the analytical solution and even go beyond the expected maximum value ($\approx 10^{-4}$ for c_{yy}/L^2).

This "bending" behaviour increases with the stress diffusivity on the c_{yy} component. Figure 3.3 shows the profiles of the normalised component of the conformation tensor for $D_\alpha = 10^{-3}$.

Note that the profile of the wall-normal component of the conformation tensor, c_{yy}, now suffers marked changes. Instead of having a parabola-like profile, similar to

[2] The subscript α in the stress diffusivity, D_α, denotes here a generalisation for the indexes c, b or k representing the stress diffusion coefficient for the standard, square-root and kernel formulations, respectively.

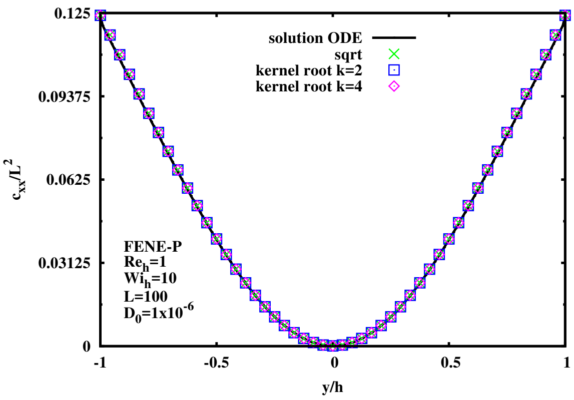

(a) Stream-wise component, c_{xx}

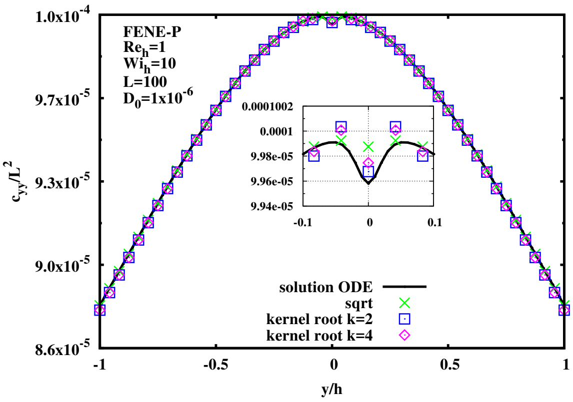

(b) Wall-normal component, c_{yy}

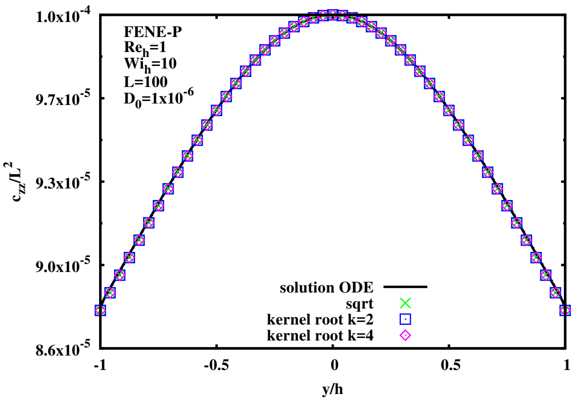

(c) Span-wise component, c_{zz}

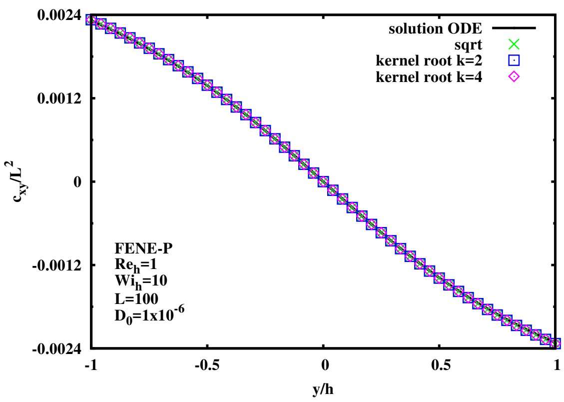

(d) Shear-wise component, c_{xy}

Figure 3.2 – Profiles of normalized components of the conformation tensor with the "*a posteriori* approach" for the artificial diffusion.($D_c = 10^{-6}$)

component c_{zz}, it bends in the middle region of the channel, becoming concave up around to the centreline. Furthermore, rather than a maximum value, the central point now has a minimum value. The analytical solution of the corresponding system of ODE shows the same behaviour, eliminating again any chance of numerical errors within the code. According to Fig. 3.3b, the smaller the degree of the root-k formulation, the closer to the analytical solution the results of the kernel formulation are.

In Fig. 3.4, the results for the formulations considering the *a priori* inclusion of artificial diffusion are presented, *i.e.* those whose diffusion terms appear from transformation of the conformation tensor equation with artificial diffusion. The same applies for the analytical results. Since artificial stress effects are most prominent at $D_c = 10^{-3}$, this value is here considered.

First, it is worth noting that the analytical result for this formulation does not contain any kind of "bend" in the profile of the component c_{yy}.

The profiles obtained from simulation, though, independently of the formulation used (term $\boldsymbol{h}$ or $\boldsymbol{h}^*$), still oscillate minimally and present a very small change of concavity

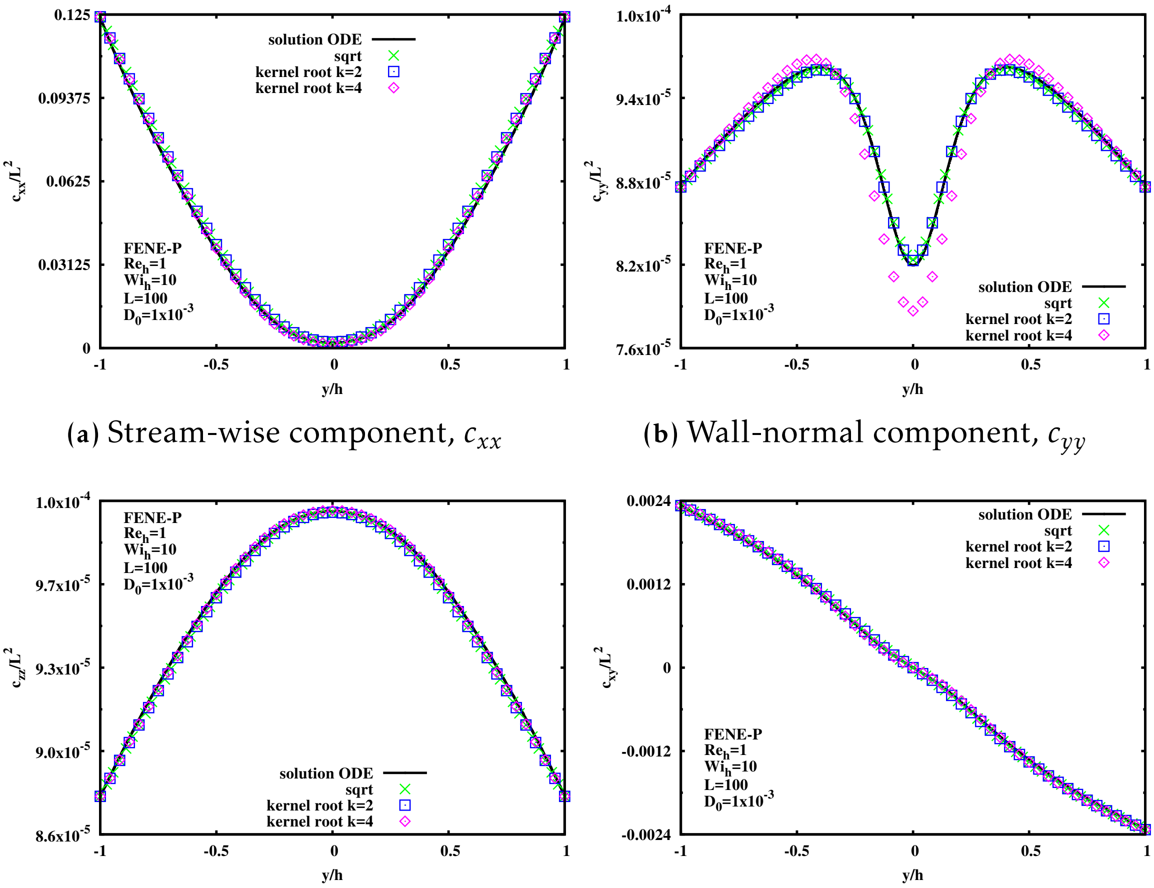

(a) Stream-wise component, c_{xx}

(b) Wall-normal component, c_{yy}

(c) Span-wise component, c_{zz}

(d) Shear-wise component, c_{xy}

Figure 3.3 – Profiles of normalized components of the conformation tensor with the "*a posteriori* approach" for the artificial diffusion.($D_\alpha = 10^{-3}$)

in the channel centreline. However, the *a priori* treatment of diffusion leads to results significantly closer to the analytical solution.

In conclusion, all the tested formulations, with or without artificial diffusion, have shown to be unconditionally stable for laminar channel flows. Regarding the inclusion of artificial diffusion into the constitutive equation, the so-called "*a priori* approach", *i.e.* when the diffusion term is considered before applying the transformations, presented very good agreement with the analytical solution for all components of the conformation tensor. A few numerical oscillations occur around the channel centreline, but the results are overall satisfactory. When including the artificial diffusion term after the transformation (*i.e.* in the "*a posteriori* approach"), the system of equations is transformed so that the wall-normal component of the conformation tensor, c_{yy}, bends downwards at the channel mid-height. The comparison of Figs. 3.2b and 3.3b indicates the deformation of the c_{yy} profile is proportional to the stress diffusivity considered. Since the "*a priori* approach" is more consistent mathematically, it is not surprise that it produces better results.

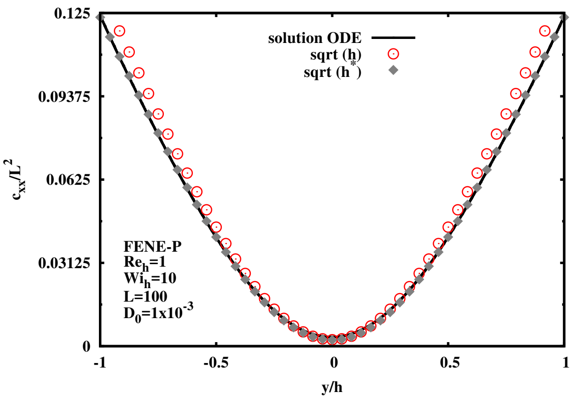

(a) Stream-wise component, c_{xx}

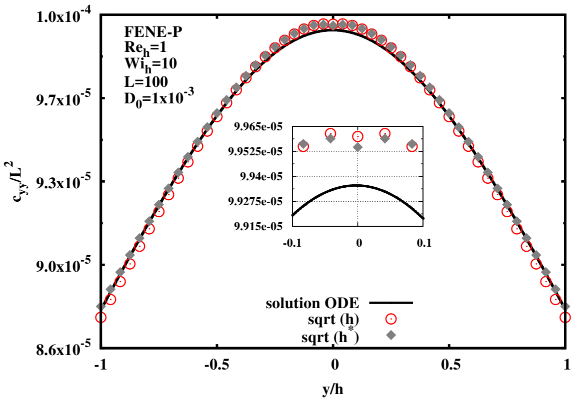

(b) Wall-normal component, c_{yy}

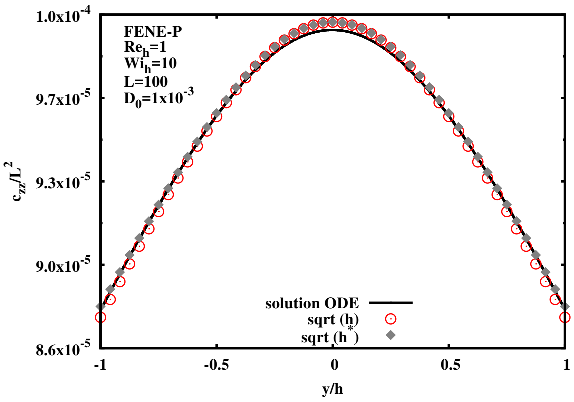

(c) Span-wise component, c_{zz}

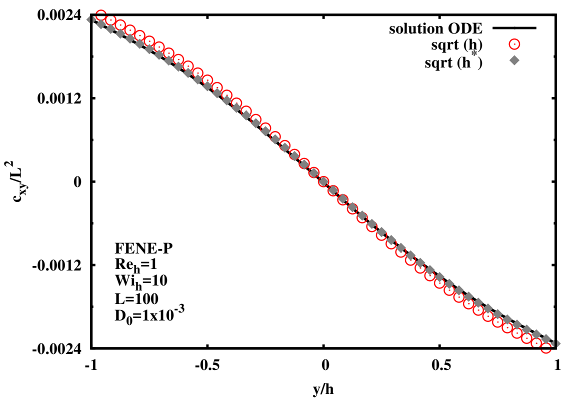

(d) Shear-wise component, c_{xy}

Figure 3.4 – Profiles of normalized components of the conformation tensor with the "*a priori* approach" for the artificial diffusion. ($D_c = 10^{-3}$)

3.3 Turbulent drag-reducing channel flow

In this section, the results for turbulent channel flows considering the same formulations as for the laminar flow will be presented. Short notes on the initialisation of turbulent simulations, the convergence rate and the stability of each method are also included.

3.3.1 Calculation of DR

Before commenting the results concerning turbulent drag-reducing channel flows, it is important to see how the relative drag reduction is calculated. As stated by Housiadas and Beris [16], the classical calculation of the relative drag reduction (DR) as a function of the wall shear stress, τ_w^*, is

$$DR = 1 - \frac{\tau_w^{*\,\text{visc}}}{\tau_w^{*\,\text{N}}} \quad , \tag{3.2}$$

where the superscripts "visc" and "N" stand respectively for viscoelastic and Newtonian.

There are two possible ways to compute a turbulent channel drag-reducing flow.

One is to impose the same sulk velocity as in the reference Newtonian flow, in which case Eq. (3.2) can be used directly. The other one, which is used within this work, is to impose the same pressure gradient in which case the bulk velocity increases in the viscoelastic flow. In this case, we need to take into account the shear-thinning effects of the FENE-P model, and Housiadas and Beris [16] proposed to use

$$DR = 1 - \mu_w^{2(1-n)/n} \left(\frac{\langle \overline{u} \rangle_y^{+\text{visc}}}{\langle \overline{u} \rangle_y^{+\text{N}}} \right)^{(-2/n)} \quad , \tag{3.3}$$

in which $\mu_w = \eta_w/\eta_0 = 1/(\overline{\mathrm{d}u^+/\mathrm{d}y^+})|_{0,w}$ is the viscosity ratio at the walls, the overline indicates time average, the superscript "+" stands for wall-units and the angle brackets, $\langle\rangle_y$, designate the spatial average in the wall-normal direction. The exponent n correlates the bulk and the shear Reynolds number, Re_h and $Re_{\tau 0}$, and is prescribed through Dean's correlation [103] (see [16] for details).

3.3.2 Initial conditions

There are several possibilities to initialise a turbulent viscoelastic channel flow:

1. use a previously calculated turbulent field for velocity and pressure, with equilibrium or a specific analytical input for the conformation tensor;

2. use previously calculated turbulent fields for velocity, pressure and conformation tensor;

3. use steady-state initial conditions with an ad-hoc disturbance to trigger the transition to turbulence.

These three possibilities have been tested in the present work. The difficulties in starting the computations are exemplified if one uses a root-type transformation to the conformation tensor. In particular, it is noteworthy that option 1 above can be complicated due to its initial steep velocity gradients in the turbulent field. Because of these strong gradients, the first iterations must be performed with time steps up to 10 times smaller than suggested by the CFL condition, and the artificial diffusion had to be multiplied by 10 in order to stabilise the algorithm.

Option 2 deserves attention if coming from standard conformation tensor simulations as well because the field of the conformation tensor may contain non-SPD values to which smoothing must be applied. Applying a root-type transformation to the conformation tensor involves diagonalising this tensor. If, for any reason, the initial conformation tensor field is not SPD, this would result in floating point exception from the onset of the computation. Most of the simulations conducted here used this approach by forcing any non-positive eigenvalue of the conformation tensor to equal a very small positive number. In general, the amount of non-SPD points in a turbulent field coming from the original algorithm is limited to a maximum of 1% of the total number of grid points.

A more elegant solution is option number 3. In order to verify that option number 2 can be used without loss (and to look somehow to the transition to turbulence), option 3 was tested for a specific flow case with a streamfunction-based disturbance [104] added to the initial velocity field . The details of this methodology can be found in Appendix B.

Using option 3, the conformation tensor was initiated in equilibrium state ($\boldsymbol{c} = \boldsymbol{I}$). For the velocity field, localised disturbances properly excited the flow. The remaining initial parameters are the same for all options: the bulk Reynolds number is $Re_h = 2800$, $L = 30$, $Wi_h = 4.3$ and $D_\alpha = 5.6$. Figure 3.5 shows the evolution of the bulk Reynolds number, Re_h, as a function of the simulation time, t, for the standard, square-root and kernel formulations, the latter two with *"a posteriori"* inclusion of artificial diffusion (explanation in Subsection 3.3.3 further on).

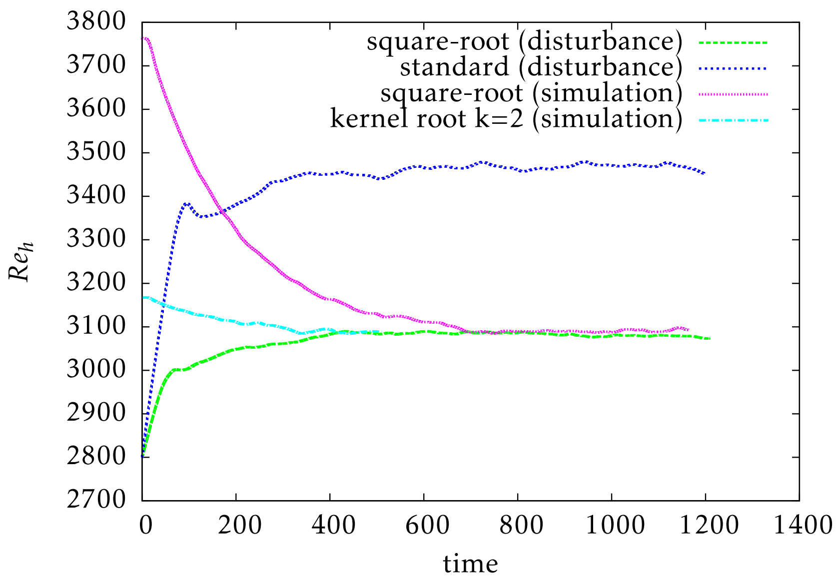

Figure 3.5 – Time evolution of the bulk Reynolds number, Re_h, for different formulations and initial conditions.

Four cases are presented in Fig. 3.5. The green line represents the evolution of the bulk Reynolds number for the square-root formulation transitioning to turbulence. The magenta line also stands for the square-root formulation, but the fields are initialised with previous results obtained with the standard conformation tensor formulation. This is also the initial condition for the kernel root simulation with $k = 2$ (light-blue line). As can be seen, regardless of the approach to initiate the turbulent simulations for the new formulations, the same statistically converged state is achieved ($Re_h \approx 3086$).

However, an interesting result is already found here with the the standard conformation tensor formulation (blue line) transitioning to turbulence. The statistically converged state, fluctuates around $Re_h \approx 3468$, leading to a relative drag reduction of approximately 28%. The value obtained for the square-root formulation, $Re_h \approx 3086$, corresponds to relative drag reduction of nearly 14%.

So, the use of the same stress diffusivity for the standard and square-root formulations led to a 50% underestimation of the relative drag reduction. This will be better explored in Section 3.3.5 below.

3.3.3 Note on the divergence of some formulations

The analysis of laminar channel flows shown above suggests that the "*a priori*" inclusion of stress diffusion is much more promising than the "*a posteriori*" approach, since it led to more realistic results. The "*a priori*" approach leading to an unfriendly equation for the kernel transformation, the expectations were all on the square-root formulation. Although its promising results under laminar regimes, when trying to initiate a turbulent simulation with this formulation, despite several attempts with varied combination of initial conditions and parameters, all simulations rapidly diverged due to unbounded values for the conformation that destabilises the code growing very fast. It is important to recall that we propose here the "*a priori*" formulation for the square-root proposed by Balci et al. [33] and a original simplified version of it as well, but unfortunately, they both fail within a few time steps. In view of this limitation, no turbulent results could be obtained with the "*a priori*" approach.

It is also important to note that all transformations in their original formulations, *i.e.* without any artificial diffusion, also quickly induced fast growth of numerical instabilities, leading to divergence.

3.3.4 CPU cost of the different methods

Although five new theoretically possible formulations were shown in Tab. 3.1, at the beginning of this chapter, only two of them are eligible to the problem here assessed. The "*a priori* approach" to the kernel root^k transformation was initially rejected because of its unfriendly formulation. The next two were eliminated due to the loss of stability caused by the growth of unbounded values for the conformation tensor.

Finally, the square-root and kernel root^k transformations, both with the so-called "*a posteriori*" approach, are the ones that were considered for computing the turbulent drag-reducing channel flows.

In Chapter 2, it was shown that one promising advantage of the square-root formulation is that it only requires to perform the eigendecomposition of the initial conformation tensor field. Henceforth, the square-root tensor is evolved in time and, each time the conformation tensor is required, it can be easily recovered by squaring the square-root tensor, which is computationally cheap. All this makes the square-root method almost as efficient as the original method.

On the other hand, the kernel conformation transformation formulation, although more versatile, is based on a decomposition that implies eigendecomposition at every time-step. This operation is computationally expensive.

In order to compare each formulation, test runs were performed with the same simulation parameters. The ratio of the mean time per iteration with respect to the standard formulation is approximately 1.12. For the kernel formulation the ratio goes over 6, but, in general, the CPU cost in simulations with the kernel formulation are around 5 times greater than those of the standard formulation (and the square-root as well, since they are very close). So, from practical point of view, the square-root formulation is by far the most promising.

3.3.5 Results for transformed conformation tensor formulations

The main results of converged turbulent viscoelastic channel flows are presented in the following. Results for both the square-root and the kernel formulations are compared to the values of the public database by Thais [105]. The results in this database were obtained with the algorithm in its original conformation tensor formulation using the standard conformation-based FENE-P with global artificial diffusion (see [19–22]).

Regarding the original algorithm, for all viscoelastic simulations at $Re_{\tau 0} = 180$, the artificial stress diffusivity used was $D_c = 5.6$ (equivalent to Schmidt number, $Sc = 0.18$). This value guarantees numerical stability by preserving the SPD property of the conformation tensor at more than 99% of the simulation grid points.

With the new formulations implemented (square-root and root-type kernel), the conformation tensor is mathematically considered to remain positive definite when evolving in time. Thus, both new versions of the code are now able to provide results that are potentially more reliable from the physical viewpoint.

Because the CPU requirements of the kernel formulation is considerably greater, only a few simulations were conducted until convergence and kept to gather a sufficient amount of information to give statistically converged results. Regarding diffusivity, as observed in the preliminary laminar cases and discussed further on for the turbulent simulations, the critical value under which the code diverges is very sensitive to the degree of the root k.

The square-root and the 4th-root kernel formulation results are first compared to the results obtained with the standard conformation tensor formulation for the flow case $Re_{\tau 0} = 180$, $L = 30$ and $Wi_{\tau 0} = 50$. The value for the artificial diffusivity (D_α) varies between 1.4 to 5.6, leading to relative drag reduction from 11.6% up to 28.5% as summarised in Tab. 3.3.

Case	D_α	$DR\%$
standard	5.6	28.5
square-root	5.6	14.1
	2.8	17.9
kernel ($k = 2$)	5.6	14.0
	2.8	17.5
kernel ($k = 4$)	1.4	11.6

Table 3.3 – Relation between artificial diffusivity and relative drag reduction for cases at $Re_{\tau 0} = 180$, $L = 30$, $Wi_{\tau 0} = 50$.

It is noteworthy that, with the same amount of artificial diffusivity, the relative drag reduction for the square-root formulation and kernel transformation (with $k = 2$) converge to the same value of 14%. This value is, however, approximately half of the relative reduction obtained with the standard conformation tensor formulation.

Figure 3.6 compares the cross-channel profiles of the mean stream-wise velocity (3.6a) and shear component of the Reynolds stress tensor (3.6b) for the new formulations with the results of the database [105] (black solid line) for the flow cases in Tab. 3.3.

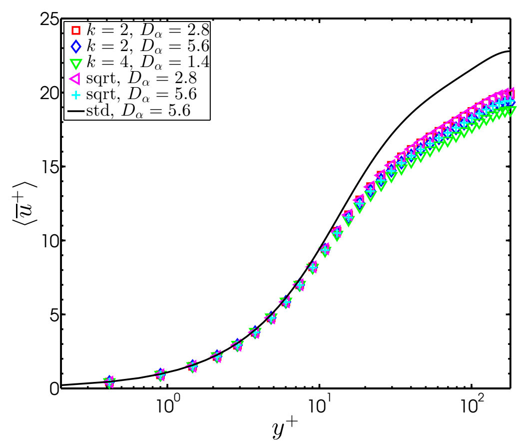

(a)

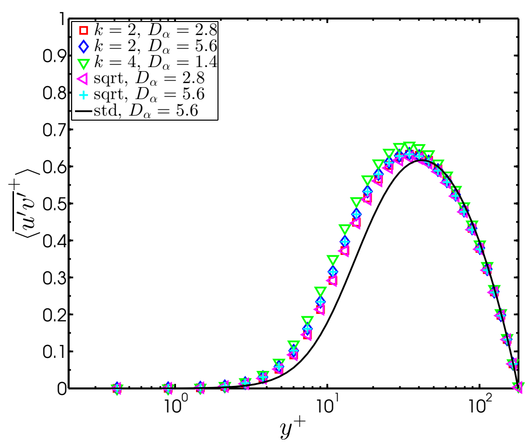

(b)

Figure 3.6 – Profiles of the mean velocity and shear component of the Reynolds stress tensor in wall-units for several transformations of the conformation tensor and for different values of stress diffusion. ($Re_{\tau 0} = 180$, $L = 30$, $Wi_{\tau 0} = 50$)

Note that the velocity profiles (Fig. 3.6a) with any of the tested transformations present good agreement with the standard results in the viscous sublayer ($0 < y^+ < 5$) but considerably underestimate the profile in the log-law region ($y^+ > 30$) and within the buffer layer ($5 < y^+ < 30$). Also, as predicted by Afonso, Pinho, and Alves [34], the kernel root^k transformation with $k = 2$ is equivalent to the square-root transformation.

The results suggest that, for a given k, the lower the stress diffusivity is, the closer to the standard conformation formulation the results are. Tab. 3.3 shows that the square-root and the kernel transformation underestimate the relative drag reduction up to a factor 2. The closest result obtained is for the square-root formulation and the root-k=2: 17% *vs* 28% drag reduction.

Regarding the shear component of the Reynolds stress ($R^+_{xy} = \langle \overline{u'v'}^+ \rangle$, Fig. 3.6b), the standard formulation predicts a peak value (of ≈ 0.6) at $y^+ \approx 40$. It is known that drag reduction occurs when turbulent energy is suppressed and stored by the polymer, leading to a decrease of the shear component compared to the Newtonian flow. Results presented here remain between those of the Newtonian and the standard formulation. Moreover, for the present cases, the peak is higher (≈ 0.65) than the one obtained with the standard formulation, which implies that less energy was subtracted from the turbulent fluctuations, leading to less drag reduction. Another noteworthy behaviour is that the peak are located closer to the wall ($y^+ \approx 30$) for the present results.

The underestimation of the relative drag reduction is corroborated from the viewpoint of polymer stretch. Figure 3.7 shows the distribution of the non-null components of the normalised conformation tensor for the same flow cases.

The time-averaged polymer stretch in the stream-wise direction, $\langle \overline{c_{xx}} \rangle / L^2$ (Fig. 3.7a), achieves a value close to 0.55 near the wall for all cases. The benchmark result from the standard formulation shows a peak in the buffer layer at $y^+ \approx 10$ and decreases as it approaches the middle of the channel. The present results, however, do not have this peak and decrease monotonically from the viscous sublayer towards the channel centreline.

The values of the wall-normal component, $\left\langle \overline{c_{yy}} \right\rangle / L^2$ (Fig. 3.7b), are very close to zero in the viscous sublayer, indicating very weak polymer stretch in this direction. In the buffer layer, there is a transition region with increased stretching and a peak is reached in the log-law region around $y^+ = 90$. Here, the results obtained with the transformed formulations do reproduce the peak. However, its magnitude is lower by up to 50% for the kernel case with $k = 4$ and $D_k = 1.4$. Furthermore, the peak is slightly moved towards the wall.

The span-wise component of the conformation tensor, $\langle \overline{c_{zz}} \rangle / L^2$ (Fig. 3.7c), behaves similarly to the wall-normal component. The main difference is that the relative stretch is slightly higher in this direction.

Finally, the shear component of the conformation tensor, $\left\langle \overline{c_{xy}} \right\rangle / L^2$ (Fig. 3.7d) presents a non-zero value at the wall. It has a maximum around $y^+ \approx 20$ and , goes towards zero at the middle of the channel, and has a peak around $y^+ = 20$. Once again, the results obtained with the square-root and the kernel transformations underestimate the polymer stretch regardless of the artificial diffusivity used.

The common feature of reduced polymer stretching corroborates the physical trends

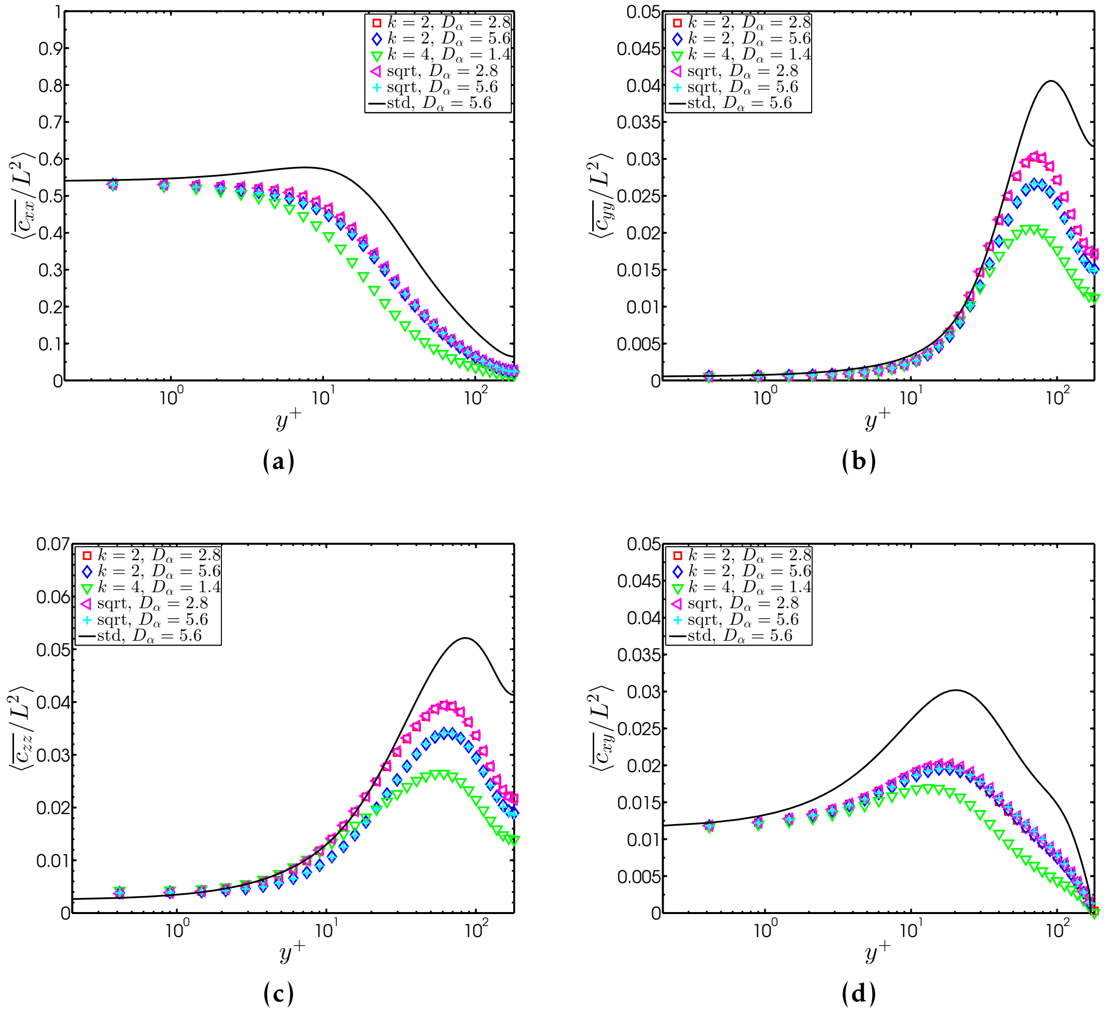

Figure 3.7 – Profiles of the mean non-null components of the conformation tensor in wall-units by means of several transformations applied to it. ($Re_{\tau 0} = 180$, $L = 30$, $Wi_{\tau 0} = 50$)

in the results of Fig. 3.6. These results also suggest that decreasing the amount of stress diffusivity improves the prediction of the transformed formulations.

However, decreasing stress diffusivity is only possible to a certain value beyond which the simulations start to breakdown. After close inspection, one sees that the breakdown occurs shortly after unbounded values fo the conformation tensor components appear ($\mathrm{tr}(\boldsymbol{c}) \gg L^2$). Unbounded values of the conformation tensor are due to a change of sign in the restoring elastic force of the polymer [26].

This phenomenon *never* appears with the standard formulation of the conformation tensor. It looks like that enforcing the SPD property of the conformation tensor promotes its tendency to become unbounded.

Simulations for other three different levels of elasticity have been performed by varying the two viscoelastic parameters of the FENE-P model ($L = 30$ and 100, and $Wi_{\tau 0} = 50$ and 115). A summary of the parameters explored is presented in Tab. 3.4

together with the respective artificial diffusivity and relative drag reduction obtained. For these new simulations, only the square-root formulation was considered.

L	$Wi_{\tau 0}$	Standard formulation D_c	$DR\%$	Square-root formulation D_b	$DR\%$
30	50	5.6	28.5	2.8	17.9
30	115	5.6	38.4	2.8	29.0
100	50	5.6	47.0	3.9	27.0
100	115	5.6	62.3	4.5	48.5

Table 3.4 – Comparison of relative drag reduction as a function of elasticity levels for the standard and square-root transformations.

With the standard formulation with an artificial diffusivity $D_c = 5.6$, four different levels of relative drag reduction are achieved from 28 to 62 %. However, when using the square-root formulation, the smallest artificial diffusion achieved leads to drag reduction levels from 18 to 48 %. Drag reduction percentages are from approximately 22 to 42 % lower than the corresponding values with the standard formulation. Hence, the tendency observed seems quite general irrespectively of the flow elasticity conditions.

A summary of the results is plotted in Fig. 3.8 which reproduces the profiles of the trace of the mean conformation tensor for the standard and square-root formulations.

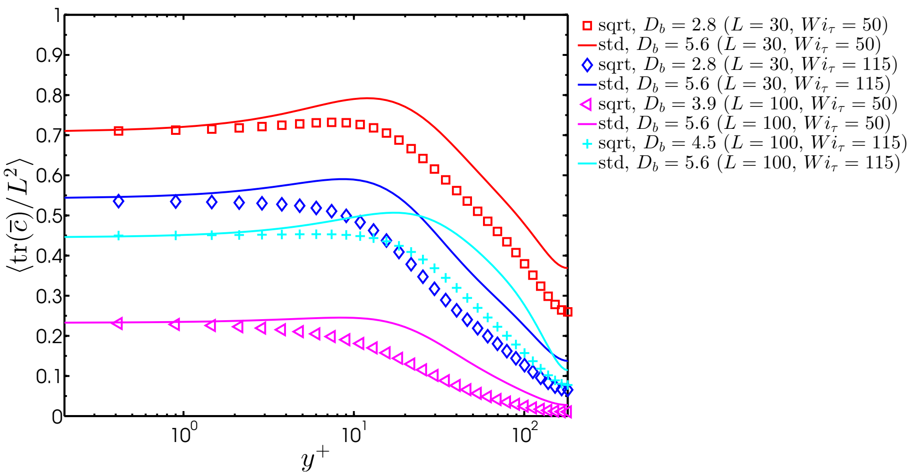

Figure 3.8 – Mean trace of the conformation tensor in wall-units obtained with the standard (solid lines) and the square-root (open symbols) formulations for several elasticity levels.

Similarly to the trend in Fig. 3.7a, the trace of the conformation tensor calculated by means of the standard formulation presents a local maximum located in the buffer layer. The magnitude of the maxima depends on the level of elasticity. In contrast, the square-root formulation result show no trace of local maxima, with the notable exception of the flow case ($L = 30, Wi_{\tau 0} = 50$) for which maximum polymer stretch does not show up at the wall, but near $y^+ \approx 10$.

3.4 Concluding remarks

The performance of different transformations applied to the conformation tensor was evaluated for turbulent viscoelastic channel flows. The square-root formulation and the root-type kernel transformation were first tested without success in their original forms, *i.e.* without any stress diffusion.

Artificial stress diffusion was then added to the constitutive equations following two approaches: either the diffusion term was added to the original conformation tensor equation and then transformed ("*a priori* approach"), or a term proportional to the Laplacian of the transformed conformation tensor was added directly to its transformed evolution equation ("*a posteriori* approach"). Validation tests for laminar channel flow indicate that the "*a posteriori* approach" is more appropriate, but it rapidly diverges in turbulent flows due to the occurrence of unbounded values in the conformation tensor.

The transformations applied to the conformation tensor do preserve its positiveness, but the inclusion of a stress diffusion term was found to be also necessary to help stabilising the code. Even guaranteeing the positiveness of the conformation tensor, its boundedness is not unconditionally preserved. Although better results are obtained when decreasing the artificial diffusivity, the smallest value which can be used in practice led to underestimation of polymer stretching, and thus of the relative drag reduction.

From inspection of Fig. 3.3b, we can see that, in laminar flows, the "*a posteriori* approach" leads to the c_{yy} component of the conformation tensor being incorrectly predicted towards the channel centreline. For $D_\alpha = 10^{-3}$, the peak is even transformed in a trough at the centreline. At this very high level of stress diffusivity, the diffusion coefficient in the constitutive equation is $D_\alpha/Re_h \sim 10^{-3}/10 \sim 10^{-4}$.

For the turbulent flows, the diffusion coefficient is $D_\alpha/Re_h \sim (3 \text{ to } 5)/(3000 \text{ to } 4000) \sim 10^{-3}$. Although the laminar and turbulent shear flows are different in nature ($\langle\overline{c_{yy}}\rangle and \langle\overline{c_{zz}}\rangle$ are not maximum at the channel centreline in turbulent flows), this could lead to believe that the square-root formulation underpredicts the local maxima in the conformation tensor field owing to this high level of stress diffusion.

However, in the standard conformation tensor approach, the stress diffusion coefficient is of the same order, e.g. $D_\alpha/Re_h \sim 10^{-3}$, and the standard conformation does not underpredict stretching. The *real* cause of the polymer stretch underestimation must therefore lie on the constraint of the positive definiteness which however has a theoretical foundation.

The limiting value under which simulations rapidly diverge due to unbounded values for the conformation tensor varies from formulation to formulation. In particular, for the root-type kernel transformation, polymer stretching underestimation is a growing function of k. Without any other treatment, the limiting artificial diffusivity may lead to underestimations up to $\approx 50\%$ in terms of relative drag reduction.

Basically, the loss of positiveness and boundedness of the conformation tensor can be tackled in two ways. If the accuracy of the numerical method is prioritised, spectral or high-order schemes are used, and the addition of artificial diffusion is crucial to achieve stability. This can be seen as a physical disadvantage, since the polymer dumbbell models do not include diffusion at the scales simulated even by DNS. On the other hand, if the physics of the dumbbell model is prioritised, one has to use flux limiter schemes with typically lower spatial resolution.

Part II

Flow classification criteria: the role of objectivity and flow classification of polymer solutions

Chapter 4

Flow classification, vortex identification and the role of objectivity

4.1 Introduction

In Fluid Mechanics, its is usual to deal with complex flows exhibiting different kinds of motion that are time and space dependent. These motions can include extension, rotation, shear, stagnation, and in some cases, combinations of them. The proper identification and localisation of theses motions may contribute to the understanding of several phenomena. For instance, extensional motion is relevant in the context of non-Newtonian instabilities and drag reduction by the addition of polymers in a Newtonian solvent. Regarding rotation, many applications are also related, such as combustion, mixture, mass and heat transfer, hydro- and aerodynamic drag. Together with rotation, a central concept in Fluid Mechanics appears: the *vortex*.

The idea of vortices is very old and has been used to explain different phenomena for a long time. Despite of the large use of such concept and the tremendous advances in Fluid Mechanics over the years, a consensual definition for a vortex is still lacking. As a matter of fact, the discussion in the literature usually gravitates around the appropriate physical and mathematical foundations to identify vortices.

Some authors defend that vortices should be defined in a Lagrangian framework, meaning that vortical regions can be identified by the features of a particle's trajectory within the flow. On the other hand, there are others who claim that vortices can be thought as consequence of the field of flow entities, which corresponds to an Eulerian approach.

Another point of discussion is whether a vortex should be identified using dynamic or kinematic entities. For those defending the former, interacting forces that change the flow kinematics are directly connected to vortices, while for the latter, the velocity field solely must be used to identify vortical regions.

The invariance with respect to changes of frames is also a non-consensual feature regarding the definition of a vortex. Some argue that the definition should be invariant when calculated in any two reference frames moving at constant relative rectilinear velocity, thus characterising a Galilean invariance. In contrast, some claim in favour of objectivity or Euclidean invariance, *i.e.* the idea that a criterion should be invariant to arbitrary changes of frames (translation and rotation).

Moreover, another cause of dissension is the fact that some criteria need a threshold value that is user-defined, rendering to the vortex identification a subjective decision on what value would be more adequate to classify each flow. On the other hand, some criteria do not depend on the flow or on user-defined thresholds, being ready to classify any flow regardless of the user.

In order to understand the evolution of the controversies on the definition for a vortex, the main flow classification criteria will be presented and commented in the following.

4.2 Vortex: from concept to definition

Despite the obscurity regarding the definition of a vortex, it is common to express turbulent motions as a tangle of interacting vortices that evolve in time [106]. This spatial and time evolution of vortices is usually referred to as *vortex dynamics*.

In this connection, it was found that turbulent flows are generally filled with regions characterised by ordered vortical motions named *coherent structures* [107–109]. The interaction between such structures and the turbulent flow is of interest, not only because of the promising better understanding of the turbulence phenomenon, but also due to the possibility of modelling and controlling it more accurately.

In this sense, flow visualisation has been a very important tool. Both experiments and DNS have been providing elucidating information on vortex dynamics. In the case of experiments, the use of tracers combined with image techniques can provide the velocity field or the streamlines of the flow. These informations are treated to provide statistics and correlations that contribute to the understanding of turbulent phenomena. In the numerical approach, the entire field of any solved variables is available for a given flow. Its space and time resolution depend on the choice of discretisation schemes.

The concept of a vortex may be quite intuitive, mainly due to the swirling motions observed with the aid of flow visualisation. However, from the first attempts to propose a solid definition for a vortex until our days, the difficulties to do it persist and have been pointed out and discussed.

This intuitive relation between vortices and swirl motion lead to three elementary ways to identify vortical structures. The first definitions for vortices related the presence of vortex cores to closed or spiral streamlines, vorticity extrema, or local pressure minima.

The idea of relating closed or spiral streamlines with vortices is primitive but very reasonable as a first approach. Nevertheless, as pointed out by Lugt [110], a quick counterargument appears concerning the transient features of vortices. Because streamlines are obtained from instantaneous fields, the referred author advocates the use of pathlines (time-integrated paths) as a more suitable approach. For him, a vortex is constituted by "any mass of fluid moving around a common axis", and this is mathematically represented by closed or spiral streamlines in a reference frame for which the flow field is steady. This definition is however non-invariant to Galilean or Euclidean transformations, as stated by the author himself and criticised by Jeong and Hussain [38].

Inspired by the concept of closed streamlines, another common argument to define a vortex is to associate it with a local pressure minimum. Jeong and Hussain [38] explain that pressure may balance the centrifugal force in swirling motions, leading to local minimum on the axis of an eddy. However, according to them, this reasoning is only valid in steady inviscid planar flow. The authors also present an example where the simple consideration of pressure minimum identifies a vortex core in a flow with no swirl. Despite the inadequacy of the direct application of this idea, it has been inspiring for some of the most used flow classification criteria such as the Q-criterion [36] and the λ_2-criterion [38], as detailed further on.

Vorticity is also commonly used to visualise vortical structures. Vorticity lines were already used, for instance, in the context of isotropic turbulence [111] and turbulent channel flow [112]. Regions with vorticity extrema are widely used in the literature to identify vortices (e.g. [113–118]). Even though most of the work using the magnitude of vorticity date from the 1980's, more recent work suggests to look to this entity again but from new perspectives [119, 120].

4.2.1 Some important definitions

Before presenting some definitions for a vortex, let us define some relevant flow entities. As commented above, the first ideas behind a vortex were closely related to its visualisation. When translating this idea of flow visualisation into mathematical entities, it is very common to deal with the velocity gradient tensor, $\nabla \boldsymbol{u}$.

In the literature, one can find two different ways to define the velocity gradient. To avoid any misunderstanding in the present work, we define the entries of the velocity gradient tensor and its transpose, $\boldsymbol{L}$, as follows,

$$\nabla u_{ij} = L_{ij}^T = \frac{\partial u_j}{\partial x_i} e_i \otimes e_j \quad \text{and} \quad \nabla u_{ij}^T = L_{ij} = \frac{\partial u_i}{\partial x_j} e_i \otimes e_j \quad . \tag{4.1}$$

At this point, it is important to remark that, even though the symbolic representation is always respected, the expression "velocity gradient tensor" may be used here interchangeably for $\nabla \boldsymbol{u}$ and $\boldsymbol{L}$.

Next, we remind that the velocity gradient tensor can be decomposed into a symmetric part, $\boldsymbol{D} = (\boldsymbol{L} + \boldsymbol{L}^T)/2$, representing the rate-of-strain tensor, and a skew-symmetric part, $\boldsymbol{W} = (\boldsymbol{L} - \boldsymbol{L}^T)/2$, which represents the rate-of-rotation (or vorticity) tensor.

Another important quantity is the vorticity vector, $\boldsymbol{\omega}$, which is defined as half of the curl of the velocity vector ($\boldsymbol{\omega} = \frac{1}{2}\nabla \times \boldsymbol{u}$). It has a close relation to the (skew-symmetric) rate-of-rotation tensor, $\boldsymbol{W}$, which can be expressed as function of the components of the vorticity vector, yielding

$$\boldsymbol{W} = \begin{bmatrix} 0 & -\omega_3 & \omega_2 \\ \omega_3 & 0 & -\omega_1 \\ -\omega_2 & \omega_1 & 0 \end{bmatrix} . \tag{4.2}$$

4.2.2 Hyperbolic, parabolic and elliptic modes in fluid motion

Weiss [121] introduced the concept of *hyperbolicity* and *ellipcity* in the context of fluid motion. According to the author, the fluid is in a hyperbolic mode when the magnitude of the strain rate exceeds that of the rotation rate. Contrarily, where the rotation rate dominates the strain rate, the fluid is in an elliptic mode of motion. Haller [122] states that the intersection between these two regions can be called *parabolic* domain, in which the magnitude of the strain and rotation rates are in equilibrium.

These definition being presented, let us show now some of the relevant flow classification criteria available in the literature and a brief idea of the basis in which they were conceived.

4.3 Definitions for a vortex

4.3.1 The criterion by Hunt, Wray, and Moin [36]

Hunt, Wray, and Moin [36] aimed to classify different flow zones in the context of turbulent flows. They defined *eddy zones*, *convergence zones*, and *streaming zones*.

The first one contains regions of a local pressure minimum (where the pressure is smaller than a threshold value) and where the magnitude of the rate-of-rotation tensor is greater than the magnitude of the strain-rate tensor, characterising thus vortical motions. The second one represents regions dominated by irrotational strain and diverging/converging streamlines, usually containing stagnation points. The latter zone is characterised by relative fast motion without diverging/converging or curved streamlines.

Let us focus here in what the authors called *eddy zones*. The relation between the magnitude of the rotation-rate and strain-rate tensors was expressed by the authors in terms of the second invariant, Q, of the velocity gradient, as follows

$$Q = \frac{1}{2}\left[(\mathrm{tr}(\nabla \boldsymbol{u}))^2 - \mathrm{tr}(\nabla \boldsymbol{u} \cdot \nabla \boldsymbol{u})\right] = \frac{1}{2}\left(\|\boldsymbol{W}\|^2 - \|\boldsymbol{D}\|^2\right) \quad , \tag{4.3}$$

where $\|\boldsymbol{A}\| = \sqrt{\mathrm{tr}(\boldsymbol{A} \cdot \boldsymbol{A}^T)}$ is the Euclidean (or Frobenius) norm of a generic tensor $\boldsymbol{A}$.

The dominance of the rotation rate with respect to the strain rate is thus mathematically expressed as

$$Q = \frac{1}{2}\left(\|\boldsymbol{W}\|^2 - \|\boldsymbol{D}\|^2\right) > 0 \quad . \tag{4.4}$$

Originally, according to Hunt, Wray, and Moin [36], the *eddy zones* corresponded to regions enjoying the criterion in Eq. (4.4) and being at a local pressure minimum spot. However, in practice, this latter condition has been neglected by most users.

It is important to remark here that a similar measure was proposed before by Truesdell [123]. The author introduced what he called *kinematic vorticity number*, defined as

$$N_k = \frac{\|\boldsymbol{W}\|}{\|\boldsymbol{D}\|} \quad , \tag{4.5}$$

and states that $N_k = \infty$ corresponds to a rigid-body rotation, while $N_k = 0$ corresponds to non-rigid irrotational motion.

Finally, it is easy to note that $Q > 0$ is equivalent to $N_k > 1$. Thus, both the Q-criterion and Truesdell's kinematic vorticity number provide a measure of the local competition between the magnitude of the strain-rate and rotation-rate tensors.

4.3.2 The criterion by Chong, Perry, and Cantwell [37]

Chong, Perry, and Cantwell [37] presented a topological classification of solution trajectories for a three-dimensional system of first-order equations using matrix invariants (study initiated in a previous work [124]). They used the velocity field, $\boldsymbol{u}$, and its associated gradient tensor, $\nabla \boldsymbol{u}$, to identify different flow patterns according to the features of the characteristic equation for $\nabla \boldsymbol{u}$, which can be written as

$$\lambda^3 - P\lambda^2 + Q\lambda - R = 0 \quad , \tag{4.6}$$

where P, Q and R are respectively the first, second and third invariants of $\nabla \boldsymbol{u}$. The first invariant, P, is the trace of $\nabla \boldsymbol{u}$, while the third invariant, R, is its determinant. The roots of Eq. (4.6) are the eigenvalues of the velocity gradient tensor.

Let us now define the discriminant, $D_{\nabla \boldsymbol{u}}$, of Eq. (4.6) as

$$D_{\nabla \boldsymbol{u}} = P^2Q^2 - 4Q^3 - 4P^3R - 27R^2 + 18PQR \quad . \tag{4.7}$$

The characteristic equation (4.6) can have three classes of solutions, depending on the sign of its discriminant, $D_{\nabla \boldsymbol{u}}$: (i) three distinct real roots (if $D_{\nabla \boldsymbol{u}} > 0$); (ii) three real roots with at least two being equal (if $D_{\nabla \boldsymbol{u}} = 0$); and (iii) one real root and a conjugate pair of complex roots (if $D_{\nabla \boldsymbol{u}} < 0$).

Let us now define

$$\delta = -D_{\nabla \boldsymbol{u}} = -P^2Q^2 + 4Q^3 + 4P^3R + 27R^2 - 18PQR \quad . \tag{4.8}$$

Then, conditions (i) and (iii) above are equivalent to $\delta < 0$ and $\delta > 0$, respectively.

Note that, for incompressible flows, which is a usual condition regarding the application of the criterion of Chong, Perry, and Cantwell [37], $P = \mathrm{tr}(\nabla \boldsymbol{u}) = 0$ and Eq. (4.8) becomes

$$\delta = 4Q^3 + 27R^2 \quad . \tag{4.9}$$

Under irrotational flow, the eigenvalues of the velocity gradient tensor are real and distinct (type (i), $\delta < 0$). When the vorticity is large enough, the nature of the eigenvalues of the velocity gradient tensor is of type (iii) ($\delta > 0$). According to Chong, Perry, and Cantwell [37], where the velocity gradient tensor presents complex eigenvalues, the velocity is associated to a swirling-like flow, revealing thus a vortex core. Thus, these regions can be identified by the relation

$$\delta = 4Q^3 + 27R^2 > 0 \quad \text{or} \quad \Delta = \frac{\delta}{108} = \left(\frac{Q}{3}\right)^3 + \left(\frac{R}{2}\right)^2 > 0 \quad . \tag{4.10}$$

It important to remark that, theses closed or spiral streamlines are observed in a reference frame moving with the same velocity as the vortex core, which characterises a Galilean invariance.

4.3.3 The criterion by Jeong and Hussain [38]

Jeong and Hussain [38] claim that pressure minimum by itself is not a strong criterion for detecting vortices, even though it provides a promising rationale. They present counterarguments showing how pressure minima can misinterpret the identification of vortex cores due to unsteady rate of strain or viscous effects. Even so, the basis of their criterion is the local pressure minimum in a plane defined by the axis of a vortex core. The authors propose thus to look to the pressure Hessian, $\mathrm{He}(p) = \nabla\nabla(p)$, which contains the necessary conditions for the pressure to be minimum.

Let us take the (scaled) Navier-Stokes equation

$$\frac{\partial \boldsymbol{u}}{\partial t} + \boldsymbol{u} \cdot \boldsymbol{\nabla} \boldsymbol{u} = -\boldsymbol{\nabla} p + \frac{1}{Re_h} \Delta \boldsymbol{u} \quad . \tag{4.11}$$

The equation for the pressure Hessian rises from taking the gradient of Eq. (4.11), which yields

$$\nabla \left(\frac{\partial \boldsymbol{u}}{\partial t} \right) + \nabla \left(\boldsymbol{u} \cdot \boldsymbol{\nabla} \boldsymbol{u} \right) = \nabla \left(-\nabla p \right) + \nabla \left(\frac{1}{Re_h} \Delta \boldsymbol{u} \right) \quad . \tag{4.12}$$

This equation can be rewritten as

$$\frac{\partial \nabla \boldsymbol{u}}{\partial t} + \boldsymbol{u} \cdot \nabla \left(\boldsymbol{\nabla} \boldsymbol{u} \right) + \nabla \boldsymbol{u} \cdot \nabla \boldsymbol{u} = -\mathrm{He}\left(p \right) + \frac{1}{Re_h} \Delta \boldsymbol{\nabla} \boldsymbol{u} \quad . \tag{4.13}$$

The velocity gradient tensor in Equation (4.13) can be decomposed into symmetric and antisymmetric parts, yielding

$$\frac{\partial (\boldsymbol{D} - \boldsymbol{W})}{\partial t} + \boldsymbol{u} \cdot \nabla \left(\boldsymbol{D} - \boldsymbol{W} \right) + \left(\boldsymbol{D} - \boldsymbol{W} \right) \cdot \left(\boldsymbol{D} - \boldsymbol{W} \right) = -\mathrm{He}\left(p \right) + \frac{1}{Re_h} \Delta \left(\boldsymbol{D} - \boldsymbol{W} \right) \quad . \tag{4.14}$$

The antisymmetric part of Eq. (4.14) is related to the evolution equation for vorticity and reads

$$\frac{\mathrm{D}\boldsymbol{W}}{\mathrm{D}t} + \boldsymbol{D}\boldsymbol{W} + \boldsymbol{W}\boldsymbol{D} = \frac{1}{Re_h} \Delta \boldsymbol{W} \quad , \tag{4.15}$$

whereas its symmetric part represents the evolution of the strain rate, which reads

$$\frac{\mathrm{D}\boldsymbol{D}}{\mathrm{D}t} + \boldsymbol{D}^2 + \boldsymbol{W}^2 = -\mathrm{He}\left(p \right) + \frac{1}{Re_h} \Delta \boldsymbol{D} \quad , \tag{4.16}$$

where $\mathrm{D}()/\mathrm{D}t = \partial()/\partial t + \boldsymbol{u} \cdot \nabla()$ is the material derivative operator.

As commented above, Jeong and Hussain [38] advocate the inadequacy of the local pressure minimum to identify a vortex. They present two arguments for that:

- Transient effects of the strain field may lead to local pressure minima, even if the flow has no vorticity. The authors present an analytical example where it occurs (see Section 2.1 in [38]);

- Under some conditions, viscous effects may balance the pressure gradient so that vortices occur in the absence of a local pressure minimum.

Because of these flaws – and despite the fact that they happen under specific conditions –, the authors generalise such inadequacy and claim that discarding the unsteady and viscous terms in Eq. (4.16) would lead to “a better indicator for the existence of a vortex”. Therefore, they postulate to discount from the pressure Hessian the contributions of that two terms, leading to a “modified” pressure Hessian expressed by the relation

$$\boldsymbol{D}^2 + \boldsymbol{W}^2 = -\mathrm{He}(p) \quad , \tag{4.17}$$

i.e. the modified pressure Hessian can be computed in kinematic terms.

A local pressure minimum at the plane of vorticity occurs where the tensor $\mathrm{He}(p)$ presents (at least) two positive eigenvalues. Considering Eq. (4.17), this condition is equivalent to regions where the tensor $\boldsymbol{D}^2 + \boldsymbol{W}^2$ presents two negative eigenvalues. Because $\boldsymbol{D}^2 + \boldsymbol{W}^2$ is symmetric, its eigenvalues are always real. Define $\lambda_1^{\boldsymbol{D}^2+\boldsymbol{W}^2}$, $\lambda_2^{\boldsymbol{D}^2+\boldsymbol{W}^2}$ and $\lambda_3^{\boldsymbol{D}^2+\boldsymbol{W}^2}$ as the eigenvalues of $\boldsymbol{D}^2 + \boldsymbol{W}^2$, so that $\lambda_1^{\boldsymbol{D}^2+\boldsymbol{W}^2} \geq \lambda_2^{\boldsymbol{D}^2+\boldsymbol{W}^2} \geq \lambda_3^{\boldsymbol{D}^2+\boldsymbol{W}^2}$. Then, $\lambda_2^{\boldsymbol{D}^2+\boldsymbol{W}^2}$ is the eigenvalue that indicates whether $\boldsymbol{D}^2+\boldsymbol{W}^2$ has two negative eigenvalues or not. Thus, a local pressure minimum can be identified by the regions where $\lambda_2^{\boldsymbol{D}^2+\boldsymbol{W}^2} < 0$.

It is important to remark though that when a user of the λ_2-criterion calculates the intermediate eigenvalue of $\boldsymbol{D}^2 + \boldsymbol{W}^2$, by the balance of Eq. (4.16), it is not possible to drop the eventual contributions of the unsteady and viscous terms added to the pressure Hessian.

Finally, the authors relate their λ_2-criterion to the Q-criterion [36] as follows

$$Q = -\frac{1}{2}\mathrm{tr}(\boldsymbol{D}^2 + \boldsymbol{W}^2) \quad , \tag{4.18}$$

and show that, for planar flows, the criteria Q, Δ, and λ_2 are equivalent.

It is worth noting that the λ_2-criterion is in fact based on dynamical aspects, albeit expressed as a function of kinematic entities. Moreover, this criterion is Eulerian, Galilean-invariant and its threshold parameter is not user-defined.

4.3.4 The criterion by Kida and Miura [125]

Kida and Miura [125] follow the rationale by Jeong and Hussain [38], but with the addition of a swirl condition together with the pressure minimum location. They use the eigenvector associated with the smallest eigenvalue of the pressure Hessian to define a plane in which the velocity gradient is projected. Besides a pressure minimum, their criterion requires that the projected rotation rate overcomes the projected strain rate for a region to be considered a vortex core.

4.3.5 The criterion by Zhou et al. [39]

Inspired by the the Δ-criterion [37], the so-called λ_{ci}-criterion also associates complex eigenvalues of the velocity gradient tensor to vortices. The complex conjugate pair of eigenvalues may be written as $\lambda_{cr} \pm i\lambda_{ci}$, with λ_{cr} and λ_{ci} being its real and imaginary parts, respectively. Zhou et al. [39] consider the imaginary part of the complex eigenvalues of the velocity gradient as a measure of swirl strength. The criterion is then defined as

$$\lambda_{ci}^2 > \delta \quad , \tag{4.19}$$

where δ is a user-defined threshold parameter usually given as a percentage of the maximum λ_{ci}^2.

4.3.6 The criterion by Cucitore, Quadrio, and Baron [126]

Until this point, all vortex identification criteria were conceived in a point-wise approach, *i.e.* the criteria are locally calculated point by point. Cucitore, Quadrio, and Baron [126] pointed out that most of these criteria privilege specific directions, usually associated with the vortex axis (e.g. Δ-criterion [37] and λ_2-criterion [38]). They claim that, due to the differences in the definitions of each criteria, these directions are generally different at any point inside a vortical structure.

In this connection, the authors came up with a non-local criterion based on the idea that the relative distance between two particles inside a vortex should not vary significantly. Their criterion basically "measures the tendency of two particles in the flow to remain near each other" in a Galilean-invariant basis. This measure is given by the following quantity

$$R(\boldsymbol{x},t) = \frac{|\int_0^t \boldsymbol{u}_a(\tau)\mathrm{d}\tau| - |\int_0^t \boldsymbol{u}_b(\tau)\mathrm{d}\tau|}{\int_0^t |\boldsymbol{u}_a(\tau) - \boldsymbol{u}_b(\tau)|\mathrm{d}\tau} \quad , \tag{4.20}$$

where $\boldsymbol{u}_a$ and $\boldsymbol{u}_b$ are the respective velocities of two particles a and b in a flow.

The quantity $R(\boldsymbol{x},t)$ has values from 0 to 1. According to the authors, the two analysed particles are within a vortical region when the inferior limit is approached. The upper limit indicates that one particle or the pair of particles is out of a vortical region.

4.3.7 The criterion by Chakraborty, Balachandar, and Adrian [127]

Chakraborty, Balachandar, and Adrian [127] introduced an additional condition to the λ_{ci}-criterion [39] in order to take into account small relative dispersion within vortex cores, just as required by Cucitore, Quadrio, and Baron [126]. However, they propose a local Eulerian approximation of the non-local Lagrangian quantity by Cucitore, Quadrio, and Baron [126]. This is done by introducing what they call *inverse spiralling compactness*, which is defined as the ratio $\lambda_{cr}/\lambda_{ci}$, a measurer of the range of the local spiralling motion.

The authors propose then the following criteria

$$\lambda_{ci} \geq \epsilon \quad , \tag{4.21}$$

and

$$\lambda_{cr}/\lambda_{ci} \leq \delta \quad , \tag{4.22}$$

where ϵ and δ are user-defined thresholds. The authors explain that a $\lambda_{cr}/\lambda_{ci}$-vortex is the intersection region between conditions in Eqs. (4.21) and (4.22).

4.3.8 The criterion by Haller [122]

A non-local objective Lagragian/Eulerian criterion was proposed by Haller [122]. According to the author, a vortex is an ensemble of trajectories that persistently defy the trend imposed by the instantaneous strain rate tensor. This defiance is measured with the aid of tensor $\boldsymbol{M}$, the covariant convected time derivative of the strain rate tensor, $\boldsymbol{D}$, which reads

$$\boldsymbol{M} = \dot{\boldsymbol{D}} + \boldsymbol{D}\boldsymbol{L} + \boldsymbol{L}^T\boldsymbol{D} \quad . \tag{4.23}$$

Haller [122] also defines the elliptical cone, Z, that appears as the limiting region between the action of a material filament to corroborate or defy (in a certain sense) the tendency of straining suggested by $\boldsymbol{D}$. This is valid for incompressible flows with non-null determinant of $\boldsymbol{D}$. The cone Z in the basis of the eigenvectors of $\boldsymbol{D}$, $\boldsymbol{e}_i^D$ (with $i = 1,2,3$), associated to its eigenvalues, λ_i^D (with $i = 1,2,3$ and $\lambda_1^D > \lambda_2^D > \lambda_3^D$), is given by

$$\eta_3^2 = a\eta_1^2 + (1-a)\eta_2^2 \quad , \tag{4.24}$$

in which a is the ratio between λ_1^D and λ_3^D, and $\boldsymbol{\eta} = \eta_1\boldsymbol{e}_1^D + \eta_2\boldsymbol{e}_2^D + \eta_3\boldsymbol{e}_3^D$ is a material filament[1].

It turns out that, at a generic point, the tensor $\boldsymbol{M}_Z$, the restriction of $\boldsymbol{M}$ to Z, can be either positive definite or indefinite[2]. According to Haller [122], regions where $\boldsymbol{M}_Z$ is positive definite corroborate with the positive strain tendency and are considered *hyperbolic*. When $\boldsymbol{M}_Z$ is indefinite, the tendency imposed by the strain rate is defied by its objective material derivative $\boldsymbol{M}$, characterising a vortex core (*elliptic* region).

4.3.9 The criterion by Zhang and Choudhury [128]

A Galilean-invariant criterion conceived for compressible flows was proposed by Zhang and Choudhury [128]. It is based on the helicity density, H_e, defined as

$$H_e = \boldsymbol{n}_{swirl} \cdot \boldsymbol{\omega} \quad , \tag{4.25}$$

[1] Material filaments are straight lines of infinitesimal size in the fluid that can rotate, stretch, compress, but not bend.

[2] Very briefly, for the present purpose, one can think of positive definite tensors as tensors whose all eigenvalues are positive, and indefinite tensors as tensors presenting both positive and negative eigenvalues.

where $\boldsymbol{n}_{swirl} = -\frac{i}{2}(\boldsymbol{e}_1 \times \boldsymbol{e}_2)$, where $\boldsymbol{e}_1$ and $\boldsymbol{e}_2$ are the eigenvectors corresponding to the conjugate complex eigenvalues of $\boldsymbol{\nabla u}$.

4.3.10 The criteria by Thompson [40]

Following Haller [122], Thompson [40] adds more consistent physical meaning to the role played by the covariant strain acceleration tensor, $\boldsymbol{M}$, proposing a (non-)persistence-of-straining criterion based on this entity.

He adopts a decomposition of the covariant strain acceleration tensor, $\boldsymbol{M} \equiv \overset{\triangle}{\boldsymbol{D}}$ (where the triangle indicates the covariant convected time derivative), with respect to the strain rate tensor, $\boldsymbol{D}$, as proposed by Thompson [129]. This decomposition splits tensor $\boldsymbol{M}$ into two additive parts: one that is *in-phase* with $\boldsymbol{D}$, $\phi_{\boldsymbol{M}}^{\boldsymbol{D}}$, and another one that is *out-of-phase* with $\boldsymbol{D}$, $\widetilde{\phi}_{\boldsymbol{M}}^{\boldsymbol{D}}$. These tensors are defined as

$$\phi_{\boldsymbol{M}}^{\boldsymbol{D}} = \mathbb{I}^{\boldsymbol{DD}} : \boldsymbol{M} \quad ; \quad \widetilde{\phi}_{\boldsymbol{M}}^{\boldsymbol{D}} = \left(\mathbb{I}^{\delta\delta} - \mathbb{I}^{\boldsymbol{DD}}\right) : \boldsymbol{M} \quad , \tag{4.26}$$

where the symbol ":" accounts for the double dot product and $\mathbb{I}^{\boldsymbol{DD}}$ is a fourth order tensor given by

$$\mathbb{I}^{\boldsymbol{DD}} = \sum_{i=1}^{3} \boldsymbol{e}_i^{\boldsymbol{D}} \boldsymbol{e}_i^{\boldsymbol{D}} \boldsymbol{e}_i^{\boldsymbol{D}} \boldsymbol{e}_i^{\boldsymbol{D}} \quad , \tag{4.27}$$

where $\boldsymbol{e}_i^{\boldsymbol{D}}$ is an eigenvector of $\boldsymbol{D}$ and $\mathbb{I}^{\delta\delta}$ is the fourth order identity tensor.

In this sense, tensor $\boldsymbol{M}$ can be completely in-phase with the eigenvectors of $\boldsymbol{D}$, meaning that it corroborates the tendency imposed by $\boldsymbol{D}$. On the other extreme, if $\boldsymbol{M}$ is totally out-of-phase with respect to $\boldsymbol{D}$, it defies the tendency of $\boldsymbol{D}$.

Aligned with the concepts presented by Haller [122], Thompson and co-workers [40, 130] define a vortex as regions where the strain acceleration, $\boldsymbol{M}$, defies the tendency suggested by $\boldsymbol{D}$. This defiance is measured by the following normalised ratio

$$N_\phi = 1 - \frac{2}{\pi}\cos^{-1}\left(\frac{\left\|\phi_{\boldsymbol{M}}^{\boldsymbol{D}}\right\|}{\|\boldsymbol{M}\|}\right) \quad . \tag{4.28}$$

In fact, the ratio N_ϕ is an indicator of how the tensor $\boldsymbol{M}$ corroborates with the tendency dictated by $\boldsymbol{D}$. Thus, $N_\phi = 0$ represents rigid-body rotation, while $N_\phi = 1$ is the limit of totally strain persistent flow.

Thompson [40] argues that because N_ϕ measures a competition between $\boldsymbol{M}$ and $\boldsymbol{D}$, it may be interesting to analyse that from an anisotropic viewpoint. Therefore, the author proposes two indicators of directional information. The first one, called "line" anisotropic ratio, is defined as follow

$$N_{lk} = 1 - \frac{2}{\pi}\cos^{-1}\left(\frac{[\boldsymbol{M}]_{\mathrm{kk}}[\boldsymbol{M}]_{\mathrm{kk}}}{[\boldsymbol{M}\boldsymbol{M}]_{\mathrm{kk}}}\right) \quad , \tag{4.29}$$

where $[\boldsymbol{M}]_{kk}$ is an element of the diagonal of tensor $\boldsymbol{M}$ (terms of $\boldsymbol{M}$ which are *in-phase* with $\boldsymbol{D}$), and $[\boldsymbol{M}\boldsymbol{M}]_{kk}$ is an element of the principal diagonal of tensor $\boldsymbol{M}^2$. The quantities N_{lk} measure how the strain acceleration, $\boldsymbol{M}$, defies the tendency imposed by the strain rate, $\boldsymbol{D}$, by comparing each diagonal component of $\boldsymbol{M}$ to the other positions of their respective line.

The second indicator is called "surface" anisotropic ratio, because it compares the relevance of diagonal components with respect to off-diagonal components of sub-matrices representing the projection of $\boldsymbol{M}$ in planes defined by eigenvectors of $\boldsymbol{D}$. This is done by the following relation

$$N_{sk} = 1 - \frac{2}{\pi}\cos^{-1}\left(\frac{\left(\boldsymbol{M}^{\boldsymbol{D}}_{ii} - \boldsymbol{M}^{\boldsymbol{D}}_{jj}\right)^2}{\Delta_{\boldsymbol{M}_k}}\right) \quad , \tag{4.30}$$

where $\Delta_{\boldsymbol{M}_k}$ is the determinant of the sub-matrix $\boldsymbol{M}_k$, the projection of tensor $\boldsymbol{M}$ on the plane defined by the kth-eigenvalue of $\boldsymbol{D}$. The sub-matrix $\boldsymbol{M}_k$ is obtained by the linear operation $\boldsymbol{M}_k = \widetilde{\boldsymbol{\psi}}_k : \boldsymbol{M}$, with $\widetilde{\boldsymbol{\psi}}_k$ being a fourth-order tensor given by

$$\widetilde{\boldsymbol{\psi}}_k = \boldsymbol{e}^{\boldsymbol{D}}_i\boldsymbol{e}^{\boldsymbol{D}}_i\boldsymbol{e}^{\boldsymbol{D}}_i\boldsymbol{e}^{\boldsymbol{D}}_i + \boldsymbol{e}^{\boldsymbol{D}}_i\boldsymbol{e}^{\boldsymbol{D}}_j\boldsymbol{e}^{\boldsymbol{D}}_j\boldsymbol{e}^{\boldsymbol{D}}_i + \boldsymbol{e}^{\boldsymbol{D}}_j\boldsymbol{e}^{\boldsymbol{D}}_i\boldsymbol{e}^{\boldsymbol{D}}_i\boldsymbol{e}^{\boldsymbol{D}}_j + \boldsymbol{e}^{\boldsymbol{D}}_j\boldsymbol{e}^{\boldsymbol{D}}_j\boldsymbol{e}^{\boldsymbol{D}}_j\boldsymbol{e}^{\boldsymbol{D}}_i \quad . \tag{4.31}$$

The isotropic ratio, N_ϕ, and both line and surface anisotropic ratios, N_l and N_s, are normalised so that elliptic modes correspond to values from 0 to less than 0.5 and hyperbolic modes correspond to values greater than 0.5 and less than or equal to 1. The limit of 0.5 indicates a parabolic mode.

Both N_l and N_s components are rearranged so that $N_{l1} \geq N_{l2} \geq N_{l3}$ and $N_{s1} \geq N_{s2} \geq N_{s3}$. Thus, when evaluating, for example, a vortical region, one may chose either a more relaxed condition (N_{l3} or $N_{s3} < 0.5$) that identifies regions where at least one direction is swirl-dominated, or a conservative condition (N_{l1} or $N_{s1} < 0.5$) for which the three directions concerned with the anisotropic ratios have to indicate elliptical dominance.

4.4 Some relevant remarks

At this point, some important remarks can be done considering the definitions for a vortex presented so far and concepts they bring with.

4.4.1 Solid foundations for a flow classification criterion as stated by Astarita [131]

According to Astarita [131], a solid flow classification criterion should be

1. *local* – calculated point-wise in the flow;
2. *objective* – invariant to Euclidean transformations (arbitrary changes of reference frame); and
3. *general* – applicable to every kind of flow without any restriction.

Furthermore, a criterion enjoying the three conditions above should belong to one of the following two types:

- *purely kinematic* – which does not consider materials' properties; or
- function of *kinematics* and *material's rheological parameters*.

This proposition seems very reasonable for flow classification. Regarding the *local* condition, it is quite common, specially in turbulent flows, to deal with flows containing different regions in which extensional or swirling motions dominate one over another. It is interesting then to properly identify and locate each region.

The invariance to arbitrary changes in the reference frame appears to be fair. In the context of vortex identification, for instance, if an objective criterion were used, *any* observer would conclude that a given region presents a vortical motion. This issue will be detailed below (see Section 4.5 and Chapter 6).

Astarita [131] also states that a criterion that is "applicable to only a restricted class of flow fields is of little utility", and therefore pleads for general applicability. For example, some criteria are restricted to incompressible flows. Other authors also defend this idea, as we will see further on (see Section 4.4.3).

Regarding the issue of whether a criterion should be purely kinematic or combine kinematics with rheological information of the fluid, it may be more interesting in other contexts than Newtonian fluids, such as non-Newtonian or magneto-sensitive fluids (see more comments in Section 4.4.3 and Chapter 5 below).

4.4.2 A special look at the rate of strain

The most intuitive ideas of a vortex rely on the velocity gradient, which can be decomposed in a symmetric part ($\boldsymbol{D}$) related to strain and a skew-symmetric part ($\boldsymbol{W}$) related to rotation. Since there is also a strong relation between vortical motion and rotation, the rate-of-rotation tensor was considerably explored throughout the years.

Nevertheless, as pointed out by Thompson [40], more recent works seem to reveal a remarkable aspect regarding vortex identification: the tendency of relating in some manner the identification of vortices to the evolution of the rate-of-strain tensor.

This tensor and its eigenbasis have been considered since the appearance of objective criteria, as commented in Section 4.5 below. However, even in some cases in which objectivity is not aimed, definitions for a vortex that are function of the strain acceleration tensor may appear.

Jeong and Hussain [38] were trying to define vortical structures based on pressure minima. This information was contained in the pressure Hessian, which in turn is obtained by taking the gradient of the momentum balance equation (Navier-Stokes equation for a Newtonian fluid). Interestingly, even though seeking for vortical structures, the authors drop the skew-symmetric part of the resulting equation, which represents the evolution equation for *vorticity*, to find their needs in the evolution equation for the strain-rate tensor.

Moreover, the works by Klein, Hua, and Lapeyre [132], Haller [122], and Thompson [40] all use a certain objective time derivative of the strain rate tensor to evaluate the flow. In particular, regarding the work by Klein, Hua, and Lapeyre [132], objectivity was not intended, but naturally appeared, contrary to Thompson [40] and Haller [122], who were seeking objective flow classification criteria.

In short, when looking for ways to identify a vortical motion, the strain rate tensor has been repeatedly considered, through its evolution equation, its time derivative (acceleration strain) or through its eigenbasis.

4.4.3 Applicability of the criteria

As commented above, one of the guidelines provided by Astarita [131] for a solid flow classification is that it should be ruled by a generally applicable criterion. In fact, maybe one can think of that appeal as an invitation to look to the extension of Fluid Mechanics and try to reach the greatest amount of sub-areas as possible in terms of application. Needless to say, it may not be trivial, but it does make sense if one thinks on some important class of flows that deserve special attention in Fluid Mechanics.

After Astarita [131], some authors defended specific causes. For example, Cucitore, Quadrio, and Baron [126] advocate the extension of flow classification criteria to compressible flows. In addition to their new criterion, the authors propose a modified version of the λ_2-criterion [38] that takes into account compressibility effects.

Further, Zhang and Choudhury [128] present a criterion based on the eigen analysis of the velocity gradient tensor that is usable under compressibility effects. They also conclude that the λ_2-criterion [38] fails to identify vortices in compressible flows, and other classic criteria (such as Q [36], Δ [37], vorticity magnitude) present only partial success.

More recently, Kolář [119, 133] reinforced the importance of the applicability of flow classification criteria to compressible flows, arguing that "the effect of compressibility plays an important role in many interesting problems, including the bifurcation, stability, and breakdown of compressible swirling flows" (e.g. [134, 135]). The author states that among the most popular criteria (Q [36], Δ [37], λ_2 [38], λ_{ci} [39]), only the criteria Δ [37] and λ_{ci} [39] are extendible to compressible flows. Moreover, Kolář [133] affirms that the $\boldsymbol{M}_Z$-criterion by Haller [122] is limited to incompressible flows.

In the context of non-Newtonian fluids, it is common to deal with complex flows exhibiting several kinds of motion. The identification of the regions where these motions take place is of fundamental importance to the evaluation of non-Newtonian effects. For example, it is known that in turbulent polymer-induced drag reduction, the proper identification of vortical structures may lead to a better understanding of the phenomenon [19, 35, 136–138].

Another field motivating general flow classification criteria is Magnetohydrodynamics. In this context, magnetic fields act directly on the rheology properties of the fluid. These changes may lead, for instance, to drag reduction and consequent modifications on vortical structures [139].

4.5 The role of objectivity

The idea of an entity to remain invariant under arbitrary changes of reference frame (*i.e.* to be objective or Euclidean-invariant) is largely diffused in Continuum Mechanics. Regarding Fluid Mechanics though, it seems that objectivity is only well-diffused among non-Newtonian fluid mechanicists. In fact, objectivity is a required condition for a constitutive model. On the other hand, this concept is not quite settled in Newtonian Fluid Mechanics.

In the context of vortex identification, Haller [122] presents a simple example where Galilean-invariant-only criteria can detect an infinite vortex in one frame and no vortex in another frame. He concludes that *Galilean-invariance is not enough for vortex identification criteria*.

Other arguments for a vortex identification criterion to be objective are pointed out (or reinforced) by Thompson [40]:

- the reference frame to identify a vortex could be arbitrarily chosen with no previous need to favour a specific one;
- objective criteria are Galilean-invariant as well;
- objectivity could lead to more appropriate interpretation of results connecting

vortex dynamics to any objective variable of interest in the flow, such as quality of mixture, amount of heat or drag reduction.

In this connection, we present bellow a brief historic of objectivity in the context of flow classification, followed by objective versions of classical criteria.

4.5.1 Persistence-of-straining and effective vorticity

A key concept relevant to the discussion on objectivity is the concept of persistence-of-straining, introduced by Lumley [86], and applied by several authors [129, 131, 140–142]. Briefly, the persistence-of-straining concept is associated with the capacity of the flow to persistently stretch a material element.

Figure 4.1 illustrates the concept of persistence-of-straining by depicting two possible scenarios when a material element that is aligned with an eigenvector of $\boldsymbol{D}$ is advected by the flow. This material element will rotate under the action of the rotation rate, $\boldsymbol{W}$, and stretch following the action of the strain-rate tensor, $\boldsymbol{D}$.

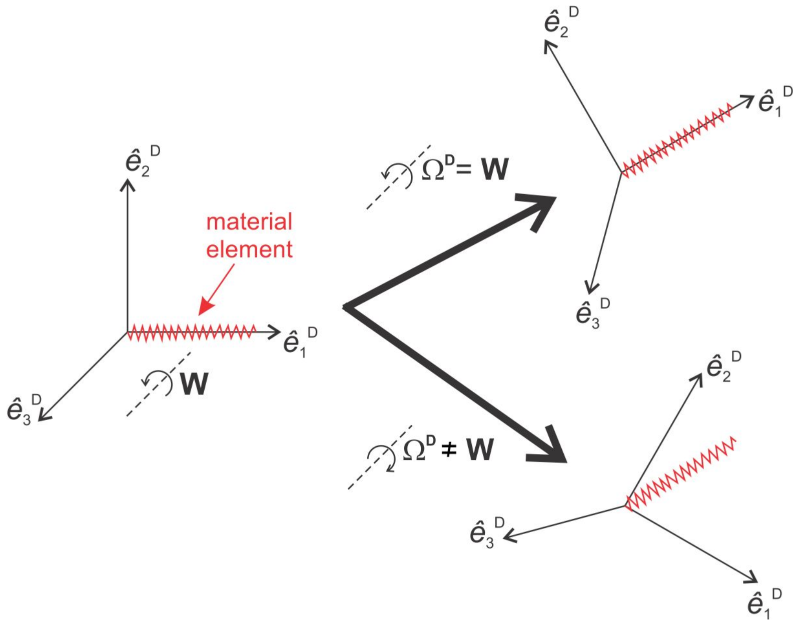

Figure 4.1 – Schematic representation of the possible scenarios involving the rotation of a material element with respect to the eigenbasis of the strain-rate tensor.

Suppose the material element is initially aligned with the principal direction of the strain-rate tensor, $\boldsymbol{D}$, represented by the first eigenvector, $\hat{\boldsymbol{e}}_1^{\boldsymbol{D}}$, associated to the largest eigenvalue of D, $\lambda_1^{\boldsymbol{D}}$. In this scenario, this material element is under the strongest stretch it could be in that point. In a short following moment, after being advected by the flow, both the direction of the material element and the eigendirections of $\boldsymbol{D}$ may have changed. Therefore, two further scenarios are possible. In a first scenario, they can rotate with the same angular velocity, *i.e.* the angular velocity of the eigenvectors of $\boldsymbol{D}$, $\boldsymbol{\Omega}^{\boldsymbol{D}}$, can be equal to the angular velocity of the material element, $\boldsymbol{W}$. This means that the material filament will persist to be strongly stretched. In the second scenario, $\boldsymbol{\Omega}^{\boldsymbol{D}}$ does not coincide with $\boldsymbol{W}$, and the material element loses the alignment with the main direction of $\boldsymbol{D}$, undergoing a stretch relief.

The persistence-of-straining concept leads to a physically consistent perspective of the motion of a fluid element, and, consequently, to a new point of view regarding flow classification. In this context, Astarita [131] proposed a criterion based on the *relative rate of rotation*, $\overline{\boldsymbol{W}}$, defined as

$$\overline{\boldsymbol{W}} = \boldsymbol{W} - \boldsymbol{\Omega}^{\boldsymbol{D}} \quad , \tag{4.32}$$

where the tensor $\boldsymbol{\Omega}^{\boldsymbol{D}} = \dot{\boldsymbol{e}}^{D}\boldsymbol{e}^{D}$ represents the rate of rotation of the eigenvectors of $\boldsymbol{D}$.

The quantity $\overline{\boldsymbol{W}}$, also called *effective rotation* [143] or *absolute rotation rate* [144], represents the relative rate of rotation with respect to the principal directions of the strain-rate tensor, $\boldsymbol{D}$. Interestingly, even though $\boldsymbol{W}$ and $\boldsymbol{\Omega}^{\boldsymbol{D}}$ are not objective, $\overline{\boldsymbol{W}}$ was proved to be objective [145, 146].

With the concept of effective rotation in mind, Astarita [131] proposed an objective criterion defined as

$$R_D = -\frac{\mathrm{tr}(\overline{\boldsymbol{W}}^2)}{\mathrm{tr}(D^2)} \quad . \tag{4.33}$$

The authors states that the limit of $R_D = \infty$ represents rigid-body rotation, $R_D = 0$ is a (purely) extensional flow and $R_D = 1$ indicates a viscometric flow. Despite this brilliant idea, the criterion proposed by Astarita has been proven to present some flaws for certain classes of 3D flows (see [147]).

By analysing these inconsistencies, Thompson and Mendes [142] proposed a criterion based on the concept of persistence-of-straining. They suggest the criterion

$$\mathcal{R} = \frac{\sqrt{\frac{1}{2}\left[\boldsymbol{D}\overline{\boldsymbol{W}} - \overline{\boldsymbol{W}}\boldsymbol{D}\right]}}{\mathrm{tr}(\boldsymbol{D}^2)} \quad , \tag{4.34}$$

for which the quantity $\boldsymbol{D}\overline{\boldsymbol{W}} - \overline{\boldsymbol{W}}\boldsymbol{D}$ is a measurer of how far from the total persistence-of-straining the flow is. This criterion is always positive. The limit $\mathcal{R} = 0$ indicates extensional flow and it tends to infinity as the flow approaches a rigid-body rotation.

Using another line of thought without invoking objectivity, Tabor and Klapper [148] verified the importance of the use of the relative-rate-of-rotation by analysing stretching and alignment of material filaments. Their analysis reinforces the criterion of Astarita [131], which can be seen as an objective version of the Q-criterion as presented in the following.

4.5.2 Objective versions for classic flow classification criteria

The majority of vortex definitions presented in the literature is based on the rate-of-rotation (or vorticity) tensor, $\boldsymbol{W}$. This tensor is not invariant under arbitrary transformations of the reference frame. In other words, these vortex definitions do not enjoy objectivity because they depend on $\boldsymbol{W}$.

Parallel to this, as discussed above, it is clear that some consistent definitions of vortex have been expressed in terms of the strain-acceleration tensor and/or on the basis of the strain-rate tensor.

Consequently, objective redefinitions of classic flow classification criteria can be achieved by replacing the non-objective term of the criteria, most usually $\boldsymbol{W}$, with the relative rate of rotation, $\overline{\boldsymbol{W}}$ (Eq. (D.1)), which is objective. For instance, as commented by Haller [122], an objective version of the Q-criterion [36] can be introduced based on the work presented by Tabor and Klapper [148], which yields

$$\hat{Q} = \frac{1}{2}\left(\|\overline{\boldsymbol{W}}\|^2 - \|\boldsymbol{D}\|^2\right) > 0 \quad . \tag{4.35}$$

The same methodology can be applied to other classical non-objective criteria [149]. The objective versions of the criteria Δ, λ_2, and $\lambda_{cr}/\lambda_{ci}$ take respectively the form

$$\hat{\Delta} = \left(\frac{\hat{Q}}{3}\right)^3 + \left(\frac{\det(\boldsymbol{D} + \overline{\boldsymbol{W}})}{2}\right)^2 > 0 \quad , \tag{4.36}$$

$$\hat{\lambda}_2 = \lambda_2^{\boldsymbol{D}^2 + \overline{\boldsymbol{W}}^2} < 0 \quad , \tag{4.37}$$

and

$$\frac{\hat{\lambda}_{cr}}{\hat{\lambda}_{ci}} = \frac{\lambda_{cr}^{\boldsymbol{D}+\overline{\boldsymbol{W}}}}{\lambda_{ci}^{\boldsymbol{D}+\overline{\boldsymbol{W}}}} = \frac{\lambda_{cr}^{\overline{\boldsymbol{L}}}}{\lambda_{ci}^{\overline{\boldsymbol{L}}}} \quad , \tag{4.38}$$

The hat over the criteria symbol indicates their objective version. Note also that in the objective versions of the criteria depending on the velocity gradient (or its transpose, $\boldsymbol{L}$), this tensor is replaced by its objective version, $\overline{\boldsymbol{L}} = \boldsymbol{D} + \overline{\boldsymbol{W}}$.

The objective versions of the four classic flow classification criteria presented above were applied to the analytical ABC flow and a sudden 4:1 contraction by Martins et al. [149] (see Appendix C). The authors stated that the criteria that enjoy objectivity provide more information about the kinematics of the flow, for example, identifying more elliptical regions than their non-objective counterparts.

Moreover, Martins et al. [138] (see Appendix D) also use the objective version of the Q-criterion and the ratios proposed by Thompson [40] in the context of turbulent drag-reduction channel flow. They showed that the objective criteria clearly indicate the thickening of the buffer layer, which is predicted by the major theories on the phenomenon and corroborated by both experiments and numerical simulations.

In Chapter 5, the influence of polymers on the identification of vortices will be evaluated using some of the most widely used criteria. Further discussions on the application of objective criteria to complex flows along the work by Martins et al. [138, 149] will be presented in Chapter 6.

Chapter 5

The influence of polymeric effects on vortex identification

Vortex identification criteria are largely used in the context of turbulent flows of Newtonian fluids. With the aid of classic vortex identification criteria, turbulent structures have been found and proven to be fundamental in the explanation of several phenomena, as, for instance, the self-sustaining mechanism of wall turbulence [150].

In this connection, when turbulent viscoelastic fluid flows are considered, vortical structures were found to weaken and elongate in the stream-wise direction [35, 151]. These turbulent structures and their morphological changes have been used to explain, the autonomous regeneration cycle of wall turbulence in the context of polymer-induced drag-reduction [13, 35]. In the wall turbulence mechanism for polymer solutions, the influence of polymers is considered by evaluating how its interaction with turbulent structures changes the flow dynamics. However, the influence of polymers on the criteria to identify the vortices has never been called into question.

In this chapter, the following question is raised: how can we stress the polymer influence on vortex identification criteria for viscoelastic turbulent flows? In order to answer this question, some criteria are revisited and applied to turbulent channel flow of Newtonian and viscoelastic fluids. The main objective is to evaluate how the presence of diluted polymers affects these criteria, but the discussion on Newtonian fluid is already enriching.

5.1 Polymer contribution

In the case of viscoelastic effects, the presence of polymers lead to the addition of an extra-stress term into the equation of momentum balance. Therefore, criteria whose definition depends on this equation may be somehow compromised in the presence of polymers.

Among the classic vortex identification criteria, the λ_2-criterion fits the condition above. Therefore, let us revisit its definition and discuss the effect of polymers on its operation.

5.1.1 Revisiting the λ_2-criterion

As previously commented, the λ_2-criterion by Jeong and Hussain [38] is based on the idea that, on the axis of a vortex core, the pressure tends to have a local minimum. They used the Hessian of the pressure to locate that by considering the symmetric part of the gradient of the Navier-Stokes equation, which reads

$$\frac{\mathrm{D}\boldsymbol{D}}{\mathrm{D}t} + \boldsymbol{D}^2 + \boldsymbol{W}^2 = -\mathrm{He}\,(p) + \frac{1}{Re_h}\Delta\boldsymbol{D} \quad . \tag{4.16}$$

Jeong and Hussain [38] argued that discarding the unsteady ($\mathrm{D}\boldsymbol{D}/\mathrm{D}t$) and viscous ($\Delta\boldsymbol{D}/Re_h$) terms, would avoid some inconsistencies between the existence of a local pressure minimum and a vortex core. The λ_2-criterion looks for regions where the intermediate eigenvalue of the Hessian of the pressure is positive (condition for a local minimum). With the neglected terms, this equals regions where the intermediate eigenvalue of the tensor $\boldsymbol{D}^2 + \boldsymbol{W}^2$ is negative.

Now, the contribution of a diluted polymer will be taken into account using the FENE-P model. As shown in Chapter 2, in the FENE-P model, an extra-stress tensor containing contributions due to the presence of polymers is added to the Navier-Stokes equation, yielding

$$\frac{\partial \boldsymbol{u}}{\partial t} + \boldsymbol{u}\cdot\nabla\boldsymbol{u} = -\nabla p + \frac{\beta}{Re_h}\Delta\boldsymbol{u} + \frac{1}{Re_h}\nabla\cdot\boldsymbol{\Xi} \quad . \tag{2.7}$$

Following the rationale of Jeong and Hussain [38], taking the gradient of Eq. (2.7) yields

$$\frac{\partial \nabla\boldsymbol{u}}{\partial t} + \boldsymbol{u}\cdot\nabla(\nabla\boldsymbol{u}) + \nabla\boldsymbol{u}\cdot\nabla\boldsymbol{u} = -\mathrm{He}\,(p) + \frac{\beta}{Re_h}\Delta\nabla\boldsymbol{u} + \frac{1}{Re_h}\nabla(\nabla\cdot\boldsymbol{\Xi}) \quad . \tag{5.1}$$

Just like Jeong and Hussain [38] proceeded with the Navier-Stokes equation, Eq. (5.1) above can be decomposed into symmetric and anti-symmetric parts. Taking the symmetric part containing the Hessian of the pressure and putting the term $\boldsymbol{D}^2 + \boldsymbol{W}^2$ in evidence yields

$$\boldsymbol{D}^2 + \boldsymbol{W}^2 = -\frac{\mathrm{D}\boldsymbol{D}}{\mathrm{D}t} - \mathrm{He}\,(p) + \frac{\beta}{Re_h}\Delta\boldsymbol{D} + \frac{1}{Re_h}\boldsymbol{S}^P \quad , \tag{5.2}$$

where $\boldsymbol{S}^P$ is the symmetric part of the tensor $\nabla(\nabla\cdot\boldsymbol{\Xi})$ [1].

[1] Making $\nabla(\nabla\cdot\boldsymbol{\Xi}) = \boldsymbol{\Phi}$, its symmetric and anti-symmetric parts are respectively obtained by

$$\boldsymbol{S}^P = \frac{1}{2}\left(\boldsymbol{\Phi} + \boldsymbol{\Phi}^T\right) \quad \text{and} \quad \boldsymbol{A}^P = \frac{1}{2}\left(\boldsymbol{\Phi} - \boldsymbol{\Phi}^T\right) \quad . \tag{5.3}$$

Thus, when applying the λ_2-criterion to a FENE-P fluid, the tensor considered is actually the sum of all terms on the right-hand side in Eq. (5.2). Further, considering the same assumptions made by Jeong and Hussain [38], the first and third terms on the right-hand side drop and the polymer contribution to the λ_2-criterion is represented by the term $(1/Re_h)\,\boldsymbol{S}^P$.

At this point, a theoretical discussion takes place on whether the polymeric term should be placed with the tensor $\boldsymbol{D}^2 + \boldsymbol{W}^2$, on the left-hand side of Eq. (5.2), or on the right-hand side with the Hessian of the pressure. In other words, when identifying vortices in a viscoelastic fluid with the λ_2-criterion, should the user still consider the intermediate eigenvalue of $\left[\boldsymbol{D}^2 + \boldsymbol{W}^2\right]$ or the intermediate eigenvalue of $\left[\boldsymbol{D}^2 + \boldsymbol{W}^2 + (1/Re_h)\,\boldsymbol{S}^P\right]$ should be the one to look at? Moreover, is the term $(1/Re_h)\,\boldsymbol{S}^P$ relevant in this calculation or it should be discarded, just like the unsteady and viscous terms?

In this connection, following the idea behind the λ_2-criterion by Jeong and Hussain [38], we perform an evaluation of the contribution of each term in Eq. (5.2) above to the characterisation of a λ_2-vortex.

In practice, users of the λ_2-criterion identify vortices by the intermediate eigenvalue of $\boldsymbol{D}^2 + \boldsymbol{W}^2$, $\lambda_2^{\boldsymbol{D}^2+\boldsymbol{W}^2}$. Therefore, let us apply the following operation to Eq. (5.2)

$$\begin{aligned}\boldsymbol{e}_2^{\boldsymbol{D}^2+\boldsymbol{W}^2}\cdot\left[\frac{\mathrm{D}\boldsymbol{D}}{\mathrm{D}t}\right]\cdot\boldsymbol{e}_2^{\boldsymbol{D}^2+\boldsymbol{W}^2}+\boldsymbol{e}_2^{\boldsymbol{D}^2+\boldsymbol{W}^2}\cdot\left[\boldsymbol{D}^2+\boldsymbol{W}^2\right]\cdot\boldsymbol{e}_2^{\boldsymbol{D}^2+\boldsymbol{W}^2} = \\ \boldsymbol{e}_2^{\boldsymbol{D}^2+\boldsymbol{W}^2}\cdot\left[-\mathrm{He}(p)\right]\cdot\boldsymbol{e}_2^{\boldsymbol{D}^2+\boldsymbol{W}^2}+\boldsymbol{e}_2^{\boldsymbol{D}^2+\boldsymbol{W}^2}\cdot\left[\frac{\beta}{Re_h}\Delta\boldsymbol{D}\right]\cdot\boldsymbol{e}_2^{\boldsymbol{D}^2+\boldsymbol{W}^2}+ \\ \boldsymbol{e}_2^{\boldsymbol{D}^2+\boldsymbol{W}^2}\cdot\left[\frac{1}{Re_h}\boldsymbol{S}^P\right]\cdot\boldsymbol{e}_2^{\boldsymbol{D}^2+\boldsymbol{W}^2}\quad ,\end{aligned} \tag{5.4}$$

where $\boldsymbol{e}_2^{\boldsymbol{D}^2+\boldsymbol{W}^2}$ is the intermediate eigenvector of $\boldsymbol{D}^2 + \boldsymbol{W}^2$ associated to $\lambda_2^{\boldsymbol{D}^2+\boldsymbol{W}^2}$. For conciseness, $\lambda_2^{\boldsymbol{D}^2+\boldsymbol{W}^2}$ and $\boldsymbol{e}_2^{\boldsymbol{D}^2+\boldsymbol{W}^2}$ may be hereafter referred to as λ_2 and $\boldsymbol{e}_2$, respectively. The same for the unsteady term, $\mathrm{D}\boldsymbol{D}/\mathrm{D}t$, that may be referred to as $\dot{\boldsymbol{D}}$ instead.

Equation (5.4) provides the projection of Eq. (5.2) on the direction of $\boldsymbol{e}_2^{\boldsymbol{D}^2+\boldsymbol{W}^2}$. Thus, the term $\boldsymbol{e}_2^{\boldsymbol{D}^2+\boldsymbol{W}^2}\cdot\left[\boldsymbol{D}^2+\boldsymbol{W}^2\right]\cdot\boldsymbol{e}_2^{\boldsymbol{D}^2+\boldsymbol{W}^2}$ equals the intermediate eigenvalue of $\boldsymbol{D}^2 + \boldsymbol{W}^2$, λ_2, and Eq. (5.4) can be rearranged as

$$\lambda_2 = \boldsymbol{e}_2\cdot\left[-\frac{\mathrm{D}\boldsymbol{D}}{\mathrm{D}t}\right]\cdot\boldsymbol{e}_2+\boldsymbol{e}_2\cdot\left[-\mathrm{He}(p)\right]\cdot\boldsymbol{e}_2+\boldsymbol{e}_2\cdot\left[\frac{\beta}{Re_h}\Delta\boldsymbol{D}\right]\cdot\boldsymbol{e}_2+\boldsymbol{e}_2\cdot\left[\frac{1}{Re_h}\boldsymbol{S}^P\right]\cdot\boldsymbol{e}_2\quad . \tag{5.5}$$

We put λ_2 in evidence on the left-hand side of Eq. (5.5) to show what is calculated in practice to identify a λ_2-criterion. Even if the proposition of Jeong and Hussain [38] is to neglect the first and third terms on the right-hand side, when λ_2 is calculated, it does take them into account. It is possible though to check whether these two terms and the polymeric one play a negligible role on the establishment of a λ_2-vortex or not.

This will be discussed in Section 5.2 below.

5.1.2 Writing the Q-criterion from a dynamical perspective

Hunt et al. [36] defined a vortex as a region where the intensity of the rate-of-rotation tensor, $\boldsymbol{W}$, is greater than that of the strain-rate tensor, $\boldsymbol{D}$. This dominance of $\boldsymbol{W}$ over $\boldsymbol{D}$ is calculated by means of the second invariant of the velocity gradient tensor as follows

$$Q = \frac{1}{2}\left(\|\boldsymbol{W}\|^2 - \|\boldsymbol{D}\|^2\right) > 0 \quad . \tag{4.4}$$

Jeong and Hussain [38] showed that the Q-criterion relates to the trace of the tensor $\boldsymbol{D}^2 + \boldsymbol{W}^2$, used to calculate the λ_2-criterion, as follows

$$Q = -\frac{1}{2}\mathrm{tr}\left(\boldsymbol{D}^2 + \boldsymbol{W}^2\right) \quad . \tag{4.18}$$

It means that the Q-criterion can also be seen as the consequence of contributions of minus half of the trace of the terms in Eq. (5.2). The Q-criterion can thus be obtained with the following relation

$$Q = -\frac{1}{2}\mathrm{tr}\left(\boldsymbol{D}^2 + \boldsymbol{W}^2\right) = -\frac{1}{2}\mathrm{tr}\left(-\frac{\mathrm{D}\boldsymbol{D}}{\mathrm{D}t}\right) - \frac{1}{2}\mathrm{tr}\left(-\mathrm{He}\left(p\right)\right) - \frac{1}{2}\mathrm{tr}\left(\frac{\beta}{Re_h}\Delta\boldsymbol{D}\right) - \frac{1}{2}\mathrm{tr}\left(\frac{1}{Re_h}\boldsymbol{S}^P\right) \quad . \tag{5.6}$$

Similarly to the case of the λ_2-criterion above, one can evaluate how each term contribute to the identification of a Q-vortex. This different look at the Q-criterion may lead to some physical and theoretical interpretations, as discussed in Section 5.2 below.

5.2 Results and Discussion

These new viewpoints for the criteria Q and λ_2 are evaluated with the aid of snapshots coming from the DNS of turbulent channel flows of Newtonian and viscoelastic (FENE-P) fluids performed by Thais and co-workers [19, 20, 105].

Simulations at $Re_{\tau 0} = 180$, 395, 590 and 1000 were conducted for Newtonian fluid. For the FENE-P simulations, at $Re_{\tau 0} = 180$, four elastic levels were achieved by the combination of two values of $L(= 30$ and $100)$ and two values of $Wi_{\tau 0}(= 50$ and $115)$, leading to four levels of relative drag reduction. At $Re_{\tau 0} = 1000$, two levels of elasticity were compared, one with $L = 30$ and $Wi_{\tau 0} = 50$, and another with $L = 100$ and $Wi_{\tau 0} = 115$. For the intermediate $Re_{\tau 0}(= 395$ and $590)$, only the most elastic case ($L = 100$ and $Wi_{\tau 0} = 115$) was considered. A summary of the simulation data is available in Tab. 5.1.

For the post-processing necessary to perform the present analyses, the meshes were

$Re_{\tau 0}$	L	$Wi_{\tau 0}$	β	$L_x \times L_y \times L_z$	$N_x \times N_y \times N_z$	δt	%DR
180	-	-	1	$8\pi \times 2 \times 3\pi/2$	$512 \times 129 \times 128$	1×10^{-3}	0
180	30	50	0.9	$8\pi \times 2 \times 3\pi/2$	$512 \times 129 \times 128$	1×10^{-3}	28.5
180	30	115	0.9	$8\pi \times 2 \times 3\pi/2$	$512 \times 129 \times 128$	1×10^{-3}	38.4
180	100	115	0.9	$8\pi \times 2 \times 3\pi/2$	$512 \times 129 \times 128$	1×10^{-3}	47.0
180	100	115	0.9	$8\pi \times 2 \times 3\pi/2$	$512 \times 129 \times 128$	1×10^{-3}	62.3
395	-	-	1	$8\pi \times 2 \times 3\pi/2$	$1024 \times 257 \times 256$	1×10^{-3}	0
395	100	115	0.9	$8\pi \times 2 \times 3\pi/2$	$1024 \times 257 \times 256$	1×10^{-3}	62.0
590	-	-	1	$8\pi \times 2 \times 3\pi/2$	$1536 \times 257 \times 512$	1×10^{-3}	0
590	100	115	0.9	$8\pi \times 2 \times 3\pi/2$	$1536 \times 257 \times 512$	7.5×10^{-4}	61.0
1000	-	-	1	$6\pi \times 2 \times 3\pi/2$	$1536 \times 385 \times 768$	8×10^{-4}	0
1000	30	50	0.9	$6\pi \times 2 \times 3\pi/2$	$1536 \times 385 \times 768$	5×10^{-4}	30.0
1000	100	115	0.9	$6\pi \times 2 \times 3\pi/2$	$1536 \times 513 \times 768$	5×10^{-4}	58.0

Table 5.1 – Summary of the simulation data that provided the snapshots for the present analysis.

respected. In fact, the same spatial discretisation scheme and differentiation stencils presented in Chapter 2 (Section 2.4.2) were used here.

It is important to remark that for the calculation of the time-depend term $\mathrm{D}\boldsymbol{D}/\mathrm{D}t$, two consecutive snapshots were considered with the same time step of the original simulation (*i.e.* δt displayed in Tab. 5.1).

The post-processors created for the present operations are also parallel (using MPI) and work with slabs parallel to the wall. To perform the present analysis, runs using from only 1 up to 128 MPI cores and taking from a few seconds to one hour of CPU time were conducted

In the following, the analysis for the effect of the Reynolds number in the Newtonian case, the effect of the Reynolds number in the viscoelastic case and the effect of elasticity at low ($Re_{\tau 0} = 180$) and high ($Re_{\tau 0} = 1000$) Reynolds number are presented.

5.2.1 Effect of Reynolds number on Newtonian fluid

The average contribution in wall-normal planes of each term in Eq. (5.6) at different Reynolds numbers for a Newtonian fluid is shown in Fig. 5.1, representing the composition of the Q-criterion. A first general comment is that the Reynolds number does not seem to play a fundamental role in this analysis, since the tendencies are mostly alike for all terms considered. In fact, increasing the Reynolds number implies achieving higher y^+ positions and increasing the intensity of each term, but the overall behaviour is the same.

Note that, since the flow is divergent-free ($\mathrm{tr}(\nabla \boldsymbol{u}) = \mathrm{tr}(\boldsymbol{D}) = 0$), the trace of the terms $\dot{\boldsymbol{D}}$ and $\Delta \boldsymbol{D}/Re_h$ are null. Consequently, when applied to a Newtonian fluid, the

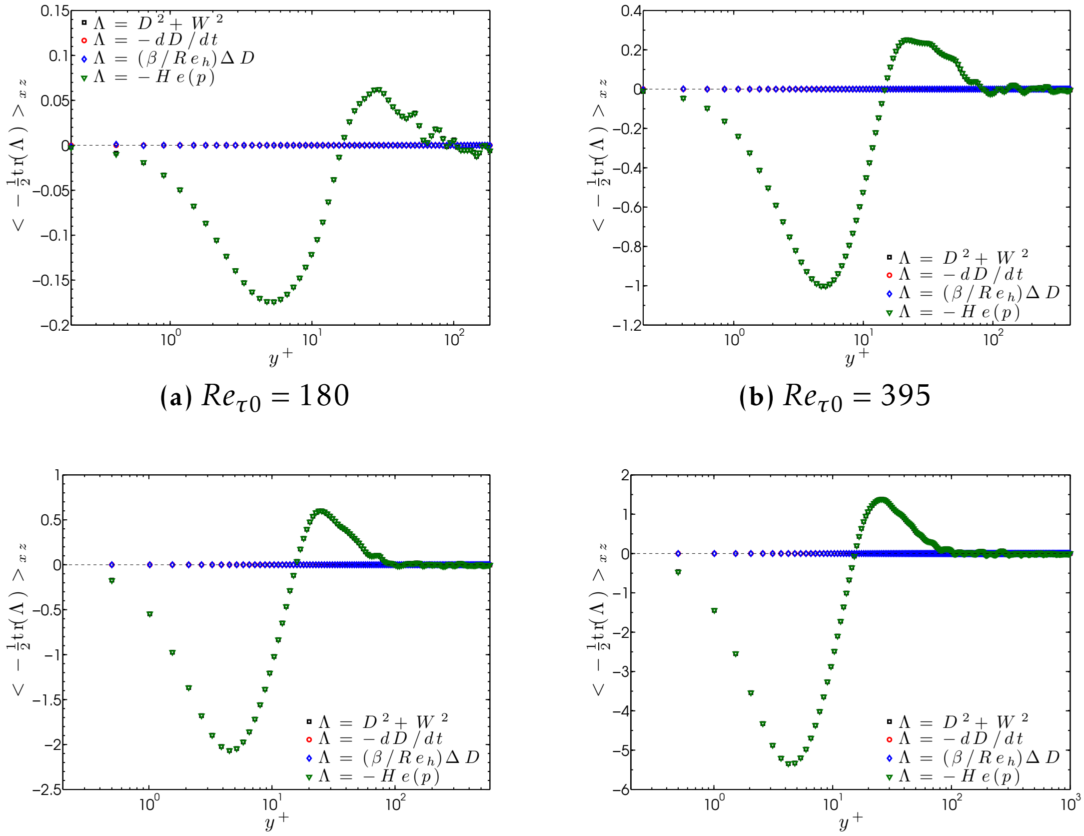

(a) $Re_{\tau 0} = 180$

(b) $Re_{\tau 0} = 395$

(c) $Re_{\tau 0} = 590$

(d) $Re_{\tau 0} = 1000$

Figure 5.1 – Contribution of each term in Eq. (5.6) (Q-criterion) at varied Reynolds numbers (Newtonian fluid): (a) $Re_{\tau 0} = 180$; (b) $Re_{\tau 0} = 395$; (c) $Re_{\tau 0} = 590$; and (d) $Re_{\tau 0} = 1000$.

Q-criterion depends only on the pressure term. This direct relation to the pressure has been presented by Jeong and Hussain [38], who showed that, from the Poisson equation for the pressure, Q can also be seen as the pressure source term by the relation $\Delta p = 2\rho Q$.

The Q-criterion (term related to $\boldsymbol{D}^2 + \boldsymbol{W}^2$) and the Hessian of the pressure, He(p), tend to zero at the wall, and a valley (minimum value) is achieved at $y^+ \approx 5$. Then, at $y^+ \approx 12$, their signs change and a peak (maximum value) occurs just after $y^+ \approx 20$. After this peak, they both tend to zero with increasing y^+.

Figure 5.2 shows $x-z$-plane-average profiles of each term in Eq. (5.5) regarding the λ_2-criterion. Similarly to the case of the Q-criterion, the Reynolds number does not play a fundamental role, except with regards to the intensity of the terms. The shape of the curves remain basically the same with increasing $Re_{\tau 0}$.

All terms tend to be null at the wall and at the channel centre. Regarding now each term separately, Fig. 5.2 shows that the Hessian of the pressure is, on average, essentially positive, contributing in the sense of hyperbolic modes, and presents a peak

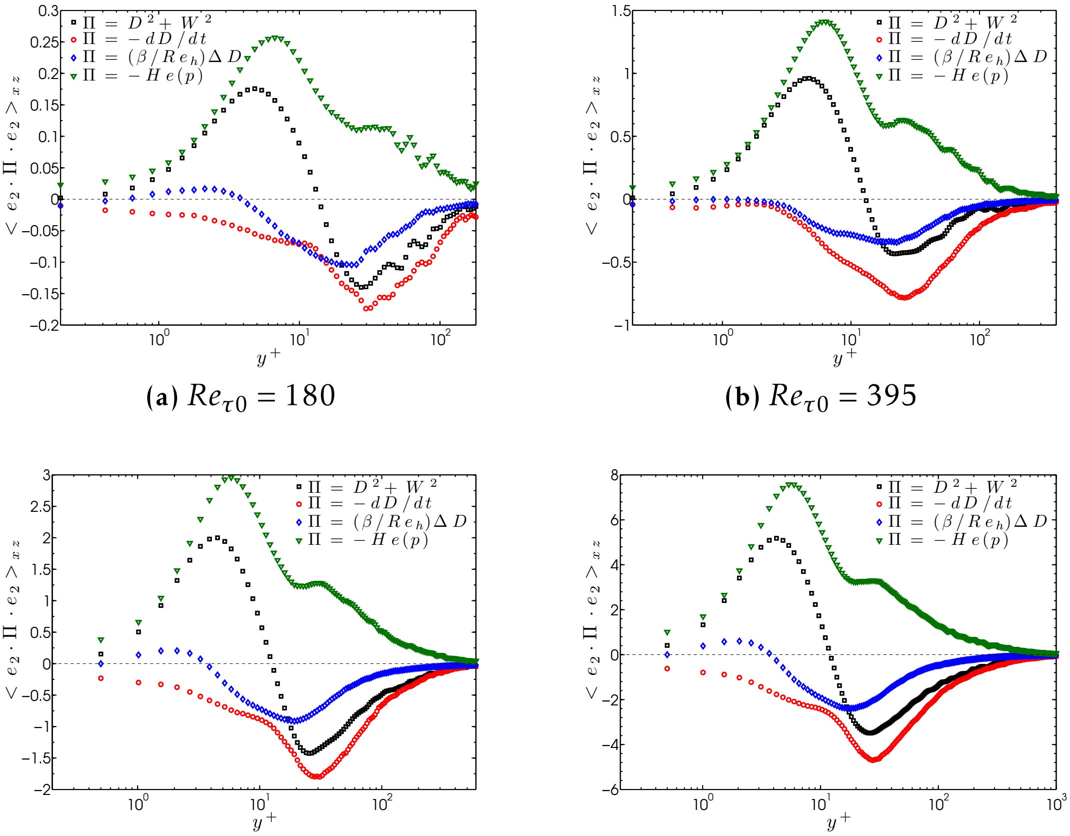

(a) $Re_{\tau 0} = 180$

(b) $Re_{\tau 0} = 395$

(c) $Re_{\tau 0} = 590$

(d) $Re_{\tau 0} = 1000$

Figure 5.2 – Contribution of each term in Eq. (5.5) (λ_2-criterion) at varied Reynolds numbers (Newtonian fluid): (a) $Re_{\tau 0} = 180$; (b) $Re_{\tau 0} = 395$; (c) $Re_{\tau 0} = 590$; and (d) $Re_{\tau 0} = 1000$; .

at $y^+ \approx 6$. A second smaller peak is observed at $y^+ \approx 30$. Contrarily, the unsteady term ($\dot{\boldsymbol{D}}$) is mostly negative, contributing in the sense of elliptic modes, and present a single minimum value at $y^+ \approx 30$. The viscous term contributes mostly negatively as well, with a minimum value at $y^+ \approx 20$. A slightly different behaviour is observed for a small region very near to the wall ($y^+ \lessapprox 4$), where this terms contributes positively (or neutrally for $Re_{\tau 0} = 395$).

As a consequence of this balance, λ_2 departs from zero at the wall to a maximum value at $y^+ \approx 5$. After this peak, it decreases to zero somewhere between $10 \lessapprox y^+ \lessapprox 20$ and achieve a minimum close to $y^+ = 20$. After this valley, λ_2 tends to zero as it approaches the centre of the channel.

It is remarkable that λ_2 is mostly dictated by the Hessian of the pressure in the vicinity of the wall, until $y^+ \approx 3$, and, conversely, away from the wall ($y^+ \gtrapprox 200$), the value of λ_2 basically equals the viscous term. Furthermore, note that the terms discarded by Jeong and Hussain [38], are actually not negligible. In fact, they both oppose the trend dictated by the Hessian of the pressure, specially within the buffer layer ($5 \lessapprox y^+ \lessapprox 30$). These results make questionable the assumptions made by Jeong and Hussain [38] for the λ_2-criterion.

Moreover, we remember that Jeong and Hussain [38] use tensor $\boldsymbol{D}^2 + \boldsymbol{W}^2$ with the intention of capturing the effects of the Hessian of the pressure. Figure 5.2 shows though that these terms are very similar for $y^+ < 5$, but, from the buffer layer on, the pressure terms actually plays against the tendency of λ_2.

5.2.2 Effect of Reynolds number on viscoelastic fluids

Now, the effect of the Reynolds number is verified for the viscoelastic cases. The elasticity level is maintained by fixing $L = 100$ and $Wi_{\tau 0} = 115$.

The average contribution of terms in Eq. (5.6) to the composition of the Q-criterion is presented in Fig. 5.3. Differently from the Newtonian case, the profiles of Q and the pressure term do not coincide, clearly because of the polymeric term that plays a significant role. Also, compared with the Newtonian case, the terms suffer a considerable decrease in intensity (one order of magnitude).

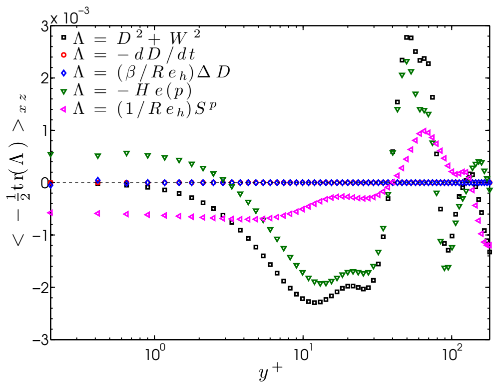

(a) $Re_{\tau 0} = 180$

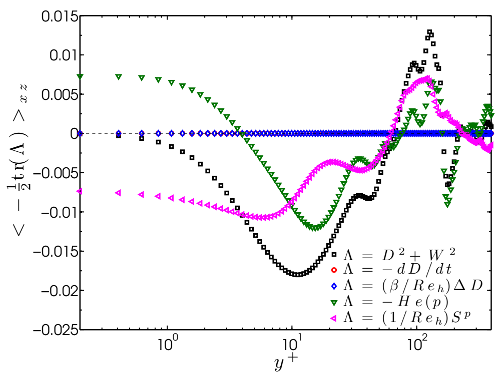

(b) $Re_{\tau 0} = 395$

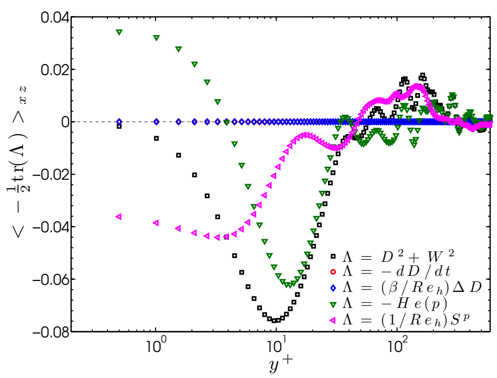

(c) $Re_{\tau 0} = 590$

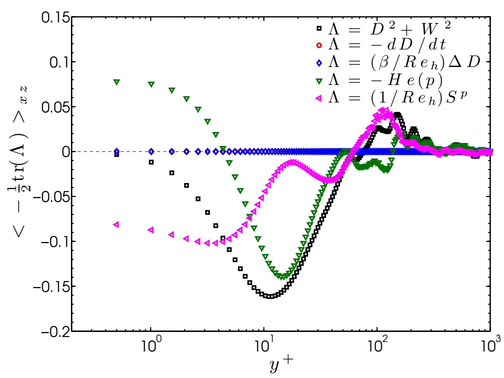

(d) $Re_{\tau 0} = 1000$

Figure 5.3 – Contribution of each term in Eq. (5.6) (Q-criterion) at varied Reynolds numbers (viscoelastic fluid - $L = 100$ and $Wi_{\tau 0} = 115$): (a) $Re_{\tau 0} = 180$; (b) $Re_{\tau 0} = 395$; (c) $Re_{\tau 0} = 590$; and (d) $Re_{\tau 0} = 1000$.

The profile of Q still departs from zero at the wall, decreases to a minimum value around $y^+ \approx 10$. Then, it changes sign between $40 \lessapprox y^+ \lessapprox 60$ and then tends gradually to zero as the centre of the channel is being reached. This means that, on average, the flow is predominantly hyperbolic close to the wall (viscous and buffer layer) and elliptic closer to the centreline.

The polymeric term starts from a negative value at the wall and changes sign approximately at the same y^+ position of Q. Then, it also tends gradually to zero with increasing y^+. The pressure term compensates the tendency of the polymeric term at the wall, starting from a positive value but keeping a shape very close to the Q-criterion.

It is important to note that, compared to the Newtonian case (Fig. 5.1), the peak positions in Fig. 5.3 are all shifted away from the wall.

Another notable effect of the Reynolds number is a relative increase of the negative (hyperbolic) extrema with respect to the positive (elliptic) peak when increasing the Reynolds number. For the lowest Reynolds number, the elliptic extrema has the same order of magnitude of the hyperbolic extrema. At $Re_{\tau 0} = 1000$, the hyperbolic extrema are approximately three times more intense than the elliptic peaks.

As regards the formation of the λ_2-criterion, Fig. 5.4 displays the average profile of each term in Eq. (5.5). A first overall comment is that the approximate position of the extrema and sign change points are also shifted away from the wall compared to the Newtonian case, just like it was observed for the λ_2-criterion. Also, the intensity of the terms is considerably lower and can be up to two orders of magnitude different at $Re_{\tau 0} = 180$, indicating a decrease in the swirl intensity, just like for the Q-criterion. Differently from the Newtonian case, the Reynolds number affects qualitatively the results.

The trend on the average behaviour of λ_2 is qualitatively the same. It is null at the wall and increases until achieving a peak value, in this case, at $y^+ \approx 10$. Then, it changes sign at $y^+ \approx 40$, except for $Re_{\tau 0} = 1000$, for which this change occurs at $y^+ \approx 60$. A minimum is than achieved usually at $100 \lessapprox y^+ \lessapprox 200$, and it tends to zero as we approach the centre of the channel. The λ_2-criterion also indicates a dominance of hyperbolic modes closer to the wall and elliptic modes closer to the centreline.

In the viscoelastic case, the Hessian of the pressure again is always contributing to hyperbolicity (on average). Its first peak is now located at $y^+ \approx 12$ and this location is independent from the Reynolds number. The second peak is now located at $y^+ \approx 100$ and its value is closer (even greater at $Re_{\tau 0} = 180$) than the first one.

Still in Fig. 5.4, the time-dependent term is considerably affected by the Reynolds number. This term is basically negative at $Re_{\tau 0} = 180$, but, with increasing Reynolds number, small positive contribution clearly tends to appear in the very beginning of the buffer layer ($5 \lessapprox y^+ \lessapprox 10$).

The viscous and polymeric terms have similar behaviour, presenting positive contri-

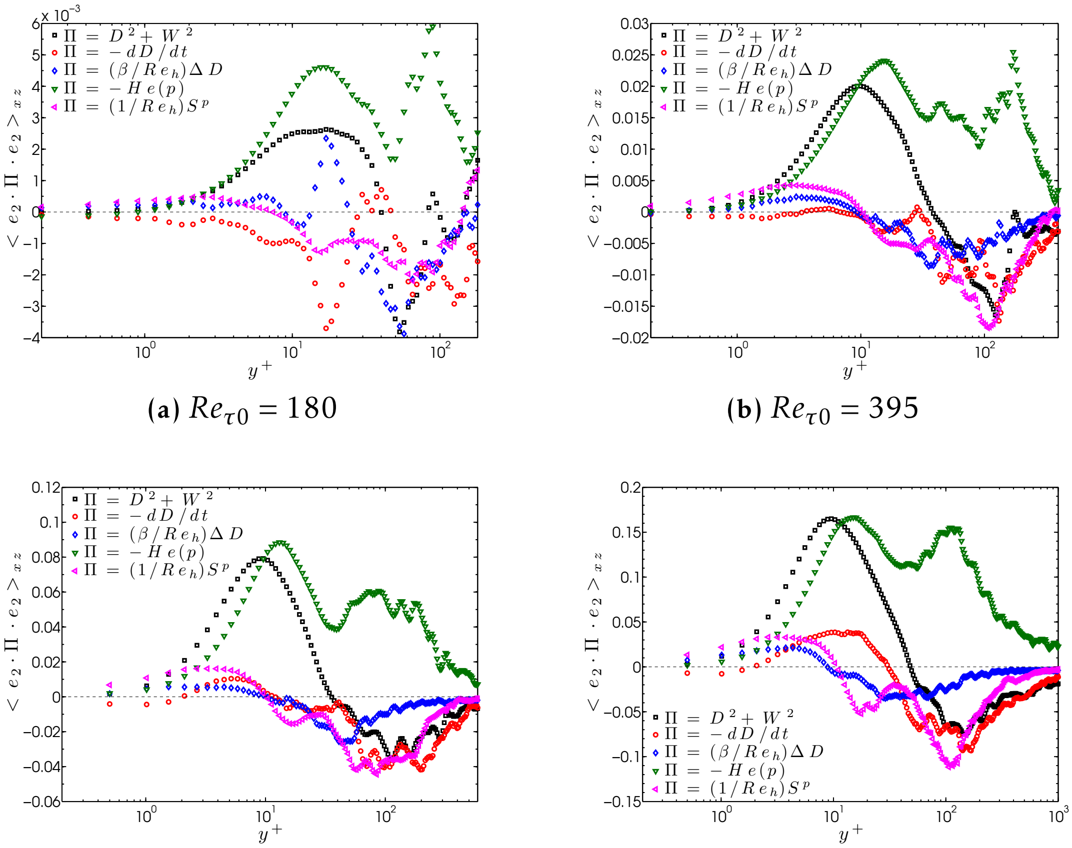

(a) $Re_{\tau 0} = 180$ (b) $Re_{\tau 0} = 395$

(c) $Re_{\tau 0} = 590$ (d) $Re_{\tau 0} = 1000$

Figure 5.4 – Contribution of each term in Eq. (5.5) (λ_2-criterion) at varied Reynolds numbers (viscoelastic fluid - $L = 100$ and $Wi_{\tau 0} = 115$): (a) $Re_{\tau 0} = 180$; (b) $Re_{\tau 0} = 395$; (c) $Re_{\tau 0} = 590$; and (d) $Re_{\tau 0} = 1000$; .

butions from the wall up to $y^+ \approx 10$ and negative contributions thereafter.

It is interesting that the changes in $\dot{\boldsymbol{D}}$ implies in similar changes in λ_2, whose peak value gets closer to the peak of the pressure with increasing Reynolds, even if they occur at slightly different y^+ positions ($y^+ \approx 9$ for λ_2 and $y^+ \approx 12$ for the pressure term).

We recall here the fundamental question raised in Section 5.1.1 above on how to consider the polymeric contribution to the evolution of $\boldsymbol{D}$. One could place it together with the term $\boldsymbol{D}^2 + \boldsymbol{W}^2$ (see Eq. (5.2)) arguing that if the Hessian of the pressure is put in evidence and the unsteady and viscous terms are discarded, as suggested by Jeong and Hussain [38], vortical regions would be represented by the intermediate eigenvalue of $\boldsymbol{D}^2 + \boldsymbol{W}^2 - \boldsymbol{S}^P/Re_h$.

Another option would be to place the polymeric term with the Hessian of the pressure and continue to consider the intermediate eigenvalue of $\boldsymbol{D}^2 + \boldsymbol{W}^2$. In fact, that is our choice here to perform this analysis because a regular user of the λ_2-criterion usually considers the tensor $\boldsymbol{D}^2 + \boldsymbol{W}^2$ regardless of what is on the other side of the equation.

Finally, one could advocate to drop the polymeric term, either because it brings inconsistencies in some case, or just to maintain the relation $\boldsymbol{D}^2+\boldsymbol{W}^2 = -\mathrm{He}(p)$ proposed by Jeong and Hussain [38].

What is important to highlight is that, even when applied to Newtonian fluids, the λ_2-criterion contain some assumptions that do not seem to be reasonable, at least in the context of turbulent channel flow. Further, when applying this criterion to viscoelastic fluid, the user is left with a fundamental question concerning how to consider the polymeric contribution. Our results here show that the contribution of the polymeric term, just like the contribution of the unsteady and viscous term discarded by Jeong and Hussain [38], is not negligible, which leads us to question the consistency of this criterion, at least in the context of turbulent viscoelastic fluid flow. Therefore, the λ_2-criterion will no longer be considered in the present work.

5.2.3 Effect of elasticity at $Re_{\tau 0} = 180$

Here, the friction Reynolds number is fixed at $Re_{\tau 0} = 180$ and the elasticity is varied so that its effect is evaluated. Two maximum polymer extensibility parameters, $L = 30$ and 100, and two friction Weissenberg numbers, $Wi_{\tau 0} = 50$ and 115, have been combined leading to relative drag reduction from 28.5% to 62.3%.

The average contribution of the terms that compose the Q-criterion is shown in Fig. 5.5 for the four elasticity levels. It is notable that the intensity of all terms decrease with increasing elasticity. This becomes clear if a reference y^+ position is chosen and the corresponding values of each term at that position is compared. For example, at $y^+ = 10$, in the less elastic case (Fig. 5.5a), Q is approximately -0.038, this value decreases to -0.024 for $L = 30$ and $Wi_{\tau 0} = 115$ (Fig. 5.5b), -0.014 for $L = 100$ and $Wi_{\tau 0} = 50$ (Fig. 5.5c) and achieves -0.0022 in the most elastic case (Fig. 5.5d).

The influence of the polymeric term is relatively small, which leads to very similar values for Q and the pressure term. In fact, it suggests that the decrease in intensity within both elliptic and hyperbolic regions is not a linear effect of the polymeric term in the evolution equation of the strain rate tensor. In other words, the intensity of Q is not diminished directly by the term $(\boldsymbol{S}^P/Re_h)$ as a consequence of the balance of Eq. (5.6). Instead, it is a consequence of the non-linearities relating the polymer stress and flow dynamics.

5.2.4 Effect of elasticity at $Re_{\tau 0} = 1000$

The elastic effect is now evaluated for the highest Reynolds number considered here ($Re_{\tau 0} = 1000$). For this analysis, only two cases are compared: a moderately elastic case with $L = 30$ and $Wi_{\tau 0} = 50$, and a highly elastic level with $L = 100$ and $Wi_{\tau 0} = 115$, leading to relative drag reduction of 30% and 58%, respectively.

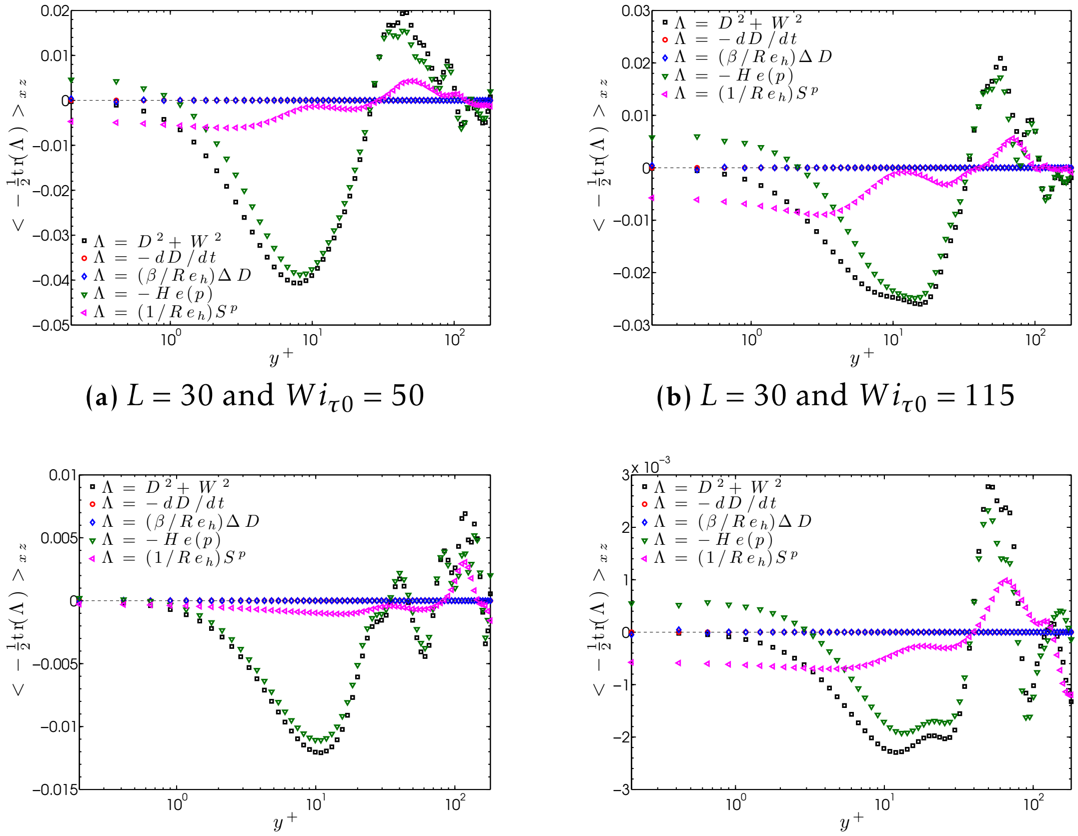

(a) $L = 30$ and $Wi_{\tau 0} = 50$ **(b)** $L = 30$ and $Wi_{\tau 0} = 115$

(c) $L = 100$ and $Wi_{\tau 0} = 50$ **(d)** $L = 100$ and $Wi_{\tau 0} = 115$

Figure 5.5 – Contribution of each term in Eq. (5.6) (Q-criterion) for varied elasticity levels at $Re_{\tau 0} = 180$: (a) $L = 30$ and $Wi_{\tau 0} = 50$; (b) $L = 30$ and $Wi_{\tau 0} = 115$; (c) $L = 100$ and $Wi_{\tau 0} = 50$; and (d) $L = 100$ and $Wi_{\tau 0} = 115$.

Differently from the results at $Re_{\tau 0} = 180$, we present in Fig. 5.6 the profiles of the non-null terms composing the Q-criterion for the Newtonian and the two viscoelastic cases at $Re_{\tau 0} = 1000$ in the same figure. From this perspective, it is clear that the intensity of all terms diminishes considerably with increasing elasticity. The main elastic effect consists then on the trend of turning elliptic (vortical) and hyperbolic (extensional) regions into parabolic ones. In other words, regions dominated by rotation or extension in Newtonian flows tend to turn into regions where the rotation and extension are equilibrated in the presence of polymers. This characterises a laminarisation of the flow.

This trend is corroborated by the location of peaks (elliptic extrema region) and valleys (hyperbolic extrema region). For the Newtonian case, the valley for Q and the pressure term are at $y^+ \approx 4$. For the low-elasticity case, these location is shifted upwards until $y^+ \approx 7$ and its intensity is approximately five times smaller. For the high-elasticity case, he valley is located at $y^+ \approx 12$ and the minimum value is more than 30 times less intense, as evidenced in the zoom box in Fig. 5.6. It is important to remark that similar

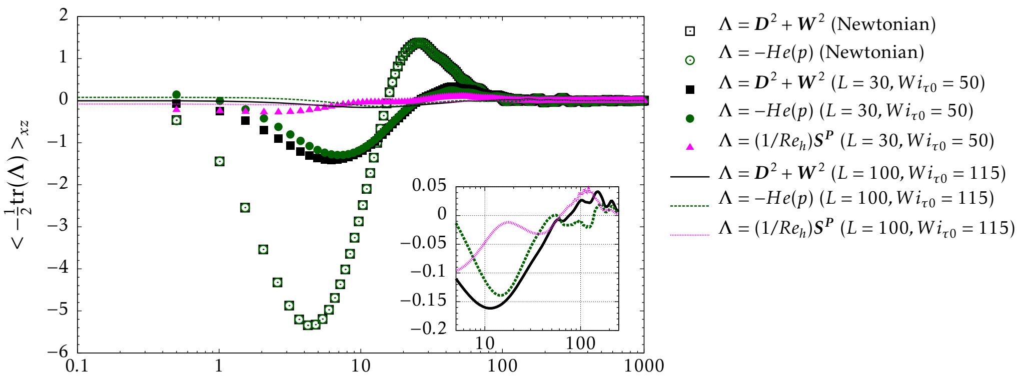

Figure 5.6 – Comparison of the contribution of each term in Eq. (5.6) (Q-criterion) between Newtonian and viscoelastic cases at $Re_{\tau 0} = 1000$.

effects can be observed for the peaks, concerning the elliptic region.

5.3 Concluding remarks

The evolution equation of the strain-rate tensor, $\boldsymbol{D}$, was used by Jeong and Hussain [38] to propose the λ_2-criterion. The authors also show that this evolution equation is related to the Q-criterion. In this chapter, we used the evolution equation of $\boldsymbol{D}$ to evaluate how each of its dynamic terms affect flow kinematics.

In the case of the λ_2-criterion, each term in Eq. (5.5) was projected in the direction of the intermediate eigenvalue of the tensor $\boldsymbol{D}^2 + \boldsymbol{W}^2$. This operation allows to evaluate the contribution of each term for the composition of the λ_2-criterion. We showed that the argument made by Jeong and Hussain [38] to drop the time-dependent and viscous terms in the evolution equation of $\boldsymbol{D}$ does not hold, at least for a turbulent channel flow. These two terms showed to be relevant to the composition of the λ_2-criterion, basically competing with the Hessian of the pressure.

Moreover, the application of the λ_2-criterion to viscoelastic fluid flows seems to be compromised by a fundamental question. This question concerns the treatment of the polymeric term that appears in the evolution equation of $\boldsymbol{D}$. Because of the controversial argumentation presented by Jeong and Hussain [38] to chose the tensor $\boldsymbol{D}^2 + \boldsymbol{W}^2$ in the place of the Hessian of the pressure, the decision of what to do with this extra term is not clear at all. Should the user discard it too? Should it be added to $\boldsymbol{D}^2 + \boldsymbol{W}^2$ before taking the intermediate eigenvalue or should it add the Hessian of the pressure? In view of this lack of clarity, we decided to abandon the λ_2-criterion in what follows in the present work.

Concerning the Q-criterion, Jeong and Hussain [38] showed that if one takes minus half of the trace of the evolution equation of $\boldsymbol{D}$, the term involving $\boldsymbol{D}^2 + \boldsymbol{W}^2$ returns the Q-criterion. By applying the same operation to all other terms, we compared how each of them helps to form a Q-vortex in terms of their average profiles. The time-dependent and viscous terms showed to be null for all cases. Therefore, for Newtonian fluids, the Q-criterion is purely dictated by the Hessian of the pressure.

When a polymer solution is considered, the polymeric contribution is not negligible, but does not seem to be the direct cause of the decrease in intensity of both elliptic (vortical) and hyperbolic (extensional) regions observed with increasing elasticity. Finally, according to the composition of the Q-criterion, the distance of the extrema of each term is an increasing function of the elasticity of the fluid.

Chapter 6

Objective flow classification criteria applied to turbulent viscoelastic channel flow

The concepts of hyperbolic, elliptic and parabolic modes [121, 122] in a flow were introduced in Section 4.2.2. They represent important information concerning fluid motion and are largely used in the context of flow classification. Briefly, hyperbolic domains are characterised by the dominance of strain over rotation, whereas elliptic domains occur where swirl motions are more intense than strain. The limiting subdomain between them where the magnitude of the rate of strain and the rate of rotation are equilibrated is named parabolic domain.

Moreover, the concept of objectivity was presented in Chapter 4 with some comments on the theoretical advantages of using frame-independent criteria. In the following, we will be able to compare the results of objective criteria with the classic (non-objective) ones.

In this chapter, non-objective and objective flow classification criteria will be used to evaluate the distribution of hyperbolic, parabolic and elliptic domains within the turbulent channel flow of Newtonian and viscoelastic fluids. Preliminary results are firstly evaluated for a Newtonian fluid concerning the analytical ABC flow and a 4:1 sudden contraction.

6.1 Criteria analysed in the present work

The choice of the criteria to be evaluated here was made according to their physical consistence. Among the most popular criteria, namely Q [36], λ_2 [38], Δ [37], and λ_{ci} [39], the latter (and its variant $\lambda_{cr}/\lambda_{ci}$ [127] as well) being a "swirling strength" measurer, it is limited to the classification of elliptic modes only. Because we are here interested in analysing the whole possibilities involving fluid motions, the λ_{ci}-criterion will not be considered in the following. We recall that we drop the analyses for the λ_2-criterion as well due to its lack of clarity concerning some assumptions made to derive it.

The criterion chosen to be applied to turbulent viscoelastic channel flow were then: the (non-objective) criteria Q [36] and Δ [37], their objective versions $\hat{Q}$ and $\hat{\Delta}$, and the objective ratios N_ϕ and N_l proposed by Thompson [40].

The objective isotropic and line anisotropic ratios (N_ϕ and N_l, respectively) are preferred here because they are objective and have a very solid physical basis. Moreover, the line anisotropic ratios provide more detailed directional information about the motions. These ratios provide values from 0 to 1 so that values smaller than 0.5 represent elliptic regions and values greater than 0.5 stand for hyperbolic regions. The frontier of 0.5 corresponds to the parabolic domain and the limits of 0 and 1 represent, respectively, rigid-body and purely-extensional motion.

The surface anisotropic ratio, N_s, as it has been defined in Section 4.3.10, does not have the same hyperbolic/elliptic polarity provided by the other criteria. It is correct to classify regions as hyperbolic domains when N_s approaches 1, but nothing guarantees that the parabolic frontier is at 0.5 and, consequently, that values under 0.5 indicate elliptic domination. [1] Therefore, the surface anisotropic ratio, N_s, is not considered here.

In order to keep the same basis to compare all criteria, we apply the same normalisation used by Bacchi [130] and Martins et al. [149] to the objective and non-objective versions of the criteria Q and Δ. The resulting normalised criteria provide the same scale (from 0 to 1) of the objective ratios and read

$$Q^* = \frac{1}{\pi}\cos^{-1}\left(\frac{||\boldsymbol{W}||^2 - ||\boldsymbol{D}||^2}{||\boldsymbol{W}||^2 + ||\boldsymbol{D}||^2}\right) \quad , \tag{6.1}$$

$$\Delta^* = \frac{1}{\pi}\cos^{-1}\left[\frac{\left(\frac{||\boldsymbol{W}||^2 - ||\boldsymbol{D}||^2}{6}\right)^3 + \left(\frac{\det(\boldsymbol{D}+\boldsymbol{W})}{2}\right)^2}{\left(\frac{||\boldsymbol{W}||^2 + ||\boldsymbol{D}||^2}{6}\right)^3 + \left(\frac{\det(\boldsymbol{D}+\boldsymbol{W})}{2}\right)^2}\right] \quad , \tag{6.2}$$

for the original non-objective versions, and

$$\hat{Q}^* = \frac{1}{\pi}\cos^{-1}\left(\frac{||\overline{\boldsymbol{W}}||^2 - ||\boldsymbol{D}||^2}{||\overline{\boldsymbol{W}}||^2 + ||\boldsymbol{D}||^2}\right), \tag{6.3}$$

[1] According to Thompson [152], one possible solution is to redefine N_s, splitting the sub-matrices $\boldsymbol{M}_k$ into diagonal and off-diagonal parts, and taking the ratio of the norm of the diagonal part of $\boldsymbol{M}_k$ to the norm of $\boldsymbol{M}_k$.

$$\hat{\Delta}^* = \frac{1}{\pi}\cos^{-1}\left[\frac{\left(\frac{\|\overline{\boldsymbol{W}}\|^2 - \|\boldsymbol{D}\|^2}{6}\right)^3 + \left(\frac{\det(\boldsymbol{D}+\overline{\boldsymbol{W}})}{2}\right)^2}{\left(\frac{\|\overline{\boldsymbol{W}}\|^2 + \|\boldsymbol{D}\|^2}{6}\right)^3 + \left(\frac{\det(\boldsymbol{D}+\overline{\boldsymbol{W}})}{2}\right)^2}\right] , \tag{6.4}$$

for their objective versions considering the effective rate of rotation.

In Eqs. (6.1-6.4), the superscript asterisk indicates normalisation and the hat over the symbol is used to distinguish the objective version from the non-objective one.

6.2 Calculation of objective entities

The acceleration strain, $\boldsymbol{M}$, computed as the covariant convected derivative of the strain-rate tensor, is a quantity used by Thompson [40] and Haller [122] to define a vortex (see Chapter 4). This tensor is defined as

$$\boldsymbol{M} = \dot{\boldsymbol{D}} + \boldsymbol{D}\boldsymbol{L} + \boldsymbol{L}^T\boldsymbol{D} \quad , \tag{4.23}$$

where $\dot{\boldsymbol{D}} = \partial \boldsymbol{D}/\partial t + \boldsymbol{u}\cdot\nabla\boldsymbol{D}$ is the material derivative of $\boldsymbol{D}$.

Two consecutive instantaneous flow fields are considered to compute the term $\partial\boldsymbol{D}/\partial t$. All other (non-time-dependent) terms are based on the first of the two consecutive flow fields. The time step between the flow fields corresponds to the simulation time step, δt (see values in Tab. 5.1).

Thompson [129] proposed the so-called *in-phase-out-of-phase* decomposition of a tensor with respect to another. In the context of flow classification, this decomposition has been used [40, 130, 153] to evaluate how the tendency dictated by the strain-rate tensor is defied by its covariant convected derivative, $\boldsymbol{M}$. For that, Thompson and co-workers [40, 130, 153] apply the *in-phase-out-of-phase* decomposition to find the parts of $\boldsymbol{M}$ that are co-axial (or in phase, $\phi_{\boldsymbol{M}}^{\boldsymbol{D}}$) and orthogonal (or out-of-phase, $\widetilde{\phi}_{\boldsymbol{M}}^{\boldsymbol{D}}$) with respect to $\boldsymbol{D}$. These two parts can be obtained by the following relation

$$\boldsymbol{M} = \phi_{\boldsymbol{M}}^{\boldsymbol{D}} + \widetilde{\phi}_{\boldsymbol{M}}^{\boldsymbol{D}} = \mathbb{I}^{\boldsymbol{DD}} : \boldsymbol{M} + (\mathbb{I}^{\delta\delta} - \mathbb{I}^{\boldsymbol{DD}}) : \boldsymbol{M} \quad , \tag{6.5}$$

where $\mathbb{I}^{\boldsymbol{DD}}$ is the fourth-order tensor defined as

$$\mathbb{I}^{\boldsymbol{DD}} = \sum_{i=1}^{3} \boldsymbol{e}_i^{\boldsymbol{D}}\boldsymbol{e}_i^{\boldsymbol{D}}\boldsymbol{e}_i^{\boldsymbol{D}}\boldsymbol{e}_i^{\boldsymbol{D}} \quad , \tag{6.6}$$

where $\boldsymbol{e}_i^{\boldsymbol{D}}$ is an eigenvector of $\boldsymbol{D}$, and $\mathbb{I}^{\delta\delta}$ is the fourth-order identity tensor defined as

$$\mathbb{I}^{\delta\delta} = \boldsymbol{e}_j\boldsymbol{e}_k\boldsymbol{e}_k\boldsymbol{e}_j \quad . \tag{6.7}$$

Thompson, Bacchi, and Machado [153] showed that

$$\phi_{\boldsymbol{M}}^{\boldsymbol{D}} = \mathbb{I}^{\boldsymbol{DD}} : \boldsymbol{M} = \boldsymbol{D}' + 2\boldsymbol{D}^2 \quad , \tag{6.8}$$

and

$$\widetilde{\phi}_{\boldsymbol{M}}^{\boldsymbol{D}} = (\mathbb{I}^{\delta\delta} - \mathbb{I}^{\boldsymbol{DD}}) : \boldsymbol{M} = \boldsymbol{D} \cdot \overline{\boldsymbol{W}} - \overline{\boldsymbol{W}} \cdot \boldsymbol{D} \quad . \tag{6.9}$$

Since $\phi_{\boldsymbol{M}}^{\boldsymbol{D}}$ is co-axial with $\boldsymbol{D}$ and $\widetilde{\phi}_{\boldsymbol{M}}^{\boldsymbol{D}}$ is orthogonal to $\boldsymbol{D}$, the tensor $\boldsymbol{D}' + 2\boldsymbol{D}^2$ is related to the *persistence-of-straining* concept, while tensor $\boldsymbol{D} \cdot \overline{\boldsymbol{W}} - \overline{\boldsymbol{W}} \cdot \boldsymbol{D}$ is related to *non-persistence-of-straining*.

Equation (6.9) can be written on the basis of the eigenvectors of $\boldsymbol{D}$ as

$$(\widetilde{\phi}_{\boldsymbol{M}}^{\boldsymbol{D}})^{\boldsymbol{D}} = \boldsymbol{D}^{\boldsymbol{D}} \cdot \overline{\boldsymbol{W}}^{\boldsymbol{D}} - \overline{\boldsymbol{W}}^{\boldsymbol{D}} \cdot \boldsymbol{D}^{\boldsymbol{D}} \quad . \tag{6.10}$$

In possession of $\boldsymbol{D}$ and having calculated $\boldsymbol{M}$ with Eq. (4.23), a system formed by Eq. (6.10) can be solved to find $\overline{\boldsymbol{W}}$ on the basis of $\boldsymbol{D}$. Thus, $\overline{\boldsymbol{W}}$ can be obtained without the direct computation of the angular velocity of the eigenvectors of $\boldsymbol{D}$, $\boldsymbol{\Omega}^{\boldsymbol{D}}$. Moreover, if needed, $\boldsymbol{\Omega}^{\boldsymbol{D}}$ can be easily calculated with $\overline{\boldsymbol{W}}$ and $\boldsymbol{W}$.

The procedure described above was used here to compute the effective rate of rotation, $\overline{\boldsymbol{W}}$, for all cases tested involving objective criteria.

6.3 Preliminary analysis with Newtonian fluids

The chosen criteria will be first applied to relatively simpler flows as a preliminary evaluation before getting into the turbulent viscoelastic channel flow. Following Martins et al. [149], the Arnold-Beltrami-Childress (ABC) flow [154–156] and the 4:1 sudden contraction are assessed.

6.3.1 Unsteady ABC flow

The Arnold-Beltrami-Childress (ABC) flow [154–156] is largely used in the study of chaotic trajectories [157, 158]. A transient version of it was already used by Haller [122] and Martins et al. [149]. The set of equations for the flow field of the unsteady ABC flow is given by trigonometric functions, as follows

$$\begin{aligned} u(y,z,t) &= A(t)\sin(z) + C\cos(y) \quad , \\ v(x,z,t) &= B\sin(x) + A(t)\cos(z) \quad , \\ w(x,y) &= C\sin(y) + B\cos(x) \quad , \end{aligned} \tag{6.11}$$

where $A(t) = A_0 + (1 - e^{-qt})\sin(\omega t)$, with $A_0 = \sqrt{3}$, $q = 0.1$ and $\omega = 2\pi$, while $B = \sqrt{2}$ and $C = 1$. These coefficients were used by Haller [122] and Martins et al. [149] and are also used here. The domain considered here is a cube limited to the interval $[0, 2\pi]$ in every direction.

For all objective criteria considered in this analysis, the relative rate of rotation, $\overline{\boldsymbol{W}}$, was calculated using two consecutive instantaneous velocity fields with a time step of 0.01 seconds.

In Fig. 6.1 the contours of all selected criteria are displayed for the ABC flow. The planes $x = 2\pi$, $y = 2\pi$ and $z = 2\pi$ are evidenced.

Let us start with the non-objective and objective versions of the classic criteria Q and Δ. Generally speaking, the results for both the original and objective versions of the Q-criterion are similar to their corresponding ones for the Δ-criterion. More precisely, both Q^* and $\hat{Q}^*$ present larger hyperbolic and elliptic domains when compared to Δ^* and $\hat{\Delta}^*$, but these domains have the same core regions. Also remarkable, the objective $\hat{Q}^*$ and $\hat{\Delta}^*$ clearly indicate more elliptic regions than observed with the non-objective criteria. Martins et al. [149] stated that this is due to the rotation of the eigenvectors of $\boldsymbol{D}$ near these regions (see Appendix C).

Detailing the analysis, we observe at the three highlighted planes ($x = 2\pi$, $y = 2\pi$ and $z = 2\pi$) that Q^* and Δ^* identify two cores of elliptical dominance and another two of hyperbolic dominance. What changes from one plane to the other and from one criterion to other is their intensities and extensions. At the plane $x = 2\pi$, the Q^*-criterion the elliptic domains are centred around ($y \approx \pi/2, z \approx \pi/2$) and ($y \approx \pi/2, z \approx 3\pi/2$), while the hyperbolic domains are centred around ($y \approx 3\pi/2, z \approx \pi/2$) and ($y \approx 3\pi/2, z \approx 3\pi/2$). Both elliptic and hyperbolic domains at this plane are close to the parabolic value.

Similar behaviour is observed at the plane $y = 2\pi$, with two elliptic regions around ($x \approx \pi/2, z \approx \pi/2$) and ($x \approx 3\pi/2, z \approx \pi/2$), and other two hyperbolic-dominant regions around ($x \approx \pi/2, z \approx 3\pi/2$) and ($x \approx 3\pi/2, z \approx 3\pi/2$). However, both elliptic and hyperbolic regions at this plane are larger and more intense (closer to rigid-body-like and purely-extensional-like motions, respectively).

At $z = 2\pi$, the elliptic and hyperbolic regions observed are more elongated in the y-direction and their intensities are approximately the same of those at plane $y = 2\pi$. The elliptic domain extends around $x \approx \pi/2$, and the hyperbolic domain, around $x \approx 3\pi/2$.

The analysis made for Q^* above also applies to Δ^*. The main difference being though that the latter presents smaller elliptic and hyperbolic domains, although their location coincides with those of Q^*. Because these extrema are smaller, Δ^* indicates more parabolic domains compared to Q^*.

As regards the objective $\hat{Q}^*$ and $\hat{\Delta}^*$, one remarkable difference with respect to their corresponding non-objective versions is that elliptic domains are considerably enhanced while hyperbolic domains are slightly weaken.

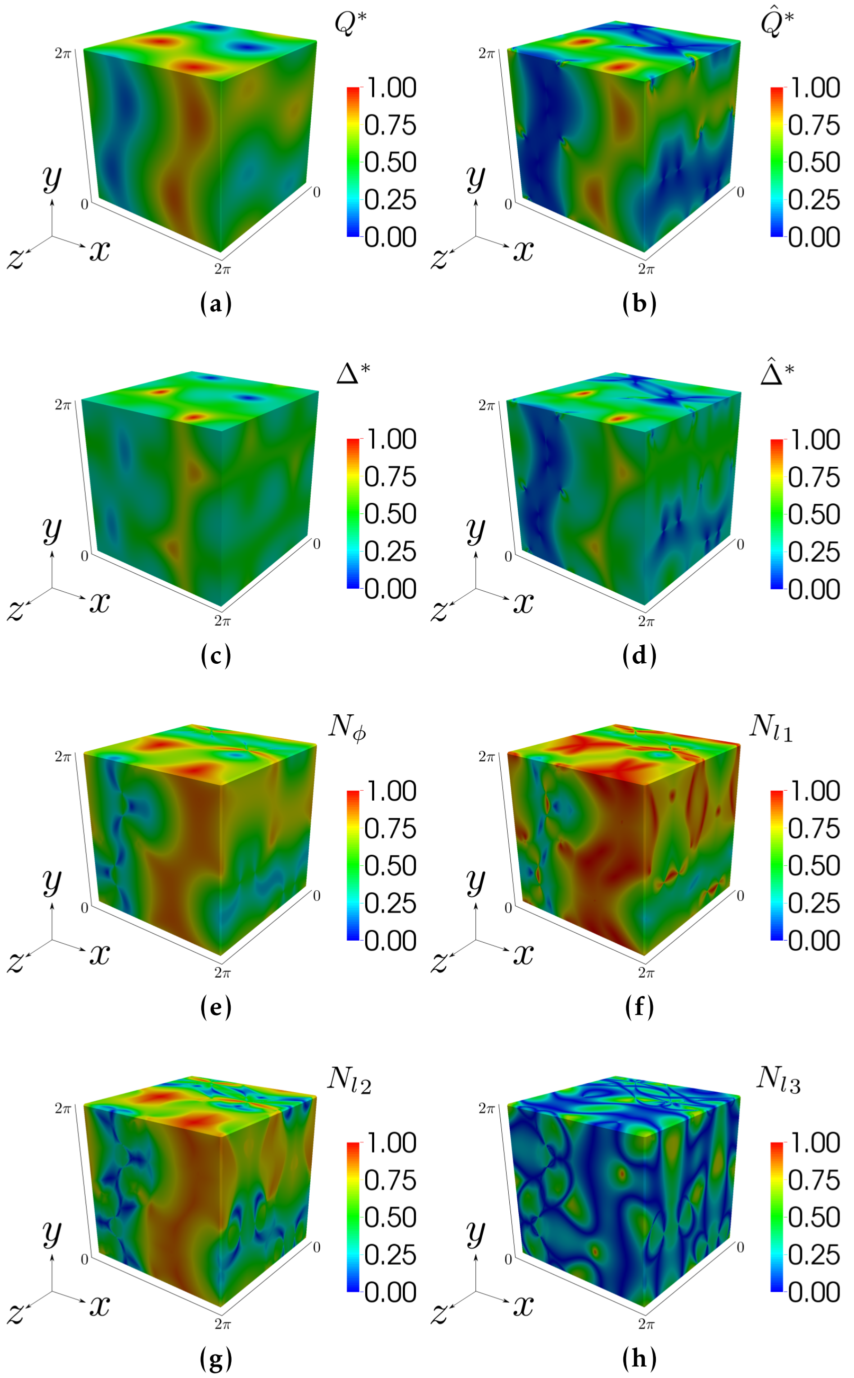

Figure 6.1 – Contour of normalised criteria applied to the ABC flow.

For the isotropic ratio, N_ϕ, at $x = 2\pi$, predominantly hyperbolic domains are observed in the region limited by $\pi \lesssim y \lesssim 2\pi$, whereas slightly elliptic domains are observed in the region limited by $0 \lesssim y \lesssim \pi$. At $y = 2\pi$, two important hyperbolic domains appear at $(x \approx \pi/2, z \approx 3\pi/2)$ and $(x \approx 3\pi/2, z \approx 3\pi/2)$, together with smaller ones and very small elliptic spots as well. Elsewhere at this plane, parabolic domains dominate. At $z = 2\pi$, two hyperbolic domains appear at $(x \approx 3\pi/2, y \approx \pi/2)$ and $(x \approx 3\pi/2, y \approx 3\pi/2)$. Moreover, two triplets of elliptic domains can be found centred around ($x \approx \pi/2, y \approx \pi/2$) and ($x \approx \pi/2, y \approx 3\pi/2$).

Regarding the line anisotropic criterion, N_l, in Fig. 6.1, we see that N_{l1} and N_{l2} behave similarly to the isotropic ratio, N_ϕ, but with more intense straining in the case of N_{l1} and more swirl strength for N_{l2}. It is important to note that some elliptic spots are observed for N_{l1}, specially at the plane $z = 2\pi$, which indicates that, within these regions, the three directions are dominated by rotation. N_{l3} basically shows a mix of parabolic and elliptic modes. However, two hyperbolic spots located at ($x \approx 3\pi/2, y \approx \pi/2$) and ($x \approx 3\pi/2, y \approx 3\pi/2$) indicate purely-extensional motion in the three directions at this regions.

6.3.2 4:1 sudden contraction

The flow in a sudden contraction is largely used in the context of Newtonian and non-Newtonian fluids. It is known for inducing the flow into different states of motion such as shear, extension and rigid-body rotation. Therefore, the sudden contraction can be very useful to evaluate flow classification criteria.

Following Martins et al. [149], a laminar steady-state flow of a Newtonian fluid passing a 4:1 sudden contraction is considered here. The Reynolds number based on the velocity and height at the outlet is equal to 0.043. The algorithm used is the one described by Mompean, Thompson, and Mendes [159] with a mesh of 150×80 grid points respectively in the stream-wise (x) and wall-normal (y) directions.

The results for all selected criteria when applied to the 4:1 contraction are depicted in Fig. 6.2.

The non-objective criteria Q^* and Δ^* capture the fully developed shear region away from the contraction. Approaching the contraction, near the centreline, a large hyperbolic domain is identified not only by Δ^* and Q^*, but by other criteria as well. This is due to the acceleration the fluid undergoes to pass through the contraction. Because of the proximity of the corners, the flow around both sharp corners presents a mix of extensional and rotational motion. These features are captured by all the criteria in Fig. 6.2.

For the objective $\hat{Q}^*$ and $\hat{\Delta}^*$, an additional elliptic domain appears near the centreline, just before the extensional region near the contraction. As commented by Martins et al. [149] and Mompean, Thompson, and Mendes [159], this is an effect of the rotation of the eigenvectors of $\boldsymbol{D}$. The shear flow in the fully developed region imposes the $\pi/4 - 3\pi/4$ directions to the eigenvectors of $\boldsymbol{D}$. In extensional regions, they are aligned with the $0 - \pi/2$ directions. Hence, when passing from shear to extension the eigenvectors of $\boldsymbol{D}$ experience a rotation that may relieve or persist the strain of material filaments therein. Because the eigenvectors of $\boldsymbol{D}$ have to return to the fully developed condition, the same rationale applies for the elliptical domain just after the contraction. It is important

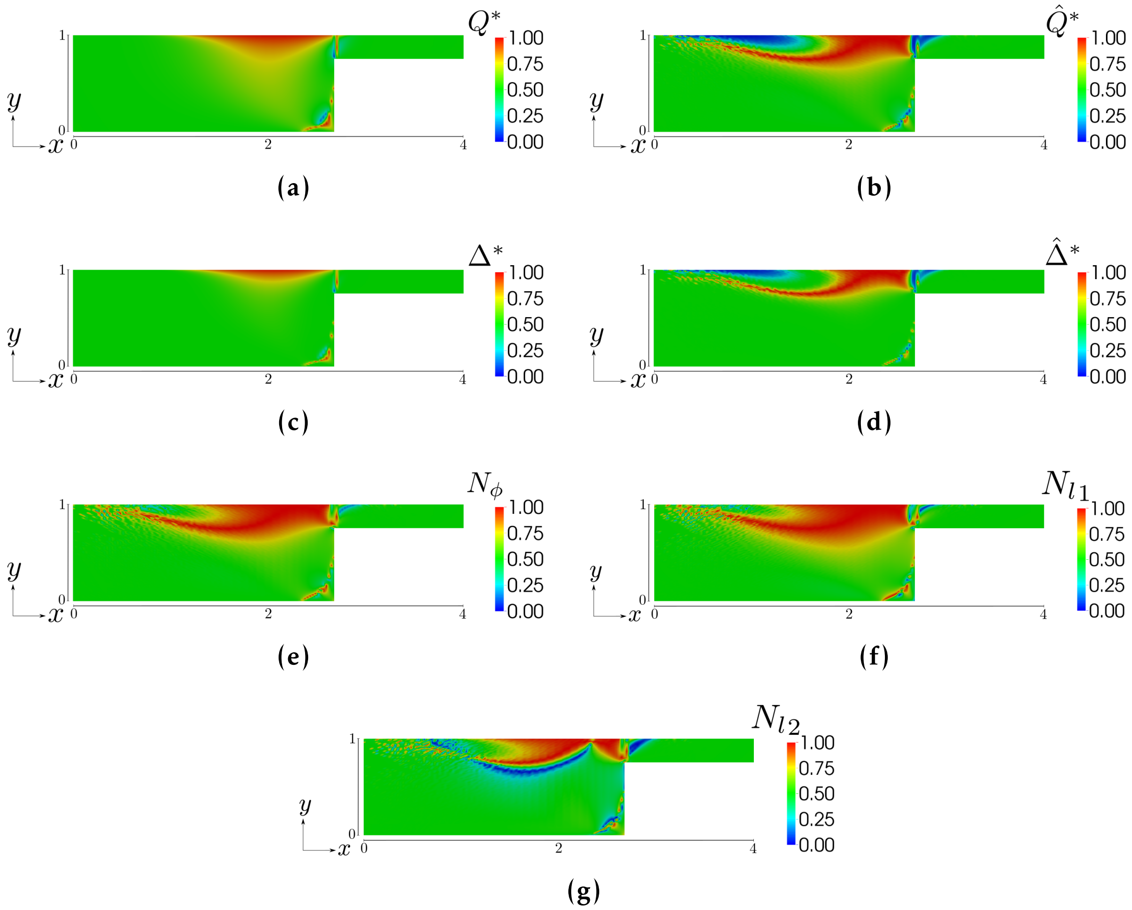

Figure 6.2 – Contour of normalised criteria applied to the flow in a 4:1 sudden contraction.

to remark that these more detailed features of the flow are frame-invariant and not detected by non-objective criteria.

The isotropic criterion, N_ϕ, and the greatest line anisotropic ratio, N_{l1}, behave very similarly. They both start from a totally parabolic domain away from the contraction, typically the case for shear flows. A small elliptic domain appears just after the contraction, which is also related to the rotation of the eigenvectors of $\boldsymbol{D}$. The elliptic region identified by the anisotropic ratio, N_{l2}, just outside of the hyperbolic region around the centreline is also related to this relative rotation. The referred elliptic region is though only detected by the N_{l2}, meaning that only one direction undergoes this swirl-domination.

6.4 Turbulent channel flow of viscoelastic fluid

When applied to turbulent boundary layers flows, the most popular flow classification criteria (Q, λ_2, Δ, λ_{ci}) can identify vortical coherent structures usually called *hairpin vortices* or *horseshoe vortices*. These spatial-time coherent structures evolve in time and were proven to play an important role in several turbulent phenomena such as drag-reduction, jets, waves, mixture, hydro- and aerodynamics, and heat transfer.

The dynamics of these coherent structures have been largely explored in the literature in the context of Newtonian fluids [39, 160]. As commented by Adrian [160], although they can appear singly, hairpins often occur in packets. According to the author, the most plausible explanation for that is the autogeneration mechanism related to such structures. Furthermore, the hairpin packages render a mechanism to transport vorticity, low momentum and turbulent kinetic energy from the wall [160].

Regarding non-Newtonian fluids, previous works [5, 7, 11, 161] have provided evidences of the inhibition of vortex stretching by polymeric effects. Kim et al. [35] explored the changes on the coherent structures in channel flow. The authors noted that in drag-reducing flows, hairpin vortices are weakened and elongated due to the polymer forces that opposes vortical motions.

We evaluate here the results for the criteria Q and Δ in their original (non-objective) and objective versions plus the objective ratios proposed by Thompson [40] applied to the instantaneous velocity fields of both Newtonian and viscoelastic channel flows. The velocity fields were obtained by DNS with the algorithm presented by Thais et al. [19] commented in Part I. The cases considered in the following are the same of those presented in Tab. 5.1. Friction Reynolds numbers equal to 180, 395, 590 and 1000 were assessed. Polymeric effects are taken into account by means of the FENE-P model (based on the original conformation tensor formulation) with maximum polymer chain extensibility, L, equal to 30 or 100 and a friction Weissenberg number, $Wi_{\tau 0}$, equal to 50 or 115, which leads to relative drag reduction from 28.5% 62.3%.

Figure 6.3 present iso-surfaces of elliptic (rotation-dominated) regions by the Q-criterion ($Q = 2$) for several cases. On the left-hand side, Newtonian cases are shown, while the right-hand side contains the viscoelastic cases with $L = 100$ and $Wi_{\tau 0} = 115$. Each line corresponds to a friction Reynolds number, varying from $Re_{\tau 0} = 180$ (first line) to $Re_{\tau 0} = 1000$ (first line). The domain visualised is limited to 4π in the stream-wise direction and 1 (half-gap) in the wall-normal position. The iso-surfaces are coloured with the local intensity of the stream-wise velocity component, u.

The hairpin-like vortical structures can be observed in Fig. 6.3 at all friction Reynolds numbers considered here. They become more numerous in the flow with increasing Reynolds number, even in the viscoelastic case. It is important to note that very similar structures can be observed with the Δ-criterion, but they are not shown here for conciseness.

Comparing the results for Newtonian (left column) and viscoelastic (right column) fluids in Fig. 6.3, it is notable that the amount of hairpins diminishes drastically in the presence of polymers. Since the value of Q is the same ($Q = 2$), this decrease means that there are less regions with that intensity of rotation in the viscoelastic fluid flow.

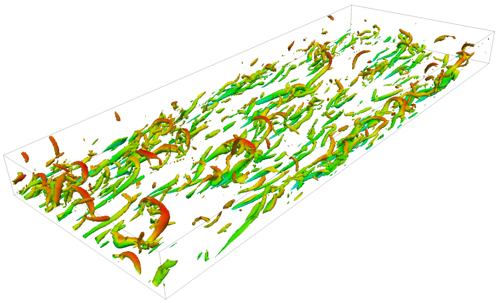

(a) $Re_{\tau 0} = 180$, Newtonian

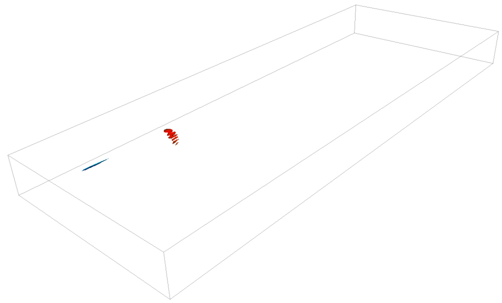

(b) $Re_{\tau 0} = 180$, viscoelastic

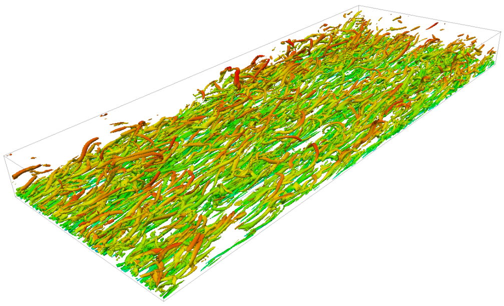

(c) $Re_{\tau 0} = 395$, Newtonian

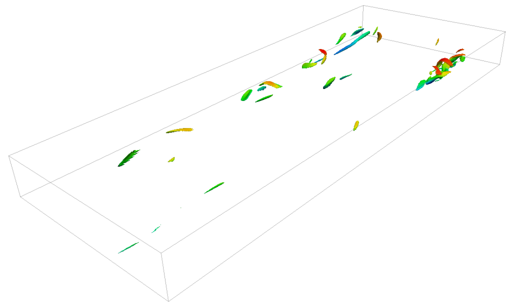

(d) $Re_{\tau 0} = 395$, viscoelastic

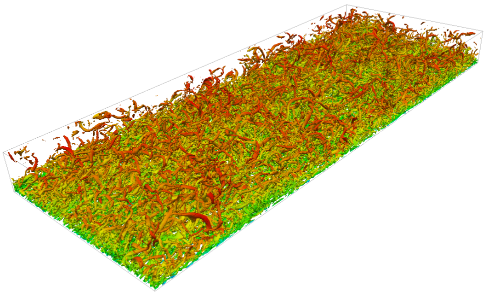

(e) $Re_{\tau 0} = 590$, Newtonian

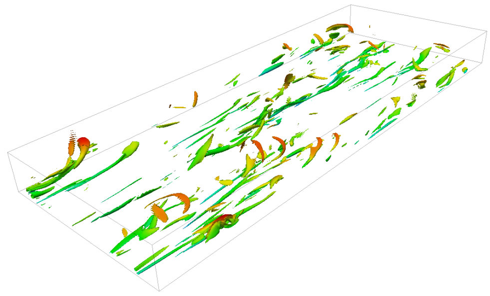

(f) $Re_{\tau 0} = 590$, viscoelastic

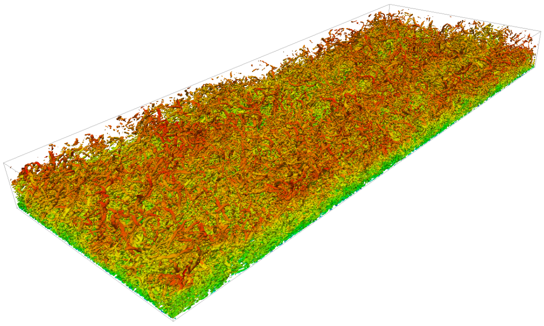

(g) $Re_{\tau 0} = 1000$, Newtonian

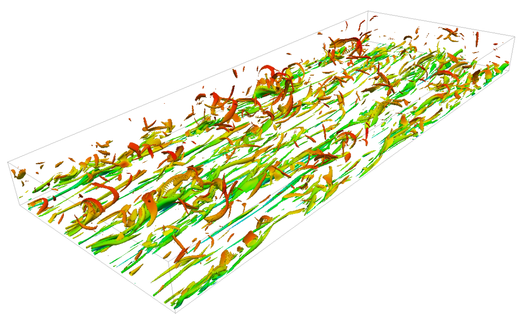

(h) $Re_{\tau 0} = 1000$, viscoelastic

Figure 6.3 – Iso-surfaces of $Q = 2$ (elliptic regions) from $Re_{\tau 0} = 180$ (first line) to $Re_{\tau 0} = 1000$ (last line). Newtonian cases are on the left-hand side and viscoelastic cases ($L = 100$ and $Wi_{\tau 0} = 115$) are on the right-hand side. The displayed domain is restricted to $0 \leq y \leq 1$ and $0 \leq x \leq 4\pi$. Iso-surfaces are coloured with the local intensity of u.

This represents then the weakening of vortical structures in polymer solution already reported in the literature [35]. As previously observed as well, for the same friction Reynolds number, these vortical structures are also more elongated.

Now, all normalised criteria will be compared in order to evaluate the influence of polymers from the perspective of objective criteria. Figure 6.4 displays the comparison for a Newtonian fluid at $Re_{\tau 0} = 1000$. The iso-surfaces of all normalised criteria at a value of 0.25, representing elliptic domains.

It is notable that the elliptic domains detected by normalised version of the Q-criterion are less organised in space than those of its non-normalised version (see Figs. 6.3g and 6.4a). On one hand, this lack of organisation in the normalised criteria precludes the visualisation of the hairpin vortices. On the other hand, the effects concerning the addition of polymers are equally observed as we will see further on.

The criteria Q^* and Δ^* present similar behaviour with lots of dispersed small elliptic domains. The main difference between these two criteria is that the Δ^*-criterion presents less intense elliptic domains, which is in accordance with the previous results. Their objective versions (criteria $\hat{Q}^*$ and $\hat{\Delta}^*$) show even closer relation, but detect much more elliptic domains than their non-objective versions. This behaviour also corroborates previous results.

The results for the isotropic criterion, N_ϕ, are comparable to those of Q^*. The elliptic regions are very dispersed and even smaller than those of the non-objective Q-criterion. Regarding the line anisotropic criteria, N_l, the results for N_{l1} show that there are very few elliptic domains in which the rotational behaviour is predominant in all three directions. However, according to N_{l2}, the number and location of domains that are elliptic-dominated in at least two directions is comparable to those detected by the criteria $\hat{Q}^*$ and $\hat{\Delta}^*$. Finally, as far as N_{l3} is concerned, we see lots of regions in which at least one directions is dominated by rotation.

Let us now evaluate the effect of polymers by looking at the iso-surfaces at the same value (0.25) used in Fig. 6.4, but for a viscoelastic fluid with $L = 100$ and $Wi_{\tau 0} = 115$ at $Re_{\tau 0} = 1000$. The results for this case is shown in Fig. 6.5 for all normalised criteria.

It is remarkable that the normalised criteria predict the same effects in the presence of elasticity. Even if the elliptic regions are not as spatially organised as in Fig. 6.3 (regarding the non-objective and non-normalised criteria), the general tendency of weakening and growth is also noticed in Fig. 6.5. One can take, for instance, the objective isotropic criterion, N_ϕ, by comparing Figs. 6.4e and 6.5e. Note that the elliptic domains are bigger in the latter but there are more blank spaces within the domain, indicating a decrease in the amount of elliptic regions and a tendency to combine with each other. The same behaviour applies to all other normalised criteria.

This tendency of the elliptic domains to join with each other in the presence of polymers can also be observed in Fig. 6.6. This figure contains the contours in plane

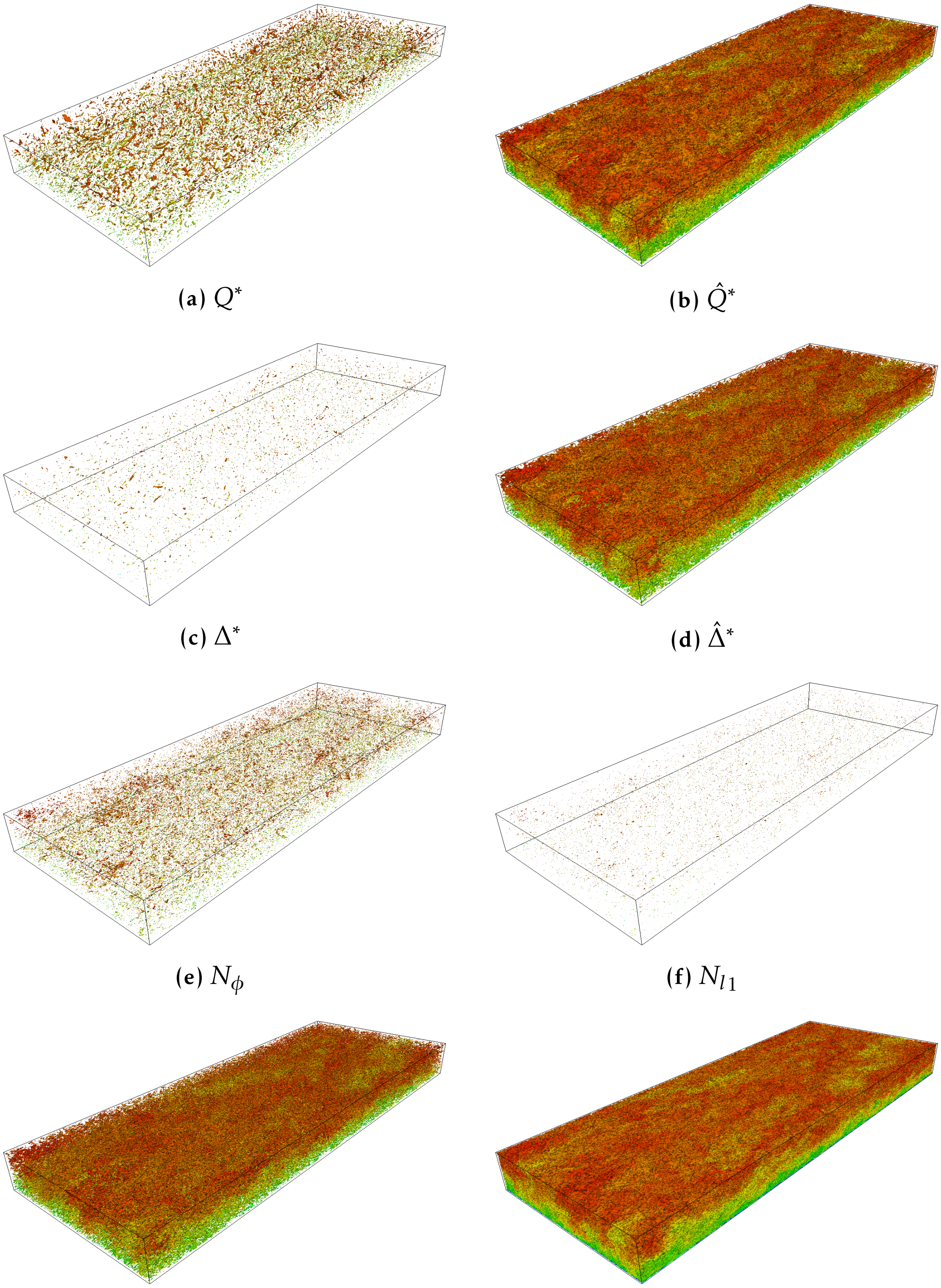

(a) Q^* (b) $\hat{Q}^*$

(c) Δ^* (d) $\hat{\Delta}^*$

(e) N_ϕ (f) N_{l1}

(g) N_{l2} (h) N_{l3}

Figure 6.4 – Iso-surfaces of normalised criteria at the value of 0.25 (elliptic regions) at $Re_{\tau 0} = 1000$ for Newtonian fluid. The displayed domain is restricted to $0 \leq y \leq 1$ and $0 \leq x \leq 4\pi$. Iso-surfaces are coloured with the local intensity of u.

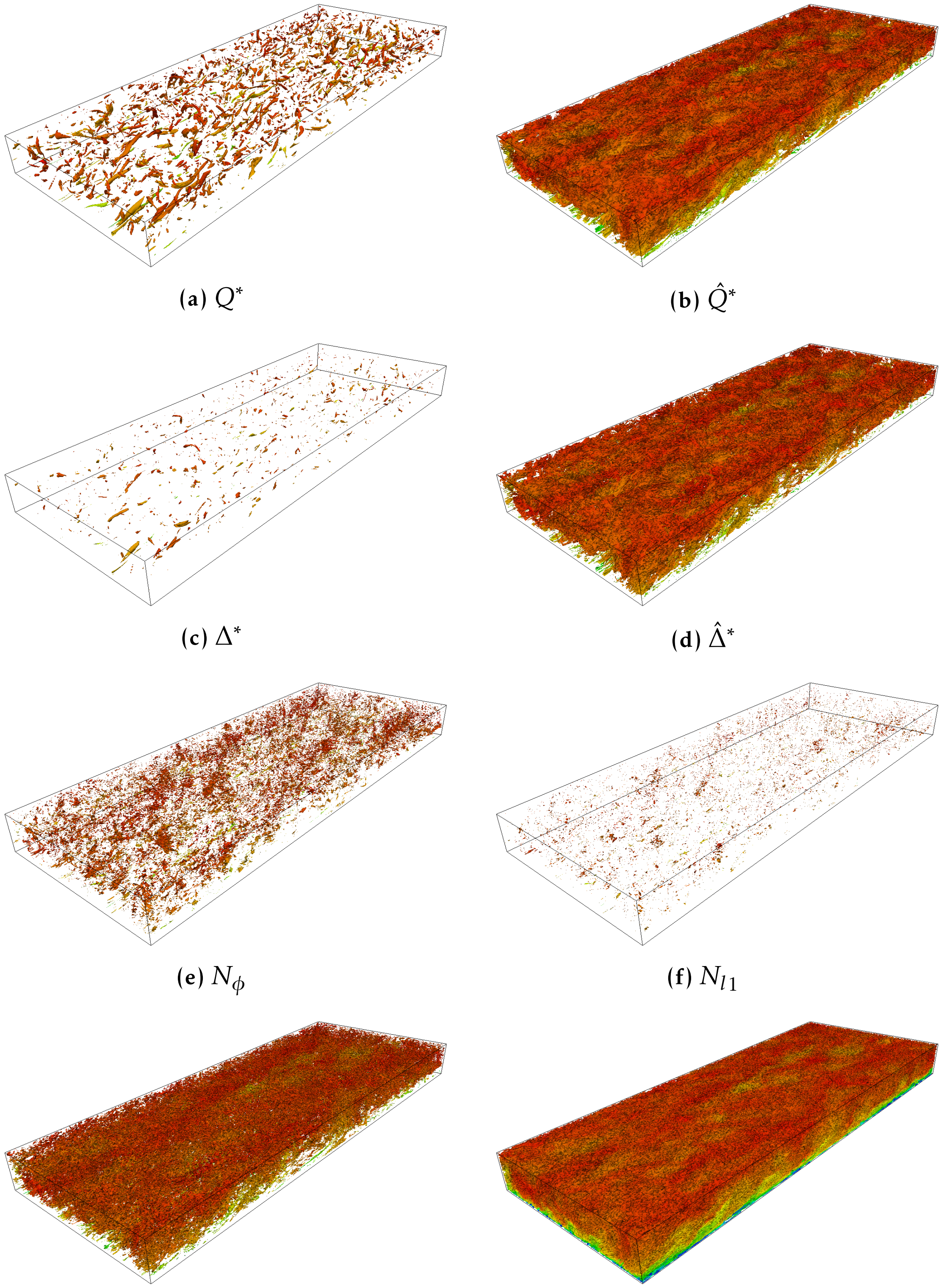

(a) Q^* **(b)** $\hat{Q}^*$

(c) Δ^* **(d)** $\hat{\Delta}^*$

(e) N_ϕ **(f)** N_{l1}

(g) N_{l2} **(h)** N_{l3}

Figure 6.5 – Iso-surfaces of normalised criteria at the value of 0.25 (elliptic regions) at $Re_{\tau 0} = 1000$ for viscoelastic fluid ($L = 100$ and $Wi_{\tau 0} = 115$). The displayed domain is restricted to $0 \leq y \leq 1$ and $0 \leq x \leq 4\pi$. Iso-surfaces are coloured with the local intensity of u.

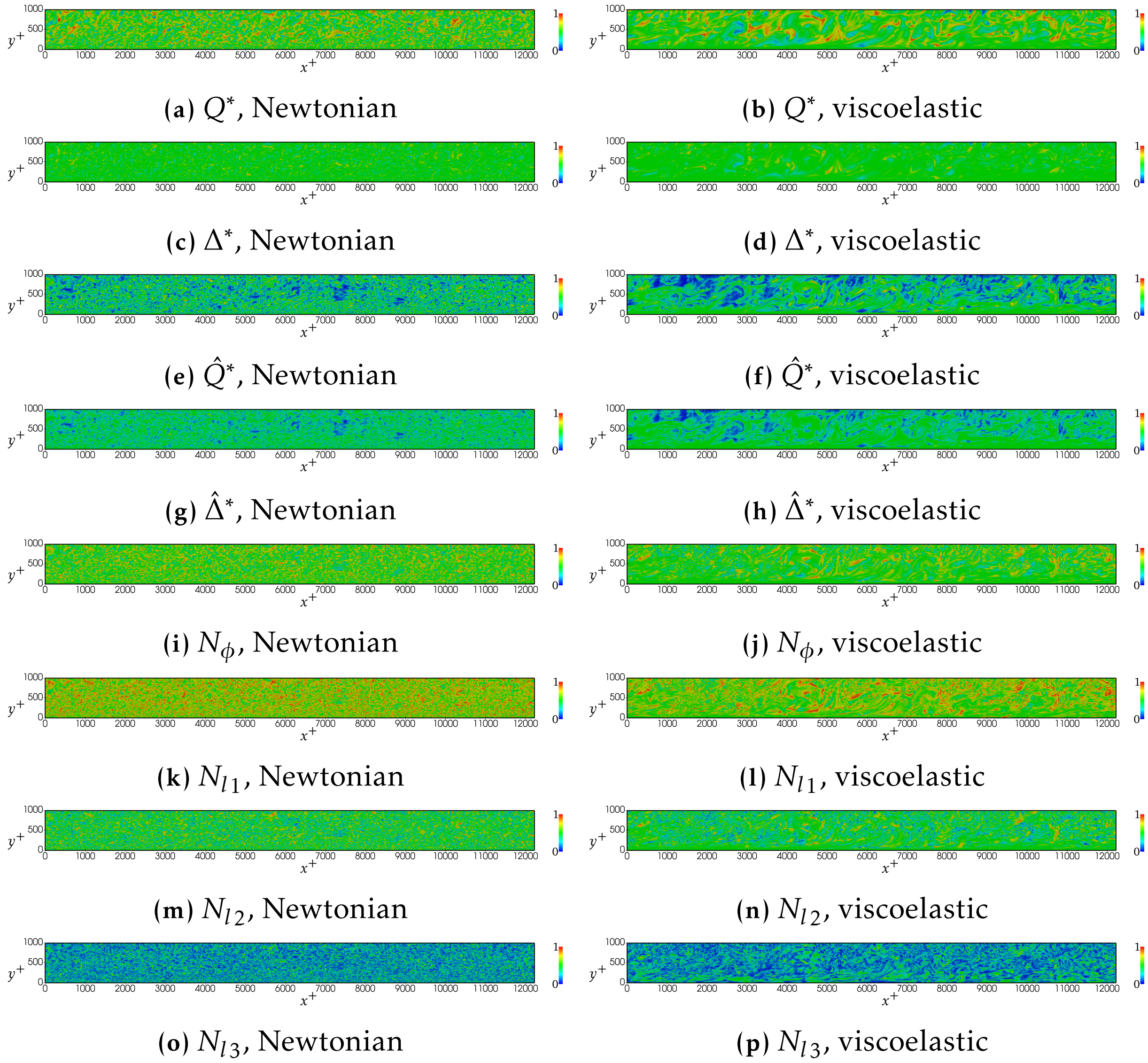

(a) Q^*, Newtonian **(b)** Q^*, viscoelastic

(c) Δ^*, Newtonian **(d)** Δ^*, viscoelastic

(e) $\hat{Q}^*$, Newtonian **(f)** $\hat{Q}^*$, viscoelastic

(g) $\hat{\Delta}^*$, Newtonian **(h)** $\hat{\Delta}^*$, viscoelastic

(i) N_ϕ, Newtonian **(j)** N_ϕ, viscoelastic

(k) N_{l1}, Newtonian **(l)** N_{l1}, viscoelastic

(m) N_{l2}, Newtonian **(n)** N_{l2}, viscoelastic

(o) N_{l3}, Newtonian **(p)** N_{l3}, viscoelastic

Figure 6.6 – Contours at $z = 3\pi/4$ of all normalised criteria applied to: (left column) Newtonian and (right column) viscoelastic ($L = 100$ and $Wi_{\tau 0} = 115$) fluid at $Re_{\tau 0} = 1000$. The displayed domain is restricted to $0 \le y \le 1$ and $0 \le x \le 4\pi$.

$z = 3\pi/4$ (middle channel in the span-wise direction) for all the normalised criteria applied to the same flow fields.

The colour scheme in Fig. 6.6 follows the normalised scale of the criteria. Blue stands for the value of zero, corresponding to extreme elliptic mode (rigid-body motion). Red indicates the value of 1 associated with extreme hyperbolic mode (purely extensional motion). The intermediate value of 0.5 is represented by the green colour and indicates parabolic domains.

The non-objective versions of the criteria Q and Δ are presented in the first two lines. At this plane, the Q-criterion presents predominant (near-)parabolic modes, meaning that strain and rotation rates are mostly in equilibrium. Dispersed hyperbolic and elliptic domains do appear, with a slightly tendency towards hyperbolic modes for both Newtonian and viscoelastic cases. Precisely for the latter, each subdomain (hyperbolic, parabolic and elliptic) seems to be less dispersed, therefore composing larger subdomains. Regarding the Δ-criterion a strongly parabolic behaviour is indicated for both fluids.

The next two lines in Fig. 6.6 (3rd and 4th lines) shows the objective versions of Q and Δ. They both follow similar trends, presenting basically parabolic and elliptic modes that are highly dispersed for the Newtonian case and less dispersed for the viscoelastic case. In fact, for viscoelastic cases, a slight trend to have parabolic modes near the wall and elliptic modes near the centreline is observed.

The fifth line in Fig. 6.6 depicts the results for the isotropic ratio, N_ϕ. Generally speaking, it behaves much the same way as the Q^*. Lines $6-8$ display the results for the line anisotropic ratio, N_l. The behaviour of N_{l1} and N_{l2} are comparable with that of Q^*, but the former clearly presents hyperbolic dominance while the latter is slightly elliptic-dominated. N_{l3} is elliptic-dominant and is generally at most parabolic, opposing to N_{l1} that is at least parabolic. Since N_{l2} shows more elliptic modes, according to the N_l-criterion, there are two direction presenting elliptic-dominance and another direction that is hyperbolic-dominant. The same tendency of decreasing dispersion for the viscoelastic case is observed for N_l, more pronouncedly for N_{l1} and N_{l3}.

In the following, the effect of Reynolds number and elasticity will be evaluated using the average on wall-normal plans of the normalised criteria considered here.

6.4.1 Effect of Reynolds number

First, let us analyse the effect of the Reynolds number for a Newtonian fluid. Figure 6.7 shows the plane-averaged profiles of normalised non-objective criteria for friction Reynolds numbers equal to 180, 395, 590 and 1000.

In a general sense, Reynolds number clearly does not play an important role in the average profile of the criteria. Regardless of the Reynolds numbers analysed, a parabolic mode (value of 0.5, characteristic of a laminar flow) is observed from the wall until $y^+ \approx 20$. There after, the Q-criterion present slightly hyperbolic values, while the Δ-criterion have even weaker elliptic tendencies that are, in fact, very near from the parabolic limit.

In view of this apparent independence with respect to the Reynolds number and for conciseness, Fig. 6.8 concerning the objective versions of the criteria Q and Δ depicts only the lowest and highest friction Reynolds number ($Re_{\tau 0} = 180$ and 1000, respectively).

The profiles for the objective versions of Q and Δ also depart from a parabolic mode at the wall, but after $y^+ \approx 8$, they both present more pronounced elliptic modes

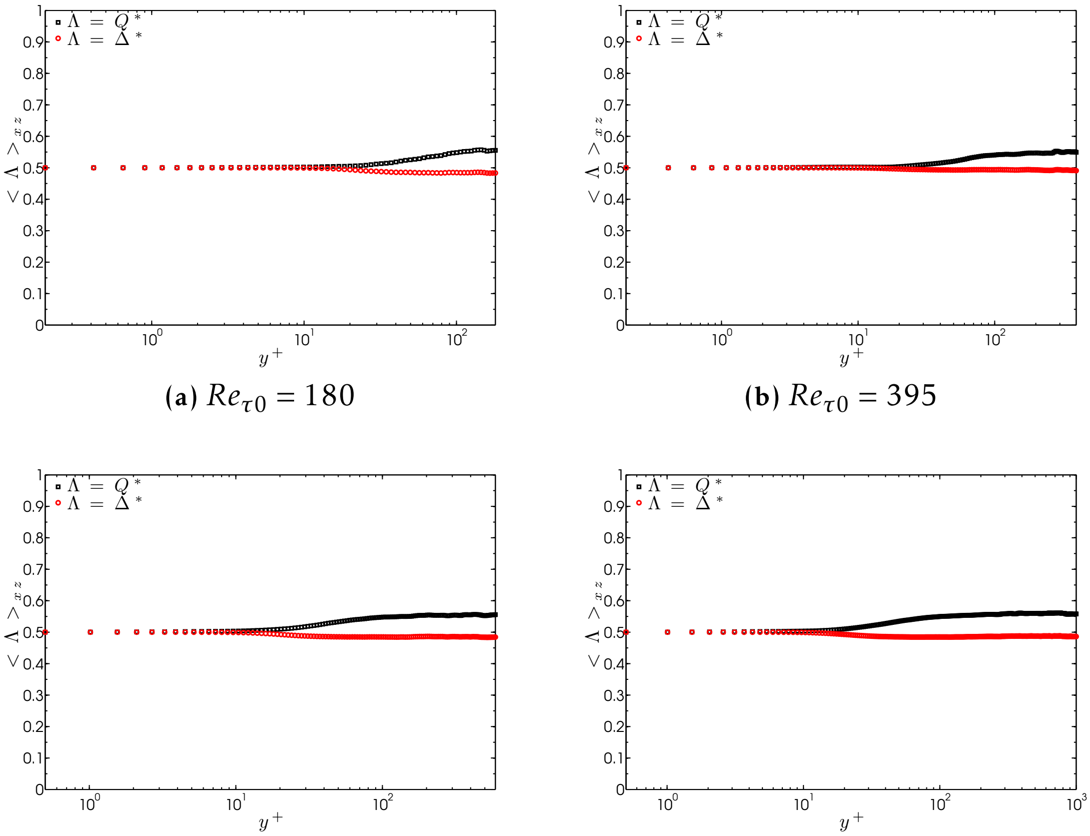

(a) $Re_{\tau 0} = 180$ (b) $Re_{\tau 0} = 395$

(c) $Re_{\tau 0} = 590$ (d) $Re_{\tau 0} = 1000$

Figure 6.7 – Profiles of the plane-averaged non-objective criteria for Newtonian fluid at: (a) $Re_{\tau 0} = 180$; (b) $Re_{\tau 0} = 395$; (c) $Re_{\tau 0} = 590$; and (d) $Re_{\tau 0} = 1000$.

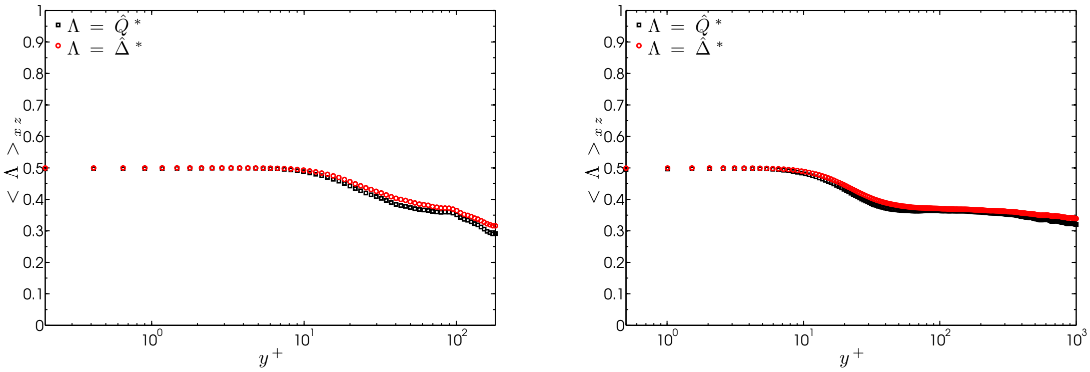

(a) $Re_{\tau 0} = 180$ (b) $Re_{\tau 0} = 1000$

Figure 6.8 – Profiles of the plane-averaged objective criteria for Newtonian fluid at: (a) $Re_{\tau 0} = 180$; and (b) $Re_{\tau 0} = 1000$.

apparently with an asymptotic behaviour tending to 0.3. It means that, from this objective perspective, more elliptic modes are identified comparing to the original (non-objective) versions of these criteria. In addition, we can notice that the objective versions are more coincident. This is in accordance with the trends found by Martins et al. [149] for the ABC and 4:1 sudden contraction.

Still concerning the effect of Reynolds number for a Newtonian fluid, Fig. 6.9 contains the profiles of the objective ratios N_ϕ and N_l for $Re_{\tau 0} = 180$ and 1000.

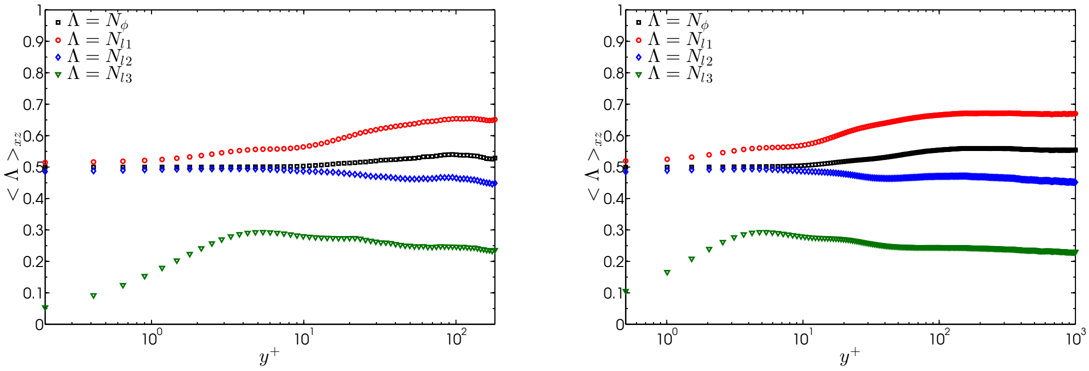

(a) $Re_{\tau 0} = 180$ **(b)** $Re_{\tau 0} = 1000$

Figure 6.9 – Profiles of the plane-averaged objective ratios for Newtonian fluid at: (a) $Re_{\tau 0} = 180$; and (b) $Re_{\tau 0} = 1000$.

Once again, the Reynolds number does not show any pronounced effect on the average profiles of the criteria. The isotropic ratio, N_ϕ, has a behaviour comparable to that of Q^*, while the line anisotropic ratio N_{l2} behaves similarly when compared to Δ^* (see Q^* and Δ^* in Fig. 6.7).

Regarding the line anisotropic ratio, N_{l1} is predominantly greater than 0.5 and N_{l3} principally less than 0.5. This means that, on average, there are no regions where extension or rotation dominates in all three directions. By analysing the quantity N_{l2}, we conclude that in the viscous sublayer ($y^+ \leq 5$), there is a one direction that is swirl-dominated, another that is extensional-dominant, and a neutral (parabolic) direction. Closer to the centreline, asymptotic behaviour is observed for all three N_l quantities. N_{l1}, N_{l2} and N_{l3} tend, respectively, to ≈ 0.7, 0.45 and 0.225. This indicates that, away from the near-wall region, there is one direction of extension-dominance, and two others of swirl-dominance. It is worth noticing that such behaviour was already reported by Martins et al. [138].

6.4.2 Effect of elasticity

It was shown above that the Reynolds number does not play a relevant role in the present analysis. Therefore, for the evaluation of the elastic effect, only the results for Reynolds $Re_{\tau 0} = 1000$ will be presented. At this friction Reynolds number, there are results for two elastic levels: one with maximum chain extensibility $L = 30$ and friction Weissenberg number $Wi_{\tau 0} = 50$, leading to a relative drag reduction of 30% and another with $L = 100$ and $Wi_{\tau 0} = 115$ yielding 58% of relative drag reduction.

The elastic effect can be observed in Fig. 6.10 below containing the results for all the criteria at $Re_{\tau 0} = 1000$. As regards the non-objective and objective versions of the criteria Q and Δ (Figs. 6.10a-6.10d), when compared to the their respective corresponding Newtonian cases (Figs. 6.7d and 6.8b), they all seem to be have the parabolic subdomain close to wall extended towards the centreline. This is more evident for the objective criteria (second line) which tend to more accentuated elliptic mode with increasing y^+. While in the Newtonian case the parabolic-dominant subdomain ended at $y^+ \approx 8$, for the low-elasticity case (left), it goes until $y^+ \approx 10$ and for the high-elasticity (right) it extends until $y^+ \approx 30$. Thus, according to the criteria Q and Δ in both their non-objective and objective versions, increasing the elasticity leads to an augmentation of the parabolic subdomains near the wall.

The profiles for the objective ratios (Figs. 6.10e and 6.10f) have behave similarly to the correspondent Newtonian curves showed in Fig. 6.9b. In general, the curves have a first behaviour starting at the wall, an asymptotic behaviour away from the wall and a transition region usually starting at the buffer layer ($5 \leq y^+ \leq 30$) and achieving the beginning of the log-law region ($y^+ > 30$). This general behaviour is maintained, but basically, the y^+ positions of this transition region is shifted away from the wall with increasing elasticity.

Since the transition region that connects the near-wall behaviour with the centreline asymptote coincides with the buffer layer and is shifted away from the wall, a connection can be done here with the thickening of buffer layer, observed experimentally [162, 163] and numerically [5, 8, 11, 12] for polymer-induced drag-reducing flows. It is worth noticing that this effect is also predicted by the two major theories on the drag reduction mechanism [86, 88].

6.5 Concluding remarks

The main propose here was to provide a new perspective for the phenomenon of turbulent drag reduction grounded in the principles of objectivity. Criteria that enjoy objectivity are preferable due to its independence from the reference frame, leading to more solid and general conclusions.

Two classic flow classification criteria were considered here: the Q-criterion by Hunt, Wray, and Moin [36] and the Δ-criterion by Chong, Perry, and Cantwell [37]. Other classic criteria such as λ_2 [38], λ_{ci} [39] and $\lambda_{cr}/\lambda_{ci}$ [127] were discarded because of either limitations on the classification of hyperbolic regions (λ_{ci} and $\lambda_{cr}/\lambda_{ci}$) or inconsistent assumptions that lead to undetermined choices when considering polymer solutions (λ_2).

Objective versions of the two classic criteria considered were also tested. The objectivity is taken into account by replacing the rotation-rate tensor, $\boldsymbol{W}$, by the effective

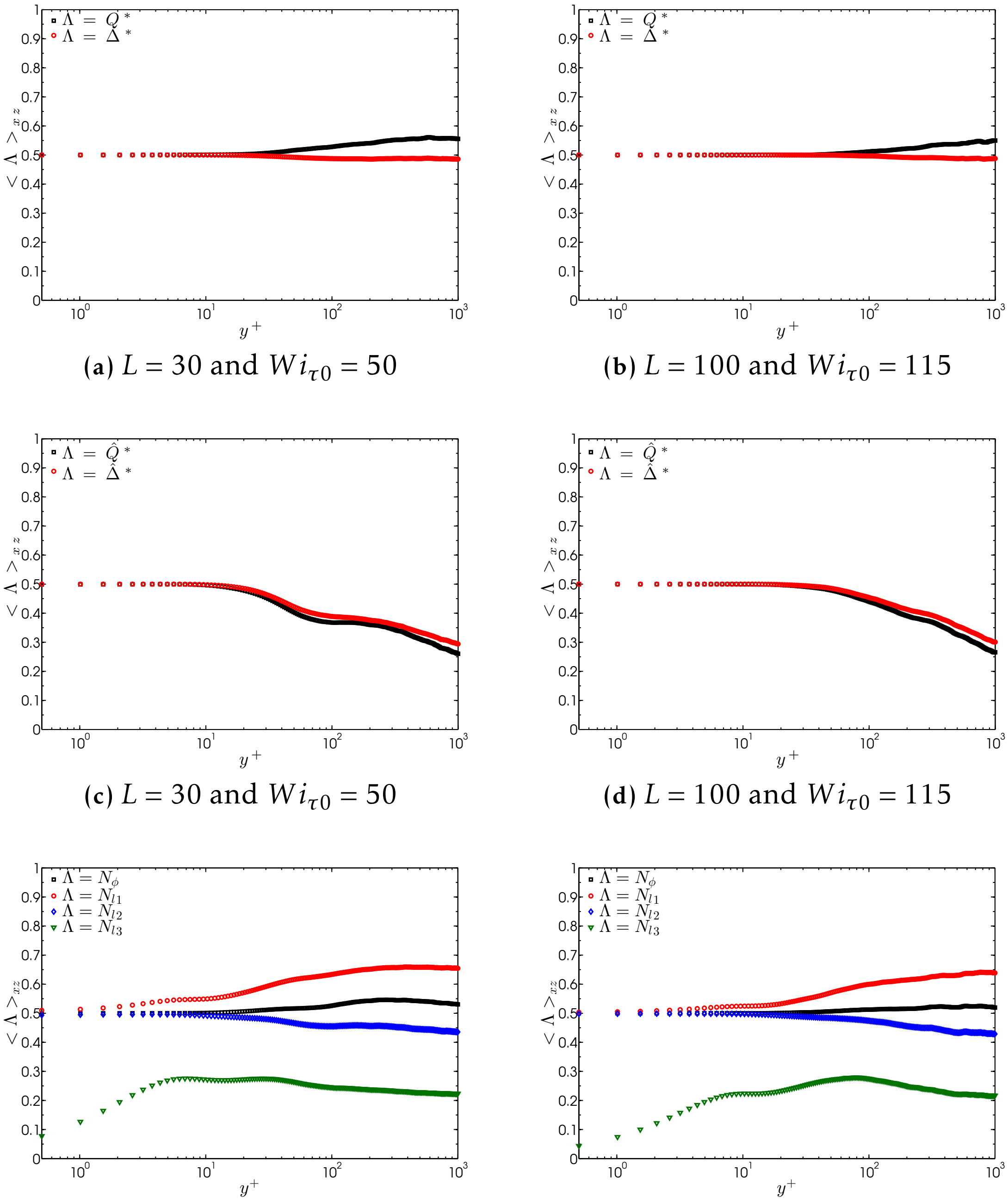

(a) $L = 30$ and $Wi_{\tau 0} = 50$ (b) $L = 100$ and $Wi_{\tau 0} = 115$

(c) $L = 30$ and $Wi_{\tau 0} = 50$ (d) $L = 100$ and $Wi_{\tau 0} = 115$

(e) $L = 30$ and $Wi_{\tau 0} = 50$ (f) $L = 100$ and $Wi_{\tau 0} = 115$

Figure 6.10 – Profiles of the plane-averaged criteria for two viscoelastic fluids (left column: $L = 30$ and $Wi_{\tau 0} = 50$; right column: $L = 100$ and $Wi_{\tau 0} = 115$) at $Re_{\tau 0} = 1000$: non-objective criteria in the first line ((a) and (b)); objective criteria in the second line ((c) and (d)); and objective ratios in the last line ((e) and (f)) .

rate-of-rotation tensor, $\overline{\boldsymbol{W}}$, the rotation rate relative to the angular velocity of the eigenvalues of the strain-rate tensor, $\boldsymbol{D}$.

The objective isotropic and line anisotropic criteria proposed by Thompson [40] were also assessed. These criteria are based on the concept of (non-)persistence-of-straining. Also, just like the criterion by Haller [122], it consists of a measure of how much the tendency suggested by the strain rate is defied.

All the selected criteria were applied to three flows: the unsteady version of the analytical ABC flow, the laminar flow of a Newtonian fluid through a 4:1 sudden contraction and the turbulent channel flow of both Newtonian fluid and polymer solutions. For all theses cases, objective criteria provided richer information about the kinematics of the flow and these informations are independent from the reference frame.

The most important results regards the turbulent channel flow of polymer solutions. By analysing iso-surfaces, wall-normal cuts and spatial averages of the criteria, some interesting observations were possible. In accordance with previous work in the literature [35], the weakening and elongation of elliptic (vortical) regions was noticed for viscoelastic fluids. When analysed by means of normalisation, the iso-surfaces of the classic criteria are not as spatially organised as the ones captured by their classic (non-normalised) version. Consequently, no hairpin vortices are observed with normalised criteria. However, the effects of elasticity are also in accordance with previous results. The elliptic regions observed in the presence of polymers are less frequent and bigger than the ones obtained for Newtonian fluid. These trends increase with increasing elasticity.

The averaged profiles usually show two distinct behaviour: one in the vicinity of the wall and another in the log-law region. The location of the transition zone between these two regions seems to be related with the buffer layer. The upper limit of this transition zone is shifted away with increasing elasticity, indicating the detection of the predicted thickening of the buffer layer in polymer induced drag-reducing flows.

General conclusions and further work

The polymer-induced drag reduction phenomenon has been addressed here in two different approaches. Firstly, root-based formulations to the conformation tensor were evaluated with the aim of preserving its positiveness. The original algorithm for DNS of turbulent channel flow of FENE-P fluid based on the standard conformation tensor formulation with global artificial diffusion has been modified to consider the square-root [33] and kernel root^k [34] formulations. The goal was to evaluate the performance of these transformations under wall-bounded turbulent flows and the need for maintain or not artificial diffusion.

According to the present simulations, the square-root and kernel transformations do preserve the positiveness of the conformation tensor, but other limitations have been found. Firstly, they both needed the inclusion of artificial diffusion to remain stable. Otherwise, simulations rapidly diverge because of the loss of boundedness of the conformation tensor.

The damping effect of artificial diffusion in the root-based formulations are more evident, leading to a significant underestimation of the polymer stretching and, consequently, of the relative drag reduction. The physical tendencies are however in accordance with benchmark results. Decreasing the artificial diffusivity would leave to better prediction of the relative drag reduction, but when proceeding so, another constraint for the conformation tensor is violated.

Before achieving values for which artificial diffusivity leads to relative drag reduction that are comparable to the usual results in the literature, the algorithm in the root-based formulations diverges, still due to unbounded values of the conformation tensor. Therefore, in contrast with the original standard formulation, the addition of artificial diffusion in the root-based formulations does not guarantee numerical stability. A suggestion to overcome this new limitation is presented further on.

It is worth noticing that, in the kernel root^k formulation, root degrees other than 2 can be tested. The results suggest that the higher the degree k of the root^k formulation, the stronger the effect of stress diffusion on underestimating the drag reduction is.

Another important verification concerns the computational time needed by each formulation. The kernel transformation showed to be about 5 times slower than the standard (conformation-tensor-based) formulation. On the other hand, the computing extra-cost of the square-root formulation with respect to the standard formulation is only about 10%. In the context of turbulent drag-reducing flows, the square-root formulation showed to be much more advantageous with respect to the kernel root^k formulation, basically because it is slightly easier to adapt when departing from a code based on the conformation tensor, and, more importantly, because it leads to the same benefits as the kernel root^k formulation but being about 5 times faster with computation times very close to the ones encountered for the original formulation.

The second study performed regards the evaluation of the influence of polymeric terms on the composition of some flow classification criteria and the advantages of using objective flow classification criteria. To evaluate that, some selected criteria have been applied to the instantaneous fields of turbulent Newtonian and viscoelastic channel flows at friction Reynolds number from 180 up to 1000.

To investigate the contribution of polymeric terms to the composition of the criteria Q and λ_2, the symmetric part of the evolution equation for the strain-rate tensor was considered. It has been shown that the assumption of dropping the time-dependent and viscous terms in the derivation of the λ_2-criterion [38] is inconsistent and should be reconsidered. The referred terms are not negligible and actually have tendencies that, on average, are contrary to that imposed by the Hessian of the pressure. Moreover, when considering viscoelastic cases, the choice of how to take into account the contributions of polymers is not clear at all.

Furthermore, it was verified that the only term contributing to the composition of the Q-criterion [36] applied to Newtonian fluids is the one related to the Hessian of the pressure. For polymer solutions, the intensities of all terms (including the polymeric one) is drastically lowered with increasing elasticity, which indicates that the weakening of vortices in polymer-induced drag-reducing flows is not a direct consequence of the contribution of the polymeric stress on its own, but the result of non-linear interactions between the polymer and the flow dynamics.

As regards objective flow classification criteria, their independence to reference frame lead to more general conclusions on the flow kinematics. The results concerning the objective criteria considered here indicate observations of the thickening of the buffer layer, an effect that is predicted by the major theories on drag reduction [86, 88].

Finally, based on the experience documented here, some ideas for future work are suggested in the following:

- Positiveness of the conformation tensor in turbulent drag-reducing channel flow

  - ***Implicit algorithm***
    As stated by Vaithianathan and Collins [26], solving the equations implicitly may help to avoid unbounded values for the conformation tensor that appear due to numerical errors and lead to divergence. Even if the price to pay is

slowing the algorithm, treating some strategical terms of the equation (such as the stretching term of the form $\boldsymbol{c}\cdot\nabla\boldsymbol{u}+\nabla\boldsymbol{u}^T\cdot\boldsymbol{c}$ or the polymer stress) may alleviate this issue. Is the gain on stability worthy regarding the increase in computational time? That is one question that arises here.

– ***Mapping***

The simulations performed here suggest that, in the context of turbulent viscoelastic channel flows, root-type transformations do preserve the positiveness of the conformation tensor, but do not guarantee its boundedness. In fact, unboundedness was the main reason of unsuccessful runs during the present work. Following Housiadas, Wang, and Beris [17], maybe mapping the conformation tensor and/or its transformed conformation (kth-root) could also guarantee boundedness of the conformation tensor, allowing to go further down for the value of artificial diffusivity.

- Classification of turbulent drag-reducing flow

  – ***Composition of M***

  The idea of evaluating the contribution of the terms composing a criterion could be applied to objective criteria by Thompson [40]. The main idea behind these criteria is the *in-phase-out-of-phase* decomposition of the strain acceleration tensor, $\boldsymbol{M}$, with respect to the strain rate tensor, $\boldsymbol{D}$. But $\boldsymbol{M}$ can be written either as $\boldsymbol{M}=\dot{\boldsymbol{D}}+\boldsymbol{D}\boldsymbol{L}+\boldsymbol{L}^T\boldsymbol{D}$ or $\boldsymbol{M}=\boldsymbol{D}'+2\boldsymbol{D}^2+\boldsymbol{D}\overline{\boldsymbol{W}}-\overline{\boldsymbol{W}}\boldsymbol{D}$. Therefore, one could apply the *in-phase-out-of-phase* decomposition to the terms that compose $\boldsymbol{M}$ and analyse how they contribute to the criteria.

  – ***Different normalisation***

  The normalisations used here to enable the comparison of the same intensities regarding vortical motion for different criteria suggested that the mathematical relation chosen can change the shape of the visualised structures, even if the physics behind is preserved. For instance, the Q-criterion enables the visualisation of the classic hairpin vortices. Nevertheless, these vortices are no longer observed with its normalised version. Therefore, the seek for other mathematical relations capable of normalising the criteria with minor changes is suggested for all the criteria used here, including the objective ratios.

Bibliography

[1] R. B. Bird and C. F. Curtiss. "Fascinanting polymeric liquids". In: *Physics Today* 38 (1984), pp. 36–43 (cit. on p. 1).

[2] R. B. Bird, R. C. Armstrong, and O. Hassager. *Dynamics of Polymeric Liquids. Fluid mechanics*. 1st ed. Vol. 1. John Wiley & Sons, 1977 (cit. on pp. 1, 22).

[3] M. D. Graham. "Drag Reduction in Turbulent Flow of Polymer Solutions". In: *Rheology Reviews* (2004), pp. 143–170 (cit. on p. 2).

[4] C. M. White and M. G. Mungal. "Mechanics and Prediction of Turbulent Drag Reduction Whit Polymer Additives". In: *Annual Review of Fluid Mechanics* 40 (2008), pp. 235–256 (cit. on p. 2).

[5] R. Sureshkumar, A. N. Beris, and R. A. Handler. "Direct numerical simulation of the turbulent channel flow of a polymer solution". In: *Phys Fluids* 9 (1997), pp. 743–755 (cit. on pp. 2, 14, 17, 18, 41, 44, 103, 112, 134, 155).

[6] C. D. Dimitropoulos, R. Sureshkumar, and A. N. Beris. "Direct numerical simulation of viscoelastic turbulent channel flow exhibiting drag reduction: effect of the variation of rheological parameters". In: *Journal of Non-Newtonian Fluid Mechanics* 79.2–3 (1998), pp. 433–468. issn: 0377-0257. doi: http://dx.doi.org/10.1016/S0377-0257(98)00115-3 (cit. on pp. 2, 17).

[7] C. D. Dimitropoulos, R. Sureshkumar, A. N. Beris, and R. A. Handler. "Budgets of Reynolds stress, kinetic energy and streamwise enstrophy in viscoelastic turbulent channel flow". In: *Physics of Fluids* 13.4 (2001), pp. 1016–1027. doi: http://dx.doi.org/10.1063/1.1345882 (cit. on pp. 2, 103).

[8] C. D. Dimitropoulos, Y. Dubief, E. S. G. Shaqfeh, P. Moin, and S. K. Lele. "Direct numerical simulation of polymer-induced drag reduction in turbulent boundary layer flow". In: *Phys Fluids* 17 (2005), pp. 1–4 (cit. on pp. 2, 112, 155).

[9] C. D. Dimitropoulos, Y. Dubief, E. S. G. Shaqfeh, and P. Moin. "Direct numerical simulation of polymer-induced drag reduction in turbulent boundary layer flow of inhomogeneous polymer solutions". In: *J Fluid Mech* 566 (2006), pp. 153–162 (cit. on p. 2).

[10] E. De Angelis, C. M. Casciola, V. S. L'vov, R. Piva, and I. Procaccia. "Drag reduction by polymers in turbulent channel flows: Energy redistribution between invariant empirical modes". In: *Phys. Rev. E* 67 (5 May 2003), p. 056312. doi: 10.1103/PhysRevE.67.056312 (cit. on pp. 2, 17).

[11] T. Min, J. Y. Yoo, H. Choi, and D. D. Joseph. "Drag reduction by polymer additives in a turbulent channel flow". In: *J Fluid Mech* 486 (2003), pp. 213–238 (cit. on pp. 2, 17, 103, 112, 155).

[12] T. Min, J. Y. Yoo, and H. Choi. "Maximum drag reduction in a turbulent channel flow by polymer additives". In: *J Fluid Mech* 492 (2003), pp. 91–100 (cit. on pp. 2, 17, 112, 155).

[13] Y. Dubief, C. M. White, V. E. Terrapon, E. S. G. Shaqfeh, P. Moin, and S. K. Lele. "On the coherent drag-reducing and turbulence-enhancing behaviour of polymers in wall flows". In: *J Fluid Mech* 514 (2004), pp. 271–280 (cit. on pp. 2, 17, 81).

[14] K. D. Housiadas and A. N. Beris. "Polymer-induced drag reduction: effects of the variations in elasticity and inertia in turbulent viscoelastic channel flow". In: *Physics of Fluids* 15.8 (2003), pp. 2369–2384 (cit. on pp. 2, 17).

[15] K. D. Housiadas and A. N. Beris. "An efficient fully implicit spectral scheme for {DNS} of turbulent viscoelastic channel flow". In: *Journal of Non-Newtonian Fluid Mechanics* 122.1–3 (2004). {XIIIth} International Workshop on Numerical Methods for Non-Newtonian Flows, pp. 243–262. ISSN: 0377-0257. DOI: http://dx.doi.org/10.1016/j.jnnfm.2004.07.001 (cit. on pp. 2, 17).

[16] K. D. Housiadas and A. N. Beris. "Characteristic scales and drag reduction evaluation in turbulent channel flow of nonconstant viscosity viscoelastic fluids". In: *Physics of Fluids* 16.5 (2004), pp. 1581–1586. DOI: http://dx.doi.org/10.1063/1.1689971 (cit. on pp. 2, 17, 48, 49).

[17] K. D. Housiadas, L. Wang, and A. N. Beris. "A new method preserving the positive definiteness of a second order tensor variable in flow simulations with application to viscoelastic turbulence". In: *Computers & Fluids* 39.2 (2010), pp. 225–241. ISSN: 0045-7930. DOI: http://dx.doi.org/10.1016/j.compfluid.2009.08.006 (cit. on pp. 2, 17, 18, 117).

[18] V. Dallas, J. C. Vassilicos, and G. F. Hewitt. "Strong polymer-turbulence interactions in viscoelastic turbulent channel flow". In: *Physical Review E* 82 (2010), pp. 066303-1–066303-19 (cit. on pp. 2, 18).

[19] L. Thais, A. Tejada-Martinez, T. B. Gatski, and G. Mompean. "A massively parallel hybrid scheme for direct numerical simulation of turbulent viscoelastic channel flow". In: *Comput Fluids* 43 (2011), pp. 134–142 (cit. on pp. 2, 4, 17, 23, 35, 38, 39, 52, 75, 84, 103, 152).

[20] L. Thais, T. B. Gatski, and G. Mompean. "Some dynamical features of the turbulent flow of a viscoelastic fluid for reduced drag". In: *Journal of Turbulence* 13 (2012), pp. 1–26 (cit. on pp. 2, 17, 35, 52, 84).

[21] L. Thais, G. Mompean, and T. Gatski. "Spectral analysis of turbulent viscoelastic and Newtonian channel flows". In: *Journal of Non-Newtonian Fluid Mechanics* 200 (2013). Special Issue: Advances in Numerical Methods for Non-Newtonian Flows, pp. 165–176. ISSN: 0377-0257. DOI: http://dx.doi.org/10.1016/j.jnnfm.2013.04.006 (cit. on pp. 2, 35, 52).

[22] L. Thais, T. Gatski, and G. Mompean. "Analysis of polymer drag reduction mechanisms from energy budgets". In: *International Journal of Heat and Fluid Flow* 43 (2013). 7th International Symposium on Turbulence Heat & Mass Transfer (THMT-7), PalermoConference on Modelling Fluid Flow (CMFF'12), pp. 52–61. ISSN: 0142-727X. DOI: http://dx.doi.org/10.1016/j.ijheatfluidflow.2013.05.016 (cit. on pp. 2, 35, 52).

[23] R. B. Bird, O. Hassager, R. C. Armstrong, and C. F. Curtiss. *Dynamics of Polymeric Liquids. Kinetic theory*. 1st ed. Vol. 2. John Wiley & Sons, 1977 (cit. on pp. 2, 10, 15–17, 21).

[24] D. Joseph. *Fluid Dynamics of Viscoelastic Liquids*. New York: Springer-Verlag, 1990 (cit. on pp. 2, 12).

[25] R. Sureshkumar and A. N. Beris. "Effect of artificial stress diffusivity on the stability of numerical calculations and the dynamics of time-dependent viscoelastic flows". In: *J Non-Newton Fluid* 60 (1995), pp. 53–80 (cit. on pp. 2, 14, 16, 18, 23, 26).

[26] T. Vaithianathan and L. R. Collins. "Numerical approach to simulating turbulent flow of a viscoelastic polymer solution". In: *Journal of Computational Physics* 187.1 (2003), pp. 1–21. issn: 0021-9991. doi: http://dx.doi.org/10.1016/S0021-9991(03)00028-7 (cit. on pp. 2, 10, 14, 17, 18, 30, 55, 116).

[27] T. Min, J. Y. Yoo, and H. Choi. "Effect of spatial discretization schemes on numerical solutions of viscoelastic fluid flows". In: *Journal of Non-Newtonian Fluid Mechanics* 100.1–3 (2001), pp. 27–47. issn: 0377-0257. doi: http://dx.doi.org/10.1016/S0377-0257(01)00128-8 (cit. on pp. 2, 17).

[28] T. Vaithianathan, A. Robert, J. G. Brasseur, and L. R. Collins. "An improved algorithm for simulating three-dimensional, viscoelastic turbulence". In: *J Non-Newton Fluid* 140 (2006), pp. 3–22 (cit. on pp. 2, 17, 18).

[29] B. Yu and Y. Kawaguchi. "Direct numerical simulation of viscoelastic drag-reducing flow: a faithful finite difference method". In: *Journal of Non-Newtonian Fluid Mechanics* 116.2–3 (2004), pp. 431–466. issn: 0377-0257. doi: http://dx.doi.org/10.1016/j.jnnfm.2003.11.006 (cit. on pp. 2, 18).

[30] B. Yu, F. Li, and Y. Kawaguchi. "Numerical and experimental investigation of turbulent characteristics in a drag-reducing flow with surfactant additives". In: *International Journal of Heat and Fluid Flow* 25 (2004), pp. 961–974 (cit. on p. 2).

[31] R. Fattal and R. Kupferman. "Constitutive laws for the matrix-logarithm of the conformation tensor". In: *J Non-Newton Fluid* 123.2-3 (2004), pp. 281–285 (cit. on pp. 2, 12, 13, 30).

[32] R. Fattal and R. Kupferman. "Time-dependent simulation of viscoelastic flows at high Weissenberg number using the log-conformation representation". In: *Journal of Non-Newtonian Fluid Mechanics* 126.1 (2005), pp. 23–37. issn: 0377-0257. doi: http://dx.doi.org/10.1016/j.jnnfm.2004.12.003 (cit. on pp. 2, 12).

[33] N. Balci, B. Thomases, M. Renardy, and C. R. Doering. "Symmetric factorization of the conformation tensor in viscoelastic fluid models". In: *J Non-Newton Fluid* 166 (2011), pp. 546–553 (cit. on pp. 2, 4, 13, 23, 24, 26, 28, 29, 42, 51, 115).

[34] A. M. Afonso, F. T. Pinho, and M. A. Alves. "The *kernel*-conformation constintutive laws". In: *J Non-Newton Fluid* 167-168 (2012), pp. 30–37 (cit. on pp. 2, 4, 13, 23, 29, 53, 115).

[35] K. Kim, C.-F. Li, R. Sureshkumar, L. Balachandar, and R. J. Adrian. "Effects of polymer stresses on eddy structures in drag-reduced turbulent channel flow". In: *J Fluid Mech* 584 (2007), pp. 281–299 (cit. on pp. 2, 75, 81, 103, 105, 114, 152, 153).

[36] J. C. R. Hunt, A. A. Wray, and P. Moin. *Eddies, stream, and convergence zones in turbulent flows*. Report CTR-S88. Center for Turbulence Research - Proceedings of Summer Program, 1988 (cit. on pp. 3, 63–65, 68, 74, 75, 78, 84, 95, 96, 112, 116, 139, 140, 147, 150).

[37] M. S. Chong, A. E. Perry, and B. J. Cantwell. "A general classification of three-dimensional flow fields". In: *Phys Fluids A-Fluid* 2.5 (1990), pp. 765–777 (cit. on pp. 3, 65, 66, 68, 69, 74, 75, 95, 96, 112, 139, 140, 147, 150).

[38] J. Jeong and F. Hussain. "On the identification of a vortex". In: *J Fluid Mech* 285 (1995), pp. 69–94 (cit. on pp. 3, 63, 66–69, 74, 75, 82–84, 86–88, 90, 91, 93, 95, 112, 116, 139, 140, 144, 148, 150).

[39] J. Zhou, R. J. Adrian, S. Balanchandar, and T. M. Kendall. "Mechanisms for generating coherent packets of hairpin vortices in channel flow". In: *J Fluid Mech* 387 (1999), pp. 353–396 (cit. on pp. 3, 68, 69, 75, 95, 103, 112, 141).

[40] R. L. Thompson. "Flow classification for viscoelastic materials". In: *International Journal of Advances in Engineering Sciences and Applied Mathematics* 1.2 (2009), pp. 69–83. ISSN: 0975-5616. DOI: 10.1007/s12572-010-0003-x (cit. on pp. 4, 71, 74, 75, 78, 96, 97, 103, 113, 117).

[41] A. Peterlin. "Hydrodynamics of macromolecules in a velocity field with longitudinal gradient". In: *Journal of Polymer Science Part B: Polymer Letters* 4.4 (1966), pp. 287–291. ISSN: 1542-6254. DOI: 10.1002/pol.1966.110040411 (cit. on pp. 10, 21, 22).

[42] M. Chilcott and J. Rallison. "Creeping flow of dilute polymer solutions past cylinders and spheres". In: *Journal of Non-Newtonian Fluid Mechanics* 29 (1988), pp. 381–432. ISSN: 0377-0257. DOI: http://dx.doi.org/10.1016/0377-0257(88)85062-6 (cit. on pp. 10, 12, 16).

[43] G. Lielens, P. Halin, I. Jaumain, R. Keunings, and V. Legat. "New closure approximations for the kinetic theory of finitely extensible dumbbells1". In: *Journal of Non-Newtonian Fluid Mechanics* 76.1–3 (1998), pp. 249–279. ISSN: 0377-0257. DOI: http://dx.doi.org/10.1016/S0377-0257(97)00121-3 (cit. on p. 10).

[44] G. Lielens, R. Keunings, and V. Legat. "The FENE-L and FENE-LS closure approximations to the kinetic theory of finitely extensible dumbbells". In: *Journal of Non-Newtonian Fluid Mechanics* 87.2–3 (1999), pp. 179–196. ISSN: 0377-0257. DOI: http://dx.doi.org/10.1016/S0377-0257(99)00063-4 (cit. on p. 10).

[45] J. Remmelgas, P. Singh, and L. Leal. "Computational studies of nonlinear elastic dumbbell models of Boger fluids in a cross-slot flow". In: *Journal of Non-Newtonian Fluid Mechanics* 88.1–2 (1999), pp. 31–61. ISSN: 0377-0257. DOI: http://dx.doi.org/10.1016/S0377-0257(99)00020-8 (cit. on p. 10).

[46] A. J. Szeri. "A deformation tensor model for nonlinear rheology of {FENE} polymer solutions". In: *Journal of Non-Newtonian Fluid Mechanics* 92.1 (2000), pp. 1–25. ISSN: 0377-0257. DOI: http://dx.doi.org/10.1016/S0377-0257(00)00090-2 (cit. on p. 10).

[47] P. Ilg, I. V. Karlin, and H. C. Öttinger. "Canonical distribution functions in polymer dynamics. (I). Dilute solutions of flexible polymers". In: *Physica A: Statistical Mechanics and its Applications* 315.3–4 (2002), pp. 367–385. ISSN: 0378-4371. DOI: http://dx.doi.org/10.1016/S0378-4371(02)01017-8 (cit. on p. 10).

[48] R. Keunings. "On the high Weissenberg number problem". In: *Journal of Non-Newtonian Fluid Mechanics* 20 (1986), pp. 209–226. ISSN: 0377-0257. DOI: http://dx.doi.org/10.1016/0377-0257(86)80022-2 (cit. on p. 11).

[49] I. Rutkevich. "Steady flow of a viscoelastic fluid in a channel with permeable walls". In: *Journal of Applied Mathematics and Mechanics* 33.3 (1969), pp. 573–580. ISSN: 0021-8928. DOI: http://dx.doi.org/10.1016/0021-8928(69)90077-X (cit. on p. 12).

[50] I. Rutkevich. "Some general properties of the equations of viscoelastic incompressible fluid dynamics". In: *Journal of Applied Mathematics and Mechanics* 33.1 (1969), pp. 30–39. ISSN: 0021-8928. DOI: http://dx.doi.org/10.1016/0021-8928(69)90111-7 (cit. on p. 12).

[51] I. Rutkevich. "The propagation of small perturbations in a viscoelastic fluid". In: *Journal of Applied Mathematics and Mechanics* 34.1 (1970), pp. 35–50. ISSN: 0021-8928. DOI: http://dx.doi.org/10.1016/0021-8928(70)90006-7 (cit. on p. 12).

[52] I. Rutkevich. "On the thermodynamic interpretation of the evolutionary conditions of the equations of the mechanics of finitely deformable viscoelastic media of Maxwell type". In: *Journal of Applied Mathematics and Mechanics* 36.2 (1972), pp. 283–295. ISSN: 0021-8928. DOI: http://dx.doi.org/10.1016/0021-8928(72)90169-4 (cit. on p. 12).

[53] D. D. Joseph, M. Renardy, and J.-C. Saut. "Hyperbolicity and change of type in the flow of viscoelastic fluids". In: *Archive for Rational Mechanics and Analysis* 87.3 (1985), pp. 213–251. ISSN: 1432-0673. DOI: 10.1007/BF00250725 (cit. on p. 12).

[54] D. Joseph and J. Saut. "Change of type and loss of evolution in the flow of viscoelastic fluids". In: *Journal of Non-Newtonian Fluid Mechanics* 20 (1986), pp. 117–141. ISSN: 0377-0257. DOI: http://dx.doi.org/10.1016/0377-0257(86)80018-0 (cit. on p. 12).

[55] F. Dupret and J. Marchal. "Loss of evolution in the flow of viscoelastic fluids". In: *Journal of Non-Newtonian Fluid Mechanics* 20 (1986), pp. 143–171. ISSN: 0377-0257. DOI: http://dx.doi.org/10.1016/0377-0257(86)80019-2 (cit. on p. 12).

[56] J. Van Der Zanden and M. Hulsen. "Mathematical and physical requirements for successful computations with viscoelastic fluid models". In: *Journal of Non-Newtonian Fluid Mechanics* 29 (1988), pp. 93–117. ISSN: 0377-0257. DOI: http://dx.doi.org/10.1016/0377-0257(88)85052-3 (cit. on p. 12).

[57] M. A. Hulsen. "Some properties and analytical expressions for plane flow of Leonov and Giesekus models". In: *Journal of Non-Newtonian Fluid Mechanics* 30.1 (1988), pp. 85–92. ISSN: 0377-0257. DOI: http://dx.doi.org/10.1016/0377-0257(88)80019-3 (cit. on p. 12).

[58] M. A. Hulsen. "A sufficient condition for a positive definite configuration tensor in differential models". In: *Journal of Non-Newtonian Fluid Mechanics* 38.1 (1990), pp. 93–100. ISSN: 0377-0257. DOI: http://dx.doi.org/10.1016/0377-0257(90)85034-V (cit. on p. 12).

[59] Y. Kwon and A. Leonov. "Stability constraints in the formulation of viscoelastic constitutive equations". In: *Journal of Non-Newtonian Fluid Mechanics* 58.1 (1995), pp. 25–46. ISSN: 0377-0257. DOI: http://dx.doi.org/10.1016/0377-0257(94)01341-E (cit. on p. 12).

[60] R. C. King, M. R. Apelian, R. C. Armstrong, and R. A. Brown. "Numerically stable finite element techniques for viscoelastic calculations in smooth and singular geometries". In: *Journal of Non-Newtonian Fluid Mechanics* 29 (1988), pp. 147–216. ISSN: 0377-0257. DOI: http://dx.doi.org/10.1016/0377-0257(88)85054-7 (cit. on p. 12).

[61] D. Rajagopalan, R. C. Armstrong, and R. A. Brown. "Finite element methdos for calculation of steady, viscoelastic flow using constitutive equations with a Newtonian viscosity". In: *Journal of Non-Newtonian Fluid Mechanics* 36 (1990), pp. 159–192. ISSN: 0377-0257. DOI: http://dx.doi.org/10.1016/0377-0257(90)85008-M (cit. on p. 12).

[62] J. Sun, N. Phan-Thien, and R. I. Tanner. "An adaptive viscoelastic stress splitting scheme and its applications: AVSS/SI and AVSS/SUPG". In: *Journal of Non-Newtonian Fluid Mechanics* 65.1 (1996), pp. 75–91. ISSN: 0377-0257. DOI: http://dx.doi.org/10.1016/0377-0257(96)01448-6 (cit. on p. 12).

[63] M. A. Alves, P. J. Oliveira, and F. T. Pinho. "A convergent and universally bounded interpolation scheme for the treatment of advection". In: *International Journal for Numerical Methods in Fluids* 41.1 (2003), pp. 47–75. ISSN: 1097-0363. DOI: 10.1002/fld.428 (cit. on p. 12).

[64] E. Mitsoulis. "Extrudate swell of Boger fluids". In: *Journal of Non-Newtonian Fluid Mechanics* 165.13–14 (2010), pp. 812–824. ISSN: 0377-0257. DOI: http://dx.doi.org/10.1016/j.jnnfm.2010.04.011 (cit. on p. 13).

[65] L. Thais, L. Helin, and G. Mompean. "Numerical simulation of viscoelastic flows with Oldroyd-B constitutive equations and novel algebraic stress models". In: *Journal of Non-Newtonian Fluid Mechanics* 140.1–3 (2006). Special Issue on the {XIVth} International Workshop on Numerical Methods for Non-Newtonian Flows, Santa Fe, 2005XIVth International Workshop on Numerical Methods for Non-Newtonian Flows, Santa Fe, 2005, pp. 145–158. ISSN: 0377-0257. DOI: http://dx.doi.org/10.1016/j.jnnfm.2006.01.016 (cit. on p. 13).

[66] X. Chen, H. Marschall, M. Schäfer, and D. Bothe. "A comparison of stabilisation approaches for finite-volume simulation of viscoelastic fluid flow". In: *International Journal of Computational Fluid Dynamics* 27.6-7 (2013), pp. 229–250. DOI: 10.1080/10618562.2013.829916. eprint: http://dx.doi.org/10.1080/10618562.2013.829916 (cit. on pp. 13, 24).

[67] M. A. Hulsen, R. Fattal, and R. Kupferman. "Flow of viscoelastic fluids past a cylinder at high Weissenberg number: Stabilized simulations using matrix logarithms". In: *Journal of Non-Newtonian Fluid Mechanics* 127.1 (2005), pp. 27–39. ISSN: 0377-0257. DOI: http://dx.doi.org/10.1016/j.jnnfm.2005.01.002 (cit. on p. 13).

[68] A. Afonso, P. Oliveira, F. Pinho, and M. Alves. "The log-conformation tensor approach in the finite-volume method framework". In: *Journal of Non-Newtonian Fluid Mechanics* 157.1–2 (2009), pp. 55–65. ISSN: 0377-0257. DOI: http://dx.doi.org/10.1016/j.jnnfm.2008.09.007 (cit. on p. 13).

[69] I. L. Palhares Junior, C. M. Oishi, A. M. Afonso, M. A. Alves, and F. T. Pinho. "Numerical study of the square-root conformation tensor formulation for confined and free-surface viscoelastic fluid flows". In: *Advanced Modeling and Simulation in Engineering Sciences* 3.1 (2016), pp. 1–23. ISSN: 2213-7467. DOI: 10.1186/s40323-015-0054-4 (cit. on p. 13).

[70] F. Martins, C. Oishi, A. Afonso, and M. Alves. "A numerical study of the Kernel-conformation transformation for transient viscoelastic fluid flows". In: *Journal of Computational Physics* 302 (2015), pp. 653–673. ISSN: 0021-9991. DOI: http://dx.doi.org/10.1016/j.jcp.2015.08.038 (cit. on p. 13).

[71] R. Figueiredo, C. Oishi, A. Afonso, I. Tasso, and J. Cuminato. "A two-phase solver for complex fluids: Studies of the Weissenberg effect". In: *International Journal of Multiphase Flow* 84 (2016), pp. 98–115. ISSN: 0301-9322. DOI: http://dx.doi.org/10.1016/j.ijmultiphaseflow.2016.04.014 (cit. on p. 13).

[72] A. Groisman and V. Steinberg. "Elastic turbulence in a polymer solution flow". In: *Nature* 405 (2000), pp. 53–55. ISSN: 0028-0836. DOI: http://dx.doi.org/10.1038/35011019 (cit. on p. 14).

[73] D. G. Thomas, R. Sureshkumar, and B. Khomami. "Pattern Formation in Taylor-Couette Flow of Dilute Polymer Solutions: Dynamical Simulations and Mechanism". In: *Phys. Rev. Lett.* 97 (5 Aug. 2006), p. 054501. DOI: 10.1103/PhysRevLett.97.054501 (cit. on p. 14).

[74] L. Feng-Chen, Z. Hong-Na, C. Yang, K. Tomoaki, K. Haruyuki, and O. Marie. "A Purely Elastic Instability and Mixing Enhancement in a 3D Curvilinear Channel Flow". In: *Chinese Physics Letters* 29.9 (2012), p. 094704 (cit. on p. 14).

[75] H. Giesekus. "A unified approach to a variety of constitutive models for polymer fluids based on the concept of configuration-dependent molecular mobility". In: *Rheologica Acta* 21.4 (1982), pp. 366–375. ISSN: 1435-1528. DOI: 10.1007/BF01534296 (cit. on p. 14).

[76] S. Berti, A. Bistagnino, G. Boffetta, A. Celani, and S. Musacchio. "Two-dimensional elastic turbulence". In: *Phys. Rev. E* 77 (5 May 2008), p. 055306. DOI: 10.1103/PhysRevE.77.055306 (cit. on p. 14).

[77] S. Berti and G. Boffetta. "Elastic waves and transition to elastic turbulence in a two-dimensional viscoelastic Kolmogorov flow". In: *Phys. Rev. E* 82 (3 Sept. 2010), p. 036314. DOI: 10.1103/PhysRevE.82.036314 (cit. on p. 14).

[78] B. Thomases and M. Shelley. "Transition to Mixing and Oscillations in a Stokesian Viscoelastic Flow". In: *Phys. Rev. Lett.* 103 (9 Aug. 2009), p. 094501. DOI: 10.1103/PhysRevLett.103.094501 (cit. on p. 14).

[79] Z. Hong-Na, L. Feng-Chen, C. Yang, K. Tomoaki, and Y. Bo. "Direct numerical simulation of elastic turbulence and its mixing-enhancement effect in a straight channel flow". In: *Chinese Physics B* 22.2 (2013), p. 024703 (cit. on p. 14).

[80] D. Samanta, Y. Dubief, M. Holzner, C. Schäfer, A. N. Morozov, C. Wagner, and B. Hof. “Elasto-inertial turbulence”. In: *Proceedings of the National Academy of Sciences of the United States of America* 110.26 (2013), pp. 10557–10562 (cit. on p. 14).

[81] S. S. Ray and D. Vincenzi. “Elastic turbulence in a shell model of polymer solution”. In: *EPL (Europhysics Letters)* 114.4 (2016), p. 44001 (cit. on p. 15).

[82] F. Forrest and G. A. Grierson. “Friction losses in cast iron pipe carrying”. In: *Paper Trade Journal* 92 (1931), pp. 39–41 (cit. on p. 15).

[83] B. A. Toms. “Some Observations on the flow of linear polymer solutions through straight tubes at large Reynolds numbers”. In: *Proceedings of the International Congress of Rheology, Holland, North-Holland, Amsterdam, Section II* (1948), pp. 135–141 (cit. on p. 15).

[84] K. J. Mysels. “Flow of thickened fluid”. In: *December 27, US Patent 2* 492 (1949), p. 173 (cit. on p. 15).

[85] P. S. Virk, H. S. Mickley, and K. A. Smith. “The Toms phenomenom: turbulent pipe flow of dilute polymer solutions”. In: *J Fluid Mech* 22 (1967), pp. 22–30 (cit. on p. 15).

[86] J. L. Lumley. “Drag reduction by additives”. In: *Annu Rev Fluid Mech* 11 (1969), pp. 367–384 (cit. on pp. 16, 76, 112, 116, 150, 155).

[87] F. A. Seyer and A. B. Metzner. “Turbulence phenomena in drag reducing systems”. In: *AIChE Journal* 492 (1949), pp. 426–434 (cit. on p. 16).

[88] M. Tabor and P. G. de Gennes. “A cascade theory of drag reduction”. In: *Europhys Lett* 7 (1986), pp. 519–522 (cit. on pp. 16, 112, 116, 155).

[89] J. M. J. Den Toonder, F. T. M. Nieuwstadt, and G. D. C. Kuiken. “The role of elongational viscosity in the mechanism of drag reduction by polymer additives”. In: *Applied Scientific Research* 54 (1995), pp. 95–123 (cit. on p. 16).

[90] P. Orlandi. “A tentative approach to the direct simulation of drag reduction by polymers”. In: *J Non-Newton Fluid* 60 (1995), pp. 277–301 (cit. on p. 16).

[91] A. N. Beris and R. Sureshkumar. “Simulation of time-dependent viscoelastic channel Poiseuille flow at high Reynolds numbers”. In: *Chemical Engineering Science* 51.9 (1996), pp. 1451–1471. ISSN: 0009-2509. DOI: http://dx.doi.org/10.1016/0009-2509(95)00313-4 (cit. on p. 16).

[92] J. C. Maxwell. “On the dynamical theory of gases”. In: *Phil. Trans. R. Soc. Lond.* 157 (1867), pp. 49–88 (cit. on p. 16).

[93] K. D. Housiadas, A. N. Beris, and R. A. Handler. “Viscoelastic effects on higher order statistics and on coherent structures in turbulent channel flow”. In: *Physics of Fluids* 17.3, 035106 (2005). DOI: http://dx.doi.org/10.1063/1.1850920 (cit. on p. 17).

[94] P. K. Ptasinski, B. J. Boersma, F. T. M. Nieuwstadt, M. A. Hulsen, B. H. A. A. Van den Brule, and J. C. R. Hunt. “Turbulent channel flow near maximum drag reduction: simulations, experiments and mechanisms”. In: *Journal of Fluid Mechanics* 490 (Sept. 2003), pp. 251–291. ISSN: 1469-7645. DOI: 10.1017/S0022112003005305 (cit. on p. 17).

[95] Y. Dubief and S. K. Lele. *Direct numerical simulation of polymer flow*. Annual Research Briefs. Center for Turbulence Research, 2001, pp. 197–208 (cit. on p. 17).

[96] A. N. Beris and K. D. Housiadas. "Computational Viscoelastic Fluid Mechanics and Numerical Studies of Turbulent Flows of Dilute Polymer Solutions". In: *Modeling and Simulation in Polymers*. Ed. by P. D. Gujrati and A. I. Leonov. Wiley-VCH Verlag GmbH & Co. KGaA, 2010, pp. 1–36. ISBN: 9783527630257. DOI: 10.1002/9783527630257.ch1 (cit. on p. 18).

[97] E. De Angelis, C. M. Casciola, R. Benzi, and R. Piva. "Homogeneous isotropic turbulence in dilute polymers". In: *Journal of Fluid Mechanics* 531 (May 2005), pp. 1–10. DOI: 10.1017/S0022112005003666 (cit. on p. 18).

[98] P. Perlekar, D. Mitra, and R. Pandit. "Manifestations of Drag Reduction by Polymer Additives in Decaying, Homogeneous, Isotropic Turbulence". In: *Phys. Rev. Lett.* 97 (26 Dec. 2006), p. 264501. DOI: 10.1103/PhysRevLett.97.264501 (cit. on p. 18).

[99] W.-H. Cai, F.-C. Li, and H.-N. Zhang. "DNS study of decaying homogeneous isotropic turbulence with polymer additives". In: *Journal of Fluid Mechanics* 665 (Oct. 2010), pp. 334–356. DOI: 10.1017/S0022112010003939 (cit. on p. 18).

[100] S. K. Lele. "Compact finite difference schemes with spectral-like resolution". In: *Journal of Computational Physics* 103.1 (1992), pp. 16–42. ISSN: 0021-9991. DOI: http://dx.doi.org/10.1016/0021-9991(92)90324-R (cit. on p. 38).

[101] M. H. Carpenter, D. Gottlieb, and S. Abarbanel. "The Stability of Numerical Boundary Treatments for Compact High-Order Finite-Difference Schemes". In: *Journal of Computational Physics* 108.2 (1993), pp. 272–295. ISSN: 0021-9991. DOI: http://dx.doi.org/10.1006/jcph.1993.1182 (cit. on p. 38).

[102] G. Kitzhofer, O. Koch, G. Pulverer, and C. S. and Ewa B. Weinmüller. *BVP-SUITE1.1. A New Matlab Solver for Singular Implicit Boundary Value Problems*. Vienna (cit. on pp. 43–45, 134).

[103] R. B. Dean. "Reynolds Number Dependence of Skin Friction and Other Bulk Flow Variables in Two-Dimensional Rectangular Duct Flow". In: *Journal of Fluids Engineering* 100 (2 1978), pp. 215–223. DOI: 10.1115/1.3448633 (cit. on p. 49).

[104] D. S. Henningson, A. Lundbladh, and A. V. Johansson. "A mechanism for bypass transition from localized disturbances in wall-bounded shear flows". In: *Journal of Fluid Mechanics* 250 (May 2003), pp. 169–207. DOI: 10.1017/S0022112093001429 (cit. on pp. 50, 137).

[105] L. Thais. *DNS of Newtonian and non-Newtonian turbulent channel flows up to* $Re_{\tau 0}$ = 3000. Last accessed: 27/01/15. Available on <http://lthais.plil.fr/channeldata/>. 2014. URL: http://lthais.plil.fr/channeldata/ (cit. on pp. 52, 53, 84).

[106] H. Tennekes and J. L. Lumley. *A First Course in Turbulence*. Cambridge, Massachusetts: MIT Press, 1972 (cit. on p. 62).

[107] A. Hussain. "Coherent structures and studies of perturbed and unperturbed jets". In: *The Role of Coherent Structures in Modelling Turbulence and Mixing: Proceedings of the International Conference Madrid, Spain, June 25–27,1980*. Ed. by J. Jimenez. Berlin, Heidelberg: Springer Berlin Heidelberg, 1981, pp. 252–291. ISBN: 978-3-540-38425-0. DOI: 10.1007/3-540-10289-2_30 (cit. on p. 62).

[108] B. J. Cantwell. "Organized Motion in Turbulent Flow". In: *Annual Review of Fluid Mechanics* 13.1 (1981), pp. 457–515. DOI: 10.1146/annurev.fl.13.010181.002325. eprint: http://dx.doi.org/10.1146/annurev.fl.13.010181.002325 (cit. on p. 62).

[109] S. K. Robinson. "Coherent Motions in the Turbulent Boundary Layer". In: *Annual Review of Fluid Mechanics* 23.1 (1991), pp. 601–639. DOI: 10.1146/annurev.fl.23.010191.003125. eprint: http://dx.doi.org/10.1146/annurev.fl.23.010191.003125 (cit. on p. 62).

[110] H. J. Lugt. "The Dilemma of Defining a Vortex". In: *Recent Developments in Theoretical and Experimental Fluid Mechanics: Compressible and Incompressible Flows*. Ed. by U. Müller, K. G. Roesner, and B. Schmidt. Berlin, Heidelberg: Springer Berlin Heidelberg, 1979, pp. 309–321. ISBN: 978-3-642-67220-0. DOI: 10.1007/978-3-642-67220-0_32 (cit. on p. 63).

[111] S. A. O. Zhen-Su She Eric Jackson. "Structure and Dynamics of Homogeneous Turbulence: Models and Simulations". In: *Proceedings: Mathematical and Physical Sciences* 434.1890 (1991), pp. 101–124. ISSN: 09628444 (cit. on p. 63).

[112] P. Moin and J. Kim. "Numerical investigation of turbulent channel flow". In: *Journal of Fluid Mechanics* 118 (May 1982), pp. 341–377. DOI: 10.1017/S0022112082001116 (cit. on p. 63).

[113] E. D. Siggia. "Numerical study of small-scale intermittency in three-dimensional turbulence". In: *Journal of Fluid Mechanics* 107 (June 1981), pp. 375–406. DOI: 10.1017/S002211208100181X (cit. on p. 63).

[114] A. K. M. F. Hussain and M. Hayakawa. "Eduction of large-scale organized structures in a turbulent plane wake". In: *Journal of Fluid Mechanics* 180 (July 1987), pp. 193–229. DOI: 10.1017/S0022112087001782 (cit. on p. 63).

[115] R. W. Metcalfe, A. K. M. F. Hussain, S. Menon, and M. Hayakawa. "Coherent Structures in a Turbulent Mixing Layer: A Comparison Between Direct Numerical Simulations and Experiments". In: *Turbulent Shear Flows 5: Selected Papers from the Fifth International Symposium on Turbulent Shear Flows, Cornell University, Ithaca, New York, USA, August 7–9, 1985*. Ed. by F. Durst, B. E. Launder, J. L. Lumley, F. W. Schmidt, and J. H. Whitelaw. Berlin, Heidelberg: Springer Berlin Heidelberg, 1987, pp. 110–123. ISBN: 978-3-642-71435-1. DOI: 10.1007/978-3-642-71435-1_11 (cit. on p. 63).

[116] K. Yamamoto and I. Hosokawa. "A Decaying Isotropic Turbulence Pursued by the Spectral Method". In: *Journal of the Physical Society of Japan* 57.5 (1988), pp. 1532–1535. DOI: 10.1143/JPSJ.57.1532. eprint: http://dx.doi.org/10.1143/JPSJ.57.1532 (cit. on p. 63).

[117] D. K. Bisset, R. A. Antonia, and L. W. B. Browne. "Spatial organization of large structures in the turbulent far wake of a cylinder". In: *Journal of Fluid Mechanics* 218 (Sept. 1990), pp. 439–461. DOI: 10.1017/S0022112090001069 (cit. on p. 63).

[118] D. H. Porter, A. Pouquet, and P. R. Woodward. "Kolmogorov-like spectra in decaying three-dimensional supersonic flows". In: *Physics of Fluids* 6.6 (1994), pp. 2133–2142. DOI: http://dx.doi.org/10.1063/1.868217 (cit. on p. 63).

[119] V. Kolář. "Vortex identification: New requirements and limitations". In: *International Journal of Heat and Fluid Flow* 28.4 (2007). Including Special Issue of Conference on Modelling Fluid Flow (CMFF'06), Budapest13th event of the international conference series in fluid flow technologies: conference on modelling fluid flow, pp. 638–652. ISSN: 0142-727X. DOI: http://dx.doi.org/10.1016/j.ijheatfluidflow.2007.03.004 (cit. on pp. 63, 75).

[120] G. Haller, A. Hadjighasem, M. Farazmand, and F. Huhn. "Defining coherent vortices objectively from the vorticity". In: *Journal of Fluid Mechanics* 795 (May 2016), pp. 136–173. DOI: 10.1017/jfm.2016.151 (cit. on p. 63).

[121] J. Weiss. "The dynamics of enstrophy transfer in two-dimensional hydrodynamics". In: *Physica D* 48 (1991), pp. 273–294 (cit. on pp. 64, 95).

[122] G. Haller. "An objective definition of a vortex". In: *J Fluid Mech* 525 (2005), pp. 1–26 (cit. on pp. 64, 70, 71, 74, 75, 78, 95, 97–99, 113, 139, 142, 143, 150, 152).

[123] C. Truesdell. *The Kinematics of Vorticity*. Bloomington: Indiana University Press, 1954 (cit. on p. 65).

[124] A. E. Perry and M. S. Chong. "A Description of Eddying Motions and Flow Patterns Using Critical-Point Concepts". In: *Annual Review of Fluid Mechanics* 19.1 (1987), pp. 125–155. DOI: 10.1146/annurev.fl.19.010187.001013. eprint: http://dx.doi.org/10.1146/annurev.fl.19.010187.001013 (cit. on p. 65).

[125] S. Kida and H. Miura. "Identification and analysis of vortical structures". In: *European Journal of Mechanics - B/Fluids* 17.4 (1998), pp. 471–488. ISSN: 0997-7546. DOI: http://dx.doi.org/10.1016/S0997-7546(98)80005-8 (cit. on p. 68).

[126] R. Cucitore, M. Quadrio, and A. Baron. "On the effectiveness and limitations of local criteria for the identification of a vortex". In: *European Journal of Mechanics - B/Fluids* 18.2 (1999), pp. 261–282. ISSN: 0997-7546. DOI: http://dx.doi.org/10.1016/S0997-7546(99)80026-0 (cit. on pp. 69, 74).

[127] P. Chakraborty, S. Balachandar, and R. J. Adrian. "On the relationships between local vortex identification schemes". In: *J Fluid Mech* 535 (July 2005), pp. 189–214. ISSN: 1469-7645. DOI: 10.1017/S0022112005004726 (cit. on pp. 69, 95, 112, 139, 141, 148).

[128] S. Zhang and D. Choudhury. "Eigen helicity density: A new vortex identification scheme and its application in accelerated inhomogeneous flows". In: *Physics of Fluids* 18.5, 058104 (2006), pp. 058104-1–058104-4. DOI: http://dx.doi.org/10.1063/1.2187071 (cit. on pp. 70, 74).

[129] R. L. Thompson. "Some perspectives on the dynamic history of a material element". In: *Int J Eng Sci* 46 (2008), pp. 524–549 (cit. on pp. 71, 76, 97, 150, 151).

[130] R. D. A. Bacchi. "What is wanted from a vortex definition?" Portuguese. MSc Dissertation. Universidade Federal Fluminense, 2009 (cit. on pp. 71, 96, 97).

[131] G. Astarita. "Objective and generally applicable criteria for flow classification". In: *J Non-Newton Fluid* 6 (1979), pp. 69–76 (cit. on pp. 73, 74, 76, 77, 141, 150, 151).

[132] P. Klein, B. L. Hua, and G. Lapeyre. "Alignment of tracer gradient vectors in 2D turbulence". In: *Physica D: Nonlinear Phenomena* 146.1–4 (2000), pp. 246–260. issn: 0167-2789. doi: http://dx.doi.org/10.1016/S0167-2789(00)00119-6 (cit. on p. 74).

[133] V. Kolář. "Compressibility Effect in Vortex Identification". In: *AIAA Journal* 47 (2 Fev 2009), pp. 473–475. doi: 10.2514/1.40131 (cit. on p. 75).

[134] Z. RUSAK and J. H. LEE. "The effect of compressibility on the critical swirl of vortex flows in a pipe". In: *Journal of Fluid Mechanics* 461 (June 2002), pp. 301–319. doi: 10.1017/S0022112002008431 (cit. on p. 75).

[135] Z. Rusak, J. J. Choi, and J.-H. Lee. "Bifurcation and stability of near-critical compressible swirling flows". In: *Physics of Fluids* 19.11, 114107 (2007). doi: http://dx.doi.org/10.1063/1.2801508 (cit. on p. 75).

[136] Y. Dubief and F. Delcayre. "On coherent-vortex identification in turbulence". In: *Journal of Turbulence* 1 (2000), N11. doi: 10.1088/1468-5248/1/1/011. eprint: http://dx.doi.org/10.1088/1468-5248/1/1/011 (cit. on p. 75).

[137] V. E. Terrapon, Y. Dubief, and J. Soria. "On the role of pressure in elasto-inertial turbulence". In: *Journal of Turbulence* 16.1 (2015), pp. 26–43. doi: 10.1080/14685248.2014.952430. eprint: http://dx.doi.org/10.1080/14685248.2014.952430 (cit. on p. 75).

[138] R. S. Martins, A. S. Pereira, G. Mompean, L. Thais, and R. L. Thompson. "On Objective and Non-objective Kinematic Flow Classification Criteria". In: *Progress in Wall Turbulence 2: Understanding and Modelling*. Ed. by M. Stanislas, J. Jimenez, and I. Marusic. Cham: Springer International Publishing, 2016, pp. 419–428. isbn: 978-3-319-20388-1. doi: 10.1007/978-3-319-20388-1_37 (cit. on pp. 75, 78, 79, 111).

[139] D. Lee and H. Choi. "Magnetohydrodynamic turbulent flow in a channel at low magnetic Reynolds number". In: *Journal of Fluid Mechanics* 439 (July 2001), pp. 367–394. doi: 10.1017/S0022112001004621 (cit. on p. 75).

[140] F. C. Frank and M. R. Mackley. "Localized flow birefringence of polyethylene oxide solutions in a two roll mill". In: *J Polym Sci* 14 (1976), pp. 69–76 (cit. on pp. 76, 150).

[141] P. R. Schunk and L. E. Scriven. "Constitutive equation for modeling mixed extension and shear in polymer solution processing". In: *J Rheol* 34.7 (1990), pp. 1085–1119 (cit. on pp. 76, 150).

[142] R. L. Thompson and P. R. S. Mendes. "Persistence of straining and flow classification". In: *Int J Eng Sci* 43 (2005), pp. 79–105 (cit. on pp. 76, 77, 150).

[143] E. Dresselhaus and M. Tabor. "The kinematics of stretching and alignment of material elements in general flow fields". In: *J Fluid Mech* 236 (Mar. 1992), pp. 415–444. issn: 1469-7645 (cit. on pp. 77, 141, 142).

[144] T. Gatski and T. Jongen. "Nonlinear eddy viscosity and algebraic stress models for solving complex turbulent flows". In: *Progress in Aerospace Sciences* 36.8 (2000), pp. 655–682. ISSN: 0376-0421. DOI: http://dx.doi.org/10.1016/S0376-0421(00)00012-9 (cit. on p. 77).

[145] R. Drouot. "Définition d'un transport associé à un modèle de fluide de deuxième ordre. Comparaison de diverses lois de comportement". In: *CR Acad Sci A Math* 282 (1976), pp. 923–926 (cit. on pp. 77, 141, 150, 151).

[146] R. Drouot and M. Lucius. "Approximation du second ordre de la loi de comportement des fluides simples. Lois classiques deduites de l'introduction d'un nouveau tenseur objectif". In: *Arch Mech* 28.2 (1976), pp. 189–198 (cit. on pp. 77, 141, 150, 151).

[147] R. Huilgol. "Comments on "Objective and generally applicable criteria for flow classification", by G. Astarita ". In: *J Non-Newton Fluid* 7.1 (1980), pp. 91–95 (cit. on pp. 77, 150).

[148] M. Tabor and I. Klapper. "Stretching and alignment in chaotic and turbulent Flows". In: *Chaos Solitons Fract* 4 (6) (1994), pp. 1031–1055 (cit. on pp. 77, 78, 141, 150).

[149] R. S. Martins, A. S. Pereira, G. Mompean, L. Thais, and R. L. Thompson. "An objective perspective for classic flow classification criteria". In: *Comptes Rendus Mécanique* 344.1 (2016), pp. 52–59. ISSN: 1631-0721. DOI: http://dx.doi.org/10.1016/j.crme.2015.08.002 (cit. on pp. 78, 79, 96, 98, 99, 101, 110).

[150] J. Jiménez and A. Pinelli. "The autonomous cycle of near-wall turbulence". In: *Journal of Fluid Mechanics* 389 (June 1999), pp. 335–359. DOI: 10.1017/S0022112099005066 (cit. on p. 81).

[151] P. A. Stone, A. Roy, R. G. Larson, F. Waleffe, and M. D. Graham. "Polymer drag reduction in exact coherent structures of plane shear flow". In: *Physics of Fluids* 16.9 (2004), pp. 3470–3482. DOI: http://dx.doi.org/10.1063/1.1775192 (cit. on p. 81).

[152] R. L. Thompson. private communication (cit. on p. 96).

[153] R. L. Thompson, R. D. A. Bacchi, and F. J. Machado. "What is a vortex?" In: *Proceedings of the 20th International Congress of Mechanical Engineering (COBEM)*. Gramado-RS, Brazil, 2009 (cit. on pp. 97, 98, 143).

[154] V. I. Arnold. "Sur une propriété topologique des applications globalement canoniques de la mécanique classique". In: *CR Acad Sci I-Math* 261 (1965), pp. 3719–3722 (cit. on pp. 98, 140, 143).

[155] S. Childress. *Construction of steady-state hydromagnetic dynamos. I. Spatially periodic fields*. Report AFOSR-67-0124 MF-53. New York: Courant Institute of Mathematical Sciences, 1967 (cit. on pp. 98, 140, 143).

[156] S. Childress. *Construction of steady-state hydromagnetic dynamos. II. The spherical conductor*. Report AFOSR-67-0976 MF-54. New York: Courant Institute of Mathematical Sciences, 1967 (cit. on pp. 98, 140, 143).

[157] S. Friedlander and M. M. Vishik. "Instability criteria for the flow of an inviscid incompressible fluid". In: *Phys Rev Lett* 66 (1991), pp. 2204–2206 (cit. on pp. 98, 143).

[158] A. Lifschitz. "Essential spectrum and local instability condition in hydrodynamics". In: *Phys Lett A* 152 (1991), pp. 199–204 (cit. on pp. 98, 143).

[159] G. Mompean, R. L. Thompson, and P. R. S. Mendes. "A general transformation procedure for differential viscoelastic models". In: *J Non-Newton Fluid* 111 (2003), pp. 151–174 (cit. on pp. 101, 146, 147).

[160] R. J. Adrian. "Hairpin vortex organization in wall turbulence $^{a)}$". In: *Phys Fluids* 19.4, 041301 (2007), pp. 041301-1–041301-16 (cit. on pp. 103, 152).

[161] A. Yarin. "On the mechanism of turbulent drag reduction in dilute polymer solutions: dynamics of vortex filaments". In: *Journal of Non-Newtonian Fluid Mechanics* 69.2 (1997), pp. 137–153. ISSN: 0377-0257. DOI: http://dx.doi.org/10.1016/S0377-0257(96)01526-1 (cit. on p. 103).

[162] W. G. Tiederman, T. S. Luchik, and D. G. Bogard. "Wall-layer structure and drag reduction". In: *Journal of Fluid Mechanics* 156 (July 1985), pp. 419–437. DOI: 10.1017/S0022112085002178 (cit. on p. 112).

[163] T. S. Luchik and W. G. Tiederman. "Turbulent structure in low-concentration drag-reducing channel flows". In: *J Fluid Mech* 190 (May 1988), pp. 241–263. ISSN: 1469-7645 (cit. on pp. 112, 155).

[164] A. Agarwal, L. Brandt, and T. A. Zaki. "Transition to Turbulence in Viscoelastic Channel Flow". In: *Procedia IUTAM* 14 (2015), pp. 519–526. ISSN: 2210-9838. DOI: http://dx.doi.org/10.1016/j.piutam.2015.03.083 (cit. on p. 137).

[165] B. Pierce, P. Moin, and T. Sayadi. "Application of vortex identification schemes to direct numerical simulation data of a transitional boundary layer". In: *Phys Fluids* 25 (2013), p. 015102 (cit. on pp. 139, 140).

Appendix A

The solution of implicit ODE with the BVPSUITE

In Chapter 2, the analytical solution for the steady-state field of the square-root conformation tensor is used as a reference for laminar Poiseuille flows. The velocity profile is $u(y) = (3/2)(1-y^2)$.

When no artificial diffusion is considered, the system of equations to solve with the square-root conformation tensor formulation is

$$
\begin{aligned}
0 &= \frac{1}{2Wi_h}\left\{\left[\frac{L^2-3}{L^2-\mathrm{tr}(\boldsymbol{c})}\right] b_{xx}(y) - b_{xx}^{-1}(y)\right\} + 6y b_{xy}(y) + a_{xy}(y) b_{xy}(y) \\
0 &= \frac{1}{2Wi_h}\left\{\left[\frac{L^2-3}{L^2-\mathrm{tr}(\boldsymbol{c})}\right] b_{yy}(y) - b_{yy}^{-1}(y)\right\} + a_{xy}(y) b_{xy}(y) \\
0 &= \frac{1}{2Wi_h}\left\{\left[\frac{L^2-3}{L^2-\mathrm{tr}(\boldsymbol{c})}\right] b_{zz}(y) - b_{zz}^{-1}(y)\right\} \\
0 &= \frac{1}{2Wi_h}\left\{\left[\frac{L^2-3}{L^2-\mathrm{tr}(\boldsymbol{c})}\right] b_{xy}(y) - b_{xy}^{-1}(y)\right\} - a_{xy}(y) b_{yy}(y) \quad .
\end{aligned}
\tag{A.1}
$$

The resulting system contains only four equations because the components b_{xz} and b_{yz} are null (c_{xz} and c_{yz} as well) and $\boldsymbol{b}$ is symmetric. The trace of the conformation tensor can be expressed as a function of the components of $\boldsymbol{b}$, and $\boldsymbol{a}$ is given as a function of $\boldsymbol{b}$ and of the velocity (see Eq. (2.27)). Once the non-null components of $\boldsymbol{b}$ are calculated, the conformation tensor is recovered using the relation $\boldsymbol{c} = \boldsymbol{b} \cdot \boldsymbol{b}$.

When including stress diffusivity into the equations of the square-root formulation, two approaches are possible, which have been discussed in Section 3.1. For both approaches, the problem formulation scales down to a system of implicit second-order

ODE. In the *"a posteriori"* approach, the resulting system of ODE is

$$\begin{aligned}
\frac{D_b}{Re_h}\frac{\mathrm{d}^2 b_{xx}(y)}{\mathrm{d}y^2} &= \frac{1}{2Wi_h}\left\{\left[\frac{L^2-3}{L^2-\mathrm{tr}(\boldsymbol{c})}\right]b_{xx}(y) - b_{xx}^{-1}(y)\right\} + 6y b_{xy}(y) + a_{xy}(y)b_{xy}(y)\\
\frac{D_b}{Re_h}\frac{\mathrm{d}^2 b_{yy}(y)}{\mathrm{d}y^2} &= \frac{1}{2Wi_h}\left\{\left[\frac{L^2-3}{L^2-\mathrm{tr}(\boldsymbol{c})}\right]b_{yy}(y) - b_{yy}^{-1}(y)\right\} + a_{xy}(y)b_{xy}(y)\\
\frac{D_b}{Re_h}\frac{\mathrm{d}^2 b_{zz}(y)}{\mathrm{d}y^2} &= \frac{1}{2Wi_h}\left\{\left[\frac{L^2-3}{L^2-\mathrm{tr}(\boldsymbol{c})}\right]b_{zz}(y) - b_{zz}^{-1}(y)\right\}\\
\frac{D_b}{Re_h}\frac{\mathrm{d}^2 b_{xy}(y)}{\mathrm{d}y^2} &= \frac{1}{2Wi_h}\left\{\left[\frac{L^2-3}{L^2-\mathrm{tr}(\boldsymbol{c})}\right]b_{xy}(y) - b_{xy}^{-1}(y)\right\} - a_{xy}(y)b_{yy}(y) \quad ,
\end{aligned} \tag{A.2}$$

whereas, for the *"a priori"* formulation (following Eq. (2.35)), one gets

$$\begin{aligned}
\frac{D_c}{2Re_h}\frac{\mathrm{d}^2 b_{xx}(y)}{\mathrm{d}y^2} &= \frac{1}{2Wi_h}\left\{\left[\frac{L^2-3}{L^2-\mathrm{tr}(\boldsymbol{c})}\right]b_{xx}(y) - b_{xx}^{-1}(y)\right\}\\
&\quad + 6y b_{xy}(y) + a_{xy}(y)b_{xy}(y) - \frac{D_c}{Re_h}h_{xx}(y)\\
\frac{D_c}{2Re_h}\frac{\mathrm{d}^2 b_{yy}(y)}{\mathrm{d}y^2} &= \frac{1}{2Wi_h}\left\{\left[\frac{L^2-3}{L^2-\mathrm{tr}(\boldsymbol{c})}\right]b_{yy}(y) - b_{yy}^{-1}(y)\right\}\\
&\quad + a_{xy}(y)b_{xy}(y) - \frac{D_c}{Re_h}h_{yy}(y)\\
\frac{D_c}{2Re_h}\frac{\mathrm{d}^2 b_{zz}(y)}{\mathrm{d}y^2} &= \frac{1}{2Wi_h}\left\{\left[\frac{L^2-3}{L^2-\mathrm{tr}(\boldsymbol{c})}\right]b_{zz}(y) - b_{zz}^{-1}(y)\right\}\\
&\quad - \frac{D_c}{Re_h}h_{zz}(y)\\
\frac{D_c}{2Re_h}\frac{\mathrm{d}^2 b_{xy}(y)}{\mathrm{d}y^2} &= \frac{1}{2Wi_h}\left\{\left[\frac{L^2-3}{L^2-\mathrm{tr}(\boldsymbol{c})}\right]b_{xy}(y) - b_{xy}^{-1}(y)\right\}\\
&\quad - a_{xy}(y)b_{yy}(y) - \frac{D_c}{Re_h}h_{xy}(y) \quad .
\end{aligned} \tag{A.3}$$

As shown in Eq. (2.34), $\boldsymbol{h}$ is also a function of $\boldsymbol{b}$ and $\boldsymbol{u}$.

To solve these sets of equations, we use the BVPSUITE [102], a MATLAB code conceived to solve boundary value problems for systems of implicit ODE.

The boundary conditions for the solution with stress diffusion are obtained from the steady-state boundary value computed with the standard conformation tensor without artificial diffusion. This steady-state solution was presented by Sureshkumar, Beris, and Handler [5] and reads

$$c_{xx}^{ss} = \frac{1}{F(y)}\left[1 + \frac{2Wi_{\tau 0}^2}{F^2(y)}\left(\frac{du}{dy}\right)^2\right] \quad , \tag{A.4a}$$

$$c_{yy}^{ss} = c_{zz}^{ss} = \frac{1}{F(y)} \quad , \tag{A.4b}$$

$$c_{xy}^{ss} = \frac{Wi_{\tau 0}}{F^2(y)}\frac{du}{dy} \quad , \tag{A.4c}$$

$$c_{xz}^{ss} = c_{yz}^{ss} = 0 \quad , \tag{A.4d}$$

with

$$F(y) = \frac{\sqrt{3}\Omega(y)}{2\sinh(\phi/3)} \quad , \tag{A.5a}$$

$$\Omega(y) = \frac{\sqrt{2}Wi_{\tau 0}}{L}\frac{du}{dy} \quad , \tag{A.5b}$$

$$\phi(y) = \sinh^{-1}\left(\frac{3\sqrt{3}\Omega(y)}{2}\right) \quad . \tag{A.5c}$$

Appendix B

Disturbed field used for transition to turbulence

The technique used here is based on the work of Henningson, Lundbladh, and Johansson [104] for Newtonian flows, and recently employed in a viscoelastic context by Agarwal, Brandt, and Zaki [164]. It consists of localised disturbances in the shape of two pairs of counter-rotating vortices in the stream-wise direction, which are added to the initial parabolic laminar velocity profile. The streamfunction for the disturbances is

$$\psi = \epsilon f(y)\overline{x}(y' - y_0)\exp\left[-\overline{x}^2 - \overline{y}^2\right] \quad , \tag{B.1}$$

where ϵ is the amplitude of the disturbance, $\overline{x} = (x' - x_0)/l_x$ and $\overline{y} = (y' - y_0)/l_y$, with x_0 and y_0 being the location of the centre of the disturbance, and l_x and l_y, the disturbance's length scales in the stream-wise and span-wise directions, respectively. Furthermore,

$$(x', y') = (x\cos\theta - y\sin\theta, x\sin\theta + y\cos\theta) \quad , \tag{B.2}$$

where θ is the angle with respect to the stream-wise direction. The power-law function relating the wall-normal dependence is

$$f(y) = (1+y)^p(1-y)^q \quad . \tag{B.3}$$

The corresponding velocity fluctuations are given by

$$(u', v', w') = \left(-\frac{\partial\psi}{\partial z}\sin\theta, \frac{\partial\psi}{\partial y'}, -\frac{\partial\psi}{\partial z}\cos\theta\right) \quad , \tag{B.4}$$

and the disturbed velocity field is finally imposed as

$$(\widetilde{u}, \widetilde{v}, \widetilde{w}) = (u + u', v + v', w + w') \quad . \tag{B.5}$$

The parameters for the initial disturbance whose centre coincides with the centre of the channel are $\epsilon = 0.1$, $(l_x, l_y) = (2, 2)$, $\theta = 0$, and $p = q = 2$.

Appendix C

An objective perspective for classic flow classification criteria

By R. S. Martins, A. S. Pereira, G. Mompean, L. Thais and R. L. Thompson
Published in *Comptes Rendus Mecanique*, vol. 344, pp. 52–59, 2016.
DOI: `http://dx.doi.org/10.1016/j.crme.2015.08.002`

C.1 Introduction

In Fluid Mechanics, flow visualization is an important subject, since fundamental aspects of the flow can be captured by observation. Post-processing Computational Fluid Dynamics (CFD) data is also a field that makes important contributions for the understanding of the flow. Complex flows exhibit different kinds of motion that depend on position and time. In these flows, it is common to find swirling motions in different parts of the domain. In order to locate and visualize these regions, a criterion of vortex identification is generally used to see the manifestation of the rotational character of the flow.

However, the concept of a *vortex* is still cause for dissension within the scientific community. As a consequence, there are several criteria available in the literature that are used to identify rotational structures in the flow. In other words, there is no quantity, in the mathematical sense, that is consensually accepted in the literature as a definition for a vortex. Some of the non-consensual issues that are present in this context are if the vortex is an Euclidean or a Lagrangian entity and if it should be defined in a kinematic or in a dynamical basis.

Comparisons among the different criteria are still a subject of investigation (e.g. [165]). An important point raised by Haller [122] is the requirement that a vortex should be an Eulerian invariant entity, i.e. invariant under arbitrary changes of the reference frame. This requirement affects the vortex concept, since, before that work, only the Galilean invariance was invoked to define a vortex [38]. We can stress here that the classic vortex definitions, such as the Q-criterion by Hunt *et al.* [36], the Δ-criterion by Chong *et al.* [37], the λ_2-criterion by Jeong and Hussain [38] and the $\lambda_{cr}/\lambda_{ci}$-criterion by Chakraborty *et al.* [127], enjoy only Galilean invariance (i.e. they are invariant to constant velocity translating frames).

The arguments to adopt an objective criterion for vortex identification are the following. First, if one observer identifies a certain region as being a vortex while, for another one, this region is not a vortex, there is no reason to privilege the verdict stated by one observer with respect to the other. Secondly, we have to have in mind the advantages of building a criterion for vortex identification. One clear purpose of identifying a region as being a vortex is to connect the rotational character of the flow with another phenomenon besides the flow itself. It is consensual that processes like: the convection in a heat transfer problem, the degree of mixture of different fluids, the percentage of components due chemical reaction in a flow, the intensity of polymer stretching due to the flow, and other transport phenomena problems, cannot be observer-dependent. Hence, if a vortex is non-objective, the logic of cause-effect that could link the flow character with one of these measurers of the intensity that a certain phenomenon is occurring is weaker, when compared to an objective criterion.

In the present work we employ objective versions of four classic criteria largely used in the literature. The classic criteria and their respective objective versions are analysed and applied for two benchmark cases, the transient Arnold-Beltrami-Childress (ABC) flow [154–156] and the flow through a 4:1 contraction.

C.2 Classic criteria

In the following we briefly present four criteria that are currently used in the literature to classify different regions of the flow. These criteria are Eulerian and Galilean-invariant and were recently selected by Pierce *et al.* [165] to evaluate for instance boundary layer flows.

The Q-criterion was proposed by Hunt *et al.* [36] in the context of incompressible flows. Besides local pressure minima, they required that, to identify a vortex, the second invariant of the velocity gradient tensor, $\nabla \boldsymbol{u}$ (defined by $\nabla \boldsymbol{u} = (\partial u_j / \partial x_i)\boldsymbol{e}_i \boldsymbol{e}_j$, where $\boldsymbol{u} = u_i \boldsymbol{e}_i$ is the velocity vector field), should be positive. This condition can be expressed for incompressible flows as a function of the Euclidean norms[1] of the symmetric, $\boldsymbol{D} = (\boldsymbol{L} + \boldsymbol{L}^T)/2$, and skew symmetric, $\boldsymbol{W} = (\boldsymbol{L} - \boldsymbol{L}^T)/2$, parts of the velocity gradient (where $\boldsymbol{L} = (\partial u_i / \partial x_j)\boldsymbol{e}_i \boldsymbol{e}_j$ is the transpose of $\nabla \boldsymbol{u}$). The condition for the Q-criterion can be expressed as follows,

$$Q = \frac{1}{2}\left(\|\boldsymbol{W}\|^2 - \|\boldsymbol{D}\|^2\right) > 0 \,. \tag{C.1}$$

The Δ-criterion proposed by Chong *et al.* [37] is based on the assumption of an equivalence between a vortex and complex eigenvalues of the velocity gradient tensor[2]. Complex eigenvalues of the velocity gradient is a sign of vorticity dominance with respect to rate-of-strain, since the symmetric rate-of-strain tensor can only have real eigenvalues. Mathematically, the Δ-criterion can be defined as

$$\Delta = \left(\frac{Q}{3}\right)^3 + \left(\frac{\det(\boldsymbol{D} + \boldsymbol{W})}{2}\right)^2 > 0 \,, \tag{C.2}$$

where $\det(\cdot)$ is the third invariant (determinant) of a given second order tensor.

The λ_2-criterion proposed by Jeong and Hussain [38] is based on the idea of joining

[1]The Euclidean norm of a generic second-order tensor $\boldsymbol{A}$ is $\|\boldsymbol{A}\| = \sqrt{\mathrm{tr}(\boldsymbol{A} \cdot \boldsymbol{A}^T)}$, where $\mathrm{tr}(\cdot)$ is the first invariant (trace) of a given second-order tensor.

[2]The expression *velocity gradient* is used interchangeably for $\boldsymbol{L}$ or $\nabla \boldsymbol{u}$.

the local pressure minima condition to a vorticity predominance over the rate-of-strain in the same mathematical condition. By making some assumptions, neglecting some terms, this condition leads to

$$\lambda_2 = \lambda_2^{\boldsymbol{D}^2+\boldsymbol{W}^2} < 0\,, \tag{C.3}$$

where $\lambda_2^{\boldsymbol{D}^2+\boldsymbol{W}^2}$ is the intermediate eigenvalue of the tensor $\boldsymbol{D}^2 + \boldsymbol{W}^2$.

The $\lambda_{cr}/\lambda_{ci}$-criterion proposed by Chakraborty *et al.* [127] is based on the concept that material points that follow orbits which remain compact during the revolutions around each other are in a vortex. λ_{ci} and λ_{cr} are the imaginary and real values, respectively, of the conjugate complex eigenvalues of the velocity gradient:

$$\frac{\lambda_{cr}}{\lambda_{ci}} = \frac{\lambda_{cr}^{\boldsymbol{D}+\boldsymbol{W}}}{\lambda_{ci}^{\boldsymbol{D}+\boldsymbol{W}}} = \frac{\lambda_{cr}^{\boldsymbol{L}}}{\lambda_{ci}^{\boldsymbol{L}}}\,. \tag{C.4}$$

The criterion was proposed in the form $\lambda_{cr}/\lambda_{ci} < \delta$ and, therefore, a threshold parameter (δ) is needed. This condition can only be applied in regions where there are complex eigenvalues of the velocity gradient. This criterion was conceived to be applied together with the $\lambda_{ci} > \epsilon$ criterion proposed by Zhou *et al.* [39], where another threshold is needed.

In order to compare the results of the above criteria, normalized dimensionless versions are used and will be presented in the next section. Specifically for the $\lambda_{cr}/\lambda_{ci}$-criterion, such normalization allows us yet to avoid the choice of a threshold parameter (see section C.3 for details).

C.2.1 Objective redefinition for classic criteria

Drouot [145], Drouot and Lucius [146] have shown that the relative rate-of-rotation tensor, $\overline{\boldsymbol{W}}$, defined by

$$\overline{\boldsymbol{W}} = \boldsymbol{W} - \Omega^D\,, \tag{C.5}$$

is an objective quantity. In Eq. (C.5), Ω^D accounts for the rate of rotation of the eigenvectors of $\boldsymbol{D}$, and is defined by

$$\boldsymbol{\Omega}^{\mathbf{D}} \equiv \hat{e}_i^{\boldsymbol{D}} \dot{\hat{e}}_i^{\boldsymbol{D}}\,, \tag{C.6}$$

where $\hat{e}_i^{\boldsymbol{D}}$ are the normalised eigenvectors of $\boldsymbol{D}$, and $\dot{\hat{e}}_i^{\boldsymbol{D}}$ are their time derivatives. This quantity was used by Astarita [131], to form an index defined by the ratio of the norm of $\overline{\boldsymbol{W}}$ to the norm of $\boldsymbol{D}$. This index was used as means for flow classification dividing the domain into extension-like motions and rigid-body-rotation-like ones. Astarita [131] was seeking for an objective quantity when he proposed that flow classifier.

Although a different path was followed by Dresselhaus and Tabor [143] and Tabor and Klapper [148] investigating the alignment and stretching of material filaments[3] in an approach of dynamic systems, they have also arrived on the necessity of expressing these quantities with the help of the relative-rate-of-rotation tensor, which was called *effective vorticity*. The physical interpretation of the effective vorticity is discussed next.

[3] *Material filaments* being straight lines of infinitesimal size in the fluid which can rotate, stretch, compress, but not bend.

The more common interpretation of the vorticity tensor is that a vorticity component associated to a certain plane is the (arithmetic) mean of the rate-of-rotation of two filaments initially orthogonal to each other in that plane. However, a less adopted interpretation is that the vorticity is the rate of rotation of the filaments which are aligned to the eigenvectors of $\boldsymbol{D}$. This fact induces the necessity of evaluating the vorticity with respect to the rate-of-rotation of the eigenvectors of $\boldsymbol{D}$. When the eigenvectors of $\boldsymbol{D}$ are fixed in certain frame of reference, the vorticity tensor is responsible for a deviation between the filaments that are initially aligned with the eigenvectors and their respective directions. However, when the flow is complex and the eigendirections of $\boldsymbol{D}$ do change in time, the effective vorticity is the entity responsible for this deviation and, by consequence, for exposing different material filaments to the eigenvectors. This also means that when effective vorticity vanishes, the same material filament is exposed to the eigendirections of the rate-of-strain tensor. In this case, the filament aligned to the eigenvector corresponding to the highest positive eigenvalue is persistently stretched. As shown by Dresselhaus and Tabor [143], effective vorticity plays an important role on the dynamics of material lines and vorticity lines, affecting vortex stretching also.

As suggested by Haller [122], an alternative but analogous form of the Q-criterion can be built by replacing vorticity by effective vorticity in Eq. (C.1) leading to

$$\hat{Q} = \frac{1}{2}\left(\|\overline{\boldsymbol{W}}\|^2 - \|\boldsymbol{D}\|^2\right) > 0\,. \tag{C.7}$$

A similar procedure can be adopted for adapting the other criteria into an objective backbone. Therefore we can define the new versions of Δ-, λ_2-, and $\lambda_{cr}/\lambda_{ci}$-criteria, respectively, as

$$\hat{\Delta} = \left(\frac{\hat{Q}}{3}\right)^3 + \left(\frac{\det(\boldsymbol{D}+\overline{\boldsymbol{W}})}{2}\right)^2 > 0\,, \tag{C.8}$$

$$\hat{\lambda}_2 = \lambda_2^{\boldsymbol{D}^2+\overline{\boldsymbol{W}}^2} < 0\,, \tag{C.9}$$

$$\frac{\hat{\lambda}_{cr}}{\hat{\lambda}_{ci}} = \frac{\lambda_{cr}^{\boldsymbol{D}+\overline{\boldsymbol{W}}}}{\lambda_{ci}^{\boldsymbol{D}+\overline{\boldsymbol{W}}}} = \frac{\lambda_{cr}^{\overline{\boldsymbol{L}}}}{\lambda_{ci}^{\overline{\boldsymbol{L}}}}\,. \tag{C.10}$$

We highlight that all objective entities hereafter will be displayed with a hat.

C.3 Results

This section presents the results obtained by applying both objective and non-objective criteria to two cases: (1) the three-dimensional analytical flow field known as the ABC flow in its unsteady version, and (2) an abrupt 4:1 planar contraction.

It is worth noting that all criteria have been normalized in order to produce values between 0 and 1. Moreover, normalized values greater than or equal to 0 and less than 0.5 represent swirling-like or elliptical regions, whereas those greater than 0.5 and less than or equal to 1 represent non-swirling-like or hyperbolic regions. The value of 0.5 represents then a transition (parabolic) region where the magnitude of rotation rate and deformation rate are alike. The only exception applies to the $\lambda_{cr}/\lambda_{ci}$- and $\hat{\lambda}_{cr}/\hat{\lambda}_{ci}$-criteria. Since these criteria apply for elliptical regions only, we decided to normalize them from 0 to 0.5, where 0.5 is the boundary of elliptical region.

The difference from the non-objective and objective versions lies on the reference frame from which the rate-of-rotation is computed. While the non-objective quantities use the original fixed frame, the objective quantities have their reference on the local frame attached to the eigenvectors of $\boldsymbol{D}$.

Normalized criteria are identified by a superscript asterisk and are given by the following equations [153]

$$Q^* = \frac{1}{\pi}\cos^{-1}\left(\frac{\|\boldsymbol{W}\|^2 - \|\boldsymbol{D}\|^2}{\|\boldsymbol{W}\|^2 + \|\boldsymbol{D}\|^2}\right), \tag{C.11}$$

$$\Delta^* = \frac{1}{\pi}\cos^{-1}\left[\frac{\left(\frac{\|\boldsymbol{W}\|^2 - \|\boldsymbol{D}\|^2}{6}\right)^3 + \left(\frac{\det(\boldsymbol{D}+\boldsymbol{W})}{2}\right)^2}{\left(\frac{\|\boldsymbol{W}\|^2 + \|\boldsymbol{D}\|^2}{6}\right)^3 + \left(\frac{\det(\boldsymbol{D}+\boldsymbol{W})}{2}\right)^2}\right], \tag{C.12}$$

$$\lambda_2^* = 1 - \frac{1}{\pi}\cos^{-1}\left[\frac{\lambda_2{}^{\boldsymbol{D}^2+\boldsymbol{W}^2}}{tr(\boldsymbol{D}^2) - \lambda_1{}^{\boldsymbol{D}^2+\boldsymbol{W}^2} - \lambda_3{}^{\boldsymbol{D}^2+\boldsymbol{W}^2}}\right], \tag{C.13}$$

$$\frac{\lambda_{cr}^*}{\lambda_{ci}^*} = \frac{2}{\pi^2}\left[\tan^{-1}\left(\frac{\lambda_{cr}{}^{\boldsymbol{D}+\boldsymbol{W}}}{\lambda_{ci}{}^{\boldsymbol{D}+\boldsymbol{W}}}\right)\right]^2, \tag{C.14}$$

$$\hat{Q}^* = \frac{1}{\pi}\cos^{-1}\left(\frac{\|\overline{\boldsymbol{W}}\|^2 - \|\boldsymbol{D}\|^2}{\|\overline{\boldsymbol{W}}\|^2 + \|\boldsymbol{D}\|^2}\right), \tag{C.15}$$

$$\hat{\Delta}^* = \frac{1}{\pi}\cos^{-1}\left[\frac{\left(\frac{\|\overline{\boldsymbol{W}}\|^2 - \|\boldsymbol{D}\|^2}{6}\right)^3 + \left(\frac{\det(\boldsymbol{D}+\overline{\boldsymbol{W}})}{2}\right)^2}{\left(\frac{\|\overline{\boldsymbol{W}}\|^2 + \|\boldsymbol{D}\|^2}{6}\right)^3 + \left(\frac{\det(\boldsymbol{D}+\overline{\boldsymbol{W}})}{2}\right)^2}\right], \tag{C.16}$$

$$\hat{\lambda}_2^* = 1 - \frac{1}{\pi}\cos^{-1}\left[\frac{\lambda_2{}^{\boldsymbol{D}^2+\overline{\boldsymbol{W}}^2}}{tr(\boldsymbol{D}^2) - \lambda_1{}^{\boldsymbol{D}^2+\overline{\boldsymbol{W}}^2} - \lambda_3{}^{\boldsymbol{D}^2+\overline{\boldsymbol{W}}^2}}\right], \tag{C.17}$$

$$\frac{\hat{\lambda}_{cr}^*}{\hat{\lambda}_{ci}^*} = \frac{2}{\pi^2}\left[\tan^{-1}\left(\frac{\lambda_{cr}{}^{\boldsymbol{D}+\overline{\boldsymbol{W}}}}{\lambda_{ci}{}^{\boldsymbol{D}+\overline{\boldsymbol{W}}}}\right)\right]^2. \tag{C.18}$$

C.3.1 Transient ABC flow

The classic ABC flow [154–156] is largely used in the study of chaotic trajectories. Aiming to investigate high-frequency instabilities [157, 158], we used a transient version of the ABC flow, also considered by Haller [122]. The flow field is given by the following set of equations:

$$\begin{aligned} u(y,z,t) &= A(t)\sin(z) + C\cos(y), \\ v(x,z,t) &= B\sin(x) + A(t)\cos(z), \\ w(x,y) &= C\sin(y) + B\cos(x). \end{aligned} \tag{C.19}$$

In the set of equations (C.19), A is time-dependent and is defined as $A(t) = A_0 + (1 - e^{-qt})\sin(\omega t)$ with $A_0 = \sqrt{3}$, $q = 0.1$ and $\omega = 2\pi$, while $B = \sqrt{2}$ and $C = 1$.

Figure C.1 contains the normalized classic flow classification criteria (Q^*, Δ^*, λ_2^* and $\lambda_{cr}^*/\lambda_{ci}^*$) on the first line and their respective normalized objective version ($\hat{Q}^*$, $\hat{\Delta}^*$, $\hat{\lambda}_2^*$ and $\hat{\lambda}_{cr}^*/\hat{\lambda}_{ci}^*$) on the second line. The non-objective criteria were obtained using the instantaneous velocity flow field (t=0 s) described by the set of equations (C.19), whereas the objective criteria need two consecutive velocity fields (at the instants t = 0 and t = 0.01 s) to compute the rate-of-rotation of the eigenvectors of $\boldsymbol{D}$, Ω^D (see Eq. (C.6) above).

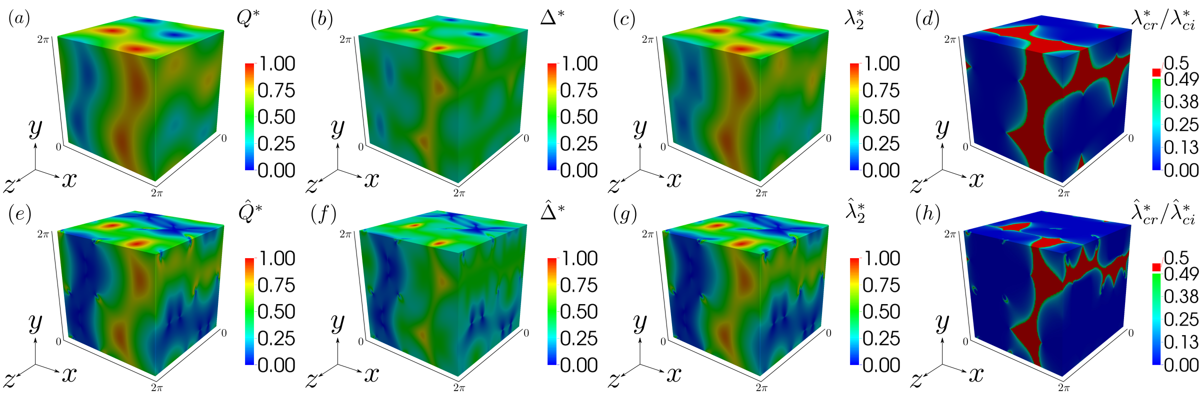

Figure C.1 – Iso-contours of the normalized flow classification criteria applied to the ABC flow field: non-objective (first line) and objective (second line) versions of Q^*-criterion, Δ^*-criterion, λ_2^*-criterion and $\lambda_{cr}^*/\lambda_{ci}^*$-criterion.

The figure shows three surfaces of the cube whose dimensions are limited to the interval $[0, 2\pi]$. Generally, the normalized Q- and λ_2-criteria (first and third columns in Fig. C.1, respectively) present very similar results, which may be explained by the strong relation between these two criteria (see [38]). The classifications of the normalized Δ-criteria (second column in Fig. C.1) are also qualitatively similar when compared to those obtained using the normalized Q-criteria, although slightly different quantitatively, which, once again, may be justified by the relation between the Δ-criterion and the Q-criterion ([38]). Both $\lambda_{cr}^*/\lambda_{ci}^*$- and $\hat{\lambda}_{cr}^*/\hat{\lambda}_{ci}^*$-criteria (last column in Fig. C.1) have a different range due to less detailed information on non-swirling-like regions. Nevertheless, they maintain a similar qualitative behaviour in terms of the location of vortex cores.

Analysing the non-objective criteria (first line in Fig. C.1) at the plane $z = 2\pi$, the Q^*-, Δ^*- and λ_2^*-criteria (Figs. C.1a-c) identify two vortex cores at $(x \approx \pi/2, y \approx \pi/2)$ and $(x \approx \pi/2, y \approx 3\pi/2)$, which are characterized by the colour blue. Once again, due to its different range, almost all the region between $0 < x < \pi$ is blue according to the $\lambda_{cr}^*/\lambda_{ci}^*$-criterion (Fig. C.1d), characterizing a swirling-like region. Still at this plane, all classic criteria seem to identify extensional (red) regions whose cores are located at approximately $(x = 3\pi/2, y = \pi/2)$ and $(x = 3\pi/2, y = 3\pi/2)$. The regions between elliptical (blue) and hyperbolic (red) regions are transition regions (green) generally referred to as *parabolic*, where the role played by rotation and extension is equivalent. Qualitatively, the results at the plane $y = 2\pi$ are very similar to those of the plane $z = 2\pi$. Two vortex (blue) cores are now identified at $(x \approx \pi/2, z \approx \pi/2)$ and $(x \approx 3\pi/2, z \approx \pi/2)$, and two extensional (red) regions are located at approximately $(x = \pi/2, z = 3\pi/2)$ and $(x = 3\pi/2, z = 3\pi/2)$. It is worth noting that the magnitude of both swirling-and non-swirling-like regions are slightly greater than those identified at the plane $z = 2\pi$. Finally, for the plane $x = 2\pi$, the behaviour is yet similar, with vortex cores now identified at $(y \approx \pi/2, z \approx \pi/2)$ and $(y \approx \pi/2, z \approx 3\pi/2)$, and extensional regions centred around $(y \approx 3\pi/2, z \approx \pi/2)$ and $(y \approx 3\pi/2, z \approx 3\pi/2)$. The main difference at this plane is the magnitude of the identified motions, which is reasonably weaker, indicating that the intensities of rotational and extensional motions are close to each other.

From the perspective of the objective criteria (second line in Fig. C.1), the flow at the three planes analysed above presents quite similar characteristics. The main difference is the remarkable increase in swirling-like (blue) regions. This fact is related to regions where the rate of rotation of the eigenvectors of $\boldsymbol{D}$ are more pronounced, see Fig. C.2. This means that there are regions where the filaments aligned with the eigenvectors of $\boldsymbol{D}$ do not rotate intensively with respect to the reference frame where the problem is being described, but rotate significantly with respect to the frame attached to the eigendirections of $\boldsymbol{D}$. This fact will be more explored in the following section for the 4:1 abrupt contraction below.

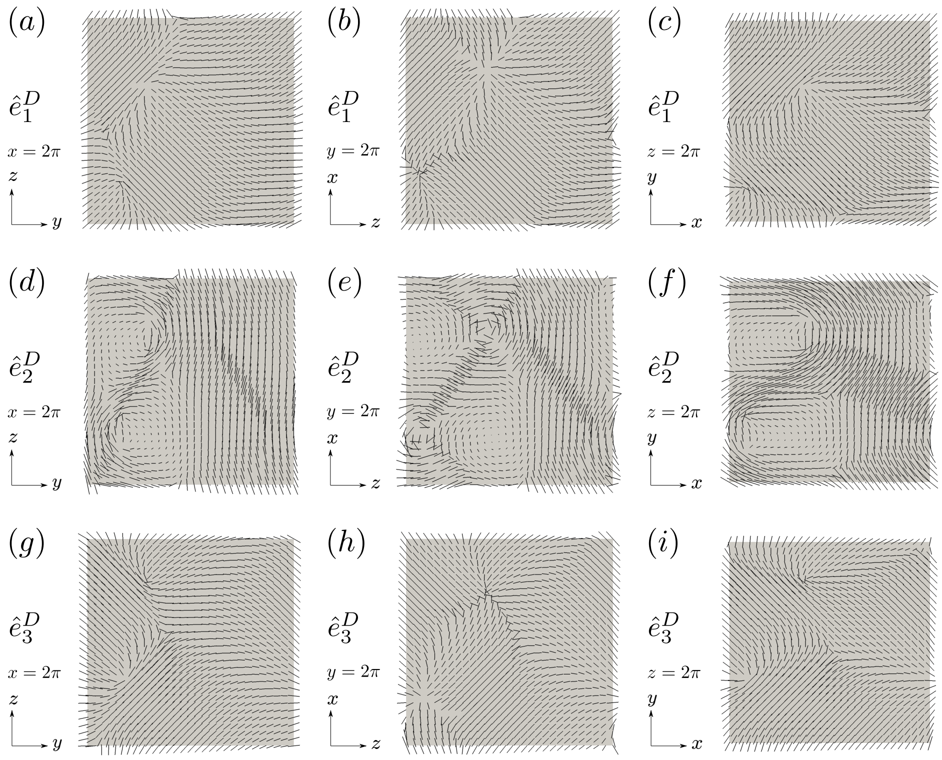

Figure C.2 – Eigendirections of tensor $\boldsymbol{D}$ in the three planes for the ABC flow considered. The ordering corresponds to the eigenvalues $\lambda_1^{\boldsymbol{D}} \geq \lambda_2^{\boldsymbol{D}} \geq \lambda_3^{\boldsymbol{D}}$.

C.3.2 Abrupt 4:1 contraction

The flow generated by an abrupt 4:1 contraction presents different regions in which the fluid is submitted to shear, extension or rigid-body motion. Because this feature can be considerably useful for a rich discussion about flow classification, we considered a laminar steady state flow of a Newtonian fluid (Reynolds number based on the outlet velocity and height equal to 0.043). The numerical approach used is the same described by Mompean *et al.* [159] and the mesh consists of 150×80 grid points respectively in the streamwise (x) and wall-normal (y) directions.

The iso-contours of non-objective (left column) and objective (right column) flow classification criteria are shown in Fig. C.3. Likewise the ABC flow, the non-objective criteria employed here provide similar identifications and classifications except for the $\lambda^*_{cr}/\lambda^*_{ci}$-criterion, since it has a different range associated to elliptical and parabolic domains only. The same rationale applies to the objective versions.

Again, the green color represents regions which are not elliptical nor hyperbolic. In the present case they are related to the shear motion typical of fully-developed flow in a geometry of constant cross sectional area.

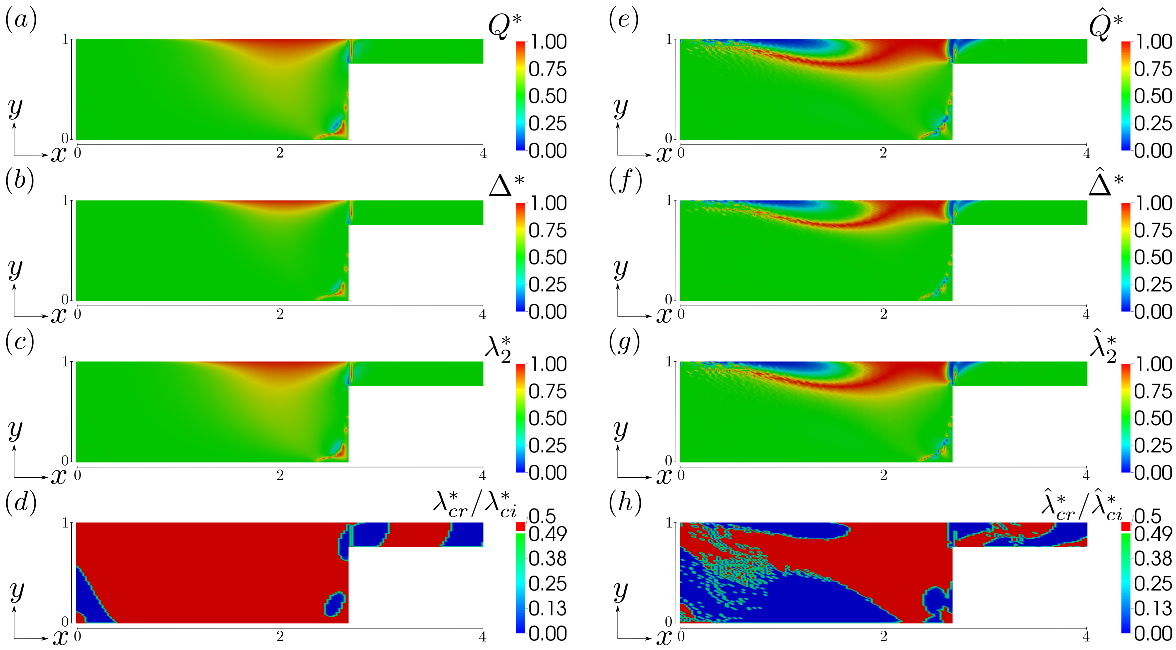

Figure C.3 – Iso-contours of flow classifiers for the flow trough a 4:1 contraction: non-objective (left-hand side) and objective (right-hand side) versions of Q^*-criterion, Δ^*-criterion, λ_2^*-criterion and $\lambda^*_{cr}/\lambda^*_{ci}$-criterion.

The non-objective criteria Q^*, Δ^* and λ_2^* (Figs. C.3a-c) identify a shear region away from the contraction, where the flow is fully developed. Close to the contraction and around the symmetry plane, an extensional region can be seen due the acceleration of the fluid passing through the contraction. Both near the sharp corner ($x \approx 2.75, 0.75 \lessapprox y \lessapprox 1$) and the corner vortex ($x \approx 2.5, 0.1 \lessapprox y \lessapprox 0.25$) a mix of extensional and rotational motions is observed. In fact, in these regions, the fluid is submitted to both extensions and rotations caused by the singularity of the geometry nearby. It is worth remembering that the $\lambda^*_{cr}/\lambda^*_{ci}$-criterion does not provide any distinction in terms of non-swirling-like motions, i.e. swirling-like motions have a degree of intensity (greater than or equal to 0 and less than 0.5) whereas non-swirling-like motions possess only the classification (equal to 0.5, without a gradation). Therefore, in Fig. C.3d, every region in red may be interpreted simply as a non-swirling-like region (possibly being either shear or extensional). The blue regions, on the other hand, can be considered as elliptical regions. Thus, except for the size and intensity, the same two regions with rotational motions pointed by the other non-objective criteria are identified by the $\lambda^*_{cr}/\lambda^*_{ci}$-criterion. However, it also identifies two extra swirling regions: (a) the one close to the wall in the inner region, and (b) the one just by the outlet region.

Concerning the objective criteria (Figs. C.3e-h), the same three elliptical (swirling-like) regions identified by Mompean *et al.* [159] are observed here. As commented by the authors, the regions (i) just after the sharp corner ($x \approx 2.75, 0.75 \lessapprox y \lessapprox 1$), and (ii) near the corner vortex ($x \approx 2.5, 0.1 \lessapprox y \lessapprox 0.25$) are intuitively understandable, since the flow is submitted to rotate at rates which are larger than the local rate-of-deformation. On the other hand, the third region (iii) just before the extensional region may be counter-intuitive at first, since it appears between regions of expected shear and extension. Again, the authors explain that this region should actually be considered as a plug flow (close to rigid-body motion) where the rates of rotation of the eigenvectors of $\boldsymbol{D}$ are larger than the local rates of deformation. One important result shown by the objective quantities is the information with a broad-spectrum of values for all the four criteria when compared with the non-objective quantities. This information is frame-invariant and related to the principal directions of the rate-of-deformation tensor, and is physically expected. Before entering a region where extension is dominant, the region just before the contraction plane, the eigenvectors of $\boldsymbol{D}$ rotate from the $\pi/4 - 3\pi/4$ directions of the shear flow in the fully-developed region to the $0 - \pi/2$ directions of the extensional flow. This rotation is overlooked by the non-objective criteria, but are captured by the objective ones. Although the filaments do not rotate predominantly with respect to the reference frame (x, y), they do rotate with respect to the eigenvectors of $\boldsymbol{D}$, as clearly shown in Fig. C.4. Because of this relative rate of rotation, new filaments are exposed to the corresponding eigenvalues. A similar rationale explains the appearance of the elliptical region just after the contraction, not detected by the non-objective quantities. The $\boldsymbol{D}$-eigenvectors need to rearrange in order to return to a fully-developed condition.

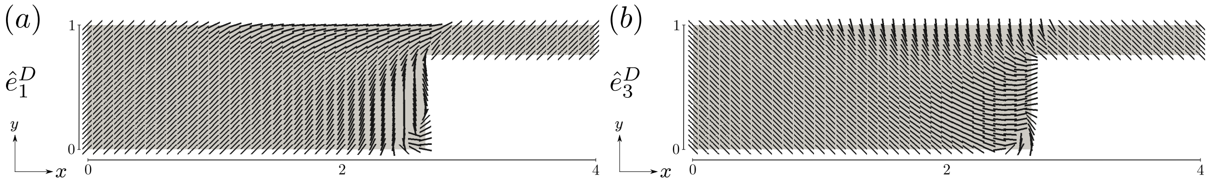

Figure C.4 – Eigendirections of tensor $\boldsymbol{D}$ in the $x - y$ plane for the 4:1 contraction flow. Again, the ordering corresponds to the eigenvalues $\lambda_1^{\boldsymbol{D}} \geq \lambda_2^{\boldsymbol{D}} \geq \lambda_3^{\boldsymbol{D}}$.

It seems that the $\lambda_{cr}/\lambda_{ci}$-criterion has some problems on the so-called *parabolic regions*, i.e. the regions of transition between hyperbolic and elliptical regions. It is difficult to delineate this intermediate region by this criterion in both, objective and non-objective versions. We can notice an almost binary color result. What we can see is that parts of the domain with no apparent physical difference that are classified as hyperbolic or elliptical. Most of these parts are in the parabolic region accordingly to other criteria.

C.4 Final remarks

In the present work we analysed the performance of normalized objective versions of classic flow classification criteria. The classic criteria are the Q-criterion proposed by Hunt *et al.* [36], the Δ-criterion proposed by Chong *et al.* [37], the λ_2-criterion proposed by Jeong and Hussain [38], and the $\lambda_{cr}/\lambda_{ci}$-criterion proposed by Chakraborty *et al.* [127]. The two flows considered were the transient ABC flow with $A(t) = A_0 + (1 - e^{-qt})\sin(\omega t)$ (with $A_0 = \sqrt{3}$, $q = 0.1$ and $\omega = 2\pi$), $B = \sqrt{2}$ and $C = 1$, and a 4:1 abrupt contraction. The ABC flow is known for its chaotic character for the values employed. The abrupt contraction is a complex flow that exhibits different types of motion distributed in the domain: extension, pure shear, and rigid-body motion.

The objective quantities in the present work use the effective vorticity as the entity associated to the elliptical character of the flow, in the place of the vorticity. The main difference between objective and non-objective quantities was the presence of elliptical regions in the objective versions which were not present in its non-objective counterparts. This happened because in these regions, the rate-of-rotation of the eigenvectors of the rate-of-strain tensor, with respect to the original frame, was significant and the effective vorticity uses this rate-of-rotation as reference for computing the rate-of-rotation of the filaments.

Finally, it was shown that the objective criteria provides more information about the kinematics of the flow. Such new features of the flow may be useful in the investigation of complex flows and phenomena, as, for instance, drag-reducing flows, convection-driven problems or the mixture between two or more fluids. We emphasize that our goal is not to appoint to a preferable particular flow classification criterion, but to stand up for the advantages of applying criteria which enjoy objectivity.

Acknowledgements

The authors would like to express their acknowledgement and gratitude to the Brazilian Scholarship Program *Science Without Borders*, managed by CNPq (Conselho Nacional de Desenvolvimento Científico e Tecnológico), for the partial financial support brought to this research (grant numbers: 201708/2012-4, 200860/2012-7 and 402394/2012-7).

Appendix D

On objective and non-objective kinematic flow classification criteria

By R. S. Martins, A. S. Pereira, G. Mompean, L. Thais and R. L. Thompson

In *Progress in Wall Turbulence 2: Understanding and Modelling*, Ed. by Michel Stanislas, Javier Jimenez and Ivan Marusic. Cham: Springer International Publishing, 2016, pp. 419–428, ERCOFTAC Series 23.

ISBN: 978-3-319-20388-1.

DOI: http://dx.doi.org/10.1007/978-3-319-20388-1_37

Abstract

Turbulent flows present several compact and spatially coherent regions generically known as coherent structures. The understanding of these structures is closely related to the concept of vortex, whose definition is still a subject of controversy within the scientific community. In particular, the role of objectivity in the definition of vortex remains a largely open question. The three most usual criteria for vortex identification (Q, Δ and λ_2) are non-objective since they all depend on the fluid's rate-of-rotation, which is not invariant to the reference frame. In the present work, we propose an objective redefinition for these criteria by using the concept of relative rate-of-rotation with respect to the principal directions of the strain rate tensor. We also explore two novel naturally objective flow classification criteria. All the criteria are applied to instantaneous velocity fields obtained by DNS of both Newtonian and viscoelastic turbulent channel flows. The analysis will be carried out here for four friction Reynolds numbers from 180 to 1000, emphasizing the difference between objective and non-objective flow classification criteria, as well as between Newtonian and non-Newtonian flows. Moreover, we try to obtain, from the results of flow classification criteria, information related to the polymer drag reduction phenomenon.

D.1 Introduction

Vortices are present in many practical flows and their dynamics dictates several phenomena, such as heat transfer, mixing, combustion, noise generation and hydrodynamic drag. Hence, a solid understanding of vortex dynamics may lead to a better comprehension of these phenomena.

D.1.1 Previous work

In fact there is not, among researches, a consensus for the definition of a vortex. Instead, there are several criteria available in the literature. Nevertheless, the majority of these definitions is based on the rate-of-rotation (or vorticity) tensor, **W**. Such tensor is not invariant under general transformations of the reference frame. In other words, tensor **W** does not enjoy the objectivity property. Thus, all criteria which depend on the rate-of-rotation tensor are not objective as well. For instance, the classic Q-criterion by Hunt *et al.* [36]), Δ-criterion by Chong *et al.* [37], and λ_2-criterion by Jeong and Hussian [38], largely employed in the literature, all depend on the tensor **W** and, therefore, are not objective criteria.

A key concept relevant to the discussion on objectivity is the concept of persistence-of-straining, introduced by Lumley [86], and applied by several authors [129, 131, 140–142]. In brief, this concept is associated to the capacity of the flow to persistently stretch a material filament. This leads to a physically consistent perspective of the motion of a fluid element, and, consequently, to a new point of view regarding flow classification. In this connection, rigid body motion opposes to maximum persistence-of-straining. In this context, Astarita [131] argued that, because flow classification is mostly used to verify the behavior of constitutive equations, a solid criteria should enjoy (among others) the same invariance properties as those required for the constitutive equations. Besides that, a legitimate flow classification should be an intrinsic character of the flow, and not something that changes depending on the observer. The author proposed a criterion based on the relative rate-of-rotation ($\overline{\mathbf{W}}$), a quantity known to be objective ([145, 146]). The tensor $\overline{\mathbf{W}}$ represents the rate-of-rotation with respect to the principal directions of the strain rate tensor (**D**).

Despite the remarkable work carried out by Astarita, the criterion proposed by him has been proven to present some flaws for certain classes of 3D flows, see [147]. By analyzing these inconsistencies, Thompson and de Souza Mendes [142] proposed a criterion based on the concept of persistence-of-straining.

By examining stretching and alignment of material filaments, Tabor and Klapper [148] verified the importance of the use of the relative rate of rotation without invoking objectivity. Their analysis reinforces Astarita's criterion which is equivalent to an objective version of the Q-criterion mentioned above.

Haller [122] conducted a remarkable work which defends the importance of objectivity on identifying a vortex and presents a criterion based on the stability analysis of the trajectory of particles immersed in the flow. His criterion uses the covariant strain acceleration tensor, obtained from the covariant convected derivative of the strain rate tensor, in order to quantify the ability of the flow to defy the stretching tendency imposed by the strain rate tensor. The author also presents a simple elucidating example regarding the role played by objectivity. In a subsequent work, Thompson [129] adds more consistent physical meaning to the role played by the covariant strain acceleration tensor, proposing a persistence-of-straining criterion based on this entity.

The present work aims to analyze the behavior of objective and non-objective kinematic flow classification criteria applied to the instantaneous velocity fields of both Newtonian and viscoelastic channel flows obtained by direct numerical simulation

(DNS). The interaction between polymer and turbulence, especially near the wall, is also aimed due to its relation to the drag reduction phenomenon.

D.2 Objective versions for classic flow classification criteria

The relative rate-of-rotation, presented by Astarita [131], is the rate-of-rotation "of the fluid" with respect to the principal directions of the strain rate tensor. Mathematically, it takes the following form given by Eq. (D.1),

$$\overline{\mathbf{W}} = \mathbf{W} - \Omega^D \,, \tag{D.1}$$

where Ω^D is the tensor that gives the rate of rotation of the eigenvectors of $\mathbf{D}$. Although both $\mathbf{W}$ and Ω^D are non-objective tensors, Drouot and Lucius [145, 146] have proven that $\overline{\mathbf{W}}$ is objective. If $\overline{\mathbf{W}}$ vanishes, the filaments that are aligned to the eigenvectors of $\mathbf{D}$ have the tendency to continue aligned. In this sense, the stretch is persistent.

An objective redefinition for the Q-criterion is now proposed by replacing the non-objective rate-of-rotation tensor, $\mathbf{W}$, by the objective relative rate-of-rotation tensor, $\overline{\mathbf{W}}$, in its respective original formulation, yielding

$$Q_s = \frac{1}{2}\left(||\overline{\mathbf{W}}||^2 - ||\mathbf{D}||^2\right) > 0 \,. \tag{D.2}$$

Applying the same methodology to the Δ and λ_2-criteria, their objective versions take the form of Eqs. (D.3) and (D.4), respectively.

$$\Delta_s = \left(\frac{Q_s}{3}\right)^3 + \left(\frac{det(\mathbf{D}+\overline{\mathbf{W}})}{2}\right)^2 > 0 \tag{D.3}$$

$$\lambda_2^{\mathbf{D}^2+\overline{\mathbf{W}}^2} < 0 \tag{D.4}$$

D.3 Novel naturally objective criteria

We adopt here a decomposition of the covariant strain acceleration tensor, $\mathbf{M} \equiv \overset{\triangle}{\mathbf{D}}$ (where the triangle indicates the covariant convected time derivative) with respect to the strain rate tensor, $\mathbf{D}$, as discussed in [129]. This decomposition splits tensor $\mathbf{M}$ into two additive parts: a part that is *in-phase* with $\mathbf{D}$, ϕ_M^D, and a part that is *out-of-phase* with $\mathbf{D}$, $\widetilde{\phi}_M^D$. These tensors are defined as

$$\phi_M^D = \mathbb{I}^{DD} : \mathbf{M} \,; \quad \widetilde{\phi}_M^D = \left(\mathbb{I}^{\delta\delta} - \mathbb{I}^{DD}\right) : \mathbf{M} \,, \tag{D.5}$$

where the symbol ":" accounts for the double dot product and $\mathbb{I}^{DD}$ is a fourth order tensor given by

$$\mathbb{I}^{DD} = \sum_{i=1}^{3} \mathbf{e}_i^D \mathbf{e}_i^D \mathbf{e}_i^D \mathbf{e}_i^D \,, \tag{D.6}$$

where $\mathbf{e}_i^D$ is an eigenvector of $\mathbf{D}$ and $\mathbb{I}^{\delta\delta}$ is the fourth order identity tensor.

Aligned to the concepts presented by Haller [122], we can define a ratio, IR, that can be interpreted as a measurer of how tensor $\mathbf{M}$ corroborates the tendency dictated by $\mathbf{D}$ as

$$IR = 1 - \frac{2}{\pi}\cos^{-1}\left(\frac{\left\|\phi_{\mathrm{M}}^{\mathrm{D}}\right\|}{\|\mathbf{M}\|}\right). \tag{D.7}$$

It can be shown that this quantity is the complement with respect to unity to the quantity we would find if we replace ϕ_M^D by $\widetilde{\phi}_M^D$. In this other case this quantity would be a measurer of how tensor $\mathbf{M}$ *defies* the tendency dictated by $\mathbf{D}$.

Because the flow character is, most of the times, anisotropic, we found the necessity to come up with anisotropic ratios that could better represent the competition between the parts that corroborates and defies the $\mathbf{D}$-tendency. Hence, we can define anisotropic ratios depending on the eigendirection of $\mathbf{D}$, as

$$AR(k) = 1 - \frac{2}{\pi}\cos^{-1}\left(\sqrt{\frac{[\mathbf{M}]_{\mathrm{kk}}\,[\mathbf{M}]_{\mathrm{kk}}}{[\mathbf{MM}]_{\mathrm{kk}}}}\right), \tag{D.8}$$

where $[\mathbf{M}]_{kk}$ is an element of the principal diagonal of tensor $\mathbf{M}$ (terms of $\mathbf{M}$ which are *in-phase* with $\mathbf{D}$), and $[\mathbf{MM}]_{kk}$ is an element of the principal diagonal of tensor $\mathbf{M}^2$.

The anisotropic ratios are reorganized so that $AR1 > AR2 > AR3$. The anisotropic ratios are better interpreted together. While the other criteria aim to give an overall verdict, the anisotropic ratios provide a directional information.

D.4 Results and discussions

We discuss here the results obtained with all criteria applied to the instantaneous velocity fields of both Newtonian and viscoelastic channel flows obtained by DNS with the massively parallel algorithm presented by Thais *et al.* [19]. Viscoelastic effects are taken into account by means of the FENE-P model with maximum polymer chain extensibility L equal to 100 and a friction Weissenberg number We_τ (being $We_\tau = \lambda u_\tau^2/\nu$, where λ is the relaxation time scale, u_τ is the friction velocity and ν is the kinematic viscosity of the solution) equal to 115, which leads to a percentage of drag reduction of 62.3%.

It is possible to identify the so called *hairpin vortices* in turbulent boundary layers by the application of classic flow classification criteria (such as Q, Δ and λ_2 criteria). The dynamic evolution of these hairpin vortices have been largely explored in the literature (see, for example, ref. [160] for a remarkable literature review). Regarding non-Newtonian fluids, one of the first analyses of the effects of elasticity on such coherent structures was carried out by Kim *et al.* [35]. In drag-reducing flow, he authors noted that hairpin vortices get larger and weaker due to rotations imposed by the polymer work, which are in opposition to that of the vortices.

Figure D.1 shows the iso-contours of the Q-criterion for both Newtonian (left column) and viscoelastic (right column) fluids at four friction Reynolds numbers, Re_τ = 180, 395, 590 and 1000 (being $Re_\tau = u_\tau h/\nu$, where h is the channel half-gap). Using the Q-criterion, the classic hairpin vortices are recovered for the Newtonian fluid and very similar structures are identified for the viscoelastic cases. Moreover, regardless of the fluid, the quantity of hairpin vortices increases with the friction Reynolds number. The same qualitative results are found for the two other classic criteria cited above (Δ and λ_2) and thus such results are not shown.

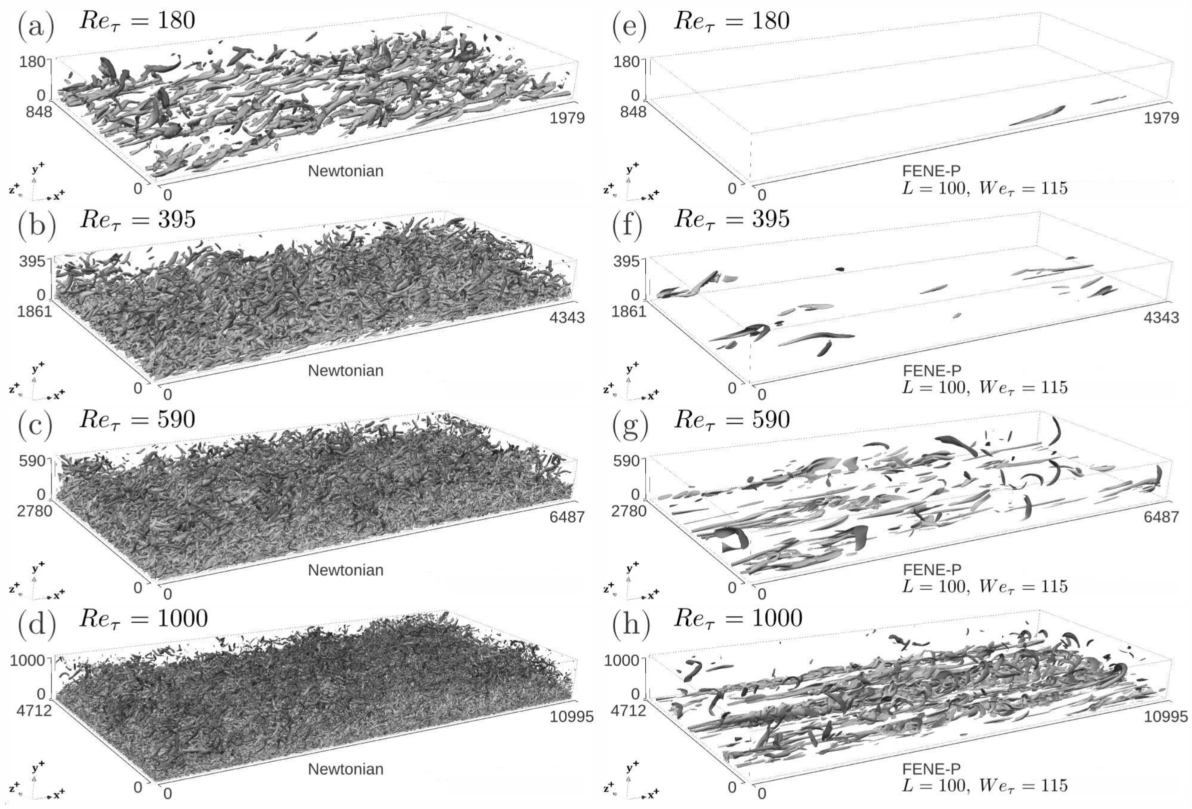

Figure D.1 – Iso-contours of Q-criterion ($Q = 1.5$) for Newtonian (left column) and viscoelastic (right column) fluids at $Re_\tau = 180$, 395, 590 and 1000.

The elastic effect observed in Fig. D.1 is also remarkable. Taking the same friction Reynolds number, the number and the size of hairpin vortices change reasonably. The results show that, for the same value of the Q-criterion (*i.e.*, for the same intensity of rotation) there are less hairpin vortices in the viscoelastic cases than in the Newtonian, which suggests that the intensity of hairpin vortices is reduced, as already observed by Kim *et al.* [35]. Furthermore, hairpin vortices seem to be bigger in the viscoelastic cases.

On the other hand, from the perspective of the objective versions, classic hairpin vortices are no longer observed, as shown in Fig. D.2. In fact, the objective criteria identify swirling-like regions, but their ensemble does not present any well-defined shape.

D.4.1 Thickening buffer layer in viscoelastic flows

Since we could not identify any well-defined shape with the objective criteria, a wall-normal plane placed in the middle of the channel and measuring the half-gap height is investigated bellow.

Aiming to better understand the differences observed between objective and non-objective approaches, the criteria are normalized so that the results are always between 0 and 1. The low values (from 0 to 0.5) represent swirling-like regions, whereas the high

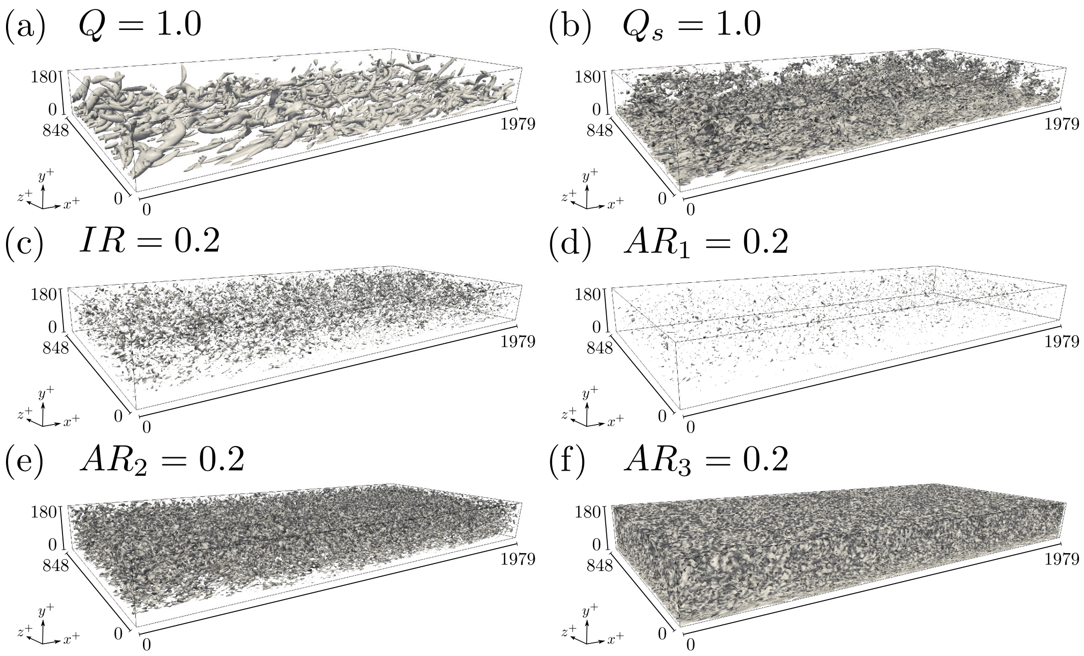

Figure D.2 – Iso-contour for non-objective (a) and objective (d) versions of Q-criterion, and IR (b) and AR (c, e and f) criteria for Newtonian fluid at $Re_\tau = 180$.

values (from 0.5 to 1) represent non-swirling-like regions. If the normalized criteria is equal to 0.5, than, in that point, the intensities of extension and rotation are equivalent. Normalized criteria are marked with a superscript asterisk, except for IR and AR, which are already normalized.

The analysis of the contours of the normalized criteria in wall-normal (xy-) planes enables the observation of an interesting behavior that seems to be related to the drag reduction phenomenon, as depicted in Figs. D.3 and D.4. Firstly, it is important to notice that from the perspective of the classic Q-criterion, the Newtonian flow (Fig. D.3(a)) is globally dominated by regions where the intensity of the rate-of-rotation is similar to the intensity of the rate-of-strain ($Q^* = 0.5$). Nevertheless, there are some swirling-like ($Q^* < 0.5$, or darker) and non-swirling-like ($Q^* > 0.5$, or lighter) regions dispersed in the plane.

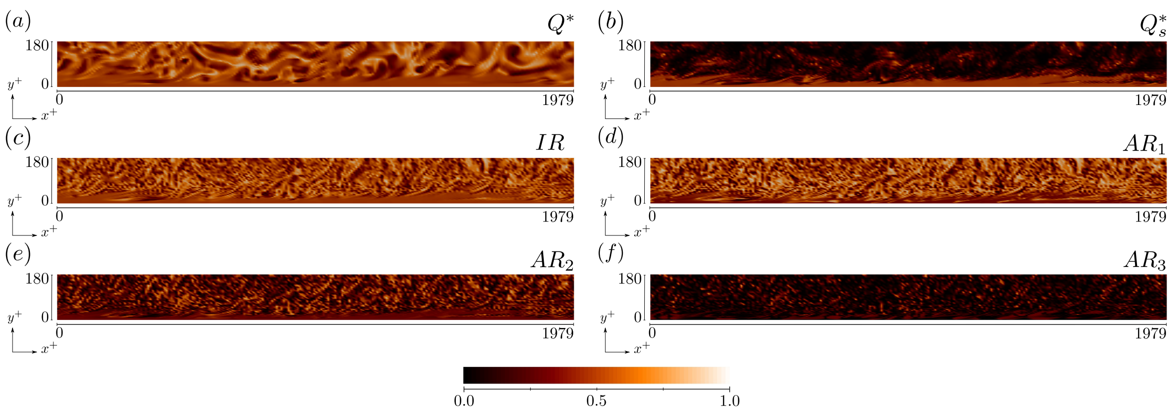

Figure D.3 – Contours of non-objective and objective criteria for Newtonian fluid at $Re_\tau = 180$. The xy-plane is located in the middle of the channel.

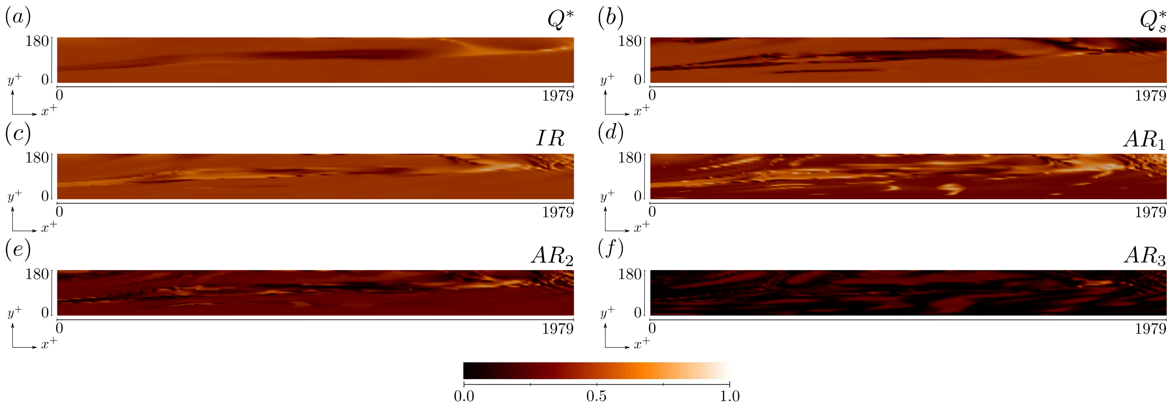

Figure D.4 – Contours of non-objective and objective criteria for viscoelastic fluid with $L = 100$ and $We_\tau = 115$ at $Re_\tau = 180$. The xy-plane is located in the middle of the channel.

On the other hand, when analyzing the same snapshot from the perspective of the normalized objective version of the Q-criterion (Fig. D.3(d)), the flow seems to be swirl dominated ($Q^*_s < 0.5$), except for a thin layer where $Q^*_s \approx 0.5$. However, the other objective criteria (Fig. D.3(b, c, e and f)) present more homogeneous results qualitatively closer to the those of the Q^*-criterion.

At a first impression, the results for the viscoelastic case depicted in Fig. D.4 present, in general, more elongated structures when compared to the Newtonian case (Fig. D.3).

Interestingly, comparing the Newtonian and the viscoelastic results for the Q^*_s-criterion (respectively, Figs. D.3(d) and D.4(d)), it is noteworthy that the thickness of the layer where $Q^*_s \approx 0.5$ increases in the latter case. We believe that this is due to the thickening of the buffer layer caused by the presence of flexible polymers, leading to drag reduction. Such physical effect has been already observed by many authors by both experiments [163] and numerical simulations [5, 8, 11, 12], and has been predicted by the two most important theories on drag reduction phenomenon (Lumley's viscous theory [86], and Tabor and De Genne's elastic theory [88]).

The effect that seems to represent the thickening of the buffer layer is even more evident in Figs. D.5 and D.6, which contain the values of all criteria evaluated in the present work averaged at wall-parallel (xz) planes for Newtonian and viscoelastic fluids, respectively, at $Re_\tau = 180$.

All non-objective criteria depicted in Figs. D.5(a) and D.6(a) present similar behavior. Extensional and swirling motions have the same intensity within the near-wall region and values tend to be slightly extensional near the center of the channel, whereas a very weak rotational tendency is found for the Δ^*-criterion. The major difference is that, for the viscoelastic case, the criteria are equal to 0.5 even near the center of the channel, which is probably related to the thickening of the buffer layer.

Regarding objective criteria in Figs. D.5(b) and D.6(b), as predicted by Figs. D.3 and D.4, the IR criterion present a behavior which is similar to those of non-objective criteria. It can be noticed that $AR1 \geq 0.5$ and $AR3 \leq 0.5$ in the whole domain. This fact suggests that there is no perfect extension, where extension acceleration overcomes rotation acceleration in the three directions, nor perfect swirling structure where the opposite happens. What we have, instead, is a situation where at every point of the domain there are directions where extension overcomes rotation and vice-versa. The quantity $AR2$ shows that near the wall, the swirling structure has one direction extensional-dominant,

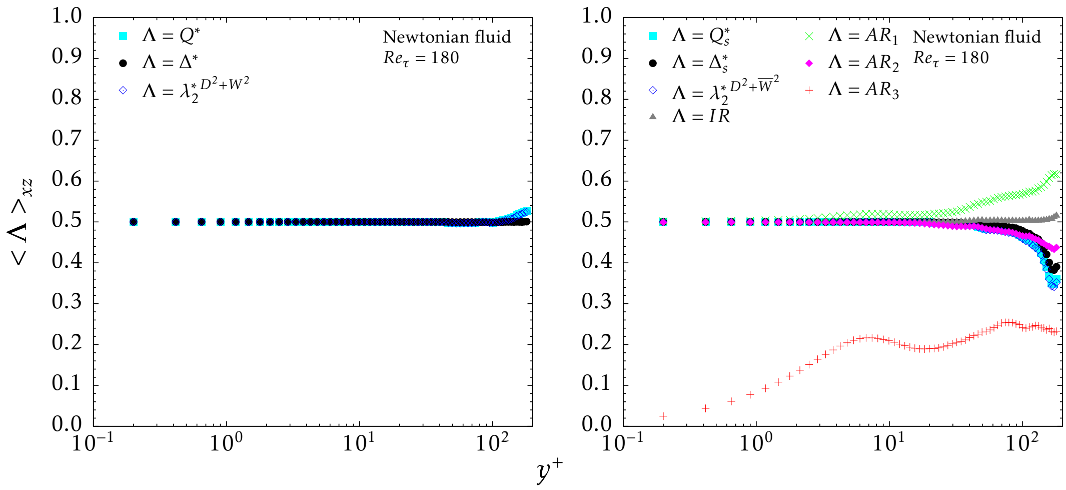

Figure D.5 – xz-plane averaged values of non-objective (left) and objective (right) criteria for Newtonian fluid at $Re_\tau = 180$.

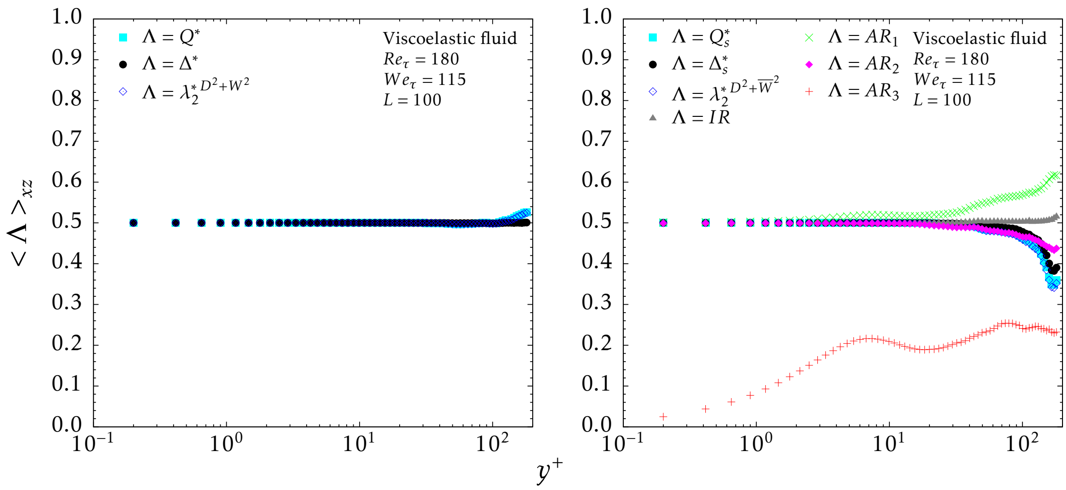

Figure D.6 – xz-plane averaged values of non-objective (left) and objective (right) criteria for viscoelastic fluid with $L = 100$ and $We_\tau = 115$ at $Re_\tau = 180$.

another swirling-dominant, and a neutral direction. Near the centerline there are two directions where rotation dominates.

The objective versions of the classic criteria present behavior which are qualitatively the same. In the near-wall region, they follow the tendency of their non-objective counterpart, with a first layer around 0.5. However, near the center of the channel, these criteria tend to identify swirl-dominated regions, opposing the modest tendency of identifying extensional motion presented by the corresponding classic non-objective criterion (except for Δ^*) in this region. Moreover, because the swirl motion identified by such criteria is reasonably more intense, the deviation gets more evident, enabling an estimation of the thickening, due to the presence of polymers, of the layer related to the buffer layer. Comparing the results of the objective version of the classic criteria in Figs. D.5(b) and D.6(b), the thickness of the near-wall layer where the value of the criteria is around 0.5 increases from $y^+ \approx 8$ in the Newtonian case to $y^+ \approx 40$ in the viscoelastic case.

It is important to remark that the same analysis have been carried out for $Re_\tau = 395$, 590 and 1000. Nevertheless, the thickness of the buffer layer seems to depend more on the percentage of drag reduction than on the Reynolds number. The results at higher friction Reynolds are qualitatively similar to the case at $Re_\tau = 180$ differing basically by the possibility to go further on the y^+ scale.

Acknowledgements

This work was granted access to the HPC resources of IDRIS under the allocation 2014-i20142b2277 made by GENCI. The authors would also like to express their acknowledgement and gratitude to the Brazilian Scholarship Program *Science Without Borders*, managed by CNPq (National Council for Scientific and Technological Development), for the partial financial support for this research.

Contents

Numerical simulation of turbulent viscoelastic fluid flows
Flow classification and preservation of positive-definiteness of the conformation tensor

Abstract

The purpose of this work is to provide an enhancement of the knowledge about the polymer-induced drag reduction phenomenon by considering some aspects of its numerical simulation and the changes that occur in the flow kinematics. In the first part, the square root and kernel root-k formulations for the conformation tensor in the FENE-P model were implemented and showed to preserve the positiveness of the conformation tensor. However they led to numerical divergence due to the loss of boundedness of the conformation tensor. This constraint was violated even with the inclusion of artificial diffusion. The damping effect of artificial diffusion helped to ensure numerical stability, but led to relative drag reduction from 22% to 42% lower than expected from traditional methods. In the second part, the composition of two classic flow classification criteria was evaluated by means of the dynamic terms in the evolution equation of the strain-rate tensor. The λ_2-criterion was criticised due to the lack of clarity concerning some assumptions. The analyses of the Q-criterion suggest that the well-known weakening of vortical regions in drag-reducing flows is a consequence of non-linear interactions between the polymer stress and flow dynamics. Moreover, the use of objective flow classification criteria provided richer information concerning the flow kinematics. Finally, the thickening of the buffer layer in drag-reducing flows was visualised.

Keywords: viscoelastic flows, flow classification, vortex identification, objectivity, turbulent channel flow, drag reduction, turbulence, direct numerical simulation, artificial diffusion, FENE-P, conformation tensor

---

Simulation numérique d'écoulements turbulents de fluides visco-élastiques
Classification d'écoulements et préservation de la positivité du tenseur de conformation

Résumé

Le but de ce travail est de fournir une amélioration de la connaissance sur le phénomène de la réduction de la traînée induite par polymère en considérant certains aspects de sa simulation numérique et les changements qui se produisent dans la cinématique de l'écoulement. Dans un premier temps, les transformations du type racine carrée et *kernel* racine-k pour le tenseur de conformation du modèle FENE-P ont été implémentées afin d'assurer la positivité du tenseur de conformation. Cependant, ces approches divergent en raison du caractère non-borné du tenseur de conformation. Cette contrainte n'a pas été respectée, même avec l'inclusion de diffusion artificielle. L'effet d'amortissement de la diffusion artificielle a permis d'assurer la stabilité numérique, mais il aboutit à une réduction de la traînée relative de 22% à 42% plus faible que prévue par les approches standards. Dans un second temps, on a évalué la composition de deux critères classiques de classification d'écoulements à l'aide des termes dynamiques dans l'équation d'évolution du tenseur de déformation. Le critère λ_2 a été critiqué en raison du manque de clarté concernant certaines hypothèses. Les analyses du critère Q suggèrent que l'affaiblissement bien connu des régions tourbillonnaires dans les écoulements avec réduction de traînée est une conséquence des interactions non linéaires entre la tension polymérique et la dynamique de l'écoulement. En outre, l'utilisation de critères de classification d'écoulements objectifs a fourni des informations plus riches concernant la cinématique de l'écoulement. Enfin, l'épaississement de la zone tampon dans les écoulements avec réduction de traînée a été visualisé.

Mots clés : écoulements viscoélastiques, classification d'écoulements, identification de vortex, objectivité, écoulement turbulent en canal plan, réduction de la traînée, turbulence, simulation numérique directe, diffusion artificielle, FENE-P, tenseur de conformation

---

Laboratoire de Mécanique de Lille (LML)
Boulevard Paul Langevin – Cité Scientifique – 59655 Villeneuve d'Ascq Cedex – France